Cranfield UNIVERSITY

School of Mechanical Engineering

PhD Thesis 1996

Stephen C. Harding

Investigation into Mixing and Combustion in an Optical, Lean, Premixed, Prevaporised Combustor.

This thesis is submitted in partial fulfilment of the requirements for the degree of Doctor of Philosophy.

Supervisor: Professor D.A. Greenhalgh Cranfield University, School of Mechanical Engineering, Cranfield, Bedford. MK43 0AL

ABSTRACT

Gaseous and particulate emissions from combustion devices are implicated in many atmospheric environmental pollution concerns. Lean, premixed, prevaporised combustion is widely regarded as the most practical technique for reducing these emissions from gas turbine combustors to levels which will not cause significant environmental impact. This technique has been proved to be capable of reducing emissions of oxides of nitrogen to ultra low levels. However, further understanding and development is necessary before LPP combustors can be reliably fitted in production gas turbines. Particular problems are flashback and autoignition in the premixer and achieving a stable, lean primary zone. This thesis details a comprehensive series of measurements made upon a realistic LPP gas turbine combustor. The measurements elucidate the important, fundamental, physical processes which govern the performance of LPP combustors whilst providing a challenging and complete data set for CFD model validation. These measurements include data on the premixer velocity field, the fuel droplet size and velocities distributions, the fuel concentration in the premixer and primary zone and the combustion temperature. This has been interpreted to provide useful information such as the location and rates of fuel-air mixing, the proportion of temporal to spatial fluctuation in fuel concentration, the premixer swirl number, the flame brush thickness and the effect on mixing and placement of fuel fraction boiling point. It has been found that for mixing multi-component fuels in a duct, the rate of mixing and physical placement will depend on the boiling fraction of the fuel. High boiling point fractions evaporate later, experience longer droplet trajectories and mix much slower when compared to lower boiling fractions.

Acknowledgements

I would like to gratefully acknowledge the technical support and advice from Lesley Hawkins, Mike Spooner and John Richardson at Rolls Royce, Derby, also Dick Kennewell, Brian Scully, Dave Whittington, Dick Dewar, Alan Hutchins and Barry Phillips at Cranfield. I would also like to acknowledge the financial support from Rolls Royce plc. and the EPSRC. I am also indebted to my supervisor and colleagues for their advice and assistance throughout my PhD in particular Professor Doug Greenhalgh, Russel Lockett, Nigel Tait and Nick Farrugia. Finally, I would like to thank my Mum and Dad for their support throughout my education and well everything!

CONTENTS

List of Figures

List of Tables

Notation

A	constant
A_i	area of interface
A_l	cross sectional flow area
A_{21}	Einstein coefficient for spontaneous emission
B_{12}	Einstein coefficient for the rate of absorbtion of photons
B_{21}	Einstein coefficient fot the rate of stimulated emission
c'^2	variance fuel concentration
$\bar{c}$	mean fuel concentration
C	Melling's parameter
C_1	convection to the combustor liner wall
C_2	convection from the combustor wall
d	diameter
$d_{x,y,f,z}$	beam dimensions
D_a	Damkholer number
D_L	diameter of the combustor liner
D_p	mass of any pollutant emittedduring the landing and take offf cycle.
E	activation energy
$\dot{F}$	fuel flow
F_{00}	thrust setting (rated output of engine)
h	Planck's constant
I	incident light intensity
I_{flux}	Mie scattered light intensity
I_0	incident light intensity
I_R	Rayleigh scattering intensity
I_S	intensity of incident light at saturation of transition
k	calibration constant for Rayleigh calculation
k	turbulent kinetic energy

k_a	thermal conductivity of the film cooling
k_g	thermal conductivity of the gas
K	conduction along the combustor liner wall
K_{1-2}	conduction through the combustor liner wall thickness
K_f	rate of formation
l	beam length
n	Arhennius constant
n	refractive index
N	number of molecules in the laser sheet volume
N_1	number of molecules in the lower state
N_2	number of molecules in the upper state
m	mass flow
m	mass flow ratio in heat transfer calculations
m_g	mass flow of gas
P	pressure
P_s	static pressure
P_D	dynamic pressure
q	air to fuel ratio
Q_{21}	overall quenching rate
R	universal gas constant
R_{ex}	Reynold's number of film cooling
R_1	radiation to the combustor liner wall
R_2	radiation from the combustor liner wall
R_f	fluorescence intensity
s	height of film cooling slot
s_{refr}	imaged fringe spacing
s'	detector spacing
t	time
T	temperature
T_{fl}	temperature of flange
T_g	temperature of the gas

t_w	thickness of the wall
T_{w1}	temperature of inside wall of combustor liner
T_{w2}	temperature of outside wall of combustor liner
T_{wad}	adiabatic temperature of the wall
U	velocity
$\tilde{U}$	fluctuating velocity
x	distance from film cooling entry
ν_D	Doppler frequency
θ	half angle in PDA calculation
Ω	solid cone angle
θ	phase angle (PDA)
θ	detection optics angle (PDA)
ε_g	emissivity of the gas
ε_w	emissivity of the wall
Ø	equivalence ratio
λ	wavelength of light
λ_*	fringe spacing
μ	dynamic viscosity
μ_a	dynamic viscosity of the air
μ_g	dynamic viscosity of the gas
ν	light frequency
π_{00}	pressure ratio
θ_K	Kolmogorov time scale
ρ	density
σ	Stefan-Boltzman constant
σ	Mie scattering coefficient of particles
σ_{eff}	effective Rayleigh cross section
τ	autoignition delay time

Abbreviations

AFR	air fuel ratio
CCD	charged coupled device
CFD	computational fluid dynamics
CLIPS	Cranfield laser image processing software
DEC	Digital Electronic Corporation
DLE	dry low emissions
EINOx	NOx emission index
FFT	fast Fourier transform
HOMREA	homogenous reaction
HV	high voltage
I.C.	internal combustion
LDA	laser Doppler anemometry
LDI	lean, direct injection
LDV	laser Doppler velocimetry (same as LDA)
LIF	laser induced fluorescence
LPP	lean, premixed,prevaporised combustion
NOx	oxides of nitrogen
PAH	polyaromatic hydrocarbons
PAN	peroxy acetyl nitrates
PIV	particle imaging velocimetry
PDA	phase Doppler anemometry
pdf	probability distribution function
PLIF	planar laser induced fluorescence
PPO	2,4, diphenyloxazole
ppm	parts per million by volume
ppmv	parts per million by volume
ΔP	delta pressure
RQL	rich burn, quick quench, lean burn

SMD	Sauter mean diameter
SNCR	selective non-catalytic reduction

1. INTRODUCTION

A comprehensive series of measurements have been made on a realistic, lean, premixed, prevaporised (LPP) combustor in order to elucidate the important, physical processes which govern the performance of LPP combustors. The measurements have been made with a variety of non-intrusive, laser techniques complemented by conventional measurements and may be used for computational fluid dynamic (CFD) model validation.

Concern over the effect that increasing pollution from combustion devices is having on the atmosphere is driving researchers into developing dry low emission (DLE) combustion strategies. This research encompasses combustion in internal combustion engines and gas turbines for road, sea and air transport, power generation and many other applications. Lean, premixed, prevaporised combustion has been proved to be capable of reducing unwanted emissions from gas turbine combustors to levels which would have a much improved, reduced environmental impact. However, even though lean, premixed gas fuelled industrial gas turbines are in service further understanding and development is required before liquid fuelled LPP combustors can be reliably employed in aero gas turbines. LPP combustion relies upon reducing emissions of oxides of nitrogen by efficiently burning fuel in a homogeneously lean, low temperature primary zone. Fuel and air are mixed into a uniform, fuel lean mixture in a premixing duct prior to combustion. The mixture is then stabilised in a primary zone which effectively burns the fuel to completion whilst keeping the flame temperature below the threshold at which there is significant formation of thermal NOx (≈1800 K). Difficulties arise from the creation and existence of a high temperature mixture of fuel and air. A high pressure mixture of kerosene and air at a typical preheat temperature of 1000 K will autoignite after a delay of only a few milliseconds. This leaves a very short time during which a uniform lean fuel air mixture can be created. Furthermore, the mixture velocity needs to be maintained above the mixture's turbulent flame speed at all points in the combustor premixer to prevent flame flashback. Combustion in the lean primary zone of an LPP combustor has to be stabilised throughout all the gas turbine cycle. Conventional combustors are inherently more stable than LPP combustors since the distribution of local stoichiometries present, provides some pockets of stoichiometric combustion

which support less stable areas. Methods of stabilising lean, premixed combustion need to be incorporated into the combustor design.

An experimental rig has been designed and commissioned comprising an optical LPP combustor for taking measurements upon. The combustor is operated at inlet temperatures, air fuel ratio's (AFR's) and a combustor pressure drop (ΔP) realistic of a gas turbine but runs at atmospheric pressure. Measurements have been made on the combustor using a variety of non-intrusive laser diagnostic techniques alongside conventional measurements such as gas analysis.

These measurements include data on the premixer velocity field, the fuel droplet size and velocities distributions, the fuel concentration in the premixer and primary zone and the combustion temperature. This has been interpreted to provide useful information such as the location and rates of fuel-air mixing, the proportion of temporal to spatial fluctuation in fuel concentration, the premixer swirl number, the flame brush thickness and the effect on mixing and placement of fuel fraction boiling point. It has been found that for mixing multi-component fuels in a duct, the rate of mixing and physical placement will depend on the boiling fraction of the fuel. High boiling point fractions evaporate later, experience longer droplet trajectories and mix much slower when compared to lower boiling fractions.

This thesis comprises a literature survey on LPP combustion, the background to environmental concerns and emissions formation in combustion, emissions regulations and a brief review of techniques for reducing combustion emissions. This is followed by a theoretical and experimental investigation into partially, premixed combustion as stabilised on a counterflow burner. A chapter follows detailing the design, commission and characterisation of an optical LPP combustor. Reviews of basic laser diagnostic theory are included in the chapters using such techniques. Rayleigh and laser induced fluorescence are reviewed in chapter 4, Mie scattering and laser Doppler anemometry are reviewed in chapter 6 and Phase Doppler anemometry is reviewed in chapter 7. Chapters 6 to 9 detail the measurements made on the LPP combustor with interpretation of the results. These include air velocities in the premixer, velocity and size distributions of droplets in the premixer, fuel measurements in the premixer and fuel and temperature measurements in the combustor primary zone. Finally, comparisons with preliminary

CFD modelled data is shown. A discussion and conclusion is included each chapter. The 'Conclusions' chapter, summarises all the measurements and their interpretations and identifies the important conclusions revealed by this work.

2. BACKGROUND

2.1 Environmental Concerns

The driving force behind low emission combustion research is the rising concern over the environmental impact of combustion products. All combustion devices emit unwanted pollutants alongside water and carbon dioxide. These are typically nitric oxide, nitrogen dioxide, nitrous oxide, carbon monoxide, unburnt hydrocarbons (including polyaromatic hydrocarbons), aldehydes, HNO_3, oxides of sulphur, compounds like peroxyacetyl nitrates and trace quantities of heavy metals. Emissions from combustion devices including aero and ground based gas turbines are partly responsible for effects such as global warming (the greenhouse effect), photochemical smog, the thinning of the stratospheric ozone layer and acid rain.

Oxides of nitrogen (NO and NO_2) and nitrous oxide (N_2O) contribute to all of these effects. NO forms NO_2 in gas turbine exhausts and in the atmosphere where it becomes an important constituent of photochemical smog. Oxides of nitrogen also form HNO_3 in the troposphere where they cause acid rain. Nitrous oxide is a greenhouse gas and remains in the stratosphere for around 170 years (Hayhurst 1992).

Stratospheric emissions of nitrogen oxides are of major concern due to their effect on the ozone layer. Tropospheric NOx emissions cannot affect stratospheric ozone chemistry since they cannot easily cross the tropopause. Current aircraft already fly in the upper troposphere and in the lower stratosphere. There is much interest in high speed supersonic civil aircraft flying in the mid stratosphere (18-22 km) for reasons of fuel economy where they would deposit their emissions directly in the ozone layer. The estimation of ozone depletion due to emissions of oxides of nitrogen is difficult to accurately quantify for a number of reasons. These include the availability of adequate data, complexities arising from other ozone reducing species such as chlorine, methane, carbon dioxide, nitrous oxide, HOx and water, complex atmospheric physics and the need for high resolution large scale models. NO_2 can actually serve to reduce ozone

depletion in the polar regions by acting as a sink tying up chlorine. The effect of nitrous oxide on stratospheric ozone is further complicated since it is already produced in significant quantities by natural bacteria.

Emissions of carbon monoxide (CO) are well known to be toxic to animal and plant life and CO is a known greenhouse gas. Unburnt hydrocarbon (UHC) emissions are carcinogenic, toxic and a constituent of smog. At ground level, atmospheric partially oxygenated hydrocarbons are irritants and odourants. The major constituents of photochemical smog are ground level ozone, NO_2 and peroxyacetyl nitrates (PAN). PAN are formed from oxidising reactions of hydrocarbons. Ozone is created in a reaction in the lower troposphere with NO_2. Photochemical smog is a major cause of urban asthma, bronchitis and other lung complaints and also irritates the eyes and lachrymal organs.

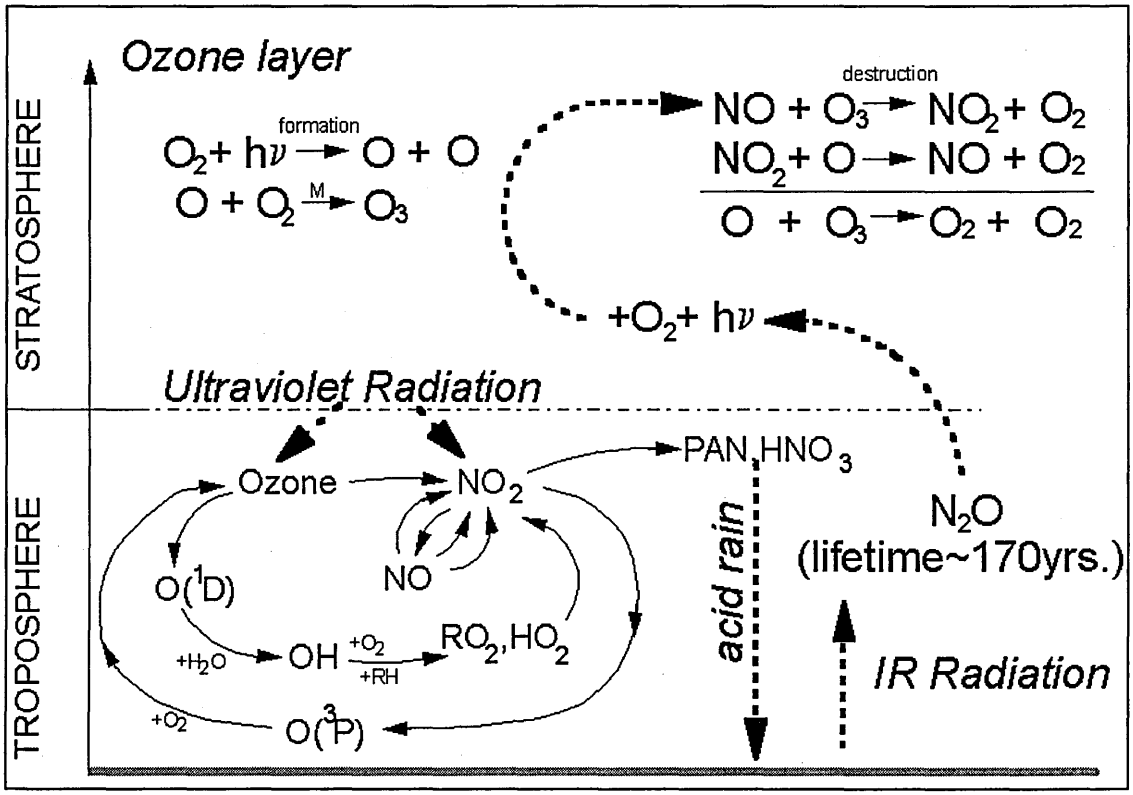

Figure 2.1 Environmental Concerns: Ozone chemistry, Photochemical smog, Acid rain and Global warming.

Soot emissions from combustion devices are toxic, cause soiling and visible pollution. Particulates of soot can also act as a carrier to the lungs for carcinogenic substances like polyaromatic hydrocarbons (PAH). The other, minor, unwanted emissions from combustion such as halogens, heavy metals and oxides of sulphur are either removable by their exclusion from fuel or only emitted in trace quantities as in the case of aviation fuels.

The inadequate understanding of environmental issues, particularly global warming and to lesser extent ozone depletion prevents their accurate quantification. Most legislation is therefore aimed at reducing emissions to the minimum levels attainable by affordable, non-hazardous technology until a non-environmental impact situation can be achieved.

2.2 Pollutant Formation in Combustion

The production of emissions in and after combustion devices is a complex process controlled by many factors. These include the combustion chemistry, the fuel-air mixing, the turbulence field, the fuel injection method, the air dilution processes, the combustion device geometry and combustion gas residence times, many of which are interdependent. The following is a review of combustion emission chemistry.

2.2.1 NO_x and N_2O Formation

Oxides of nitrogen and nitrous oxide are all formed at different rates in combustion. There are four important NO production mechanisms in flames; thermal NO_X which is produced in hot zones (over 1800 K), prompt NO_X which formed in the very fast Fenimore reaction occurring predominantly in fuel rich zones, NO_X formed through the fast nitrous oxide mechanism and fuel NO_X which is an almost complete conversion of fuel bound nitrogen to NO. The in-flame production of NO is greater than NO_2 which is in turn much greater than N_2O. Most of the total NO_2 emission from gas turbines is formed non-exothermically in the dilution zones, turbine and exhaust. The relative contribution of these mechanisms to NOx production depends on the combustion

stoichiometry, the fluid strain rates, the residence times, the temperature field and pressure.

In premixed flames, the equivalence ratio and hence the temperature is the dominant controlling factor for thermal NO production so that theoretically NO_X production would peak at Ø = 1. NO production peaks just on the lean side of stoichiometric due to the lower specific heat of the products of lean combustion. In diffusion flames, even where the stoichiometry is lean, the flame is adiabatic and significantly more NO_X is produced than equilibrium would predict. Some NO_X reduction takes place in fuel rich flames.

There is no pressure dependence of NO production in perfectly premixed flames (Correa 1992). In non-premixed flames, high local temperatures at high pressure increase NO production, whilst at low pressures super-equilibrium O atom concentration accelerates NO production. The NOx production mechanisms in lean, premixed flames are too slow and do not couple with turbulence. This implies that NOx emissions are relatively independent of flameholder type or geometry (Keller 1994, Correa 1992).

2.2.1.1 Thermal NO_X

Thermal NO_X is produced in hot regions of combustion by the following reactions known as the Zeldovich reactions. The rate constants below are supplied by Glassman.

$$N_2 + O \Leftrightarrow NO + N \qquad \text{where } K_f = 2.0\times10^{14} T^0 . e^{\left(\frac{-76,500}{RT}\right)} \qquad [1]$$

$$N + O_2 \Leftrightarrow NO + O \qquad \text{where } K_f = 6.4\times10^{9} T^1 . e^{\left(\frac{-6,280.0}{RT}\right)} \qquad [2]$$

$$N + OH \Leftrightarrow NO + H \qquad \text{where } K_f = 3.8\times10^{13} T^0 . e^{\left(\frac{-0.0000}{RT}\right)} \qquad [3]$$

These reactions form the most productive NO_X formation mechanism. The first two reactions are endothermic and rely on the existence of atomic oxygen and atomic

nitrogen, which only occur in significant concentrations above 1700 K. Since the reactions are catalytic the monatomic species are conserved and the rate of NO production is high. The final fast reaction requires two radicals and is only important at higher temperatures. This means that the creation of thermal NO_X can be eliminated by keeping flame temperatures below this level. Since this mechanism is highly temperature dependant due to its high activation energy, thermal NO_X production can be changed by a factor of two by perturbations of only 90 K from mean flame temperatures of 2200 K. The reaction times are always longer than the flame front residence time. However, the Zeldovich reactions are relatively fast and as such thermal NO_X can only be reduced minimally by shortening residence times and most effectively at high temperature and at non-lean conditions. Reducing oxygen levels will also reduce the NO_X formation rate. Thermal NOx production will therefore be most favoured by maintaining high temperatures in the presence of oxygen. In lean, premixed systems, NOx production is minimised, by controlling peak flame temperature to below 2000 K and minimising residence time.

Significant levels of thermal NO_X can also be created due to super equilibrium levels of O and OH radicals. Bowman (1992), found that in experiments in stirred reactors burning low pressure, lean, premixed flames that super equilibrium thermal NO_X can be a major contributor to total NO_X emissions.

2.2.1.2 Prompt NO_X

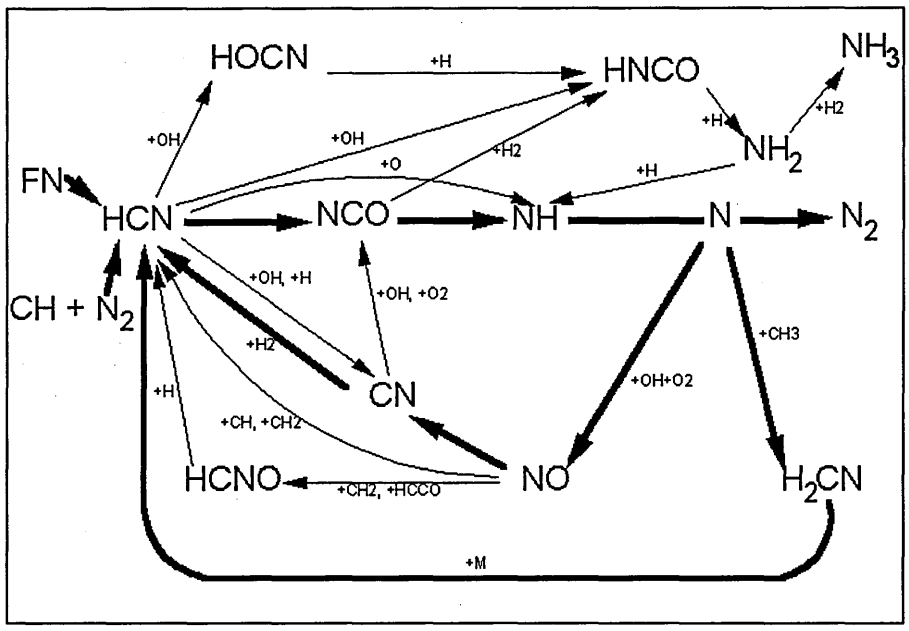

2.2 The Prompt NOx Mechanism

Prompt NO_X was first discovered by Fenimore (1970), observing the non-zero NO level at the flame front in a flat hydrocarbon flame. 'Prompt' or rapidly formed nitric oxide can be created by three mechanisms; thermal NO_X enhanced by rapidly formed super equilibrium concentrations of radicals, NOx formed through the nitrous oxide mechanism and through the prompt NO_X mechanism suggested by Fenimore. From here on the term 'Prompt NOx' is used only to describe the mechanism stated by Fenimore. Prompt NO_X is a very fast mechanism and has a complex reaction scheme. The scheme relies on the presence of hydrocarbon species and is therefore not apparent in pure hydrogen fuel flames. Prompt NO_X is usually only significantly produced in the flame front and in fuel rich areas of flames peaking at equivalence ratios of about 1.4 (depending on the fuel). As the flame becomes leaner, there is a transformation of NO_X production from prompt to thermal mechanisms. Prompt NO_X is typically responsible for 0-30 ppmv of the products in conventional gas turbine combustors. In lean combustion ($\emptyset < 0.5$) prompt NOx again becomes a significant NOx production mechanism relative to total NOx production.

The main reactions involved in prompt NO_X are shown below.

$$CH + N_2 \Leftrightarrow HCN + N \quad [4]$$

$$CH_2 + N_2 \Leftrightarrow HCN + NH \quad [5]$$

$$CH_2 + N_2 \Leftrightarrow H_2CN + N \quad [6]$$

$$C + N_2 \Leftrightarrow CN + N \quad [7]$$

These reactions are predominant in rich zones where the CH_X species are common. The first reaction has a small activation energy (14-22 kcal/mol) and being the dominant reaction means that prompt NO_X is most noticeable at low temperatures. The reactions involving CH_2 are endothermic and have a large activation barrier. These reactions produce pools of HCN and NH radicals which then use O and OH to produce NCO. The NCO then reacts with H atoms to give NH followed by the nitrogen atom in the reactions listed below. The rapidly formed N atoms are then either converted to N_2 or NO in the last two Zeldovich reactions listed above [2,3].

$$HCN + O \Leftrightarrow NCO + H \quad [8]$$

$$NCO + H \Leftrightarrow NH + CO \quad [9]$$

$$NH + H \Leftrightarrow N + H_2 \quad [10]$$

As the lean flame becomes more rich, the concentrations of O and OH deplete reducing prompt NO_X. Under fuel rich conditions, NO reacts with C atoms to return to CN and HCN whilst N atoms react with methyl radicals as follows:

$$N + CH_3 \Leftrightarrow H_2CN + H \quad [11]$$

The H_2CN then reacts with a third body losing H to form HCN in the reaction.

$$H_2CN + M \Leftrightarrow HCN + N + M \quad [12]$$

Hence, when the flame is quite rich some N atoms are converted to N_2, and some nitrogen is tied up in a cycle between N and HCN. As the condition becomes leaner,

and the CH_3 radicals concentration depletes and N atoms can be converted directly to NO.

NO concentrations have been observed to become depleted in very rich, premixed flames (Gupta 1991). Bowman (1992) suggests also that in the early flame development, NO can be converted to HCN by CH_x (x=1,2,3) species where it may eventually re-occur as NO or N_2 as in the above mechanism.

2.2.1.3 Nitrous Oxide Mechanism

Nitric oxide may also be formed through the nitrous oxide mechanism (Malte 1974). Nitrous oxide is a largely intermediate species in combustion but can play an important role in the creation of nitric oxide particularly in lean, methane flames (Bowman 1992). At high temperatures nitric oxide is formed in the flame front as below in a recombination reaction from N_2 and O involving a third body.

$$N_2 + O + M \Leftrightarrow N_2O + M \qquad [13]$$

In lower temperature flames (less than 1350 K), nitrous oxide is formed via the following reaction with HO_2 (Lewis 1993).

$$HO_2 + N_2 \Leftrightarrow N_2O + OH \qquad [14]$$

The nitrous oxide then has one of four routes; dissociation with a third body (reverse of reaction [13]), dissociation through H attack, dissociation through O attack and conversion to NO [18]. Above 1500 K, nitrous oxide has a residence time of less than 10 ms, and will only survive in significant quantities if the removal species are quenched.

$$N_2O + H \Leftrightarrow N_2 + OH \qquad [15]$$

$$N_2O + O \Leftrightarrow N_2 + O_2 \qquad [16]$$

$$N_2O + OH \Leftrightarrow N_2 + HO_2 \quad [17]$$

$$N_2O + O \Leftrightarrow NO + NO \quad [18]$$

Reaction [15] is most common in fuel rich flames, whilst reactions [16,17,18] are obviously more prevalent in lean flames. The nitrous oxide mechanism is most prominent in low temperature flames and CO flames where the H attack reaction cannot occur. This is likely to be a major contributor to NO_X in lean premixed combustion. As premixed flames become leaner, the relative contribution of NOx from the nitrous oxide mechanism and from super equilibrium thermal NOx increases. In LPP combustors delivering sub 15 ppm NOx, thermal NOx becomes negligible and most of remaining NOx is produced via the nitrous oxide mechanism with little being contributed through the prompt mechanism (Nicol 1995, Correa 1992). Experiments and chemical kinetic modelling by Steele burning CH_4 and CO flames attempted to identify which NOx mechanisms were responsible for NOx creation. They estimate that for methane flames the percentages of nitrous oxide, Zeldovich and prompt mechanisms were 35:50:15 at 1850 K.

2.2.1.4 Fuel NO_X

Fuel NOx arises from the almost complete conversion of nitrogen bound to fuel molecules to nitric oxide. Its production is greatest in regions of lean and stoichiometric combustion. Fuel nitrogen is broken down to form cyano species, mainly HCN and CN, from where it takes the same path as prompt NO_X. The reactions which convert fuel nitrogen to HCN are very fast as are the oxidation reactions of HCN to NO and occur on the same time scale as important combustion initiating chain branching reactions. Hence, controlling fuel NO_X is difficult and can only be reduced slightly by thermal quenching in fuel lean conditions or by burning under very fuel rich conditions to convert nitrogen to N_2 as per prompt NO_X.

Kerosene contains no relevant quantities of fuel bound nitrogen and therefore fuel NO_X is of little interest to aero LPP combustors. For fuel nitrogen concentrations below

0.5%, the conversion to NO is typically 100% efficient in fuel lean flames. Above these levels the conversion becomes less efficient and will increase with flame temperature. The fuel nitrogen bearing compound bears no effect on the production of fuel NO_X.

2.2.1.5 Nitrous Oxide Formation

Nitrous oxide is emitted in very small quantities from gas turbines; typically 1-2 ppm. However, due to its very long lifetime in the troposphere it is an active part of ozone depletion chemistry and is an important greenhouse gas. Nitrous oxide measurements can easily be exaggerated by probe sampling. N_2O formation is particularly problematic to combustion devices using exhaust catalysts and in fluidised bed combustion. Nitrous oxide is produced by the reactions listed in section 2.2.1.3 and by the reactions shown below (Hayhurst 92). Reaction [19] dominates under low temperature conditions, whilst reactions [20,21] dominate under fuel rich conditions. Reaction [21] is only relevant at high temperatures where there is a significant O atom concentration.

$$NH + NO \Leftrightarrow N_2O + H \quad [19]$$

$$NCO + NO \Leftrightarrow N_2O + CO \quad [20]$$

$$N_2 + O + M \Leftrightarrow N_2O + M \quad [21]$$

N_2O is removed by a very fast and important reaction with atomic hydrogen shown below and reactions [16,18] stated earlier.

$$N_2O + H \Leftrightarrow N_2 + OH \quad [22]$$

$$N_2O + OH \Leftrightarrow N_2 + HO_2 \quad [23]$$

Martin (1990), state that for H_2 - O_2 - Ar - N_2 flames that the dominant nitrous oxide formation mechanisms involved NH_X and NO reacting to nitrous oxide and H_X. These reactions exhibit a weak temperature dependence. There is a strong temperature dependence for the fast nitrous oxide removal reaction [22] and the less important

removal channel with OH [23]. Hence, N_2O emissions can be increased by rapid quenching, impeding the N_2O removal channel.

2.2.1.6 NO_2 formation

Nitrogen dioxide is mostly formed at low temperatures in the gas turbine dilution zones, turbine and exhaust when high concentrations of NO are present and in combustion where large quantities of excess air exist. NO_2 is more stable at low temperatures than NO. For example, in combustion with a 0.1 ms residence time at 700 K the exhaust NO_X comprises 25% NO_2 and 75% NO, whilst at similar conditions at 900 K only 6% of exhaust NO_X comprises NO_2. Actual concentration measurements of NO_2 from combustion devices have been demonstrated to become easily exaggerated by quenching effects and catalysis in the sampling probe.

The principal reaction forming NO_2 at near flame temperatures is with the radical HO_2 (Bowman 1992). NO_2 is also formed in a reaction with ozone as in the troposphere.

$$NO + HO_2 \Leftrightarrow NO_2 + OH \qquad [24]$$

$$NO + O_3 \Leftrightarrow NO_2 + O_2 \qquad [25]$$

NO_2 may also be formed by the following self catalysing reaction in the presence of high NO concentrations. This reaction is favoured in conditions with low temperatures and low hydrocarbon concentrations as in a combustor exhaust.

$$NO + O_2 \Leftrightarrow NO_2 + O \qquad [26]$$

NO_2 is conserved if it is rapidly quenched as in highly turbulent flames with cold dilution air since HO_2 is more abundant in the quenched areas. However, NO_2 is removed by the following fast removal channels making it a largely transient species in combustion. The following reactions are common at high temperatures.

$$NO_2 + H \Leftrightarrow NO + OH \quad [27]$$

$$NO_2 + O \Leftrightarrow NO + O_2 \quad [28]$$

2.2.2 Carbon Monoxide Formation

Carbon monoxide is emitted from gas turbine combustors due to its incomplete oxidation in the primary and dilution zones. In the flame primary zone, CH_x species react much more rapidly with oxidising radicals such as OH than with carbon monoxide. Thus CO cannot oxidise until the gases leave the primary zone when the CH_x species concentration has dropped. Low post-flame temperatures slow CO oxidation further. The oxidation rate at 1150 K is two orders of magnitude slower than at 1800 K (Correa 1992). The gases immediately leaving a combustor primary zone contain between 100-1000 ppm CO and 10-100 ppm UHC (Correa 92). Carbon monoxide may also be formed due to the lack of oxygen needed to complete the reaction to CO_2 as in very rich flames. In all flames further carbon monoxide is produced from the dissociation of carbon dioxide.

Incomplete CO oxidation may be caused by several different effects:
i) inadequate burning rates due to insufficient residence times, aerodynamic straining (high velocity gradients) or too off-stoichiometric mixture strength. All of these factors are problematic in LPP combustion systems.
ii) poor mixing of fuel and air resulting in areas locally too rich causing incomplete combustion or too lean causing weak combustion.
iii) quenching of post flame products preventing the complete oxidation of CO, for example in regions close to cold combustor walls, near film cooling and dilution jets.

The rate of CO oxidation is sufficiently fast to interact with Batchelor/Kolmogorov scales of turbulence. This introduces the possibility of CO oxidising reactions being quenched by film cooling air, cold boundary layers and dilution jets. However, theoretical calculations (Correa 1992) show that close to a wall boundary layer the cooling effect is too slow to affect CO chemistry unless the post-flame gas impinges

directly to the wall in stagnation point flow. Similarly, the likelihood of CO oxidation from quenching due to cold air jet mixing is theoretically small, unless the oxidation is sufficiently slowed by strain rates exceeding 2000 s^{-1}.

Carbon monoxide is produced at all stoichiometries but is a minimum at equivalence ratios of between 0.7 and 0.9. Above Ø = 0.9, equilibrium levels of CO dominate. Below Ø = 0.7, the temperature is too low and CO oxidation is slow requiring long residence times. Gradual admixing of dilution air has beneficial effects on reducing equilibrium CO emissions. By using larger combustor primary or intermediate zones with longer residence times CO can also be reduced. At equivalence ratios of Ø = 0.8 carbon monoxide typically takes 5-6 ms to completely burn out which is longer than a typical primary zone residence time.

In gas turbine combustors, carbon monoxide and unburnt hydrocarbon emissions are highest at low power conditions since thermal quenching and dilution are greatest. This effect can be reduced by bleeding off excess air. Conversely, NOx and soot are highest at high power conditions where the temperatures and pressures are high.

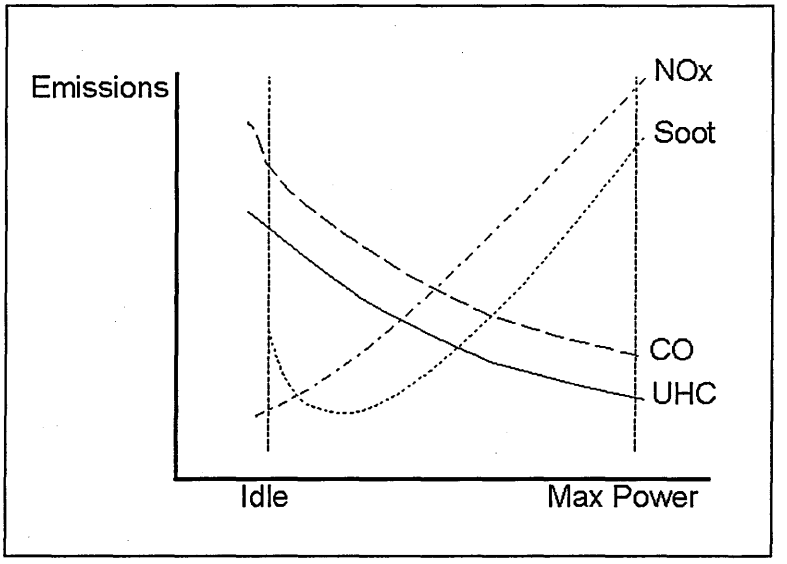

Figure 2.3 Combustor Emissions through the Gas Turbine Cycle.

2.2.3 Unburnt Hydrocarbons Emissions

Unburnt hydrocarbon (UHC) emissions comprise unburnt fuel in droplet or vapour form and thermally degraded species of lower molecular weight such as methane and acetylene. UHC emissions are usually caused by inadequate burning rates or residence times, poor atomisation or quenching effects.

In practice, UHC emissions can be reduced by increasing the inlet temperature and pressure, by improved atomisation and by the same methods applied to reducing emissions of CO.

2.2.4 SO_X Production

Sulphur contained in fuel is virtually entirely converted to SO_2 and SO_3 during combustion. The only effective solution to SO_X emissions in gas turbine combustors is to remove all sulphur from the fuel. Current aviation fuel sulphur levels are very low but could rise in the future.

2.2.5 Soot Production

Soot is usually formed in pockets of fuel vapour enveloped in oxygen deficient gases at high temperature. Soot typically consists of carbon (96%), with a mixture of hydrogen, oxygen and other species. It is formed from aromatic hydrocarbons by two processes; either condensation of aromatic rings into graphite-like structures, or break up to small hydrocarbon fragments which polymerise to form hydrogen deficient molecules which then nucleate to soot.

Fuel properties such as viscosity and volatility affect the rate of soot production by controlling their ability to form small droplets. The fuel's hydrogen and aromatic content control the availability of soot nucleation species. Increases in combustion pressure will increase soot production in non-premixed flames by enhancing the reaction rates and the

mixture's flammability causing earlier combustion closer to the fuel spray. Soot will only form at local equivalence ratios above Ø = 3. In premixed combustors, soot is not produced below 0.6 MPa at significant levels. Lean, premixed flames rarely suffer from significant soot emission since there are essentially no areas where the local fuel concentration is sufficiently high to form a soot production zone and soot consumption rates should be high.

2.3 Emissions Targets

Gas turbine emissions are targeted to eventually reach a point where the total gross emission of pollutants will have no significant effect on the environment. The global average emissions index for aircraft is currently 39.5 EINOx (Johnston 1991). In order to meet goals for non-environmental impact for stratospheric cruise aircraft, NO_x emission indices need to be reduced to at least single figure levels. LPP combustors are targeted to reduce emissions to less than 5 EINOx. This would reduce the ozone column by an estimated 0.2 % (Dunston).

There are a number of units for measuring NO_x emissions, including EINOx, g/kWhr (grams NOx per kilowatt hour operation), ppm (parts per million by volume) and ppm at 15% O_2. The most useful unit for nitrogen oxide emission is emission index (EI) or grams NOx per kilogram fuel burnt. To make any stated emission level useful it needs to be shown that the NO_x emission was achieved at a relevant pressure and without exceeding the regulated levels of carbon monoxide. This is because NO_x levels can easily be traded off against CO emissions by reducing the combustion temperature. To complicate the matter further, some emission indices, are quoted as total grams NO_x ($NO + NO_2$), whilst others quote equivalent NO_2 emission as calculated below from the ratio of molecular weights.

$$\text{Equivalent } NO_2, \text{ EINOx} = \frac{46}{30}[NO]+[NO_2]$$

The International Civil Aviation Organisation (ICAO) regulates the emissions levels from aircraft engines using the characteristic level, D_p/F_{00}. This parameter relates grams of pollutant species emitted per kW of thrust and is calculated for each aircraft mode, specifying particular thrust settings. The characteristic level is then summed for 0.7 minutes at take-off, 2.2 minutes at climb, 4.0 minutes on approach and 26 minutes taxiing or at ground idle as shown below.

Phase	Thrust Setting	Time in each mode (minutes)
Take-off	F_{00}	0.7
Climb	0.85. F_{00}	2.2
Approach	0.3. F_{00}	4.0
Taxi / Ground idle	0.07. F_{00}	26.0

Table 2.1 Thrust setting and time in each mode for D_p/F_{00} emissions calculation.

The characteristic level may also be calculated from the equation below.

$$D_p = EI.\ \dot{F}.\ t.\ 60$$

For emission index EI (g/kg fuel), fuel flow $\dot{F}$, time t (minutes). The values of the characteristic level are calculated for carbon monoxide, NOx, unburnt hydrocarbons and smoke. The NOx values are calculated from the sum of NO and NO_2. The current ICAO regulatory maximum levels are shown below in Table 2.1. The pressure ratio is defined as π_{00}.

Pollutant Species	D_p/F_{00}
Smoke	$83.6.(F_{00})^{-0.274}$ or 50 which ever is lower
UHC	19.6 g/kN
CO	118 g/kN
NOx for aircraft manufactured before 31/12/95	$40 + 2.\pi_{00}$ g/kN
NOx for aircraft manufactured after 31/12/95	$32 + 1.6.\pi_{00}$ g/kN

Table 2.2 Current ICAO regulated emissions levels.

2.4 Available low emission combustor technologies

Conventional gas turbine combustors employ fuel injectors placing fuel directly into the primary zone of the combustor so that the fuel and air mix before and during combustion. The injectors are either airblast (using shear at prefilming lips to atomise the fuel), or pressure jet (squirting fuel through a nozzle at high pressure), or air assist (using separate air sources to augment atomisation). The degree of atomisation significantly affects fuel air mixing and consequent emissions. Inadequate mixing can result in high levels of soot formation, UHC and CO emissions. Current gas turbine combustors burn non-premixed with slightly lean primary zones resulting in NO_X emission indices varying from 20-55 EINOx.

There are several methods of reducing emissions from gas turbines already in use. These include lean, non-premixed combustion, rich-burn quick-quench lean-burn combustion, water injection, selective non-catalytic abatement (SNCR) and more recently gas turbines fitted with gaseous fuelled lean, premixed combustors. However, practical solutions for further reductions in exhaust emissions are still required. The following is a review of current combustor technologies for dry low emissions (DLE).

2.4.1 Lean Direct Injection Combustion

Emissions of oxides of nitrogen can be reduced in non-premixed combustors by burning a leaner mixture to lower than the mean flame temperature. Since the mixture is non-

premixed and is therefore heterogeneous, local regions of combustion exist with a variety of stoichiometries. Even with lean overall equivalence ratios, significant amounts of NO_X are produced in hot areas such as the stoichiometric or near stoichiometric combustion surrounding the droplets. Combustion in these devices is particularly stable, since the lean limit is unlikely to be exceeded due to support from other more stoichiometric, hotter regions.

A current research area for low NO_X combustion is lean direct injection (LDI) combustion. The fuel is injected into the high velocity shear layers around the primary zone recirculation to reduce the formation time for thermal NO_X reactions. The potential advantages of LDI are the avoidance of autoignition and flashback and hence improved stability. LDI combustion has arguably not yet been demonstrated to be capable of improving stability over LPP devices, operating at similar NOx emission levels. However, lean direct injection combustors may eventually be useful acting as pilot zones in LPP gas turbines for low power operation and overall stability improvement by forfeiting some NOx emission for stability.

In order to impede the NO_X formation mechanisms in a simultaneous mixing and reaction zone by direct injection, the reaction time must be slow relative to the mixing processes. The fuel and air have to be mixed prior to combustion so that the Damkholer (D_a) number is less than 1.

In order to extend the thermal NO_X reaction time to more than the mixing time, strain and turbulence are used. Correa (1992) showed that to achieve Damkohler numbers less than one, the necessary turbulence levels can be estimated from the Integral time scale, the Kolmogorov time scale with the characteristic chemical time scales. So

$$\text{Damkholer No., Da} = \frac{\text{characteristic mixing time}}{\text{characteristic reaction time}} = \frac{\theta}{\tau_c}$$

$$\text{Integral Time Scale, } \theta_I = \frac{\lambda_I}{u'}$$

$$\text{Kolmogorov Time Scale, } \theta_K = \left(\frac{\upsilon}{\varepsilon}\right)^{0.5}$$

Characteristic reaction time (time to form 100 ppm NOx)	τ_c	0.5 ms
Integral length scale	λ_I	0.005 m
Fluctuating velocity	u'	10 m/s
Kinematic viscosity	ν	6.544e-05 m^2/s
Mechanical dissipation rate	ε	2.0E-05 m^2/s^3

Table 2.3 Values for Damkholer Number Calculation.

Using a mean velocity of 100 m/s, a fluctuating rms velocity of 10 m/s, integral length scale 0.005 m and typical values for kinematic viscosity for burnt gases with the required reaction time to produce 100 ppm of thermal NO_X the following result can be calculated:

Damkohler Number	**Gas Turbine Combustor**: 10 atm, 600 K inlet
Da_I	1.05
Da_K	0.038

Table 2.3 Damkholer Number Calculation Results

The mixture lies in the well mixed regime on the Kolmogorov scale and in the intermediate (partially premixed) regime on the Integral length scale. Bilger (1988) claims that the actual mixing scale is approximately an order of magnitude larger than the Kolmogorov scale. Assuming that this applies to turbulent exothermic regions the Damkohler numbers may be regarded as bounding values. Therefore, in most devices the thermal reactions would take place faster than the mixing processes. However, in the lower temperature regions of overall lean combustion the formation of NO_X is slower and the reactions proceed in a well-mixed manner. Experiments by Sattelmayer (1990), show that the NO_X levels in partially premixed propane combustion on a laboratory injector at atmospheric pressure in near adiabatic conditions were

comparable to those in a premixed flame, verifying the possibility that the above Damkohler numbers can be achieved in gas turbine combustors.

2.4.2 Staged Combustion - Rich burn Quick quench Lean burn

Another strategy for achieving dry low emissions is Rich-burn Quick-quench Lean-burn (RQL) combustion. Here the combustion is staged into two zones, the first one fuel rich and the second fuel lean. The flame temperature in each zone is low due to the combusting mixture's displacement from stoichiometry thereby reducing thermal NO_X. The products of combustion from the first rich zone are rapidly diluted with fresh air in a narrow section and fed into the lean combustion zone. It is hoped that all the unburned hydrocarbons, CO and soot are oxidised in the lean zone. Some stoichiometric combustion inevitably takes place in the quick quench dilution zone which results in thermal NO_X. The first rich zone acts as a pilot during the low power operating conditions enhancing stability. This strategy is practical and can reduce NO_X emissions to 7-8 EINOx.

Since residence times in the stoichiometric quenching zone of 10-100 μs yield too high levels of oxides of nitrogen for ultra low NO_X applications, RQL combustors are of limited use. Much work is applied to finding efficient methods of mixing in air in the quench zone. RQL combustors are useful for reducing NO_X emissions when burning fuels containing high concentrations of fuel bound nitrogen since much fuel bound nitrogen is converted to N_2 in fuel rich zones instead of NO.

2.4.3 Lean, Premixed, Prevaporised Combustion

It has been shown that by completely vaporising a fuel and mixing with the oxidant to form a homogeneous mixture prior to combustion, that extremely low emissions of NO_X can be achieved. The mixture's uniformity avoids hot areas of NO_X producing stoichiometric combustion and virtually eliminates emissions of UHC and soot. The only emissions emitted are due to inhomogeneities of the mixture, quenching, super

equilibrium thermal NOx, prompt NO_X, nitrous oxide derived NO_X or due to transient effects. Experiments by Corr (1991) in a highly loaded, turbulent, lean, well premixed combustor showed that the NO_X emissions comprised an estimated 85% prompt NOx, 15% NO_X from the nitrous oxide mechanism and no significant super equilibrium thermal NO_X. Maximum CO emissions are regulated to be of the same order as of NOx defined in emission indices.

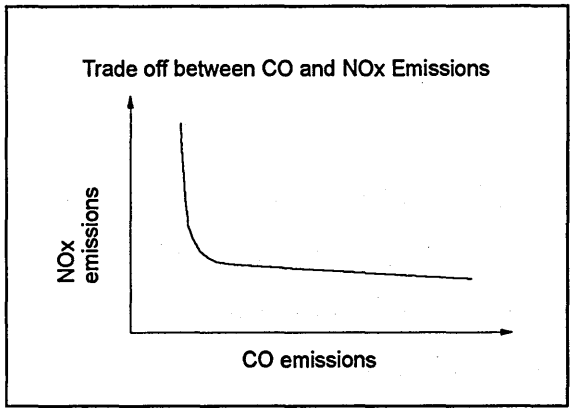

Figure 2.4 Trade Off Between CO and NOx Emissions.

Operating LPP gas turbine combustors over a wide range of cycle conditions causes problems since the fuel flow cannot be regulated to each premixer whilst maintaining the correct stoichiometry of each of the combustors. This has to be overcome either by staging the air or by staging the fuel. Variable geometry can be used to change the flow of air into each premixer dependant on the cycle condition. Controlling variable geometry inside a gas turbine combustor provides a complex engineering problem. Alternatively, the fuel can be regulated by switching off one or more premixers around the gas turbine annulus. This then causes the problem of applying cyclic thermal fatigue onto the turbine section. LPP combustors suffer difficulties related to the generation and existence of a hot, highly-flammable premixture and with stabilising lean, homogeneous combustion.

Since LPP combustion is the topic of this thesis, more is dealt with in the following chapters.

2.4.4 Catalytic Combustion

The ultimate foreseeable low emission technology for oxidising hydrocarbon fuel is arguably catalytic combustion. Ultra-lean, normally non-flammable homogenous mixtures of fuel and air are passed through catalytic monoliths which oxidise the fuel through third body reactions. Monoliths are blocks of ceramic material of extremely high surface area to provide a large catalytic surface coated with very thin layers of the catalyst. Heat is liberated at low peak temperatures (<1000 K) virtually eliminating emissions of thermal NOx. Catalytic combustion liberates very low percentages of fuel NOx.

However, large surface areas of catalyst are required which inherently causes a pressure drop. The catalysts tend to be expensive and therefore are very thinly coated. Inhomogeneities in the mixture burn off the catalyst layer if the temperature rises too high. Catalysts also suffer from blockage and are inefficient at burning out soot. In practice it is difficult to create a highly uniform ultra lean mixture particularly in conditions which prevent autoignition. Current catalysts are only effective above ambient temperature necessitating some form of preheat for the first monolith and during start up.

3. LITERATURE REVIEW

Lean, premixed, prevaporised combustion is still in its development stage, with a number of areas requiring further research. The following section is a review of the issues relevant to LPP combustors. The main problems with LPP combustors are preventing unwanted ignition in the premixer (autoignition and flashback) and stabilising a lean flame in the primary zone through a variety of engine cycle conditions. Flashback is the upstream propagation of the flame front from the primary zone into the premixer. Autoignition is defined to include any other form of unwanted ignition in the premixer. Combustion in the premixer results in severe damage to the combustor and a consequent increase in emissions. Furthermore, practical methods of controlling the combustor AFR throughout the whole gas turbine cycle conditions need to be found before LPP technology may be implemented into production gas turbines.

3.1 Flashback

Flashback into the premixer will occur when the local mixture velocity is lower than the local turbulent flame speed. The turbulent flame speed for kerosene-air mixtures at 900 K is between 30 and 60 m/s. However, the flame propagation velocity in the premixer is complicated by effects due to strain, quenching, stoichiometry, radical concentration, temperature, turbulent intensity and pressure oscillations in the flow field. The axial velocity in LPP premixers is usually kept well above 40 m/s to avoid flashback.

Lewis (1961) devised the velocity gradient criterion to determine whether flashback would occur along a duct boundary layer. This states that 'flashback will occur when the mixture velocity gradient at the wall becomes small enough for the local mixture velocity at the edge of the wall quenching layer to be less than the flame speed'. The wall quenching layer is closely related to the mixture's quenching distance. Lee (1982) showed in a series of experiments of flashback using a circular section tube that in turbulent flows of high reference velocities, the premixer boundary layers are very thin.

They also showed that due to the high pressures and high wall temperatures present in combustors the quenching distance is much reduced. Using high speed cinematography, it was possible to visualise flames propagating upstream along the boundary layer into the premixer. However, flashback always coincided with increasing pressure fluctuations suggesting that there was a coupling between the premixer flow field and combustion oscillations. For this reason they were not able to show a dependency of mixture reference velocity on flashback. More recent experiments by Braynin (1993), show that a flame can propagate across the entire cross-section of the duct where it is unaffected by the near wall boundary layer.

A common mechanism for flashback can be through flow reversals or retardations due to transient pressure effects. Oscillations in a combustor's primary zone can couple with resonant modes in the premixer or compressor supply frequencies to increase pressure fluctuation amplitudes. This can be sufficient to transiently cause a complete reversal of the flow in the combustor and allow the upstream propagation of the flame.

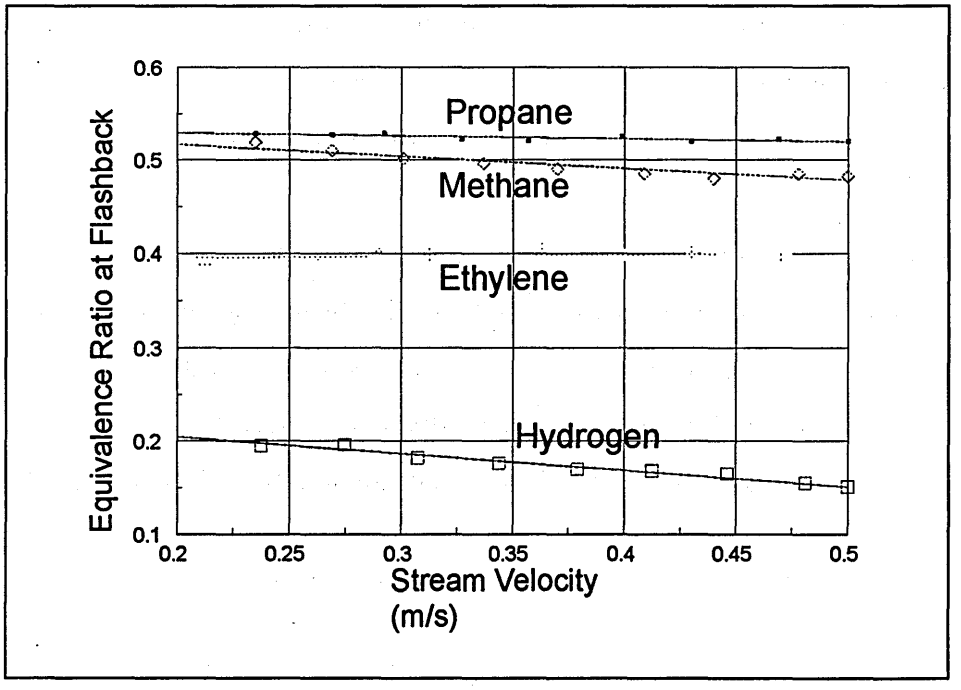

Figure 3.1 Effect of Fuel Type and Stream Velocity on Flashback Limits. (Karim 1985).

Using a rectangular section premixer and combustor, with high speed photography and pressure transducers the effect of inlet air temperatures, wall temperatures and reference velocities were investigated on a propane flame by Proctor (1985). It was observed that as flashback is approached pressure oscillations of 40-80 Hz appeared with amplitudes of order 10 kPa (1.4 psi). As the mixture approached stoichiometry, the amplitude of the oscillations peaked just before flashback. There appeared to be a small phase shift between the combustor oscillations and the premixer oscillations. As the pressure oscillation increased in amplitude the flame penetration increased too up until flashback. In premixers with low pressure drops complete flow reversals are more likely to occur.

Flashback induced by the acoustic coupling will occur when the combustion chamber is insufficiently damped for the degree of pulsations arising from the coupling between between fluctuating heat release rates and pressure pulsations. The heat release rate fluctuations are a complicated function of the incoming reactant turbulence, fuel delivery fluctuations, atomisation and vaporisation variations, hydrodynamic instabilities and vortex shedding and variation in chemical kinetic rates. This instability is dictated by the Rayleigh criterion which states that sufficient coupling may occur between the pressure and heat release oscillations leading to the growth of disturbances only when these oscillations are in phase (Rayleigh). These effects have been modelled to attempt to predict the onset of acoustic coupling by Darling (1995) and Najm (1994).

In experiments by Karim (1985) and Wierzba (1993), premixer flashback was shown to be independent of reference velocity for all fuels except hydrogen due to its high diffusivity. This is shown in figure 3.1.

The effect of increasing the inlet air temperature on flashback limits is slight, the stoichiometry being the dominant variable. It appears that when using sufficiently high premixer velocities to reduce the premixer residence times to safe limits for autoignition, the mixture reference velocity is well above the mixture's flame speed. Flashback can then be best avoided by ensuring that there is no acoustic coupling between the combustion flow field and the premixer and eliminating vortices.

3.2 Autoignition

A mixture of fuel and air will spontaneously ignite without the need of any external ignition source provided that it is above what is known as the autoignition temperature. There is a finite delay between the fuel meeting the air and the consequent autoignition which comprises two parts. The first part is the physical delay time during which the droplets are formed, heated and vaporised and diffusion and mixing take place to form a flammable mixture. This is followed by a chemical delay time from the combustible mixture's formation to the appearance of a hot flame. The chemical delay time is controlled by the kinetics of preflame reactions. This results in the decomposition of high molecular weight hydrocarbon species and the formation of precursors or radicals; mainly aldehydes and peroxides. The preflame reactions initiate immediately upon the fuel meeting the air, but provided that the mixing is efficient only a small fraction of mass will undergo reaction before mixture formation. There is little rise in temperature due to preflame reactions during the mixture formation period. The two parts of the autoignition delay time can only be temporally resolved when the delay is sufficiently long. The chemical autoignition delay time for fuel air mixtures may be as long several seconds or only a few microseconds.

Cool flames are formed during the lead up to autoignition. Cool flame reactions proceed until sufficient heat has been liberated and a sufficiently large radical pool formed to initiate a hot flame. Intermediate species such as CH, OH and HCO are formed in oxidising reactions resulting in a temperature rise of usually 200-400 K but always less than 700 K. The temperature the rise is a function of equivalence ratio $\varnothing$, inlet temperature, residence time and pressure. Hot flames are easily discernible by their larger temperature rise of over 1000 K. Cool flames emit a pale blue chemi-luminescence at 300-500 nm from formaldehyde. No carbon is formed in cool flames.

The resulting autoignition is characterised by a sudden increase in temperature, pressure and a high concentration of radicals and light emission. There are two basic types of autoignition; strong ignition resulting in a propagating wave front or blast wave and

mild ignition where chain reactions are initiated simultaneously at several points. In the case of a premixed gas turbine combustor, either forms of autoignition may result in combustion stabilising in the premixer or the flame blowing out. Premature combustion can also occur in an LPP gas turbine premixer caused by other sources such as ignition from hot, abraded particles from the compressor.

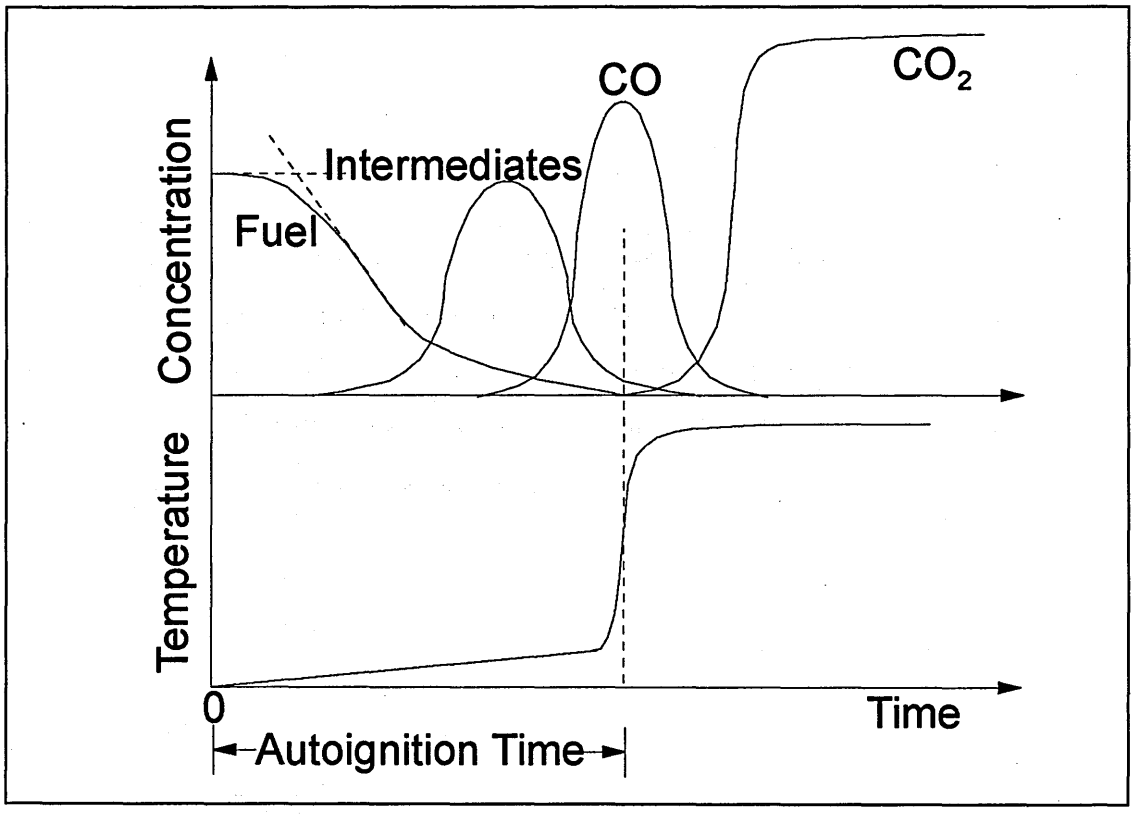

Figure 3.2 Temperature and Concentrations through Autoignition.

Autoignition under gas turbine conditions suitable for the high speed supersonic transport (HSST) jet cycle is too fast for cool flames to be observed since the inlet temperatures are of order 1000 K with pressures up to 14 bar. Under these conditions, fuel molecules are first broken up followed by chain branching reactions forming OH and HO_2.

Above 1100 K the following chain branching reaction dominates (Chevalier 1992).

$$H + O_2 \Leftrightarrow O + OH \qquad [29]$$

At lower temperatures between 900 and 1100 K, the reactions [30,31] are more important.

$$HO_2 + RH \Leftrightarrow H_2O_2 + R \qquad [30]$$

$$H_2O_2 + M \Leftrightarrow OH + OH + M \qquad [31]$$

These reactions are followed by the exothermic consumption of RH in the standard combustion reaction [32]. The radical then reacts with oxygen to form HO_2.

$$RH + OH \Leftrightarrow R + H_2O \qquad [32]$$

$$R + O_2 \Leftrightarrow R + HO_2 \qquad [33]$$

R denotes an alkyl radical and RH the fuel. The overall effect of reactions [29-33] is to increase the overall concentration of radicals (chain branching) and mixture temperature which eventually results in rapid ignition.

Simplified reaction schemes are available for estimating the autoignition behaviour of hydrocarbon-air mixtures. Such models also need to account for the cleavage of molecules. One important cleavage reaction of the ROOH radical results in the formation of OH and helps explain the autoignition behaviour of iso-octane / n-heptane mixtures (Morley 1987). A n-heptane molecule can undergo a cleavage reaction resulting in the production of an OH radical, whereas the iso-octane being short a molecule with side chains cannot. The OH radicals generated then proceed to accelerate autoignition. This cleavage reaction begins with the formation of the alkylperoxy radical

from a C_5 skeleton. The 2,4 disubstituted oxetan ring then forms a β hydroperoxyalkyl radical and OH (Cox 1985). This is shown below in reactions 34 and 35.

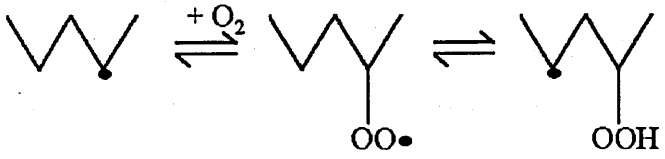

- [34]

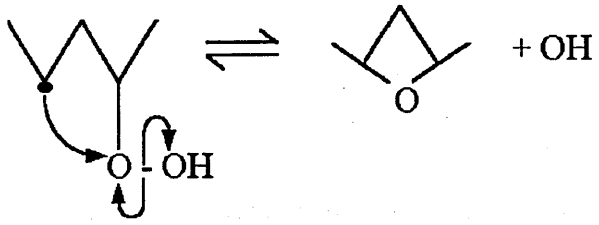

- [35]

3.2.1 Physical Effects on Autoignition

The length of the chemical and physical delay time can be changed by many physical effects. The chemical delay time may be altered by the addition of water, carbon dioxide, aromatics with side chains or other species and by changes in stoichiometry. The physical delay time can be affected by the fuel droplet sizes, fuel preheat levels, vaporisation rates, the flow field or anything which can control the mixture uniformity. Both delay times will be affected by equivalence ratio, temperature and pressure.

Autoignition caused from excessive residence time becomes further complicated by the mixture's flammability and the existence of a point for a flame to stabilise. Autoignition may result in combustion stabilising in the premixer or blowing out and becoming a transient phenomena. Danis (1986) showed that a spray-vapour mixture's flammability was maximised when the ignition point vapour phase equivalence ratio was between 1.5 and 2.

The effect of equivalence ratio on ignition delay time is complex. For rich mixtures, the delay time shortens with decreasing equivalence ratio. The delay time is minimum at ∅

< 1 since cool flame reactions are heavily dependant on oxygen. As the mixture becomes still leaner, the mixture's flammability and propagation efficiency reduce, impeding full autoignition. Lean minima for delay time against equivalence ratio ∅ have been found experimentally by Hurn (1952, 1956). Mullins (1951) found that the ignition delay time was inversely proportional to the concentration of oxygen squared.

High inlet temperatures and pressures accelerate the transition from cool to hot flames. Raising fuel temperature can reduce autoignition delay by affecting the droplet formation time from poor injectors and enhancing evaporation rates. The temperature of any liquid fuel-air mixture reduces by about 60 K due to heat loss to the fuel during heating and evaporation, extending the autoignition delay time.

3.2.2 Chemical Effects on Autoignition

Cowell (1986) showed that the autoignition flame stability improves with low mixture flame speeds and low carbon to hydrogen ratios.

Autoignition delay times may also be affected by the addition of other chemical species. Using a kinetic model of autoignition, Laster (1988) found that for constant oxygen concentrations the delay time will decrease with the addition of NO or NO_2 into H_2/air mixtures. The delay time was shortest with concentrations of 0.5% NO. This level is much higher than would typically be found in most reactants such as vitiated preheater exhausts. This is mainly due the OH formation reactions [36] and [37],

$$NO + HO_2 \Leftrightarrow NO_2 + OH \qquad [36]$$

$$NO_2 + H \Leftrightarrow NO + OH \qquad [37]$$

and also due to the reduced effect of the HO_2 termination reaction.

$$H + O_2 + M \Leftrightarrow HO_2 + M \qquad [38]$$

The effect of NO_2 addition was also demonstrated to reduce the ignition delay time by adding a second H atom production path shown in reaction [38].

$$NO_2 + H_2 \Leftrightarrow HNO_2 + H \qquad [38]$$

The delay time was shortest at NO_2 concentrations of 0.5 %. The delay shortening effects of NO and NO_2 addition become less important at low pressures and high temperatures. Also the addition of H_2O and CO_2 will reduce the ignition delay time due to the increased formation of radicals such as HO_2 and OH in cool flame reactions. These effects are further explained in the section on vitiation in chapter 5.

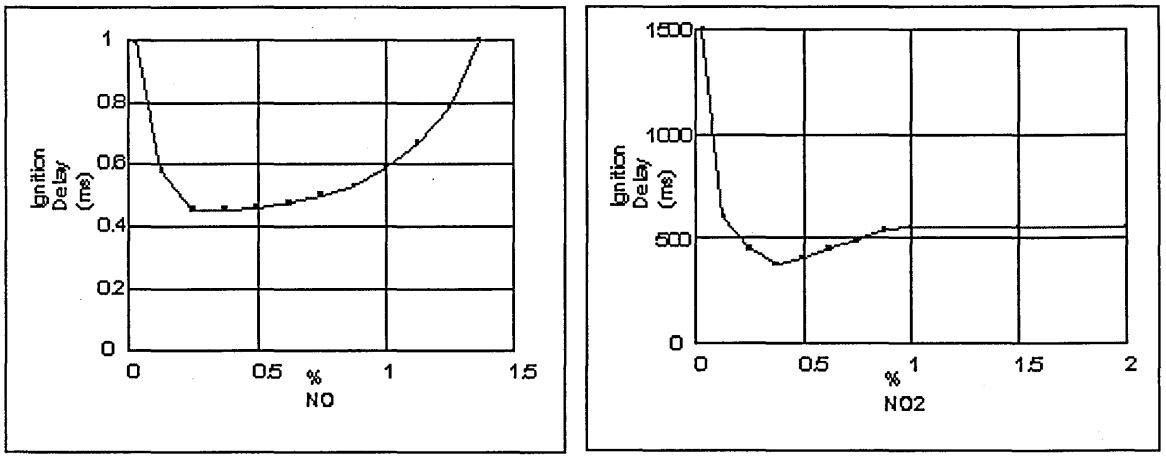

Figure 3.3 and 3.4 Effects of NO and NO_2 on Autoignition Delay (Laster 1989).

Research into autoignition often disagrees due to the differing degree to which physical delay times have been measured and confused with chemical delay time as a result of different experimental apparatus and variations in mixture uniformity. In premixed combustors, it is the longest residence time in the premixer which is of relevance. Boundary layers, recirculation zones and slow core velocities in highly swirling flows raise residence times above the mean. The following is a summary of the physical effects on autoignition delay times.

- In practical devices with lean mixtures, increasing AFR reduces the delay time.
- Inhomogeneity reduces the autoignition delay times for lean mixtures.
- Increases in fuel aromatic content cause longer ignition delay times (however, adding aromatics with side chains will enhance autoignition).
- For long mixing lengths the effect of fuel concentration is small.
- Increases in pressure and temperature reduce ignition delay times.
- Preheating the fuel has no effect on ignition delay time, unless it can affect injection (mixing) as in poorly designed systems where it will shorten the delay.
- There are a number of other unquantifiable, physical effects which affect autoignition delay times including airstream cooling (due to the fuel's latent heat of vaporisation), convective heat loss, degree of vaporisation and turbulence.

These effect of fuel type, equivalence ratio, temperature and pressure are shown in figures 3.5 (Cowell and Lefebvre 1986) and 3.6 (Goodjer 1987).

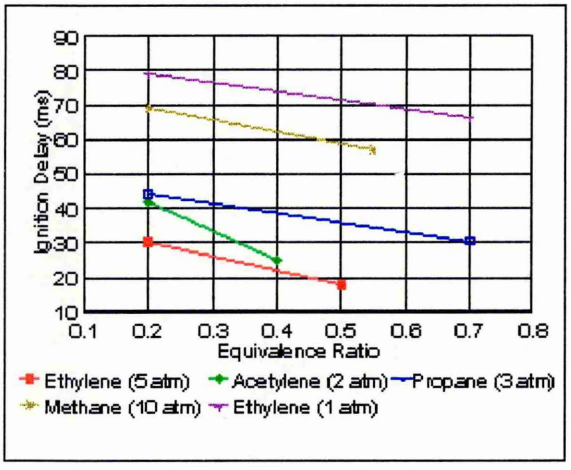

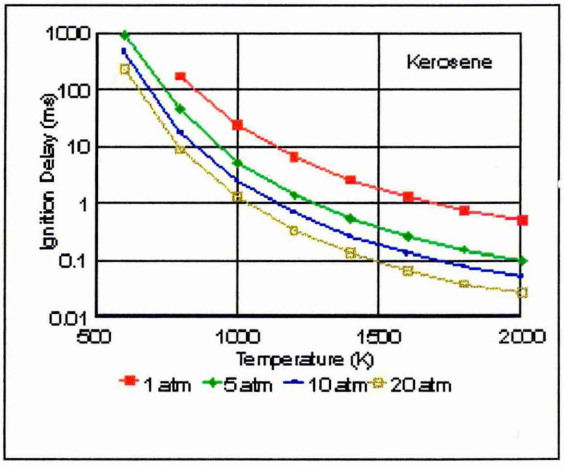

Figures 3.5 and 3.6 Effect of Temperature, Equivalence Ratio and Pressure on Autoignition Delay.

3.2.3 Calculation of Autoignition Delay Times

The length of the chemical autoignition delay time is a complicated function of chemical kinetics, mixing, temperature and pressure. With low temperature autoignition, the

temperature is often seen to flatten or even decline due to an inverse temperature dependence of the overall reaction rate, sometimes referred to as a 'negative temperature coefficient'. This has been verified in a study by Gibson (1984) in a continuous stirred turbulent reactor burning acetaldehyde where complex multiple stage ignitions were observed resulting from oscillatory cool flames. The mixture produced several peak levels of intermediates (CH_4, CH_2O and H_2O_2) during the cool flame prior to autoignition. Between 40 and 50% of the fuel was consumed in this stage with temperature rises of less than 250 K. Two stage ignitions have also been observed by chemical kinetic modelling of butane-air mixtures (Cox 1985, Minetti 1994, Kojima 1994). This suggests that the best method of calculating autoignition delay is with chemical kinetic modelling or from direct measurement. However, under the high temperature conditions realistic of premixed gas turbine combustors (>1000 K), the autoignition process is dominated by formation of the degenerate branching agent H_2O_2. This then allows a simple Arhennius correlation of chemical ignition delay to be used.

$$\text{Autoignition delay time, } \tau = \frac{A.e^{\left(\frac{E}{R.T}\right)}}{P^n}$$

where P is the pressure in Pa, E is the activation energy in J/mol, R is the universal gas constant J/molK, T is the temperature in K and A and n are constants.

The following table lists the values for the constants in the above equation for several references.

Reference	Fuel	A	E	n
Odgers and Kretschmer1986	Diesel	40.4944×10^{-6}	45.63774×10^{3}	0.751
"	Avtur	9.397764×10^{-6}	65.11838×10^{3}	0.991
"	Avtag	8.90855×10^{-6}	59.48953×10^{3}	0.751
Spadacinni 1980	Jet A	6.89×10^{-9}	146.915×10^{3}	1
at 10-20 atm	JP-4	4.87×10^{-9}	153.907×10^{3}	1
"	No.2 Diesel	4.00×10^{-9}	166.970×10^{3}	1
"	ERBS	5.14×10^{-10}	165.695×10^{3}	1
Marek 1977	Jet A	3.3555×10^{-6}	64.0209×10^{3}	1
Hayashi	Kerosene (liq)	2.073×10^{-9}	92×10^{3}	1
"	Kerosene (vap)	2.073×10^{-9}	184×10^{3}	1

Table 3.1 Constants for Arhennius Calculation of Autoignition Delay.

The physical ignition delay time is dependant on the particular device and the mixing technique employed. Mullins showed that the effects of droplet size, air preheat and prevaporisation on the physical ignition delay, τ are as follows.

- Increases in droplet diameter (SMD) of 3 um raise τ by 1%
- 60 K increase in air preheat reduces τ by 15%
- Fuel prevaporisation reduces τ by 25%

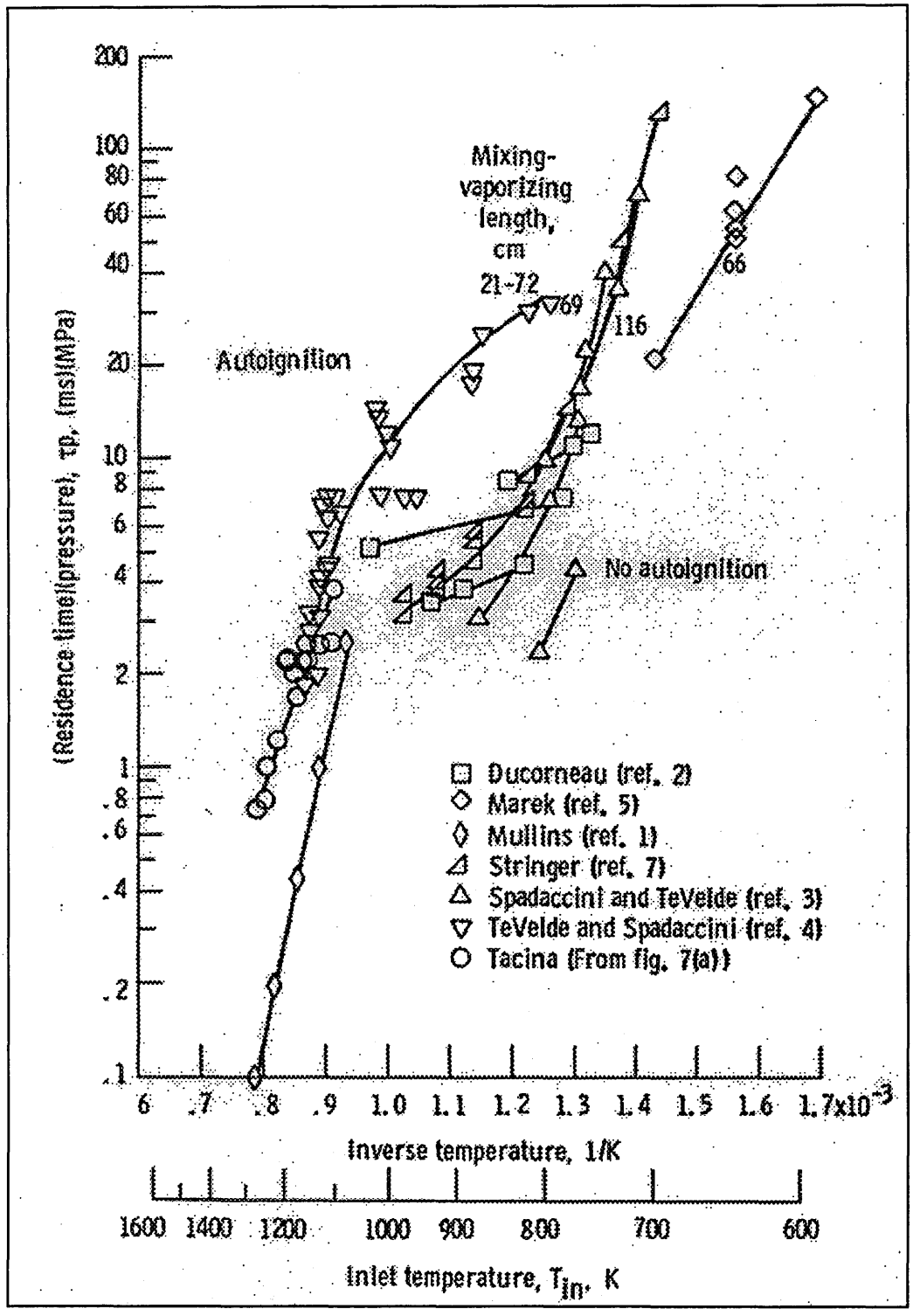

Figure 3.7 Measured Autoignition Delays. (Tacina 1983)

3.3 Lean Flame Stability

A stable flame relies upon sufficient heat and radical transfer to the preheat zone in the unburnt fuel regime to maintain a high enough reaction rate for maintaining continuous combustion. These transfer processes can be impeded by a number of mechanisms, namely excessive heat transfer to the surroundings (thermal quenching), preferential diffusion of radicals (a function of flame front curvature), flame stretch and aerodynamic strain. These local flame parameters are controlled or affected by global flame parameters like turbulence intensity, the overall stoichiometry, the mixture homogeneity, the fuel composition and properties, the combustion chemistry, the velocity field, the combustor geometry and the inlet temperature and pressure.

Traditionally in non-premixed combustors, fuel is injected in a cone at the head of a can inside a region of axially fed swirling flow. The primary zone stabilises in a recirculation zone. Since the fuel is mixing and burning simultaneously, the flame has a wide distribution of local stoichiometries. Even if the overall equivalence ratio is lean, there are ample pockets of hot, stoichiometric combustion which stabilise the remainder of combustion with their supply of heat and radicals.

In lean, premixed combustors, the fuel and air are premixed to an overall lean equivalence ratio and the distribution of stoichiometries is greatly narrowed. The combustion is therefore inherently less stable since there are no regions of stoichiometric combustion supporting the leaner areas. Furthermore, if the air supply is increased with a change in engine cycle the flame is likely to exceed its lean limit. The air has to be regulated using some form of air staging. Mixing in the premixing duct can be affected by pressure pulsations in the primary zone causing fluctuations in the mixture's stoichiometry. In order to stabilise lean, premixed combustion a number of steps are possible. The primary zone can be designed using ceramic liners which are capable of withstanding combustion temperature and do not require as much film cooling thereby reducing wall quenching. The recirculation zone can be optimised to provide a favourable flow field void of excessive velocity gradients. Also, small

quantities of hydrogen (1-4%) can be added to the fuel significantly enhancing combustion stability, with a tolerably small increase in NO_x emissions (Anderson 1975).

The most common methods used to stabilise the primary zone use either a toroidal, recirculation formed by the ejection of reactants at a high swirl angle or use a recirculation formed behind a bluff body flameholder. The recirculation brings the hot burnt products, rich in radicals directly into close proximity and direct contact with the cool, unburnt reactants. The recirculation becomes larger and stronger as the mixture ignites. In conventional combustors the recirculation zone is pegged in place by primary air jets.

In a swirl stabilised primary zone, a swirling reactant mixture is thrown outwards by centrifugal forces leaving a low pressure region in the core. The gases then collapse into the core forming the recirculation. The level of swirl is set to maximise the recirculation without suffering vortex breakdown.

Vortex breakdown occurs when the swirl component of a flow becomes sufficiently large that the flow field changes and forms a central vortex along the duct centreline. For a given swirling or rotating solid body of gas in a closed duct, as the swirl number is increased, the flow will eventually suffer vortex breakdown. The swirl number being the ratio of the flow's swirling momentum component to axial momentum component. A flow with a high swirl number has a high swirl velocity component and low axial velocity, so that on expansion to a wider section it is more conducive to forming a recirculation. At the critical swirl number when the flow forms a central vortex, the core axial velocity is very low and could stabilise a flame. The onset of vortex breakdown can be controlled by accelerating or decelerating the flow. As a flow enters a convergent section of duct, the core flow accelerates faster relative to the annular flow resulting in a more centre peaked velocity profile. This results in a consequent increase in the axial momentum component and hence a lower swirl number. Conversely, a decelerating flow in a diverging duct will suffer vortex breakdown sooner since the swirl number is increasing.

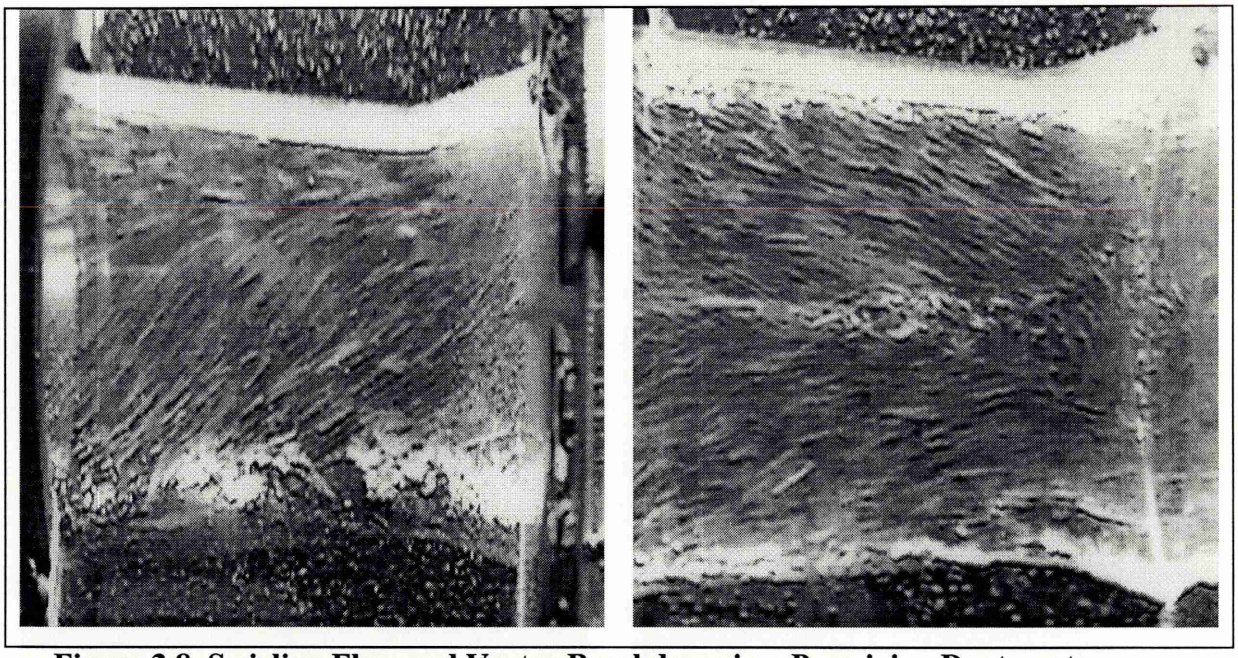

Figure 3.8. Swirling Flow and Vortex Breakdown in a Premixing Duct; water analogy. (Spooner).

In lean, premixed combustors the recirculation zone is less stable and often a bluff body is used to provide an effective flame stabilisation region. When using bluff bodies, the initial reactant swirl is unnecessary as the recirculation naturally forms in the bluff body wake. Bluff bodies may need water cooling in order to maintain their mechanical integrity. Cooper (1981) showed that bluff bodies or flameholders can enhance evaporation of any remaining liquid fuel.

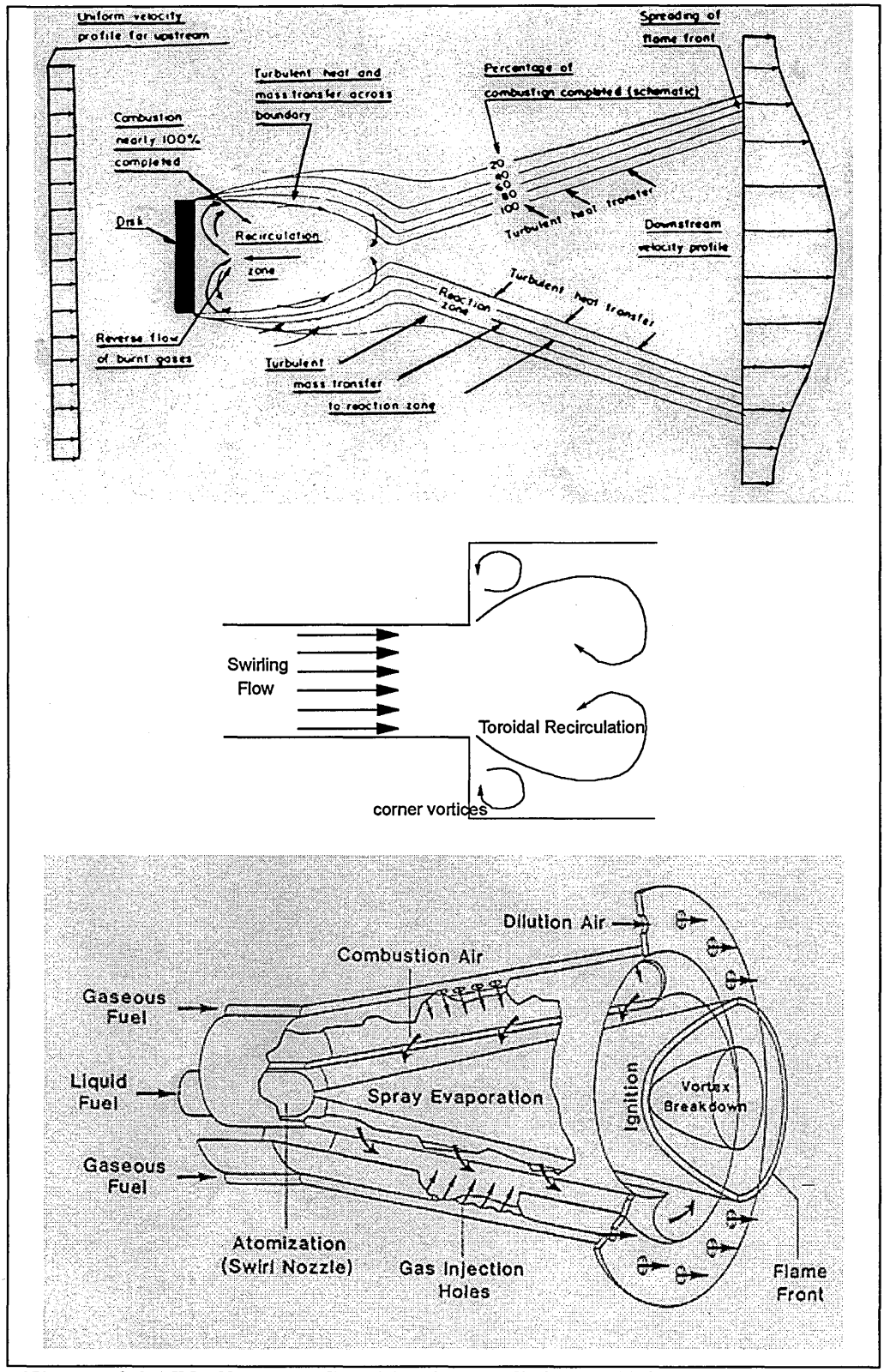

Figure 3.9. Bluff Body Stabilisation (Williams 1966), Swirl Stabilisation and Conical, Swirl Stabilisation (ABB Combustor Aigner 1990).

3.4 Effects on LPP combustors

There are a number of studies completed concerning the effects of various parameters have on LPP combustion stability and emissions. The following is a brief review of the effects of temperature, pressure, premixing quality or mixture uniformity, flameholder properties and swirl.

3.4.1 The Effect of Inlet Temperature and Pressure on Emissions

The effect of increasing inlet temperature and pressure on an LPP combustor premixer is well understood to reduce autoignition delay times, enhance the likelihood of flashback and change the premixing efficiency. Similarly, the effect of raising inlet temperature and pressure on the emissions of a lean, premixed combustor has been clearly demonstrated by many researchers.

The reactant temperature and NO_x emission may be correlated exponentially once the adiabatic flame temperature is high enough for thermal NO_x to be the dominant mechanism. Roffe in 1976 conducted a series of experiments on combustor emissions over temperature ranges from 700-1000 K and pressures from 4-12 atm with combustor residence times of 3 to 4 ms using JP-5 fuel at equivalence ratios from 0.35 to 0.65. He found that the NO_x levels, unburnt hydrocarbon emissions (UHC) and combustion inefficiency (calculated from CO and UHC emissions) correlated well with adiabatic flame temperature. A 200 K increase in inlet temperature caused a tenfold rise in NO_x emission index. Increasing the equivalence ratio had the same effect. The combustion inefficiency and UHC emissions rose tenfold for an inlet temperature increase of 263 K. For LPP combustors operating efficiently premixed and lean, the effect of pressure on emissions of oxides of nitrogen is negligible.

3.4.2 The Effect of Premixing Quality on Stability and Emissions

The effect of improving premixing quality or mixture uniformity for lean mixtures has been consistently shown to reduce NO_x emissions (Roffe 1976, Lee 1995, Fric 1995) and also to lower flame stability.

The effect of improving premixing quality on NO_x emissions was demonstrated convincingly by Roffe (1976). Using three different fuel injection methods to obtain differing degrees of premixing and measuring the NO_x levels and combustion efficiency with gas analysis, the results clearly indicated a significant improvement in NO_x with better fuel injection/mixing.

Injection Technique	Combustion Efficiency	NO_x Emission Index
Single Axial Injection	$\eta = 99\ \%$	10 $EINO_x$
	$\eta = 95\ \%$	2.5 $EINO_x$
Four Pressure Atomising Nozzles	$\eta = 99\ \%$	2 $EINO_x$
	$\eta = 98\ \%$	0.45 $EINO_x$
Twelve Normal Orifice Injectors	$\eta = 99.7\ \%$	0.4 $EINO_x$
	$\eta = 99.0\ \%$	< 0.2 $EINO_x$

Table 3.2 Combustion Efficiencies and NO_x emissions for several Fuel Injector Configurations (Roffe 1976).

A similar experiment by Lee (1995), using three injection configurations shows the consequent increase in NO_x emissions with poorer premixing.

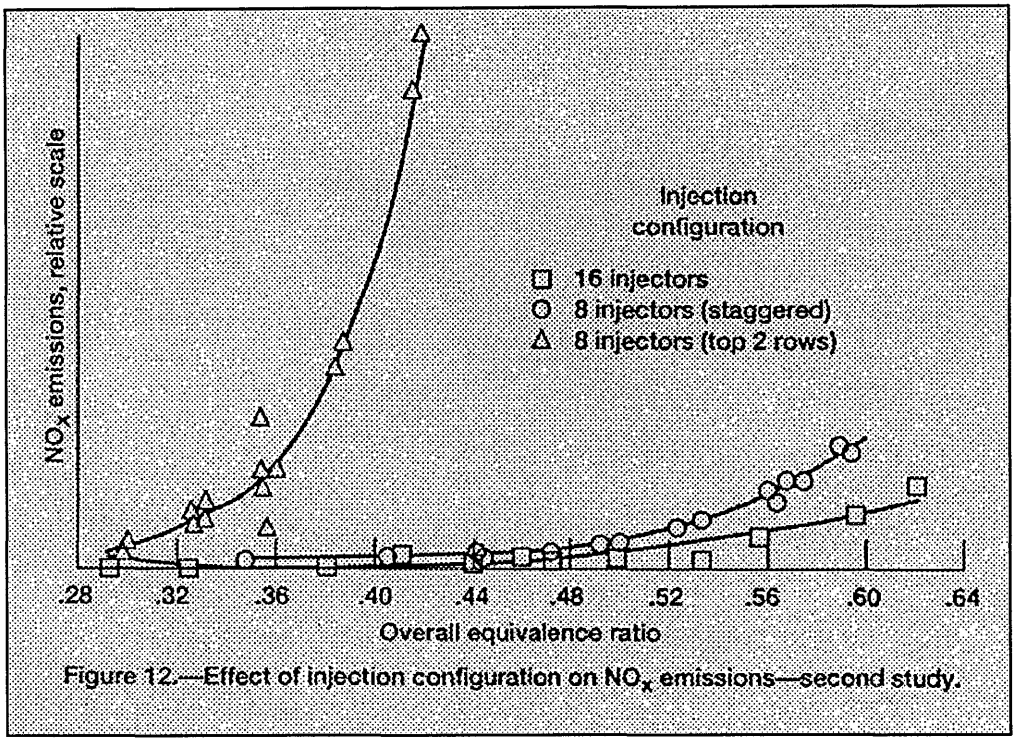

Figure 3.10 NO_x Emission for 3 Injector Configurations. (Lee 1995.)

The degree of vaporisation was found to be linearly related to NO_x emission by Cooper (1986). Using mixtures with between 72 and 100% of the fuel evaporated, at equivalence ratios from 0.6 to 0.72. He showed that droplets below 50 μm burned largely as a well mixed vapour and above 50 μm as a diffusion flame. For residence times of 3-4 ms, the carbon monoxide emissions increased uniformly with the degree of vaporisation. Longer residence times resulted in the complete oxidisation of CO.

Percentage Fuel Evaporated	NO_x Emission Index	
100 %	1.5 $EINO_x$	600K and $\varnothing = 0.6$
72 %	2.8 $EINO_x$	600K
100 %	2.3 $EINO_x$	700K
72 %	4.3 $EINO_x$	700K
100 %	4.5 $EINO_x$	600K and $\varnothing = 0.72$
73 %	4.6 $EINO_x$	600K
100 %	8.3 $EINO_x$	700K
73 %	8.4 $EINO_x$	700K

Table 3. 3 NO_x Emission at Different Fuel Evaporation Points. (Cooper 1986)

Fric (1995) demonstrated that both temporal and spatial non-uniformities in premixing quality contribute to NO_x emissions. Using LIF measurements on NO_2 seeded flows to measure reactant unmixedness for different configurations a direct correlation between unmixedness, U and NO_x emissions was found.

$$\text{Unmixedness, } U = \frac{\overline{c'^2}}{\bar{c}.(1-\bar{c})}$$

Where c is represents fuel concentration, c'^2 is the variance and $\bar{c}$ is the time mean. The premixing configurations studied had different probability distributions of fuel concentration and different levels of spatial premixing. The results show that small levels of temporal unmixedness, $c'/\bar{c}$ of 10% (U = 0.004), doubled NO_x emission relative to a perfectly premixed combustor.

3.4.3 Effects on Flame Stability

In an experimental and theoretical investigation into premixing quality, Radhakrishnan (1979) observed the significant rise in NO_x emissions and a lowering of the lean limit equivalence ratio with increases in mixture non-uniformity. The blowout limit also rises significantly with mixture non-uniformity.

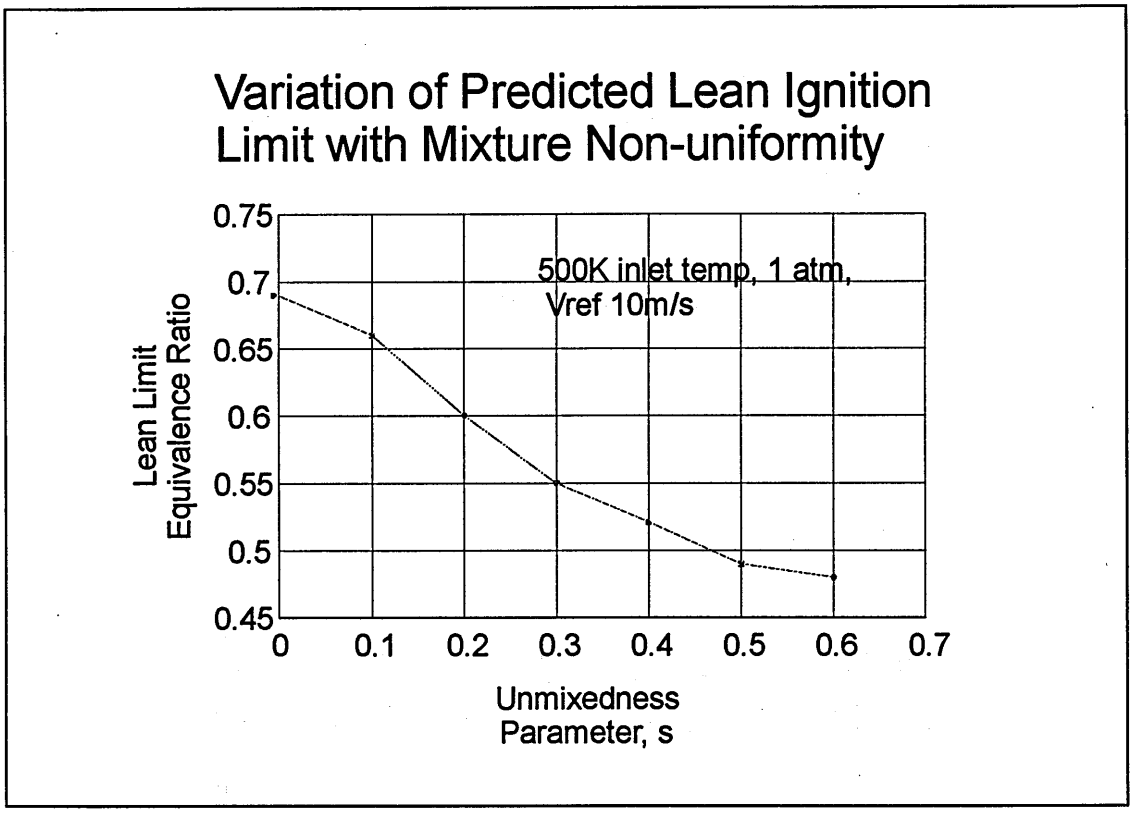

Figure 3.11 Effect of Mixture Uniformity on Lean Stability.

(Radhakrishnan 1979)

3.4.4. The Effect of Flameholder Design

The flameholder employed in a combustor affects the combustion by controlling the flow field affecting the residence time, the recirculation zone dimensions, the degree of quenching, the pressure drop and the amount of turbulence generated. A combustor flameholder or swirl stabilised recirculation zone should provide sufficient residence time to complete most hydrocarbon oxidation. A flameholder should also have a sufficiently large ignition perimeter to maintain stable ignition of oncoming reactants. The flameholder pressure drop should be high enough to create sufficient turbulence and prevent flashback but be sufficiently small so as not to significantly reduce overall efficiency (<5 %).

Using six different flameholder designs in a combustion rig burning lean, premixed, propane-air mixtures Roffe (1978) showed that the flameholder pressure drop was the principal determinant of NO_x emissions. The flameholders tested were a wire grid, perforated plate, multiple cone, single cone, vee gutter and swirler. The pressure drop was a function of geometry and the maximum velocity of the mixture through the flameholder. Flameholders with higher pressure drops, produced lower emissions of NO_x, CO and UHC. Lower pressure drop flameholders continued to reduce the CO and UHC further downstream. At low equivalence ratios the NO_x could be reduced by an order of magnitude by changing the flameholder, whilst at higher equivalence ratios it could only be lowered by a factor of three. The flameholder geometry, reference velocity or blockage ratio did not significantly affect the lean stability limit. Flashback occurred in the combustor when the maximum axial component of velocity at the flameholder was between 30 and 40 m/s. The wire grid and perforated plate flameholders produced no flashback at all. The flameholders with the highest peak velocities were most resistant to flashback.

Similar results were obtained by Duerr (1983), who showed that as the flameholder blockage increased, the pressure drop increased, the efficiency improved and NO_x emissions reduced slightly. He also found that as the residence time went up, the NO_x emissions increased and the efficiency increased. Water cooling the flameholder quenched reactions and resulted in a rise in UHC and CO emissions.

The effect of flameholder blockage on lean stability was shown using perforated plate flameholders with and without counterbores on the downstream side of the plate holes by Bosque Fernandez (1983). As the mixture reference velocity was increased, the blowout limit equivalence ratio was raised. Increasing the blockage ratio of the flameholder reduces the lean limit equivalence ratio by enlarging the recirculation zone. Counterboring the flameholder holes increases the surface area exposed to the flame resulting in reduced stability.

The optimum flameholder blockage was calculated theoretically to be 33 % by Radhakrishnan (1979) and found experimentally to be between 30 and 40 %.

3.4.5 The Effect of Secondary Air Admission

Air from combustor secondary ports (dilution ports) and film cooling can entrain into the primary zone recirculation (Roffe 1981). Experiments with a combustor using a perforated plate flameholder demonstrated that the primary zone recirculation equivalence ratio can be lowered through dilution to between 72 and 86% of its original value. The reduction by dilution for a vee gutter flameholder was between 42 and 65%. The entrainement was maximised by raising the reference velocity. The changes in primary zone stoichiometry will affect the combustor's tendency to flashback, lean stability and emissions. For a fixed primary zone equivalence ratio, increasing the proportion of dilution air can increase NO_x emissions. The levels of CO also increase as the dilution air proportion increases due to quenching the completion reaction to CO_2. The axial location of the dilution air ports did not affect the combustor emissions or stability suggesting that most of the air was entrained from the film cooling holes.

Future gas turbine combustors are likely to employ ceramic composites or ceramic lined combustor walls which would eliminate the necessity for film cooling.

3.4.6 The Effect of Swirl

In conventional gas turbines, swirl is used in the combustor head or dome to stabilise a recirculation zone and promote mixing of the fuel. The primary swirler directs most of the can head air mass flow creating a recirculation zone, while a smaller swirler is often used surrounding the injector to create turbulent shear and accelerate mixing. In premixed combustors the same can apply to mixing in the premixer, using residual swirl from the premixer to form a recirculation as the mixture expands into the primary zone. Increasing the swirl number, increases mixing in the premixer but extends the residence time and reduces the axial velocity. The optimum swirl number for strong recirculation

is around 0.6 (Smith 1987). Using more than one swirler in the premixer in counterflow improves the mixing (Anand 1985, Ahmad 1986) but reduces the final residual swirl at the premixer end for stabilisation. Smith and Kurzynski (1987) also showed that radial swirlers are more effective at mixing fuel and air than axial swirl. The efficiency of a swirler to create recirculation and enhance mixing depends much on its design (Micklow 1990). Curved vane swirlers have significantly lower discharge coefficients compared to straight vane swirlers. Swirlers can be further enhanced by using vane twist (changing the flow turning as a function of radius, typically 40^{o} at the hub to 70^{o} at the tip). This again increases the recirculation zone size and generates a secondary flow vortex pattern in the plane of the vane which increases shear and turbulence.

3.5 Other Work Completed on LPP Combustors

Measurements and modelled data of CO concentration in an atmospheric, LPP combustor have been completed by Nguyen (1995). They have compared laser based measurements of CO, gas sampled measurements and modelled data. These results suggest that the actual combustor CO levels might be up to ten times higher than as measured by gas analysis.

Kappler (1994) have made LIF measurements of OH, n-Heptane and NO in an optical LPP combustor running at atmospheric pressure and 600 K inlet temperature. They have also measured temperature by laser excitation of two ro-vibronic transitions in the Schumann-Runge band system of oyxgen.

LDA and gas analysis measurements have been made on an optical, LPP combustor running with inlet temperatures up to 560 K at the Volvo Aero Corporation by Freitholtz (1995). Similarly, NASA have a high pressure, optically accessible, LPP combustor interrogating with laser diagnostics (Hicks 1995).

3.6 Combustor Geometries and Implementation

The advantages of using LPP combustors in gas turbines exceeds simple reduction in unwanted emissions. The homogenous combustion eliminates hot spots which damage liner walls and aids the formation of a flat temperature profile at the first row of turbine blades. LPP combustors do not suffer hot streaks which can damage the turbine section. However, their implementation is far from simple and liquid fuelled LPP combustors have not to date been successfully incorporated in production gas turbines. An LPP combustor at a suitable equivalence ratio at cruise condition would blow out at the higher AFR during low power conditions such as ground idle. To accommodate for this effect, some form of air or fuel staging is necessary, possibly by by-passing air around the primary zone.

Air staging can be accomplished by by-passing more air into the dilution zones during low power conditions. This can be effected partially by using fluidic devices whose discharge coefficients vary with mass flow. Alternatively, air may be diverted by using variable geometry. The combustor variable geometry could be controlled by levers fed through seals controlled externally to the gas turbine. The reliability of variable geometry devices and the control lever seals under high pressure, hostile conditions is mechanically challenging.

A simpler method is to employ fuel staging. The fuel supply to the series of carburettors surrounding the periphery of the gas turbine can be selectively used. Either a continuous bank of the annular combustor can be used with the remainder switched off, or a combination of alternate carburettors used. This causes temperature variations around the combustor exit circumference which can cause excessive wear on nozzle guide vanes. Using alternately operational premixers around the combustor annulus increases thermal quenching and CO emissions.

A practical method for implementing LPP technology into gas turbine combustors is to employ non-premixed pilot zones in the combustor which only run when required as

during idle and may be switched off at cruise. The pilot zones also solve the problems of the difficulty of altitude relight with premixed combustors, but naturally emit more NO_x.

4. INVESTIGATION INTO PARTIALLY PREMIXED COMBUSTION

Partially premixed combustion is a feature of many 'premixed' combustion devices, since perfect, homogenous premixing is almost impossible to achieve. It is possible that LPP combustors may employ partial vaporisation under particular conditions to enhance combustion stability (Cooper 1981). The degree of partial premixing in an LPP gas turbine combustor has a significant effect on the rate of production of NOx and upon the combustion stability.

Laminar flame studies show that non-premixed or diffusion flames can co-exist with rich premixed and lean premixed flames. However, the structure of such flames at high turbulence levels and at high flow velocities is little understood. Triple flames consisting of a rich and a lean premixed flame and a diffusion flame can be stabilised in laboratory gas fuelled burners. By studying partially premixed combustion in laminar and turbulent triple flames, understanding of flame structure and chemistry can be improved.

This chapter details some measurements made on a laminar triple flame stabilised on a laboratory scale counterflow burner, using methane as a fuel. Comparisons with modelled data of the triple flame in the same counterflow geometry and flow field provide a good insight into partially premixed combustion under laminar conditions. The triple flame has been modelled in one dimension since the flame is axially symmetric, allowing the use of full methane chemistry. By looking at the flame stability limits of triple flames experiencing high turbulence and strain rates, information regarding partially premixed combustion in practical combustion devices may be inferred.

4.1 Laser Diagnostic Measurements

Laser diagnostics are frequently used to measure species concentrations, velocities, droplet or particle diameters and velocities and temperature without perturbing the flow being interrogated. Laser diagnostic measurements also have the advantage that they can provide instantaneous, two dimensional measurements across a whole section of flow. Radicals of low concentration such as OH and CH may be measured in combusting environments using laser induced fluorescence providing useful information on the location of flame fronts, heat release rates and mass burning rate.

All diagnostic techniques however, rely upon having suitable optical access for the introduction of the probe laser beams and for light signal collection. Designing and producing devices with sufficient optical access close to the harsh, combustion environment of gas turbine combustors or I.C. engines can be expensive.

4.1.1 Elastic Scattering of Light - Rayleigh and Mie Scattering

The elastic, unshifted scattering of light from molecules is termed Rayleigh scattering. Here, the molecular dimension is considerably smaller than the wavelength of light. Rayleigh scattered light is therefore at the same wavelength as the incident light and is not species specific. Rayleigh scattering is a function of the molecular number density of the fluid, the incident wavelength and the fluid's effective Rayleigh cross section. This is shown in equation 3 in section 4.3.

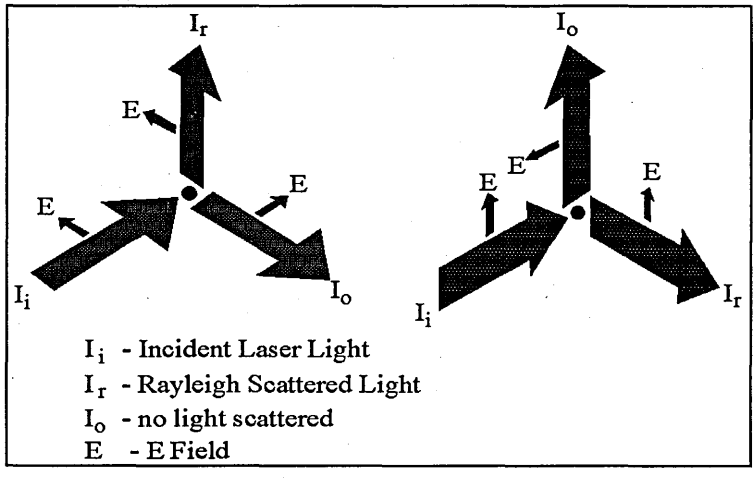

Figure 4.1 Polarisation Effects on Rayleigh Scattering.

Imaging Rayleigh scattering for laser diagnostic measurements requires the flow to be free of Mie scattering and any extraneous laser scatter. The intensity of Rayleigh light is directionally dependent on the incident polarisation. Rayleigh scattering intensity will be a cosine function of the maximum scattering intensity perpendicular to the laser sheet. This effect can be used to minimise Rayleigh scattering interference from other measurements such as LIF by using polarising filters at image collection. This is shown in figure 4.1.

Mie scattering is the elastic scattering of light from particles considerably larger than the wavelength of light ($d/\lambda << 1$ does not hold). Mie scattering is 10 to 20 orders of magnitude greater than Rayleigh scattering. A brief review of Mie theory is contained in section 6.1.7 with particle seeding of flows.

4.1.2 Inelastic Scattering of Light - Laser Induced Fluorescence and Raman Scattering

The inelastic scattering of light occurs when a photon interacts with a molecule or atom and a photon is scattered at a new wavelength. During an inelastic scattering event, the molecule or atom undergoes a change in internal energy resulting in the light being scattered to a new wavelength. The most common processes are fluorescence, phosphorescence and Raman scattering. The total internal energy of a molecule is discretely quantised and is apportioned between electronic energy, vibrational energy and rotational energy. The internal energy of a molecule is therefore defined by its occupation of specific electronic, vibrational and rotational levels. The distribution of kinetic and internal energies of the molecules occupying a volume of gas comprise the mean gas energy equivalent to the gas temperature. A photon interacting with a molecule can change the internal energy level resulting in changes in electronic, vibrational or rotational levels. Energy changes between electronic levels are considerably greater than vibrational energy level changes which are in turn greater than rotational level changes. The energy levels for the OH radical are shown in figure 4.2. The notation for the energy states is detailed in Herzberg (1951).

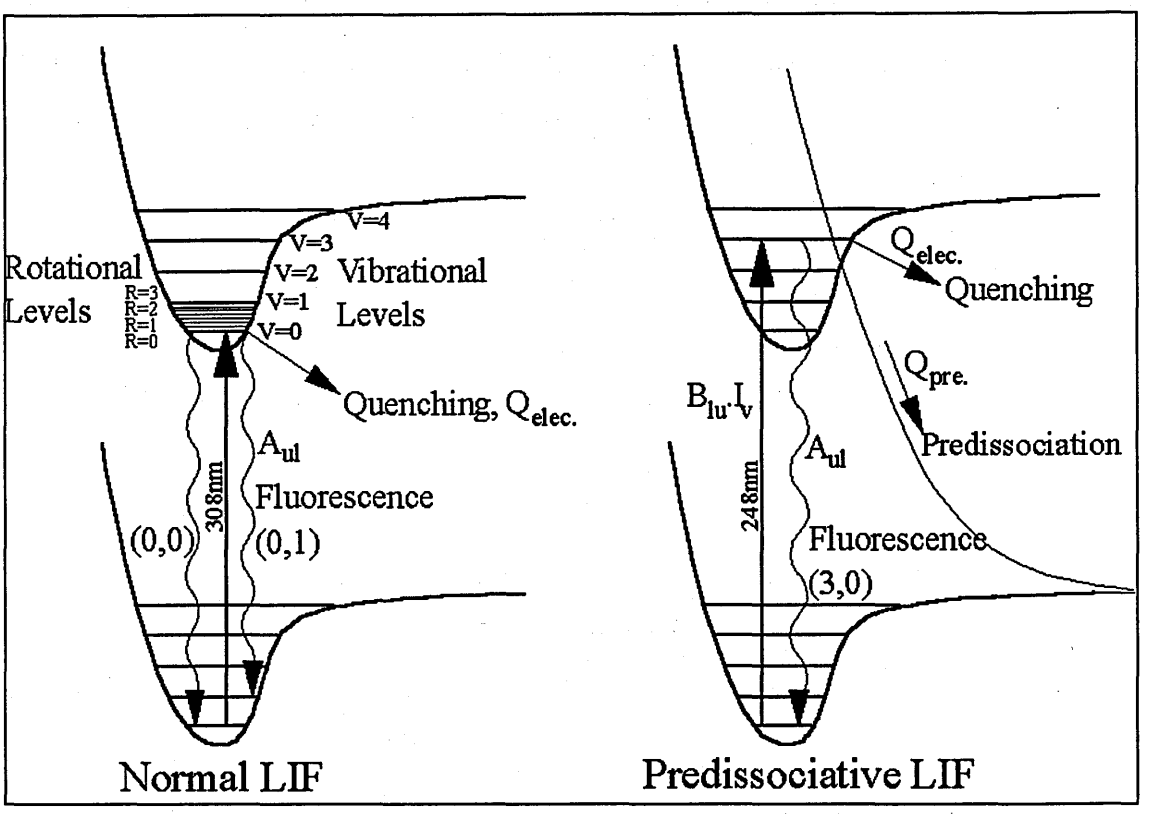

Figure 4.2 OH LIF Energy Level Diagram for Excimer Laser Excitation. x-axis: Inter Nuclear Co-ordinate (atom to atom distance), y-axis: Energy.

For each molecule, selection rules apply which only allow particular photon induced transitions to occur. These rules depend on the molecule's structure and together with the energy level spacing's determine the shape of the fluorescence emission and excitation spectra. Fluorescence spectra from large molecules show little fine detail for many reasons. Once excited a molecule's energy state can change between the rotational and vibrational states. Similarly on de-excitation of a molecule, the lower energy state can be to any of the vibrational or rotational levels. The ability of a molecule to move around the rotational and vibrational energy levels in the upper and lower states is the reason why the consequent fluorescence is spread over a number of wavelengths. Pressure broadening of the linewidth of fluorescence will also affect the final fluorescence spectrum. Rotational structure in molecular spectra is only ever detectable on very high resolution spectrometers. The spectra of aromatics are contained in chapter 8 and Appendix II.

When a photon interacts with a molecule and scatters inelastically, the scattered light may be of longer or shorter wavelength. This inelastic scattering which accompanies vibrational energy level changes is termed Raman scattering. Radiation or light scattered at a lower frequency is termed the Stokes component whilst that scattered at a higher frequency is the anti-Stokes component. The Raman shifted light is low in intensity but contains useful information on the gas species concentrations and temperatures.

If the incident light is from a laser, tuned to a particular molecular or atomic electronic resonance, then the probed molecules or atoms will be efficiently raised to an excited state. As the molecule or atom relaxes to its ground state it emits light which is termed fluorescence. The fluorescence is nearly always of longer wavelength. The fluorescence emitted at the same wavelength as the excitation is termed resonance fluorescence. The fluorescing lifetime of most molecules is between 10^{-10} and 10^{-7} seconds.

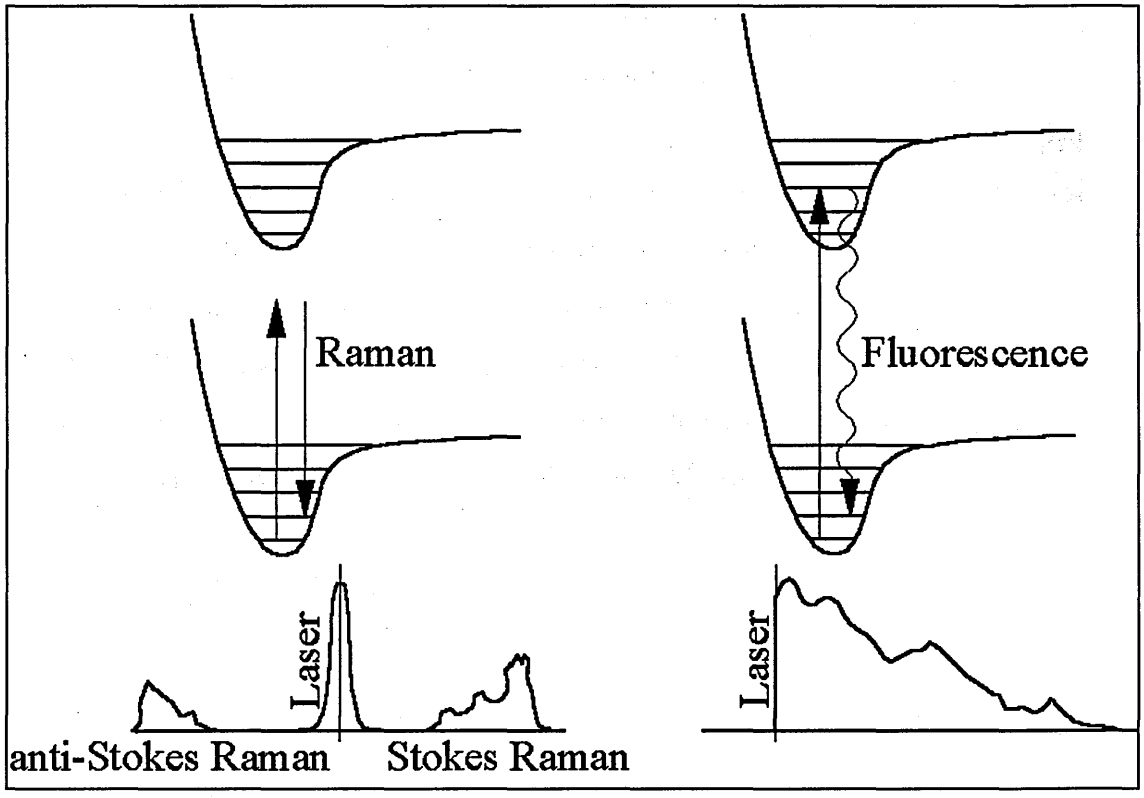

Figure 4.3 Inelastic Scattering Processes. - x-axis: Internuclear co-ordinate, y-axis: Energy; the horizontal lines refer to discrete energy levels.

Laser induced fluorescence can be used to quantify the concentration of species since the fluorescence is directly related to the population of excited state atoms or molecules. In order to relate the fluorescence directly to the initial probed concentration, the paths populating the excited state and relaxing from the excited state need to be understood and quantified. The molecule or atom can enter the excited state through chemical reaction, molecular collision or by radiative interaction. In LIF, the chemical reaction and molecular collision routes are insignificant compared with the more efficient laser excitation route. However, LIF measurements are complicated by four other possible routes from the upper or excited state to the relaxed state. A molecule in the excited state can avoid spontaneous emission (fluorescing) by either absorption of an additional photon and further excitation, inelastic collisions resulting in inter-system crossing into an electronic state that cannot radiatively release, electronic energy transfer to another molecule (quenching) or dissociation of an electronically excited molecule. These routes are shown schematically in figure 4.4.

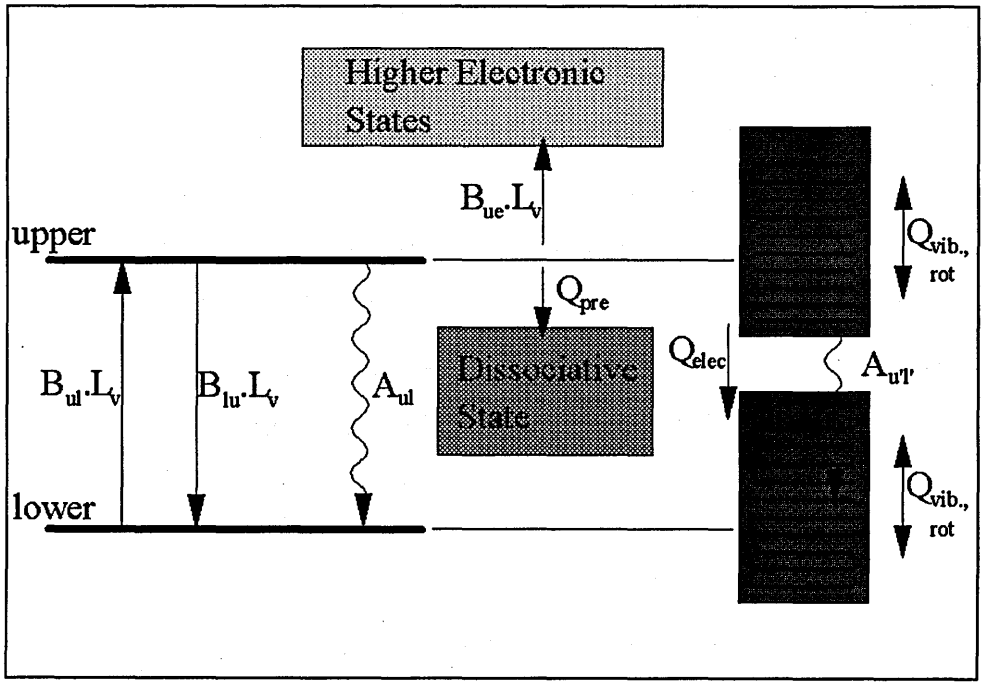

Figure 4.4 Energy Level Diagram of Important Transfer Processes in LIF (Seitzman and Hanson 1993).

In order to make absolute measurements of concentration using LIF, the alternative routes from the upper state need to be accounted for. This can be done by saturating the transition so that the fluorescence becomes independent of quenching processes. However, any laser sheet has low intensity wings across its thickness which will not saturate the fluorescence. The collected signal then becomes contaminated with non-saturated LIF. A practical solution to achieving quantifiable LIF measurements is to gain accurate knowledge of the quenching rates or choose a regime where the quenching rates are constant. For the non-saturated case, the fluorescence, R_f over solid angle, Ω may be calculated from the steady state, two level equations below.

$$R_f = \frac{h.\upsilon}{4.\pi}.\Omega.A_{21}.N_2 \qquad [1]$$

$$\text{where } N_2 = N_1.\frac{B_{12}.I}{(B_{12} + B_{21}).I + A_{21} + Q_{21}} \qquad [2]$$

$$\text{so} \quad R_f \propto A_{21}.N_2 \quad \text{where } N_2 \text{ is a function of I and } Q_{21}$$

$$\text{setting} \quad I_s = \frac{Q_{21} + A_{21}}{B_{12} + B_{21}} \quad \text{gives} \qquad [3]$$

$$S_f \propto \frac{1}{2}.A_{21}.N_1.\frac{1}{1 + \frac{I_s}{I}} \qquad [4]$$

Where Planck's constant is *h*, the light frequency is ν, the number of molecules in the lower state is N_1, the number of molecules in the upper state is N_2, the Einstein coefficient for spontaneous emission is A_{21}, the Einstein coefficient for the rate of absorption of photons is B_{12}, the Einstein coefficient for the rate of stimulated emission is B_{21}, the incident laser intensity is I, the overall quenching rate coefficient is Q_{21}, and

the saturation laser intensity is I_s. When the laser intensity, I_s far exceeds the saturation limit I_s, the following equation applies;

$$R_f \alpha \frac{1}{2}.A_{21}.N_1. \qquad [5]$$

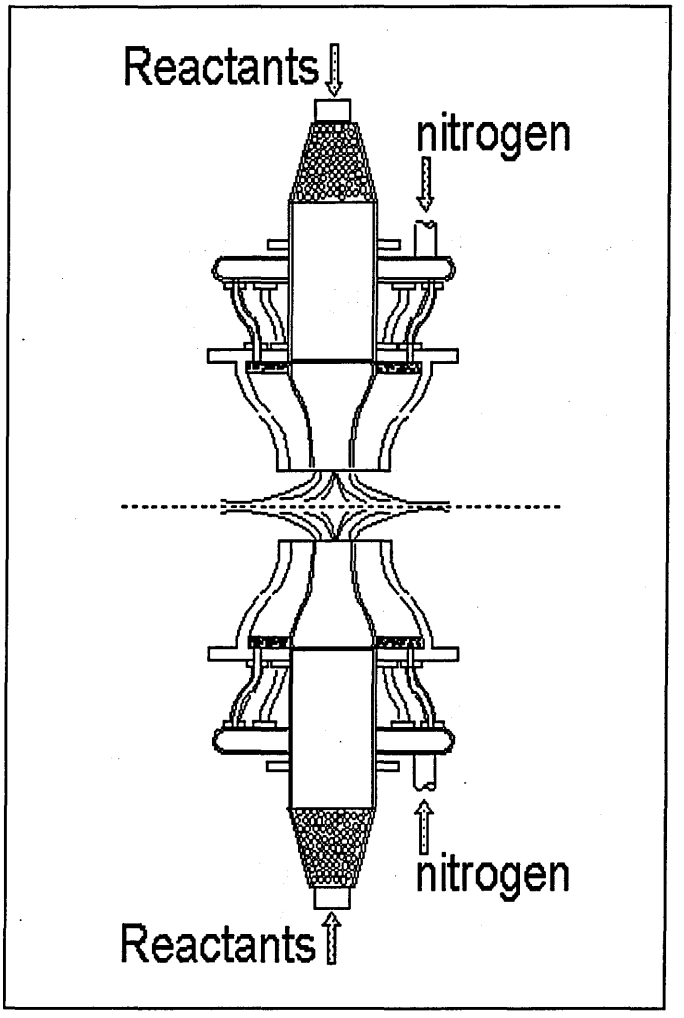

Figure 4.5 The Counterflow Burner

4.2 The Counterflow Triple Flame

The triple flame studied was stabilised on a counterflow burner designed and commissioned by the author as part of a Master of Science thesis (Harding 1992). The device consists of two burners situated axially opposed to each other in a vertical plane. The burners eject a plug flow of reactants in counterflow geometry forming a stagnation plane between the two burner nozzles. Premixed and non-premixed flames can stabilise in the region close to the stagnation plane.

Each burner may be supplied with any gaseous mixture of fuel and air. The reactant mass flows are accurately measured using calibrated sonic nozzles. The burners may also be fitted with turbulence grids to add turbulence to the reaction zone. The combustion stabilises in disc shaped flames located in free space between the two

burners, providing simple access for measurement interrogation using laser diagnostics and physical probes.

The flow field between the two burners consists of two opposed, decelerating flows of reactants, which meet at a stagnation plane where the axial components of velocity reach zero. The stagnation plane is situated at a point determined by the balance of momenta between the two burners. The stagnation plane position is held stable because the high fluid viscosity at combustion temperature damps out fluctuations or instabilities and also because the burner exit velocities aerodynamically squash the flow field into a confined volume. The strain rates in the flow field are determined from the flow's velocity gradients. The fluid strain rates in the combusting flow field may be controlled by adjusting the distance between the two burners or by varying the reactant jet velocities. The combustion products and the unburnt portion of the reactants become ejected horizontally away from the vertical burner axis. To prevent combustion between the reactants and the ambient air, a curtain flow of nitrogen surrounds the ejecting reactant jets as they leave the burner nozzles.

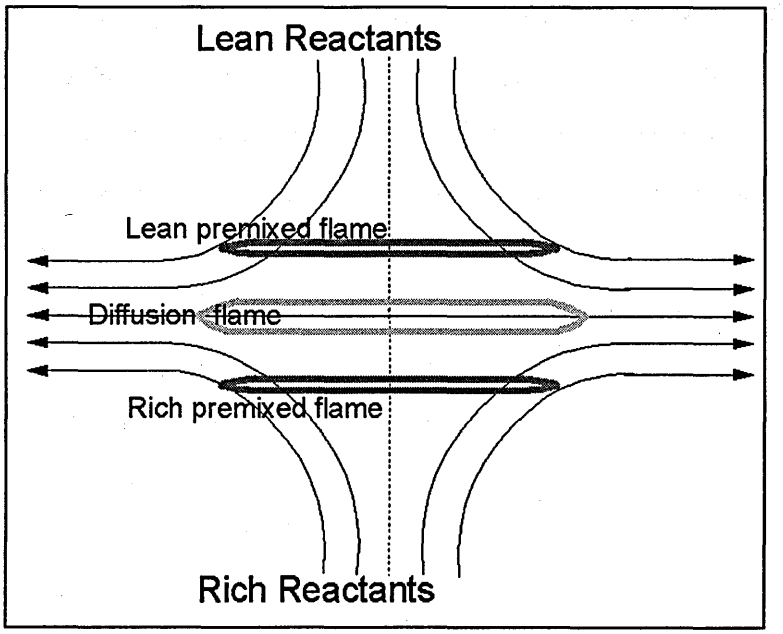

Figure 4.6 Diagram of the Triple Flame Structure

By feeding one of the burners with a fuel lean mixture and one burner with a fuel rich mixture, a triple flame may be stabilised. As the lean mixture reactants leave one of the burner nozzles, a lean premixed flame stabilises where the reactant mixture flame speed meets the reactant flow's velocity. Similarly, a rich premixed flame can be stabilised by supplying the other burner with a fuel rich mixture. The excess air from the lean premixed flame continues towards the stagnation plane, where it meets the combustible products of the rich premixed flame. A wet, diffusion flame then stabilises at the stagnation plane. The products of the rich premixed flame are largely carbon monoxide, hydrogen and fragments of methane. This is because the rich premixed flame is under ventilated causing incomplete combustion and results in the break up of fuel molecules. The overall stoichiometry of the diffusion flame is usually rich. The triple flame conditions used in the experiment and later modelled are shown in the table below. The separation between the burners was 44 mm.

Lower Burner - rich reactants	**Upper Burner** - lean reactants
methane : 0.063g/s	methane : 0.025 g/s
air : 0.915 g/s	air : 0.826 g/s
$\varnothing = 1.18$	$\varnothing = 0.52$
Nozzle Exit Velocity = 0.747 m/s	Nozzle Exit Velocity =0.710 m/s

Table 4.1 Conditions of Triple Flame.

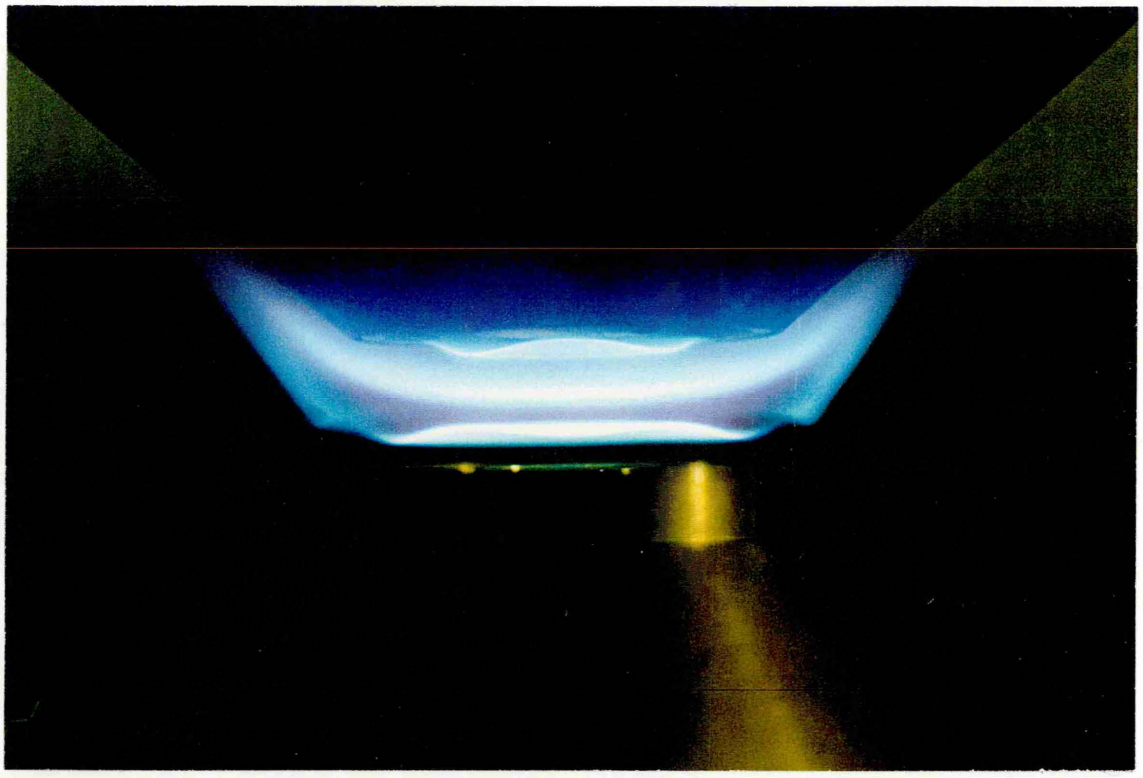

Figure 4.7 Photograph of a Triple Flame Stabilised on the Counterflow Burner.

4.3 OH LIF measurements in the triple flame.

The OH radical is instrumental in the process of the oxidation of combustibles to water and carbon dioxide in all flames. By studying the concentration of OH in the triple flame, valuable information on the location of the flame fronts and heat release rates can be found.

The relative concentration of OH in the counterflow burner triple flame was measured using planar laser induced fluorescence, exciting the $Q_1(3)$ line of the OH radical. The fluorescence was collected on resonance with the transition in the non-saturated regime. A Lambda Physik EMG 150 MSC tuneable excimer laser filled with a xenon chloride gaseous mixture was used to provide a laser sheet at 308.24 nm. This was fine tuned to the excitation line of OH and formed into a thin sheet using a combination of two cylindrical lenses and one spherical lens. The cylindrical lenses had focal lengths -75 mm (plano concave) and +150 mm (plano convex). The focal length of the spherical

lens was 2 m. This provides a sheet approximately 30 mm wide and 250 μm in thickness.

The resonant fluorescence from the OH radical was collected onto a CCD camera system placed perpendicular to the laser sheet. The camera system incorporated a f/4.5 105 mm micro UV fused silica lens collecting the fluorescence, focusing onto a gated image intensifier which was lens coupled to the CCD camera. The camera was controlled from a 486 PC computer and the images were stored onto the hard disk. The experiment was synchronised to open the camera shutter first, then after an 80 ms delay to trigger the excimer laser which in turn triggered the HV power supply for the intensifier tube. The intensifier was operated to provide a gate or intensifier duration of 100-200 nanoseconds. By using a very short intensifier gate tightly synchronised around the laser pulse, the fluorescence signal and the laser scatter will be imaged with virtually no contribution from the ambient light or from the flame's natural luminosity. The minor contribution of non-fluorescent background light and laser scatter can be subtracted later by taking a similar image with the laser de-tuned to avoid excitation of OH. The effect of non-uniformity in the laser sheet was accommodated for by flatfielding the OH image with another image representing laser sheet intensity and intensifier gain. The flat fielding image was made by taking an image of acetone fluorescence. Acetone fluorescence does not saturate at these laser fluences. This results in an image of acetone fluorescence which is directly proportional to laser sheet intensity and intensifier gain.

Once set up, the OH fluorescence images along with the background and flatfielding images can then be digitally recorded on the CCD camera and downloaded onto a DEC workstation for image processing. The final image of OH fluorescence is found from the following formula.

$$\text{Final OH Fluorescence Image} = \frac{(\text{Measured Image} - \text{Background Image})}{(\text{Flatfield Image} - \text{Background Image})} \quad [6]$$

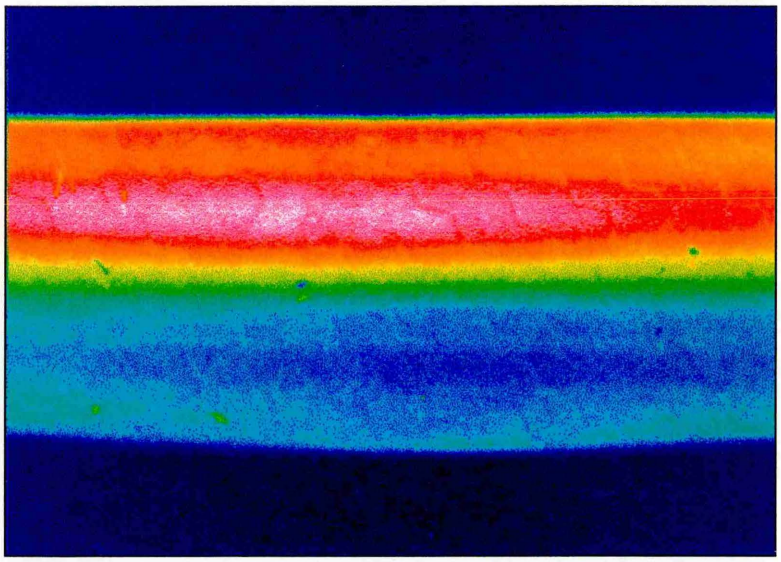

Figure 4.8 OH LIF Image of Triple Flame. The lean, premixed, flame is at the top, the diffusion flame is in the middle and the rich premixed flame is at the bottom.

By taking a one dimensional profile of OH fluorescence in the flame down its axis, the relative OH concentration profile can be compared with the modelled OH profile. The concentration of OH can then be related to the heat release and reaction rates in the flame (Starner 1992). The position of the peaks in OH concentration are also accurate indicators of flame front position.

4.4 Temperature Measurements in the Triple Flame

In order to obtain further information on the triple flame, a 2D Rayleigh scattering image was taken. This image may be used to find the reactant temperatures and for comparison with a modelled Rayleigh scattering profile. Rayleigh scattering is light scattering off molecules of gas. By shining a laser sheet into a region of known gas, the Rayleigh signal can be correlated to the gas density and therefore its temperature. Rayleigh scattering signal is a function of the molecular concentration or gas density, the scattering molecule's Rayleigh cross section or gas mixture's effective Rayleigh cross section and the incident light intensity.

$$\text{Rayleigh Scattering Intensity, } I_R = K.I_0.N.\sigma_{eff} \qquad [4]$$

where $\sigma_{eff} = \Sigma x_i . \sigma_i$

and K is the calibration constant for the optical collection efficiency, I_0 is the incident light intensity, N is the number of molecules in the laser sheet volume, σ_{eff} is the effective Rayleigh scattering cross section, x_i is the mole fraction and σ_i is the molecule's Rayleigh cross-section. A table of the Rayleigh cross section of relevant gas molecules is shown in Table 4.2.

Gas Species	Rayleigh cross-section ($x10^{-28}$ cm^2 $ster^{-1}$)
Hydrogen	1.1
Methane	11.6
Carbon Monoxide	6.8
Oxygen	4.4
Nitrogen	5.1
Air	5.1
Water Vapour	3.8
Carbon Dioxide	11.9
Nitric Oxide	5.2

Table 4.2 Rayleigh Cross-sections of Various Gases.

A Continuum Surelite 1 Nd:YAG laser, frequency doubled to give a light beam at 532 nm was used to form a high intensity laser sheet. The laser sheet was formed as in the OH LIF experiment using a combination of two cylindrical lenses and one spherical lens. The sheet was passed through the centre of the triple flame to provide the Rayleigh scattering signal. The laser sheet had to be heavily masked to prevent unwanted laser light from entering the camera image. The camera system used was identical to the OH experiment, but was synchronised with a signal originating from the laser power supply to trigger the PC computer which controlled the camera. The intensifier was triggered from an output trigger signal from the Nd:Yag laser power supply.

An image of the Rayleigh scattering from the triple flame was then recorded and saved to the hard disk. In order to find the calibration constant for the collection efficiency of

the camera system, Rayleigh scattering signals from pure air and methane at ambient temperature were found. These were generated by flooding the measurement with the required gas via the counterflow burner nozzles. Helium has a very small Rayleigh cross section and consequently may be used as a background image. The helium Rayleigh scattering is too weak to allow the laser structure to be visible. A flatfielding image was obtained by taking a Rayleigh scattering signal of methane which provides a strong scattering signal proportional to laser sheet intensity. The region between the burners can easily be flooded with pure gas by supplying both burners with a high flow rate of the relevant gas.

The final image of triple flame Rayleigh scattering was calculated as follows. - [7]

$$\text{Final Rayleigh Image} = \left(\frac{\text{Measured Rayleigh Image - Helium Background Image}}{\text{Methane Rayleigh Image * 0.1 - Helium Background Image}} \right)$$

Since the concentration of the initial reactants in the triple flame is known, the effective Rayleigh cross-section can be calculated and the reactant temperatures found. Using the methane Rayleigh image as a calibration for the optical collection efficiency and the methane image to flat-field, the reactant temperatures were calculated to be 297 K for the lower burner, and 333 K for the upper burner.

In the reaction zone, the exact concentration field is unknown and the effective Rayleigh cross-section can only be estimated from modelled data, hence the absolute temperatures cannot be found without the use of modelled data.

4.5 Modelling the Triple Flame

The triple flame may be modelled on a one dimensional grid representing the centreline between the two burners that passes from the initial reactant, through the flame fronts and into the opposing reactant. Since the grid is one dimensional a full chemistry

mechanism can be incorporated into the model including effects such as aerodynamic straining.

The triple flame was modelled on a code called DIFLAM written by Warnatz the boundary conditions entered are listed in Table 4.1. The species profiles in Mol fraction, temperature, reactant velocities and heat release rates are plotted in Figure 4.9. Three flames are clearly apparent on the modelled results. The two premixed flames can be observed by the temperature rise, the heat release rates and the formation of CO and H_2 along with intermediates such as CH and HO_2. However, the central diffusion flame at the stagnation plane is only identifiable by the existence of peaks in OH, H and O concentration.

The central OH peak is likely to be equilibrium OH or OH diffusing into the stagnation plane. The model shows no OH in the premixed flames indicating that the code is basically modelling autoignition or preignition chemistry in these regions. The triple flame measured and modelled is close to its extinction limits due to the premixed flames stoichiometries. The model initially appears to have underestimated the flammability of the whole triple flame system resulting in insufficient OH.

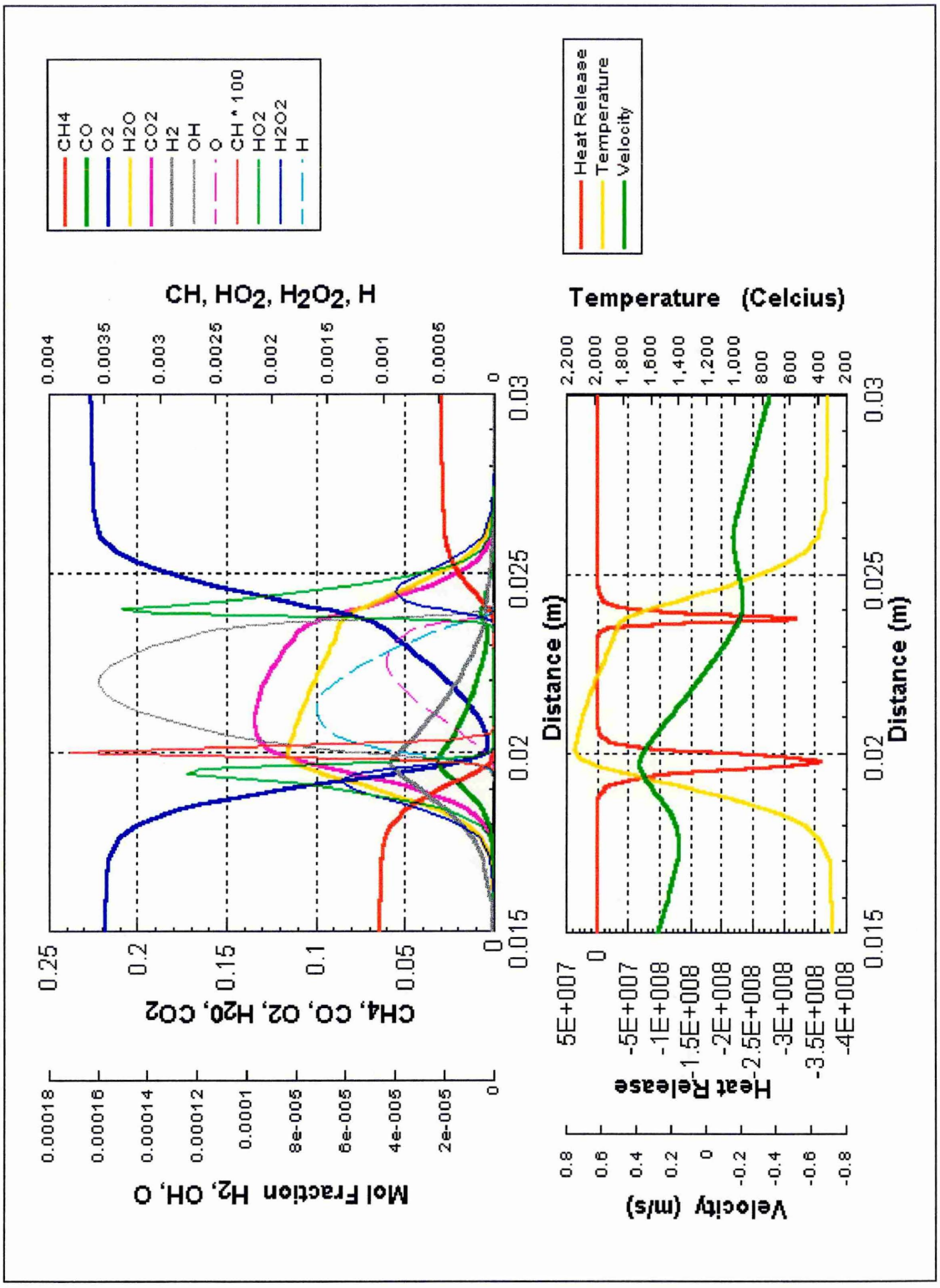

Figure 4.9 Species Profiles through Triple Flame - modelled on the Warnatz code.

4.6 Discussion of Results

The OH profiles modelled are obviously different from the measured profiles. The flame distances and the chemistry differ between the model and the experiment.

The distance between the premixed flames is smaller on the modelled data than the actual, measured distance. This is due to the model under-predicting the premixed flame speeds. This could have been augmented by the model incorrectly estimating the entire velocity field causing inaccurate estimations of the extraction of reactants and products perpendicular to the axis or grid. The use of a potential flow model to predict the flow field is insufficiently accurate for modelling counterflow flames (Egofopoulos 1994, Puri 1986, Sick 1990). This would result in incorrectly positioned flame fronts. The Rayleigh profile compares favourably in shape with the predicted temperature profile, showing that the rate of temperature rise approaching the premixed flames are similar.

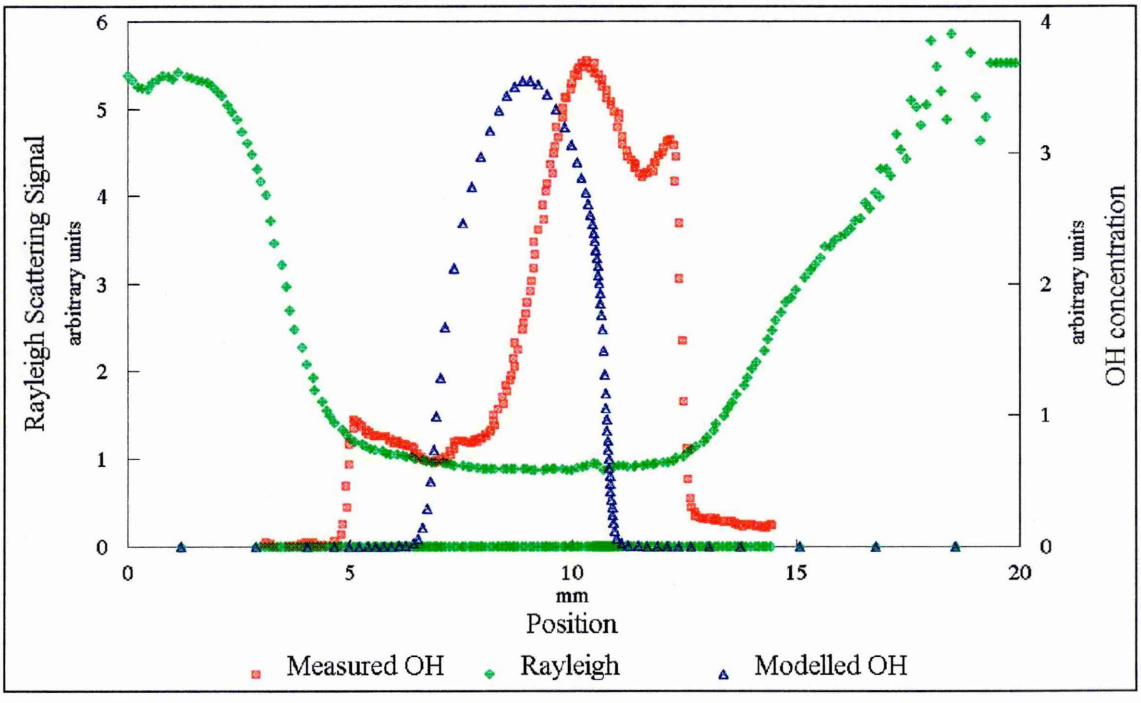

Figure 4.10 Graph of Measured Rayleigh Scattering Profile, Measured OH Profile and Modelled OH Profile.

The chemistry of the triple flame has been incorrectly predicted by the model since no OH is present in the premixed flames and the central OH peak comprises only sub-equilibrium OH. The model appears to show premixed combustion taking place but appears to be predicting autoignition chemistry rather than the three strong flame fronts which appear in the actual case. The reasons for the discrepancy between the modelled and measured data is likely to be due to the model either not reaching genuine convergence or inaccuracy due to insufficient grid densities. The modelled solution presented code did not result in any significant changes in the output after considerable extended running of the code but was very slow to converge. The lack of OH in the premixed flames could also be caused by preferential diffusion of light species such as O, H, and OH towards the stagnation plane. Preferential diffusion will take place in the actual case but since there is clearly OH measured in the premixed flames the model would be over predicting the preferential diffusion.

Studies of triple flame stability by Lockett show that triple flame extinction is a complex phenomena (see section 4.6). As the premixed flames reach rich or lean extinction they merge with the diffusion flame. The extinction is a continuous process as the premixed flames merge into the central diffusion flame. The OH radical is present throughout the merging process. Lockett's modelled data and this result suggests that the real premixed flames undergo extinction (defined by the absence of OH) after merging of the flames. The code shows the extinction to be prior to merging of the flames as defined by the absence of OH in the premixed flames.

4.7 Triple Flame Stability Limits

A flammability map of the triple flame extinction limits has been compiled for the counterflow burner (Locket R.D.). This shows the limits of triple flame stability, confined by premixed flame flashback, premixed flame rich and lean extinction and the complex interaction between the premixed flames and the diffusion flames. For a triple flame to exist, the rich flame has to be sufficiently rich to leave enough unburnt fuel to stabilise diffusion controlled combustion at the stagnation plane. Similarly, the lean

premixed flame must leave sufficient oxidant for the diffusion flame if a triple flame is to be stabilised. A stability map has been completed using OH LIF to determine the existence of the flames for nozzle exit velocities up to 3.5 m/s where the flow becomes turbulent and the diffusion flame extinguishes.

The turbulence in the triple flame can be created using turbulence grids but can also arise due to the collision effect of the two opposing high velocity reactant jets colliding at the stagnation plane. This ignition map includes the effect of turbulence arising solely due to the reactant jet velocities. As the nozzle exit velocities become higher, the turbulent shear in the triple flame eventually extinguishes the diffusion flame. This is relevant to LPP combustion since in real devices burning partially premixed, the high turbulence levels are likely to extinguish some or all of the non-premixed combustion. The counterflow burner triple flame is more susceptible to diffusion flame extinction due to its rich stoichiometry. However, the turbulence levels in the primary zones of LPP combustors are usually considerably higher than the levels at which the diffusion flame extinguishes in the counterflow burner triple flame. The turbulent intensity in the triple flame is of order 10 %, whereas in a lean, premixed gas turbine combustor primary zone it often exceeds 40 %.

The effect of reducing the non-premixed combustion in a practical LPP combustor, would be to allow more time for turbulent mixing in the primary zone, reducing NOx emissions. This shows that with partially premixed combustion the NOx emissions are likely to be affected by mixing in the premixer as well as in the primary zone. The strain rate at strain induced extinction is known to be much higher for premixed flames than for diffusion flames. (Law et al 1986, Puri et al 1986). Typical experimental strain rates at extinction for stoichiometric methane-air diffusion flames are 271 s^{-1} (Puri et al 1986), 320 s^{-1} (Tsuji et al 1969). Law (1986) quotes the strain extinction to be 1772 s^{-1} for premixed methane air flames as opposed to 1760 s^{-1} by Egofopouolos (1994).

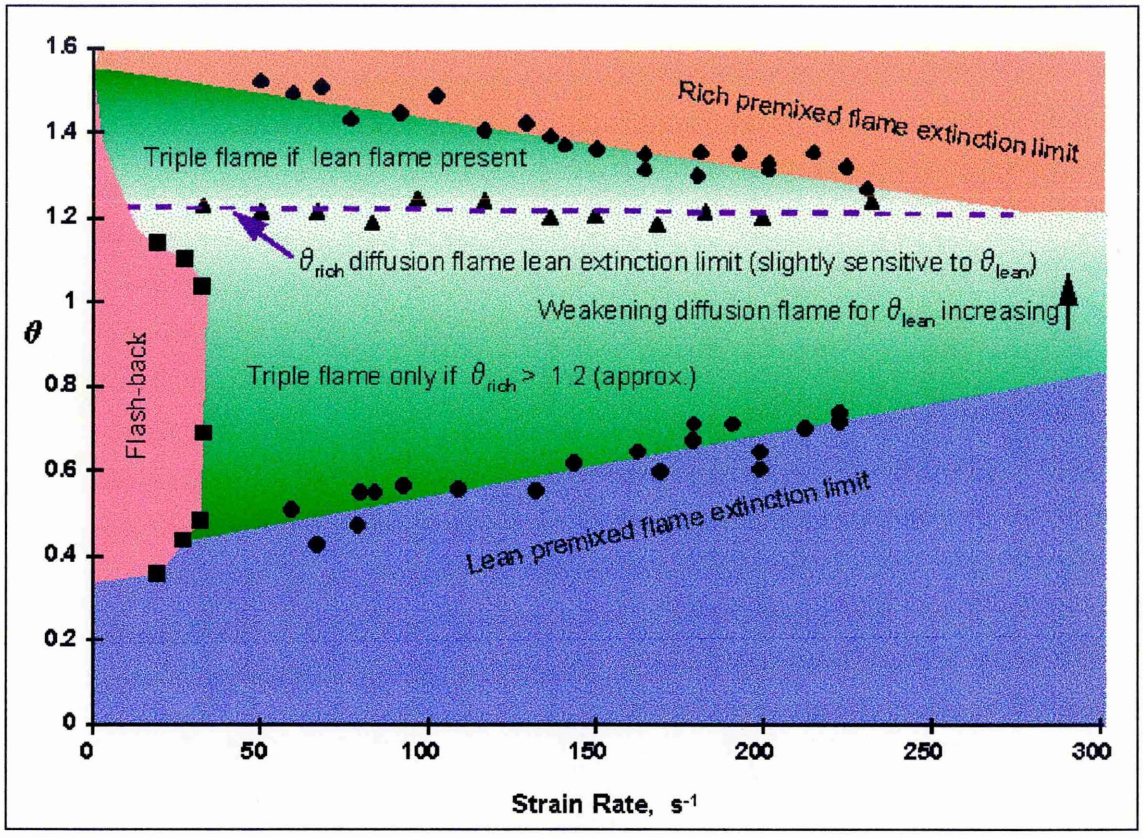

Figure 4.11 Stability Map of the Counterflow Triple Flame

4.8 Conclusions

A methane triple flame stabilised on a counterflow burner has been studied in order to further understanding of partially, premixed combustion. Measurements of the OH radical concentration and Rayleigh scattering to indicate the temperature field have been made on a triple flame close to extinction. These measurements clearly identify three OH peaks representing the two premixed flames and non-premixed flame that comprise the triple flame system. One dimensional profiles taken from these measurements have then been compared with modelled data.

The model fails to adequately predict the chemistry or the flow field of the triple flame. Triple flames are complicated in terms of stability and the coupling effect between flames, making their simulation a challenging test for one dimensional models. The model predicts the production of OH only in the central diffusion flame region but no

OH in the premixed flames. This is despite the clear presence of premixed flames identified by the production of intermediates, consumption of reactants and rises in temperature. The discrepancy between the modelled and measured OH species profiles is due to the failure of the model. This is caused by several effects. The flow field is inadequately predicted by the potential flow model, the grid density may be insufficient and the solution may not have fully converged. The model may also have over estimated the preferential diffusion of low molecular weight species towards the stagnation plane. The rich chemistry is likely to be incorrectly predicted due to over estimation of the rate at which the reaction with CO and OH to CO_2 proceeds.

The triple flame stability map provides a useful indicator of the complicated nature of triple flame extinction mechanisms. It verifies the understanding that non-premixed or diffusion flames suffer strain extinction much earlier than premixed flames. The consequence of this in an LPP combustor is that any gases leaving the premixer unmixed may not burn non-premixed due to the turbulence induced local strain rates. This would have a favourable consequence on NOx emissions when partially premixed fuel-air mixtures are burnt.

5. DESIGN AND PERFORMANCE OF THE OPTICAL LPP COMBUSTOR RIG

This chapter details the features of the experimental combustor rig, the design calculations performed, the design decisions made and the rig's subsequent performance. The purpose of the rig is to operate a full scale lean, premixed, prevaporised combustor under realistic conditions for taking measurements upon. The combustor is equivalent to one sector or carburettor of a series that would occupy an annular combustion chamber in a gas turbine. The combustor has inlet conditions realistic of compressor exit temperatures (900 K) and has a non-dimensional mass flow (flow function or $m\sqrt{T}/P$) equivalent to a high pressure combustor. The combustor runs at nominally atmospheric pressure to maximise optical access and simplicity.

5.1 Design Specification

Combustor:	
Mass flow air	0.107 kg/s
Fuel Flow (AFR 22)	4.86 g/s
Power	225 kW
$M\sqrt{T}/P$	3.21 kg K/s atm
Mass flow film cooling air	0.005 kg/s
Inlet Air Temperature	900 K
Inlet Air Pressure	1 atm (nominal)
Service Rig:	
Turbotron Blower:	
Mass flow range	0.05 - 0.45 kg/s
Pressure range	0.1 - 1 bar
Exit Temperature	328 K
Oxygen Enrichment: mass flow oxygen	5.0 g/s
Preheater: vitiating combustor	
Mass flow propane	2.4 g/s
Overall AFR	45
Primary Zone equivalence ratio	0.62
Power	112 kW
Mean exit temperature	900 K

Table 5.1 Specification of Optical LPP Combustor Rig

The rig comprises of an air blower which delivers air through an oxygen enrichment system, to a vitiating preheater. The preheater is another combustor fuelled with propane. The levels of oxygen enrichment are such that at the exit of the preheater the oxygen levels are restored to the normal 20.9 % equivalent in ambient air. The preheater emissions as measured by gas analysis comprise of a mixture of 21 % oxygen, 2.33 % carbon dioxide, 3.12 % water and 73.6 % nitrogen at 900 K to the LPP combustor inlet.

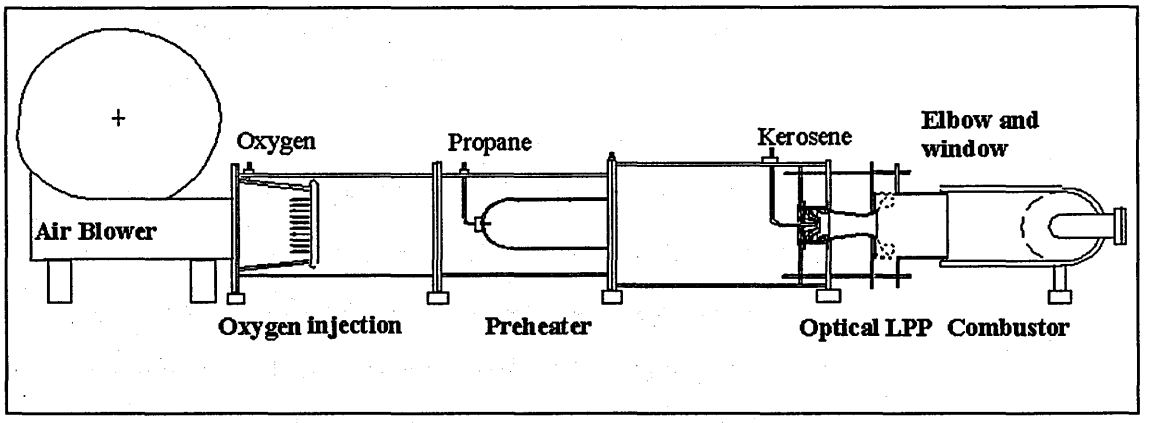

Figure 5.1 Schematic of Optical LPP Combustor Rig

The LPP combustor consists of a set of radial co-flow swirlers surrounding a kerosene injector delivering the fuel-air mixture to a premixing duct. The mixture then leaves the premixing duct into a wider section dump combustor or flame tube. The primary zone is swirl stabilised. The premixing duct and first section of the primary zone are made from transparent fused silica. The flame tube then exhausts into a water cooled elbow section which incorporates a window fitted in an air purged stub. The window in the elbow stub is also made from fused silica and allows axial viewing directly into the primary zone and premixer.

The rig is instrumented to continuously measure all the necessary parameters. A services flow diagram and the rig instrumentation are detailed in Appendix I. The flange located between the premixer and flame tube is water cooled and delivers film cooling air to the inside of the flame tube. The fused silica components are sandwiched between

ceramic gaskets and are fitted to allow for any differential expansion of their mating components due to variations in temperature and expansivity.

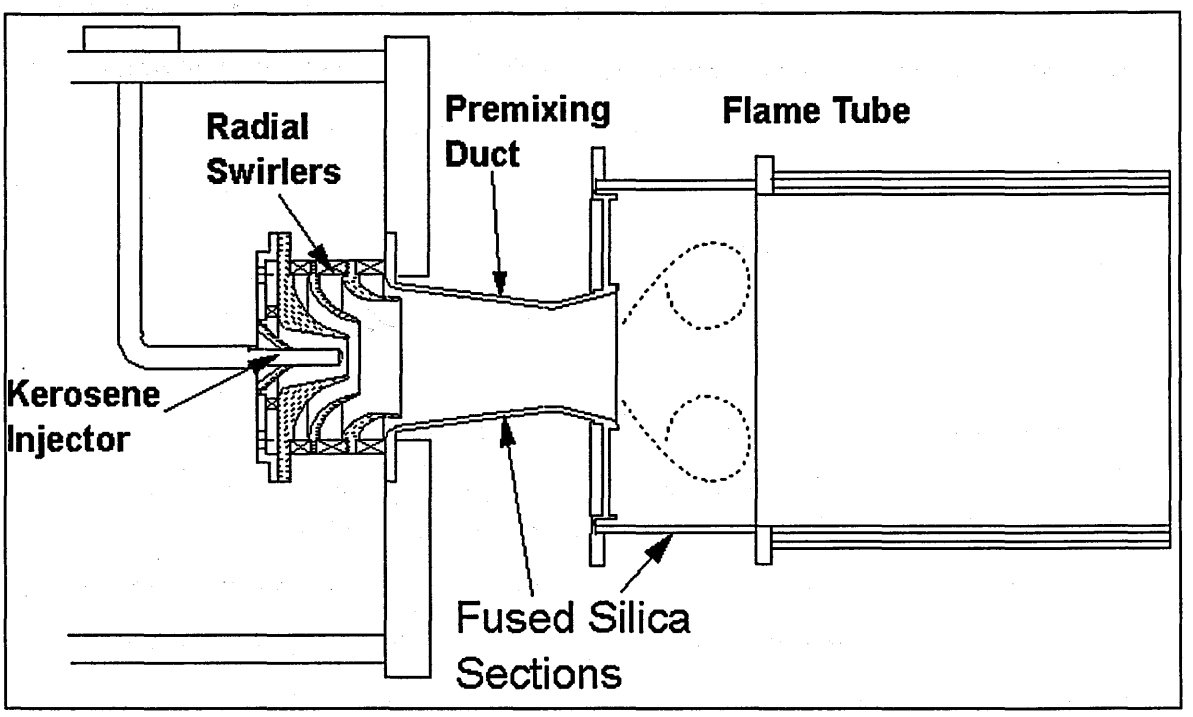

Figure 5.2 Section of the LPP Combustor

5.1.1 LPP Combustor Design Features

The combustor design is based on an early Rolls Royce prototype LPP combustor. The purpose of the first section of the LPP combustor is to generate a uniform mixture of fuel and air. The kerosene is injected in a manner to distribute the fuel as evenly as possible across the premixer diameter using the high momentum of liquid droplets. The swirlers set up a highly turbulent flow field in the premixer which is conducive to rapid mixing of fuel and air. The swirlers are installed in co-flow with each other in order to leave some residual swirl at the exit of the duct to augment the primary zone recirculation zone. The degree of swirl is set to maximise the primary zone stability and is small enough to ensure that the premixer flow does not suffer vortex breakdown. Using co-swirl reduces the turbulence and shear in the duct compared with counter swirl. However, the flow in the duct is still sufficiently turbulent to produce rapid

mixing. The premixing duct Reynolds number is 27,000. A core flow of air passes through the centre of the injector. This enhances the premixer axial velocity which is depleted by the centrifugal effect of the swirling flow. This lowers the likelihood of a vortex forming which would result in flame flashback. The fuel and air is mixed by turbulent mixing and diffusion. The premixing duct geometry is designed to accelerate the flow through a slight neck to further reduce the likelihood of flame flashback. The final outer swirler delivers a high velocity flow of air inside the premixing duct wall. This air velocity is large enough to reduce the boundary layer thickness to less than the mixture's quenching distance. This prevents flashback along the boundary layer and minimises the residence time avoiding autoignition. The primary zone stabilises at the premixing duct exit in a toroidal recirculation region as the mixture expands into the flame tube. Film cooling air lines the first section of the flame tube cooling the transparent fused silica section.

The final section of the flame tube is water cooled, as is the exhaust elbow and premixer to flame tube flange in order to maintain the mechanical integrity of the combustor. This will have the effect of quenching combustion reactions and increasing emissions of carbon monoxide and unburnt hydrocarbons.

5.2 The Effect of Vitiation on Premixed Combustion

The inlet air to the LPP combustor needs to be preheated to 900 K. Vitiation is an economical way of providing preheat up to temperatures higher than it is possible to achieve using electrical filament heaters. However, the vitiated exhaust is a mixture of depleted oxygen, nitrogen, water and carbon dioxide. The oxygen levels can simply be replenished from a bottle bank, but the water and carbon dioxide will affect the LPP combustor, particularly by shortening the mixture autoignition delay. A study has been completed to quantify this effect on autoignition delay for a variety of fuel air mixtures.

Using a zero dimensional model of the chemistry of autoignition in homogenous reaction the chemical autoignition delay can be estimated. The model employed was

devised by J.Warnatz et al and is known as HOMREA for homogenous reaction. The closest available fuel to kerosene that it was practical to model was n-heptane. A number of mixtures of n-heptane with vitiated and pure air were modelled for different vitiation fuels and mixture stoichiometries to evaluate their chemical autoignition delays. An artificially high pressure of 13.6 bar was incorporated into the model to achieve realistic chemical ignition delay times of order 5 ms. The results shown in figures 5.3 and 5.4 show that both H_2O and CO_2 reduce the autoignition delay time as does NO and NO_2. Laster (1989) found that the ignition delay reduces from 0.2 to 0.1 ms with 0.5% NO or 4% NO_2 at 1000 K. This is due to the increased rate of formation of intermediate radicals and species like CH, H_2, H, OH ,CO and HCO. Other important intermediates that increase more rapidly due to the effect of vitiation are HO_2, CH_4, CH_2O and H_2O_2. These radicals help consume small hydrocarbon molecules causing a small but detectable rise in temperature. These intermediate radicals eventually become consumed and created in chain branching reactions which eventually leads to full ignition and the propagation of a flame front. Spadacinni (1993) measured a 4 % reduction in the autoignition delay for vitiation preheat of 1000 K.

Figures 5.3 and 5.4 Modelled Effect of Vitiation Fuel and Species on Autoignition Delay.

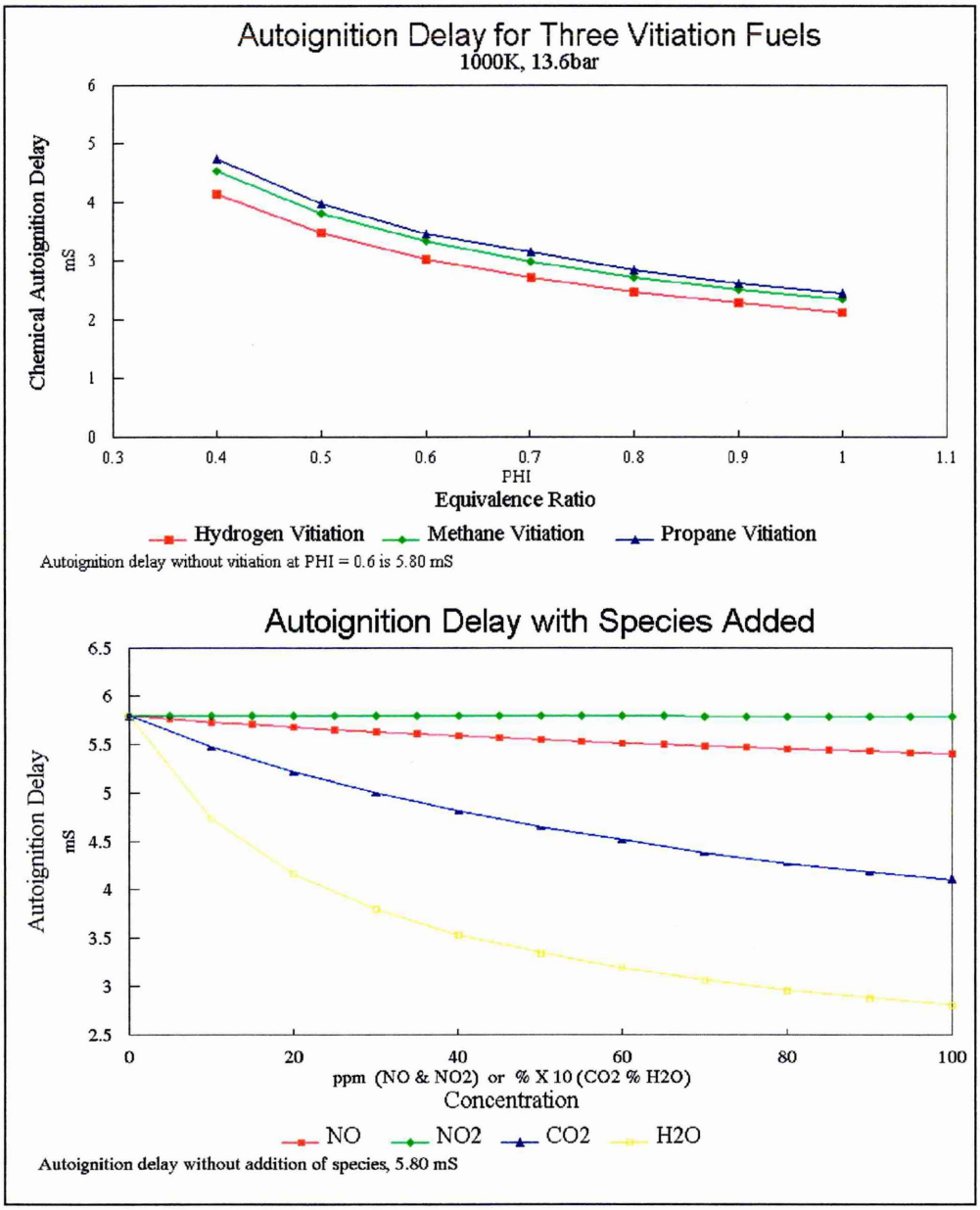

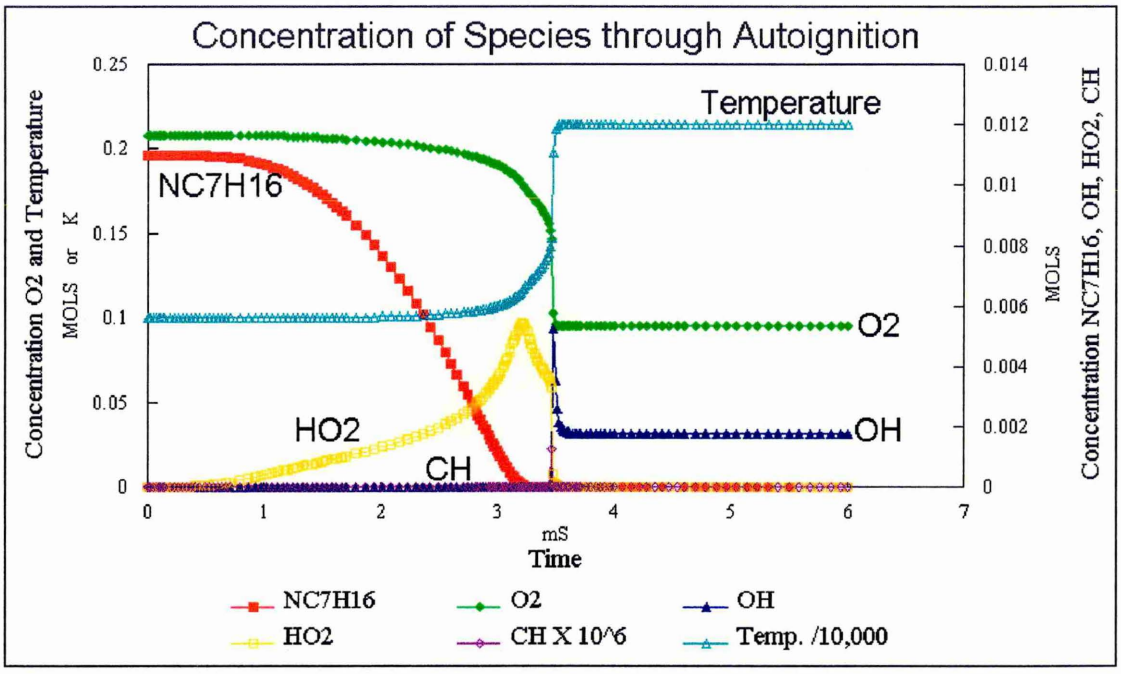

Figure 5.5 Modelled Species Concentration through Autoignition (intermediate species in Appendix I).

The dependence of pressure on chemical autoignition delay time is shown in the Arhennius equation; $delay\ time, \tau = \frac{A.e^{\frac{e}{R.T}}}{P}$. Since the autoignition delay time of hot kerosene air mixtures at atmospheric pressure is at least an order of magnitude longer than the likely maximum design pressures experienced in a gas turbine, the reduction of autoignition delay due to vitiation under conditions experienced in the experimental rig is insignificant.

5.3 Premixer and Flame Tube Wall Temperatures

In order to ensure that the fused silica premixing duct and flame tube sections would withstand combustion temperatures, calculations were performed to estimate the radiative and convective heat fluxes to and from the fused silica duct walls. Using the semi-empirical equations of heat transfer given, it is possible to solve for inner and outer wall temperature (Lefebvre 1983).

Balance of Heat Transfer per unit area

$$R_1 + C_1 + K = R_2 + C_2 = K_{1-2}$$

where R_1 Radiation to the wall

C_1 Convection to the wall

K Conduction along the wall (negligible).

R_2 Radiation from the wall

C_2 Convection from the wall

K_{1-2} Conduction through the wall thickness

Radiation to the wall

$$R_1 = 0.5.\sigma.(1+\varepsilon_w).\varepsilon_g.T_g^{1.5}.\left(T_g^{2.5} - T_{w1}^{2.5}\right)$$

The emissivity of the gas, ε_g can be estimated from the concentration of H_2O and CO_2, since these are the two main radiating species. The values can be found from graphs by Hottel and Egbert. At atmospheric pressure there needs to be no correction for pressure or spectral overlap. Alternatively, in primary zone combustion the emissivity of a gas, ε_g can be estimated using a formula by Reeves.

$$\varepsilon_g = 1 - e\left(-290.P.(q.l_b)^{0.5} T_g^{-1.5}\right)$$

Convection to the wall with no film cooling

$$C_1 = 0.020.\left(\frac{k_g}{D_L^{0.2}}\right).\left(\frac{m_{pz}}{A_L.\mu_g}\right)^{0.8}.\left(T_g - T_{w1}\right)$$

Convection to the wall with film cooling

$$C_1 = 0.069.\left(\frac{k_a}{x}\right).(R_{ex})^{0.7}.(T_{wad} - T_{w1})$$

The Reynolds number of the film cooling can easily be found from known air properties, but to calculate the adiabatic wall temperature, the film cooling effectiveness has to be found first.

$$film\ cooling\ effectiveness, \mu = \left(\frac{T_g - T_{wad}}{T_g - T_a}\right)$$

and derived from wall jet theory models,

$$\mu = 1.10.m^{0.65}.\left(\frac{\mu_a}{\mu_g}\right)^{0.15}.\left(\frac{x}{s}\right)^{-0.2}.\left(\frac{t}{s}\right)^{-0.2}$$

Radiation from the wall

$$R_2 = \sigma.(T_{w2}^4 - T_3^4)$$

The convective heat transfer from the wall should be negligible since there is no significant flow of cooling air passing over the duct exterior walls. The conduction of heat through the wall is represented by the following equation of heat transfer through a solid.

$$K_{1-2} = \left(\frac{k_w}{t_w}\right).(T_{w1} - T_{w2})$$

For the conduction of heat from the premixing duct end to the water cooled flange the following was used.

$$C_2 = \frac{k_w . A_i}{t_w}\left(T_{w1} - T_{fl}\right)$$

The constants used in these equations are listed in Table 8.2.

Table 5.2 Constants for Wall Temperature Calculations.

Property	notation	value
Area of interface	A_i	82.5e-03 m^2
Cross Sectional Flow Area	A_L	2.463e-03 m^2
Diameter of combustor	D_L	0.056 m
Thermal Conductivity - film cooling	k_a	2.816e-02 W/mK
Thermal Conductivity - gas 900K	k_g	6.276e-02 W/mK
Thermal Conductivity - gas 2000K	k_g	10.233e-05 W/mK
Thermal Conductivity - fused silica	k_w	2.5121 W/mK @900K 5.8615 W/mK @1400K
Beam Length,3.4.volume/surf. area	l_b	0.04924 m
Mass Velocity Ratio	m	0.83
Mass Flow Gas	m_g	0.107 kg/s
Pressure	P	101325 Pa
Fuel to Air Ratio	q	22
Reynolds Number - film cooling	Re_x	111,895
Height of film cooling slot	s	0.002 m
Temperature of flange	T_{fl}	288 K
Temperature Wall - inner	T_{w1}	-
Temperature Wall - outer	T_{w2}	-
Temperature wall - adiabatic	T_{wad}	856 K
Thickness of wall	t_w	0.005 m
Distance from film cooling entry	x	0.040 m
Emissivity - fused silica	ε_w	0.8
Emissivity - air 900K	ε_g	0.16
Emissivity - gas 2000K	ε_g	0.016
Dynamic Viscosity - film cooling air	μ_a	1.2174e-05 @325K
Dynamic Viscosity - gas	μ_g	3.897e-05 @900K 6.008e-05 @2000K
Stefan-Boltzman Constant	σ	5.67e-08 W/mK

5.3.1 Premixer

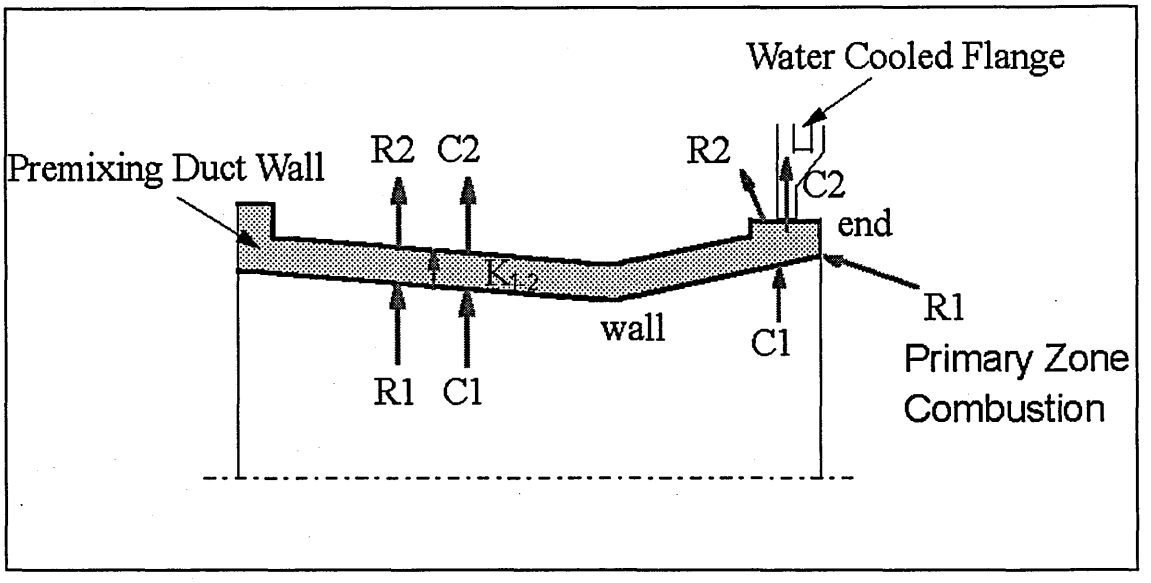

Figure 5.6. Heat Flux Components to and from Premixing Duct Walls

By solving these four equations in the heat transfer balance, the values of inner and outer wall temperatures T_{w1}, T_{w2} can be found. The measured and calculated premixing duct wall temperatures are shown below.

Along the premixer wall

Radiation to the wall, $R1 = 3.274 \times 10^{1}$ W/m^2

Convection to the wall, $C1 = 1.517 \times 10^{4}$ W/m^2

Radiation from the wall, $R2 = 1.520 \times 10^{4}$ W/m^2

Convection from the wall, C2 = negligible

At the premixer end

Radiation to the wall, $R1 = 1.158 \times 10^{4}$ W/m^2

Convection to the wall, $C1 = 6.894 \times 10^{3}$ W/m^2

Radiation from the wall, $R2 = 1.824 \times 10^{4}$ W/m^2

Conduction from the wall, $C2 = 1.523 \times 10^{1}$ W/m^2

Premixing Duct	Wall Temperature	End Temperature	Measured Temp.
inner wall	796 K	838 K	
outer wall	766 K	801 K	558K

Table 5.3 Premixing Duct Wall Temperatures

The measured outer wall temperature is over 200 K cooler than the estimated value. This could be due to cooling along the premixing duct length to the water cooled flange and cooling convective currents external to the premixer. The premixing duct is partially insulated from its interfacing components with a ceramic gasket at one end.

5.3.2 Flame Tube

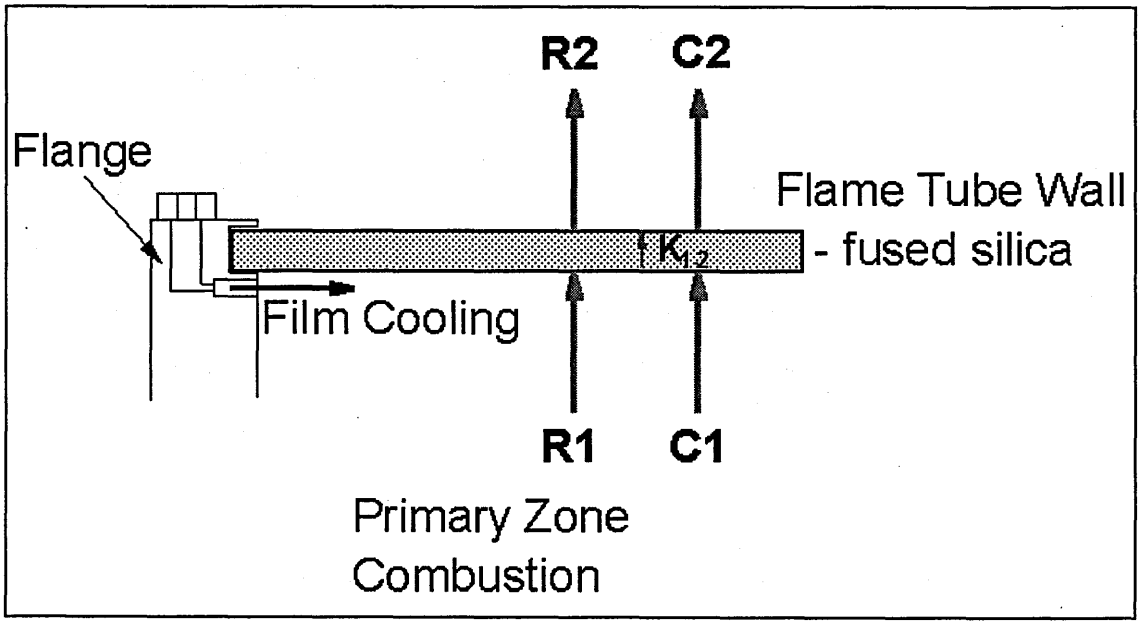

Figure 5.7 Heat Flux Components to and from Flame Tube Walls

Without film cooling		With 5g/s film cooling
Radiation to the wall,	R1 = 1.069×10^4 W/m^2	1.154×10^4 W/m^2
Convection to the wall,	C1 = 2.998×10^4 W/m^2	9.378×10^3 W/m^2
Radiation from the wall,	R2 = 4.068×10^4 W/m^2	2.092×10^4 W/m^2
Convection from the wall,	C2 = negligible	negligible

Flame Tube	Wall Temperature no film cooling	Wall Temperature 5g/s film cooling	Measured Temp. 5g/s film cooling
inner wall	1011 K	846 K	
outer wall	976 K	829 K	823 K

Table 5.4 Flame Tube Wall Temperatures

The measured flame tube outer wall temperature is 6 K lower than estimated. This could again be due to cooling along the length of the section to the water cooled section and through external convection currents but is within the accuracy of the calculation. The fused silica flame tube section is insulated at both ends from the water cooled part by ceramic gaskets. To optimise the film cooling air the graph in figure 3.8 was drawn and a suitable film cooling mass flow selected. Fused silica can sustain continuous use at 1223 K and limited use at 1473 K, suggesting that there would be no problem with overheating the fused silica components. The hoop stresses due to the temperature gradient across the fused silica walls are well within the material's mechanical strength.

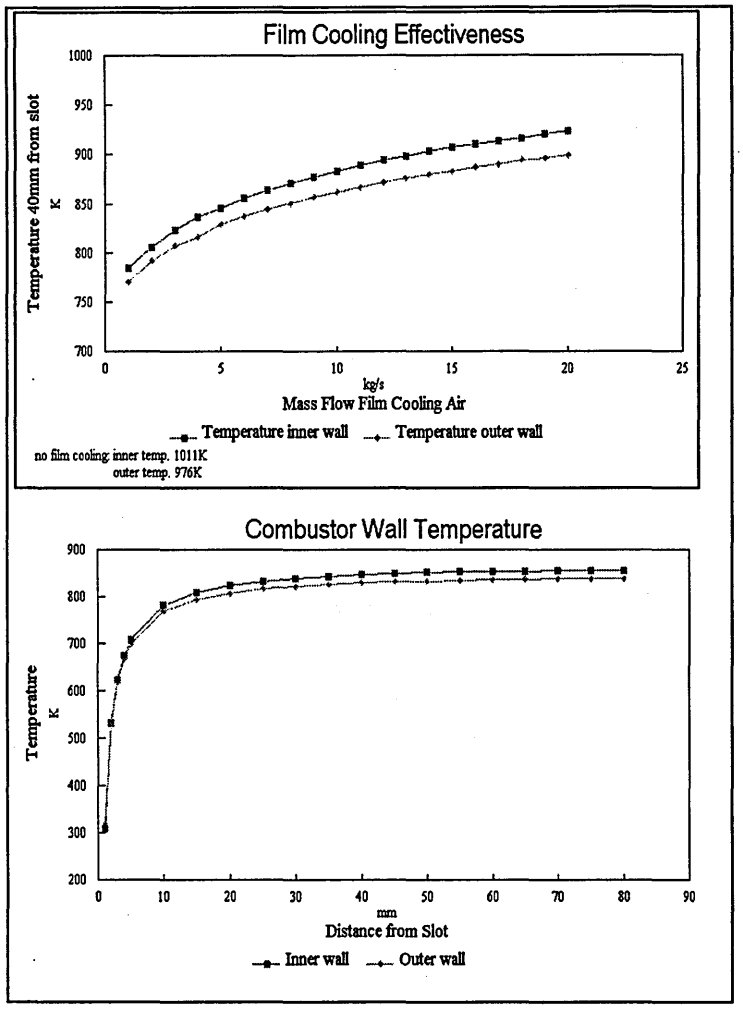

Figure 5.8 Graphs of Flame Tube Wall Temperatures against Film Cooling Mass Flow and Distance from Exit Slot.

Increasing the mass flow of cooling air through a small slot, increases turbulent mixing between the cooling air and the combustion gases. This can have the effect of reducing the film cooling effectiveness. The heat fluxes to and from the water cooled section of the flame tube were estimated by the same method to find the amount of cooling required. Using a 3 mm water cooling jacket and a water flow of 0.1 kg/s the inner and outer wall temperatures were calculated to be 453 K and 447 K respectively.

5.4 Modifications to Preheater Combustor

The air preheater is a propane fuelled experimental, rich burn combustor manufactured by Snecma and originally designed to burn liquid fuel at high pressure. This was the only available suitably sized combustor and consequently required substantial modification to stabley burn gaseous fuel under lean conditions to provide low emissions of CO and NOx. This section is concerned with the seven main modifications to the combustor.

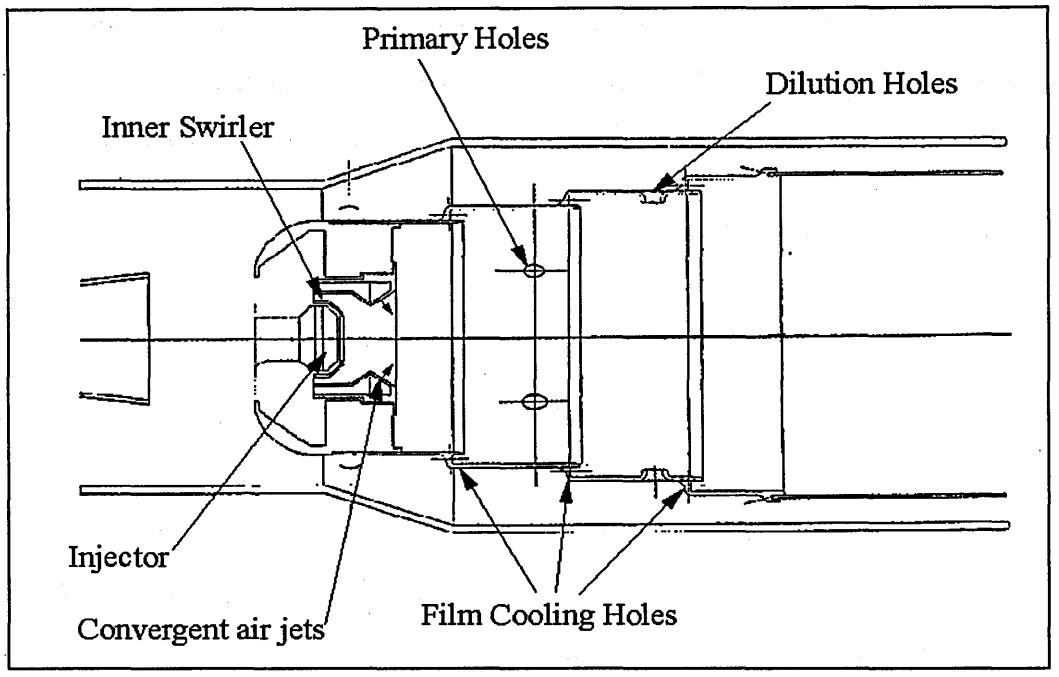

Figure 5.9 The Snecma Combustor

The first problem with the combustor was to achieve ignition in the primary zone! The combustor would light but only with the flame stabilised at the exit of the combustor. Using a piece of wool attached to the end of a rod as a primitive flow direction indicator, it was possible to observe whilst running cold that there was no recirculation in the primary zone. The main reason for this was the effect of convergent air jets in the swirler cup initially designed to break up ligaments of liquid fuel. This air jet penetrated and destroyed the recirculation zone when using gaseous fuel. The recirculation zone was further destabilised by the injector fuel jets ejecting in counterflow to the air swirler in the combustor head. This creates extra turbulence and reduces the overall swirl impeding the formation of a recirculation. The swirler cup was modified to divert the convergent air jets to a wider diameter and angle where they would augment the recirculating air. The inner swirler was also changed to deliver a higher mass flow of air in *co-flow* to the fuel injection swirl. The gas injector was also redesigned to deliver a higher fuel jet velocity for atmospheric combustion, and to penetrate further into the primary zone. These modifications resulted in stable, blue combustion in the primary zone, and wide flammability limits for a variety of combustor loadings.

The second main problem with the combustor was excessive CO emissions. At suitable levels of preheat, the combustor emitted very low concentrations of NOx with concentrations of carbon monoxide exceeding 0.25 %. This suggested that the primary zone flame was burning too rich, was heavily quenched and burning incompletely. This was largely caused by a very high film cooling mass flow, a rich primary zone and a very short intermediate zone. The intermediate zone is the region between the primary zone and the dilution air holes where partially burnt combustion products reach equilibrium. Thermal paint measurements showed that the combustor wall temperatures were very cool. The film cooling was reduced to virtually zero and more air was diverted into the primary zone to improve the primary zone combustion stoichiometry. It can be shown experimentally and by modelling with HOMREA that carbon monoxide typically requires approximately 10 ms to reach equilibrium. In order to enhance the burnout of carbon monoxide the intermediate zone length was extended by a factor of three. These modifications resulted in preheater emissions of 200-400 ppm CO and 18 ppm of NOx, at overall preheat levels of 900 K. The alterations were designed to achieve the mass flow splits shown below resulting in a primary zone equivalence ratio of 0.62. The air mass flow split between the different entry ports was estimated by calculating the pressure drop across each port and summing up the pressure loss factors, ϕ. The calculations of pressure loss factor, ϕ and mass flow splits are shown in more detail in Appendix I. These are listed below before and after modification in Table 5.5. From looking at flow visualisation images of a similar model combustor using water analogy, it was decided to modify the proportion of primary air as follows. The primary zone air comprises air to the inner swirler, the cup and flare, the first row of film cooling and half the primary air. This means 37.1% of the inlet air is directed into the preheater primary zone. The final preheater emissions are listed in section 5.6.2.

Table 5.5 Mass Flow Splits of the Preheater.

Air Entry Port	Before Modification	After Modification
Inner Swirler	4.8 %	5.6%
Cup and Flare	9.7 %	11.3 %
First Row of Film Cooling	21.2 %	7.5 %
Primary Holes	12.6 %	22.0 %
Second Row of Film Cooling	19.0 %	6.6 %
Dilution Holes	10.4 %	37.7 %
Third Row of Film Cooling	20.3 %	7.1 %
Final Ring Inclined Holes	1.9 %	2.3 %

5.5 Oxygen Replenishment

The method chosen to mix oxygen into the air was to inject the oxygen, into the turbulent region situated downstream of a turbulence grid. This technique mixes the two gases together in a very short mixing length. The turbulence grid was designed to provide an acceptable pressure drop and turbulence intensity. The grid hole sizes are small to prevent any oxygen jets from penetrating the grid. The oxygen was injected via a ring injector and manifold.

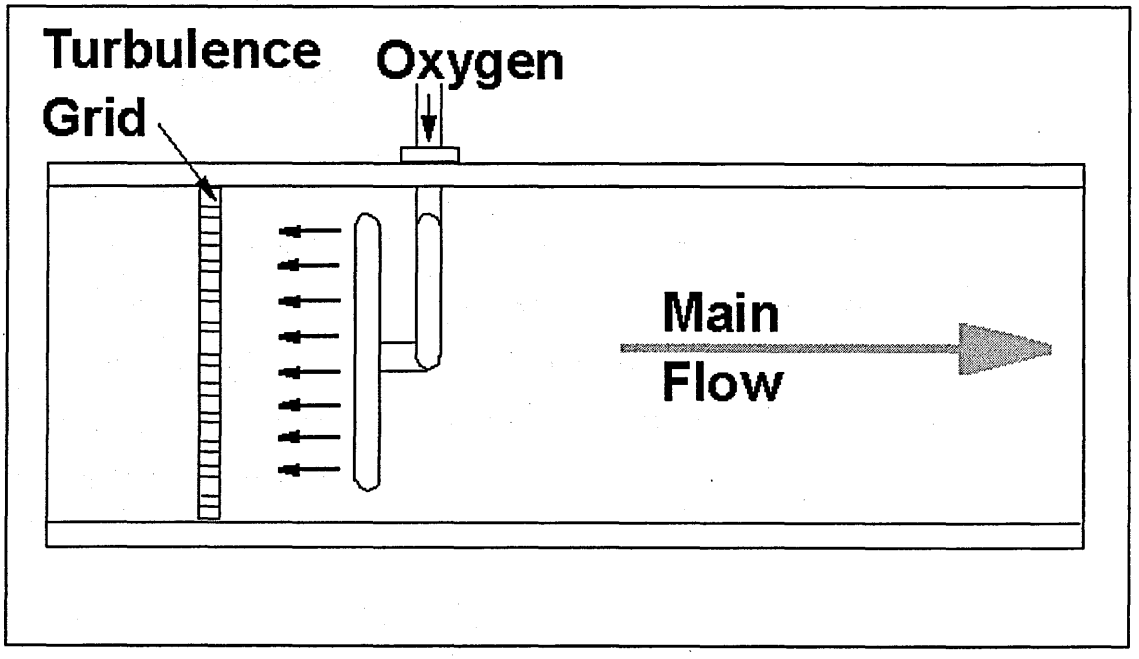

Figure 5.10 Oxygen Injection System

The levels of turbulence downstream of the turbulence grid can be calculated from formulae by Baines and Peterson. These are listed in Appendix I. The turbulence grid generates a turbulence intensity of 12%, 100 mm downstream of the grid and has a pressure drop of 20 Pa. The oxygen is mixed upstream of the preheater to maximise mixing prior to combustion in the LPP combustor. Assuming 37.1% of the inlet air is used in the primary zone, the adiabatic flame temperature of the mixture is 2359 K with the oxygen added. This temperature is higher than in reality due to non-premixed combustion, non-equilibrium effects and high heat losses to the rig and surroundings. To ensure that the oxygen is well mixed a traverse of oxygen concentration on entry to the preheater was measured.

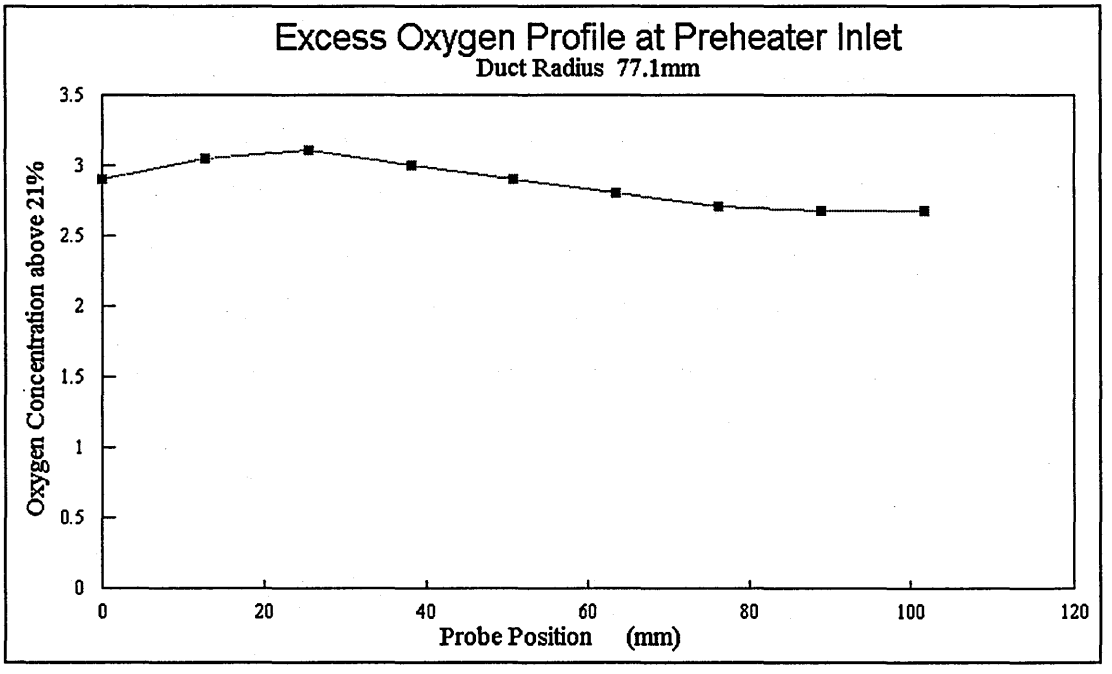

Figure 5.11 Graph of Oxygen Concentration on Entry to Preheater Section

5.6 Performance and Operation of Rig

5.6.1 Operation Condition

The operation condition at which the measurements were taken was 0.107 kg/s, 900 K inlet temperature, nominal atmospheric pressure with an LPP combustor overall air fuel

ratio of 22. The preheat level of 900 K was chosen to be representative of a gas turbine compressor exit temperature and to deliver a sensible compromise between CO and NOx for the preheater. A film cooling mass flow of 5 g/s is sufficient to insulate the fused silica flame tube section from the primary zone gases and minimise flame dilution and quenching. The procedure devised to light up and shut down the rig is shown in Appendix I. The adiabatic temperature for kerosene combustion is shown in Appendix I for several AFRs.

Mass Flow Air = 0.1 kg/s

Mass Flow Fuel = 4.86 g/s

Mass Flow C_3H_8 = 2.4 g/s

Mass Flow oxygen= 5 g/s

5.6.2 Preheater Performance

The performance of the preheater was tested for stability, emissions and reliability. The preheater operation limits were found for a range of air mass flows, with and without oxygen. The lean flammability limit was determined by slowly reducing the propane mass flow until the combustion extinguished. The upper operation limit is set by determining a suitable tolerance level of carbon monoxide emission. The preheater emissions and limits of flammability are below in figures 5.12 - 5.14.

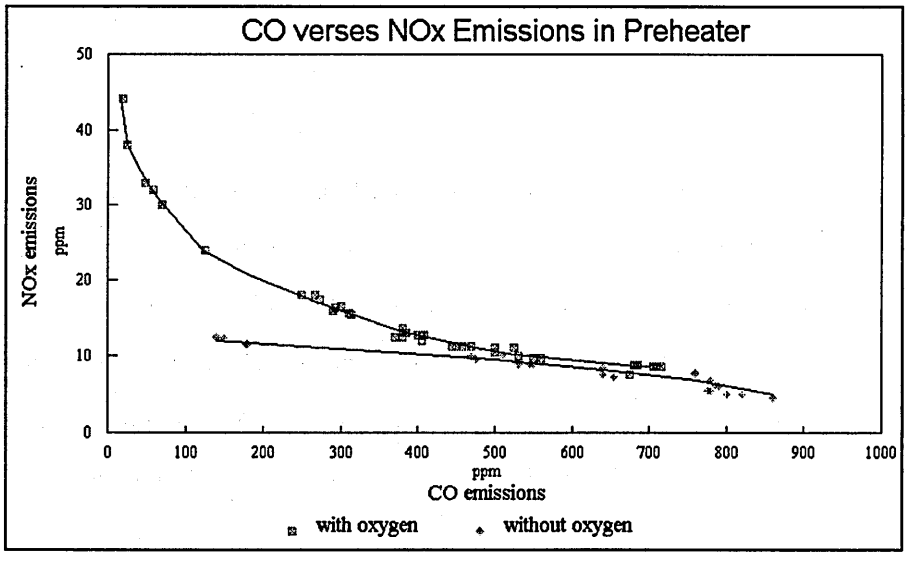

Figure 5.12 Graph relating Carbon Monoxide Emissions to Nitrogen Oxide

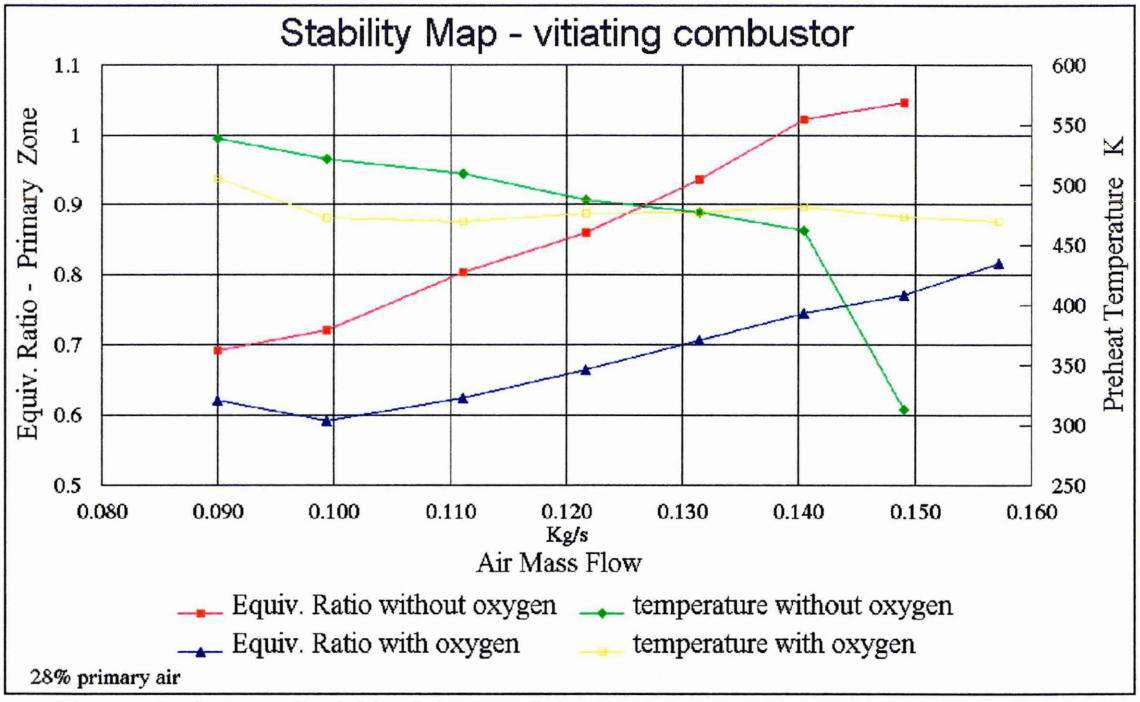

Figure 5.13 Lean Stability Limits of the Preheater with and without Oxygen Replenishment.

Preheater emissions measurements at the entrance of the LPP combustor were taken using gas analysis to observe any gradients in species concentration. The background (preheater) emissions levels measured when taking LPP measurements were sampled at the LPP combustor exit. These show a reduction in CO caused by the extended residence time.

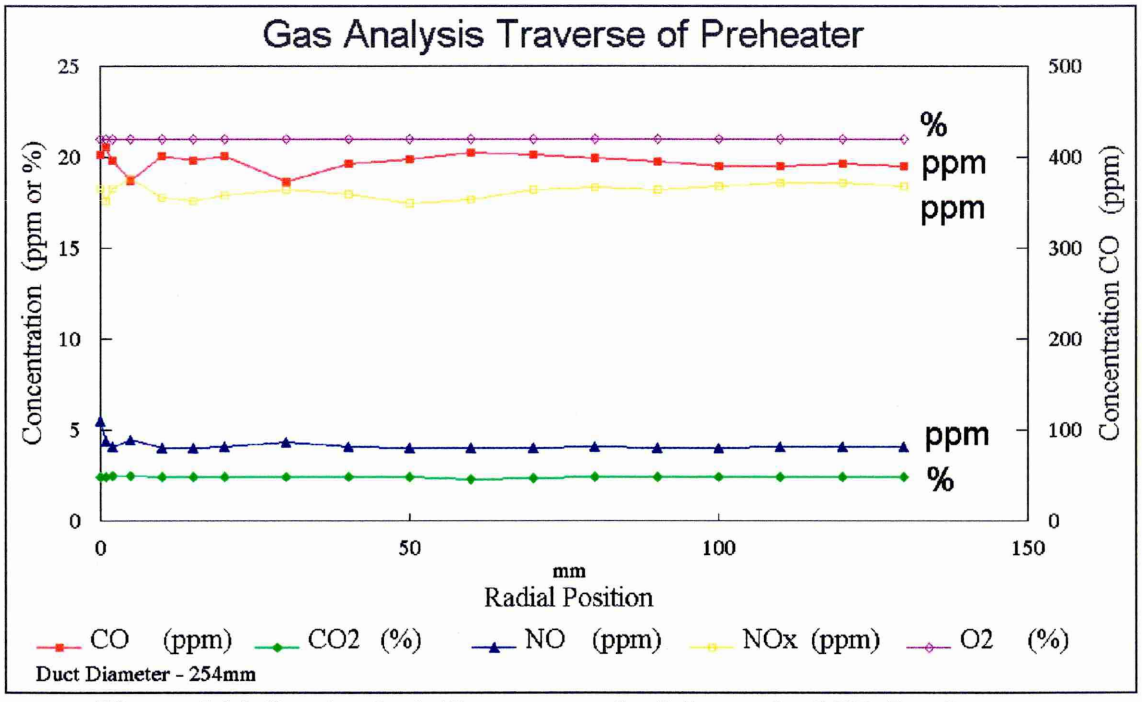

Figure 5.14 Gas Analysis Traverse at the Inlet to the LPP Combustor.

5.6.3 LPP Combustor Performance

The stability of the LPP combustor was determined by finding its lean flammability limit. The fuel flow was reduced slowly until the primary zone extinguished. The LPP combustor reaches lean extinction at an air fuel ratio of 40. This excludes the effect of dilution of the primary zone from film cooling air.

A traverse of emission species was taken at the exit of the LPP combustor using gas analysis. This shows the carbon monoxide production is at a maximum near the cold water cooled walls. The formation of NOx is slow in the cool region close to the walls. The species concentrations immediately close to the walls all decrease to zero due to dilution from the film cooling. The hottest region, in the centre of the exhaust creates the least carbon monoxide and the most NOx.

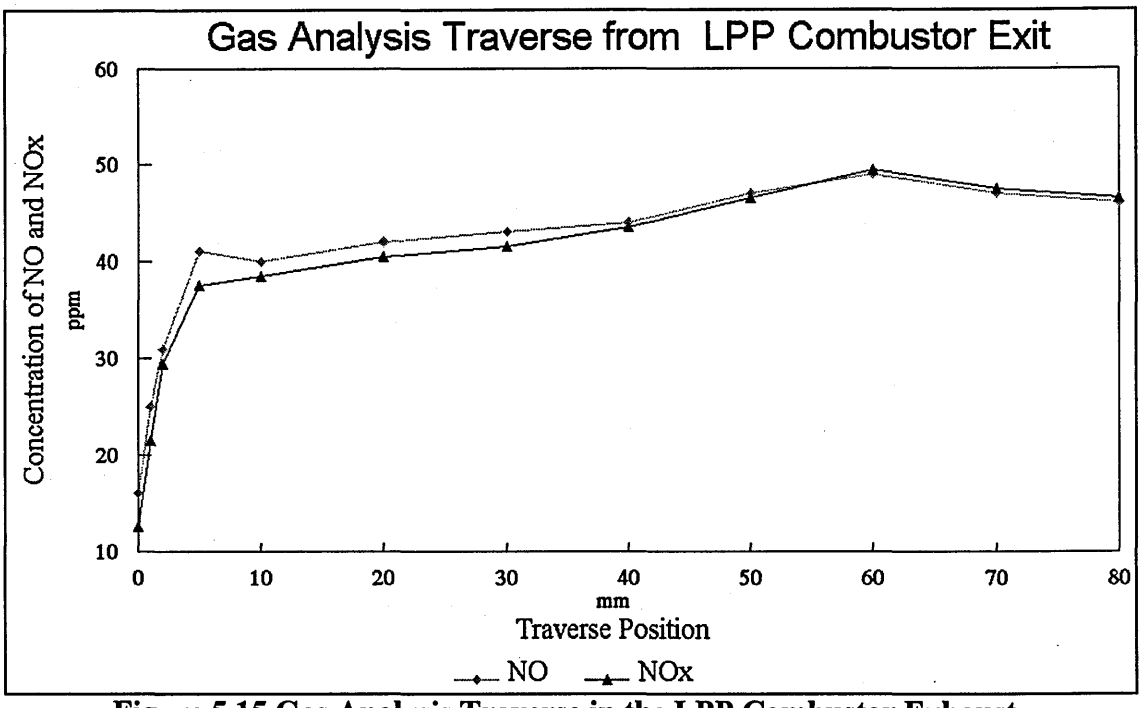

Figure 5.15 Gas Analysis Traverse in the LPP Combustor Exhaust.

The variation in the LPP combustor emissions at different air fuel ratios was measured by gas analysis with the sample probe centrally located in the exhaust, 300 mm from the premixer end. These measurements are shown below along with the background levels caused by the preheater alone. Assuming that the final emission of NOx is a sum of the preheater NOx emission and the LPP combustion emission, the premixed combustor NOx values can be found. The emissions levels on condition at AFR 22 are equivalent to between 1.0 and 1.7 EINOx, depending on the contribution of NOx from the preheater. This compares with target levels for stratospheric flight at cruise of 5 EINOx. The NOx levels reduce as the overall AFR is increased due to the lower flame temperature. The emissions of carbon monoxide also reduce with increasing AFR. This is most likely due to dissociation of CO_2 under richer operation. As the mixture AFR increases towards the lean limit (40), the carbon monoxide emissions eventually rise again due to the lower flame temperature causing incomplete oxidation. The combustor design is likely to contribute to CO emissions due to the high usage of water cooled components like the flame tube end and from using cold, ambient air for film cooling.

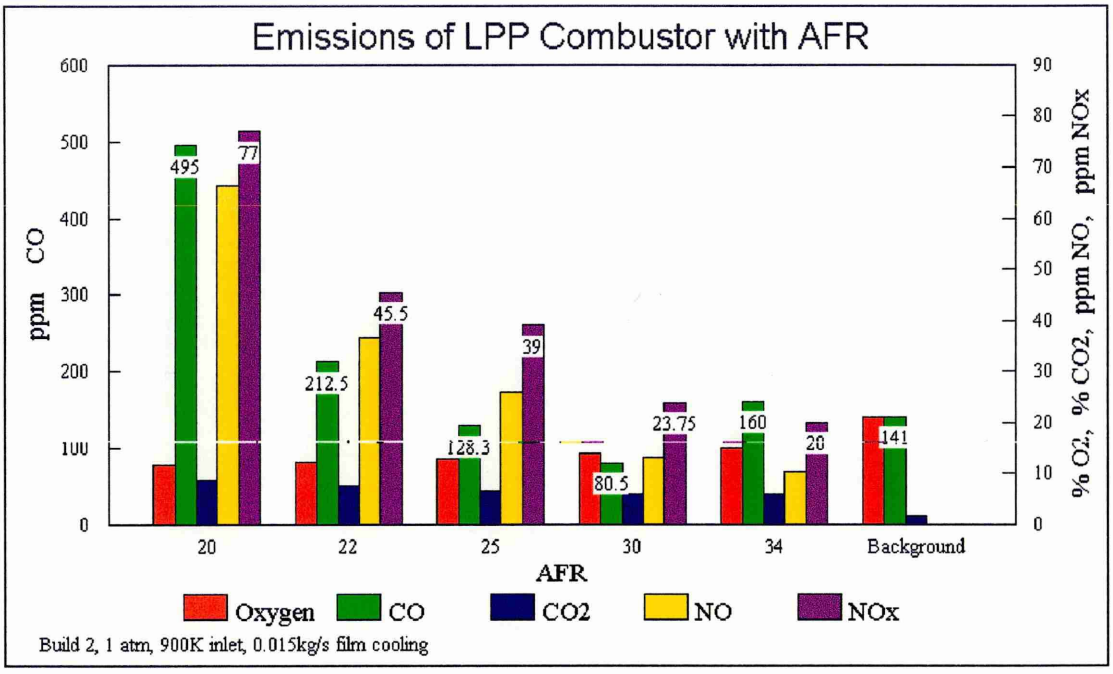

Figure 5.16 Variation in LPP Combustor Emissions with Air Fuel Ratio.

5.7 Summary

An experimental rig has been built to operate a full scale, high inlet temperature, atmospheric pressure lean, premixed, prevaporised combustor. The combustor provides wide optical access for taking non-intrusive laser diagnostic measurements and has access for physical gas analysis and temperature probes. The preheater has been fully characterised for stability and emissions and provides oxygen replenished preheat up to 1000 K. The LPP combustor operates stabley up to a lean limit of AFR 40. The emissions on the design condition of AFR 22 are between 1 and 1.7 EINOx with 200 to 400 ppm carbon monoxide.

The following figures 5.17 -5.20:

Figure 5.17 Actual Build of LPP Combustor

Figure 5.18 Engineering Scheme of Mounting of LPP Combustor

Figure 5.19 Photograph of LPP Combustor : non-combusting

Figure 5.20 Photograph of LPP Combustor : combusting

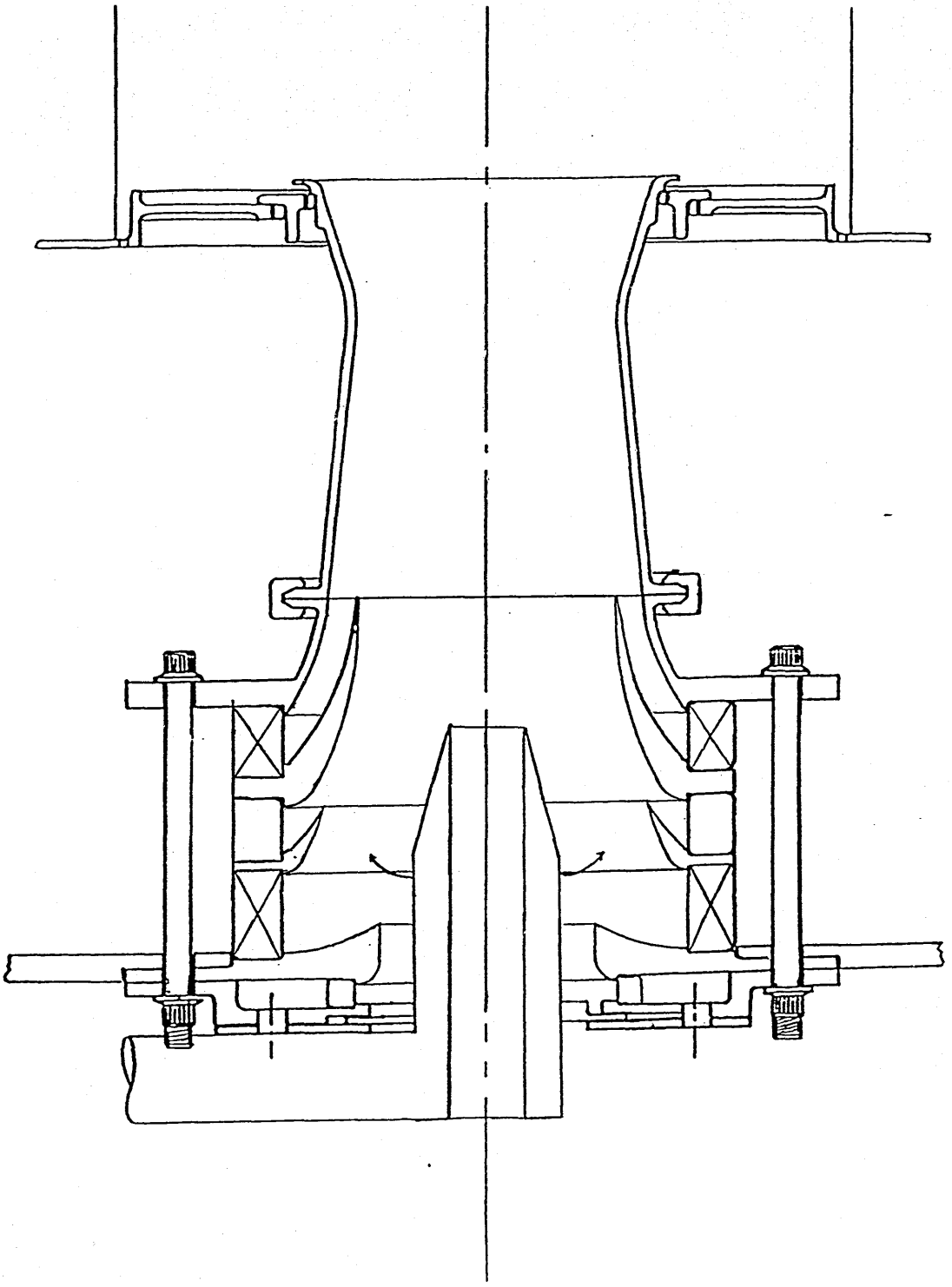

ALL DIMENSIONS IN MILLIMETRES UNLESS OTHERWISE STATED.

DRAWING No. PB43394

BUILT	MODIFICATION
A	—
B	ITEMS 3,5&6 SUPPLIED BY RR. ITEM 9 NOW MADE BY CRANFIELD RHD 20/10/92
C	ITEMS 28 & 30 ADDED RHD 5/2/94

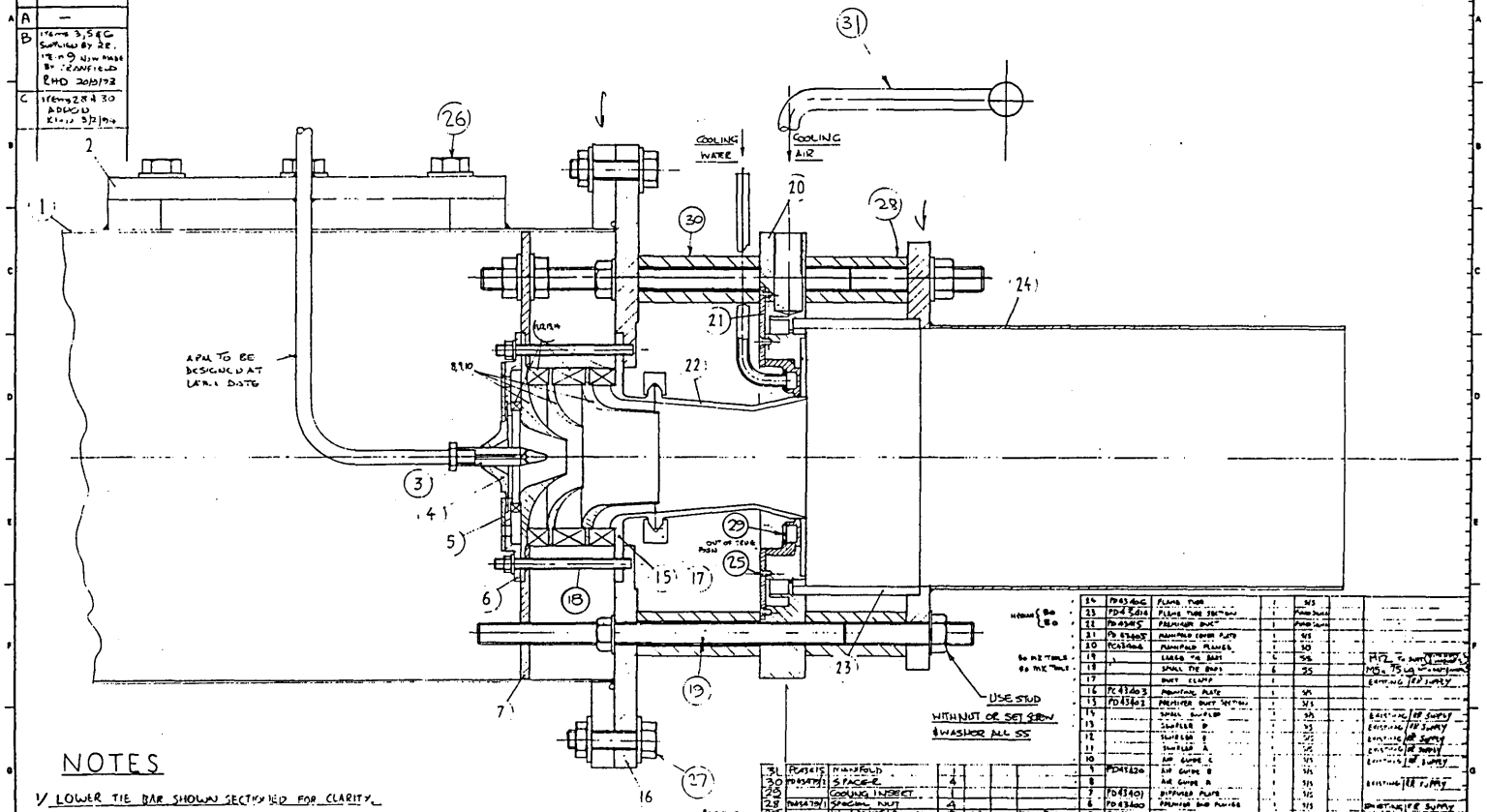

NOTES

1/ LOWER TIE BAR SHOWN SECTIONED FOR CLARITY.

2/ ITEM 3 CAN BE CHANGED

3/ USE ASP AT ALL BOLT & STUD/NUT FIXINGS.

4 USE 3 x A GASKETS AT ALL JOINTS 1mm. Tk (EXCEPT VFLANGE)

ITEM	PART No.	DESCRIPTION	No. OFF	MATL	SPEC.	REMARKS
34	PD43406	FLAME TUBE	1	SS		
33	PD43414	FLAME TUBE JOINTING	1	Fibre Gasket		
32	PD43415	PREHEATER DUCT	1	Fibre Gasket		
31	PD43405	MANIFOLD FORM PLATE	1	SS		
30	PD43406	MANIFOLD FLANGE	1	SS		
29		LARGE TIE BARS	2	SS		M24 To suit existing LP Supply
28		SMALL TIE BARS	6	SS		M24 To suit existing HP Supply
27		BURT CLAMP	1			EXISTING LP SUPPLY
26	PD43403	PRIMITIVE PLATE	1	SS		
25	PD43402	PRIMITIVE BURT SECTION	1	SS		
24		SPOOL DUCTED	1	SS		EXISTING HP SUPPLY
23		SPOOLER D	1	SS		EXISTING HP SUPPLY
22		SPOOLER C	1	SS		EXISTING HP SUPPLY
21		SPOOLER B	1	SS		EXISTING HP SUPPLY
20		SPOOLER A	1	SS		EXISTING HP SUPPLY
19		AIR SWIRL C	1	SS		
18		AIR SWIRL B	1	SS		
17		AIR SWIRL A	1	SS		EXISTING HP SUPPLY
16	PD43420	AIR SWIRL D	1	SS		
15	PD43419	DIFFUSER PLATE	1	SS		
14	PD43400	PRIMITIVE END PLATE	1	SS		
13	PD43399	END PLATE	1	SS		EXISTING HP SUPPLY
12		INJECTOR MOUNT	1	SS		EXISTING HP SUPPLY
11	PD43398	INJECTOR	1	Inconel		EXISTING HP SUPPLY
10	PD43397	INJECTA PLATE	1	SS		EXISTING HP SUPPLY and PC 43-478
9	PC43395	FLOW CHAMBER	1	SS		

ITEM	PART No.	DESCRIPTION	No. OFF	MATL	SPEC.	REMARKS
31	PC43404	MANIFOLD	1	SS		
30	PD43413	SPACER	4			
29		COOLING INSERT	1			
28	PD43396	SPECIAL NUT	4			
27		M6 SET NUT & WASHER	12	SS		M10x50 Lg.
26		STUD WITH NUT & WASHER	6	SS		M10x45 Lg.
25		SOCKET CAP HEAD SCREW	32	SS		M6x Lg.
ITEM No.	DRG No.	DESCRIPTION	No OF UNIT	MATL	SPEC.	REMARKS

THIRD ANGLE PROJECTION

SHEET SIZE A1

SCALE N

FINISH SELF

GENERAL TOLERANCE ON DIMENSIONS
MACHINED ±
UNMACHINED ±
OTHER DIMENSIONS AS STATED

JOB No. E6641N

WELD WHERE SHOWN THUS

MACHINE WHERE SHOWN THUS ✓ USED ON DRG. PB43393

	DRAWN	CHD	APPVD	DATE
S.C.HARDING	[illegible]			17-3-93

TITLE:- GENERAL ASSEMBLY L.P. PHASE 7 RIG

SCHOOL OF MECHANICAL ENGINEERING
CRANFIELD INSTITUTE OF TECHNOLOGY

DRAWING No. PB 43394

SHT. 1 OF 1 SHEETS

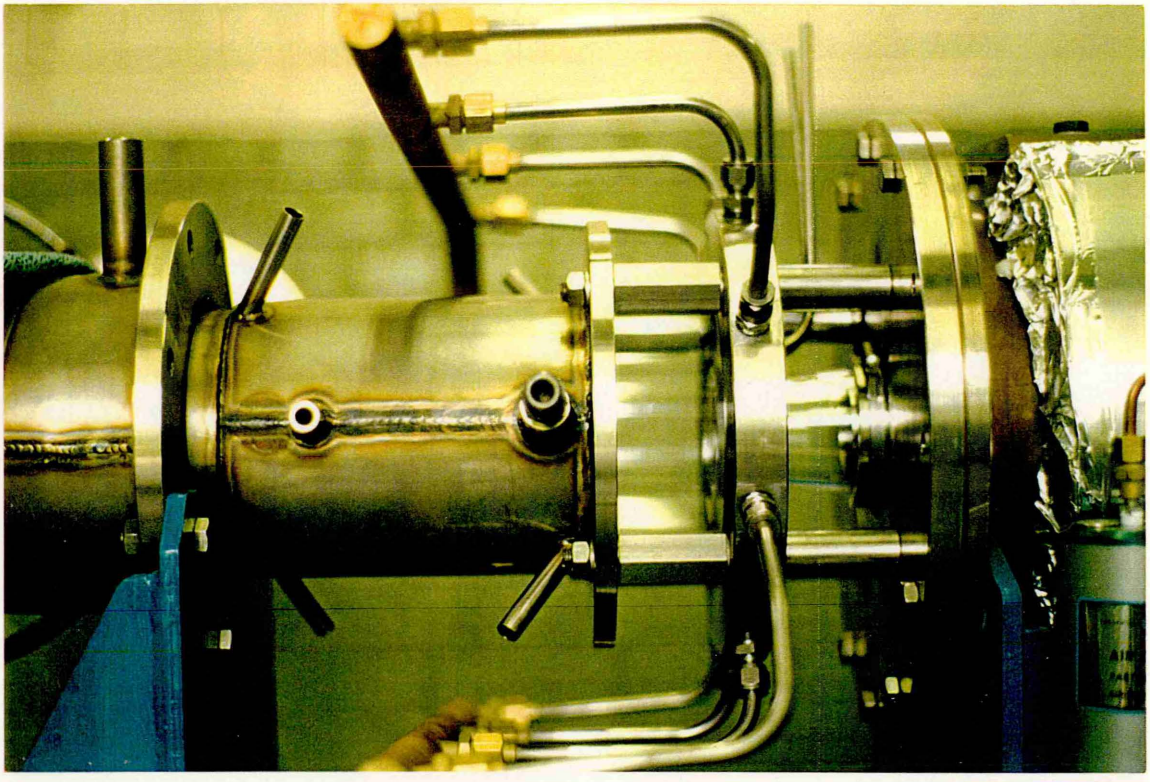

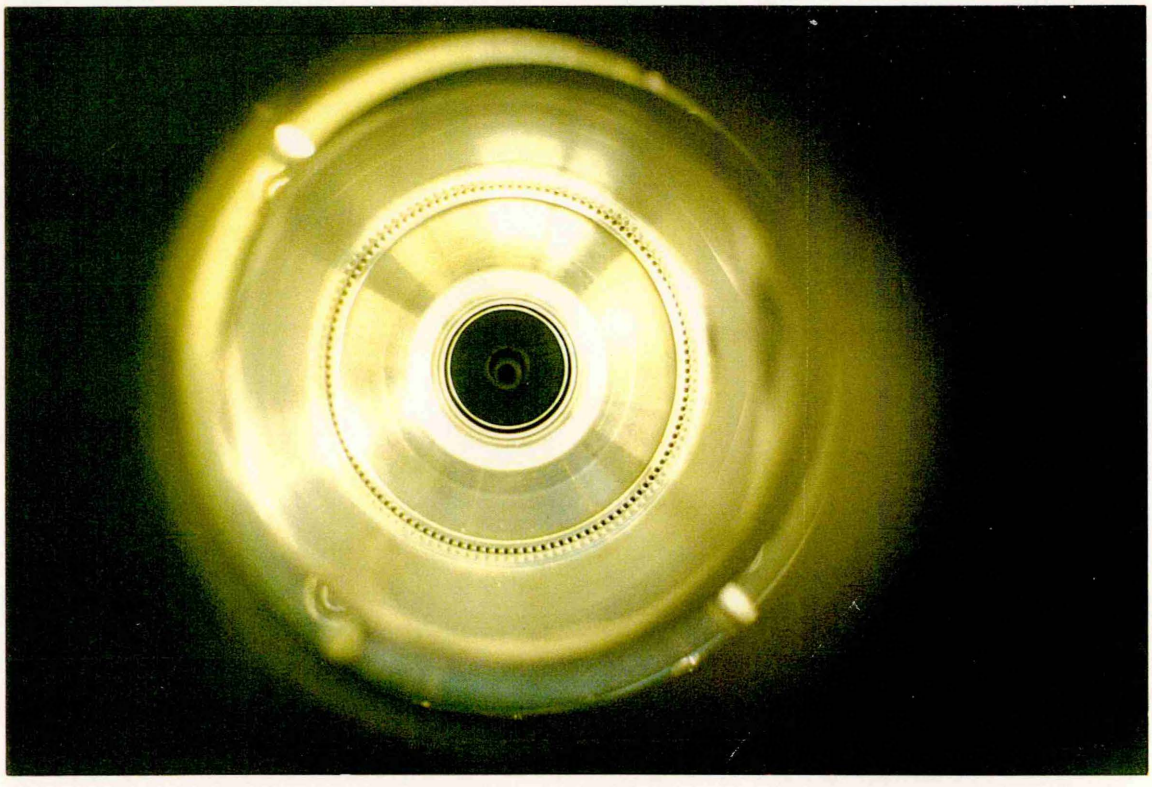

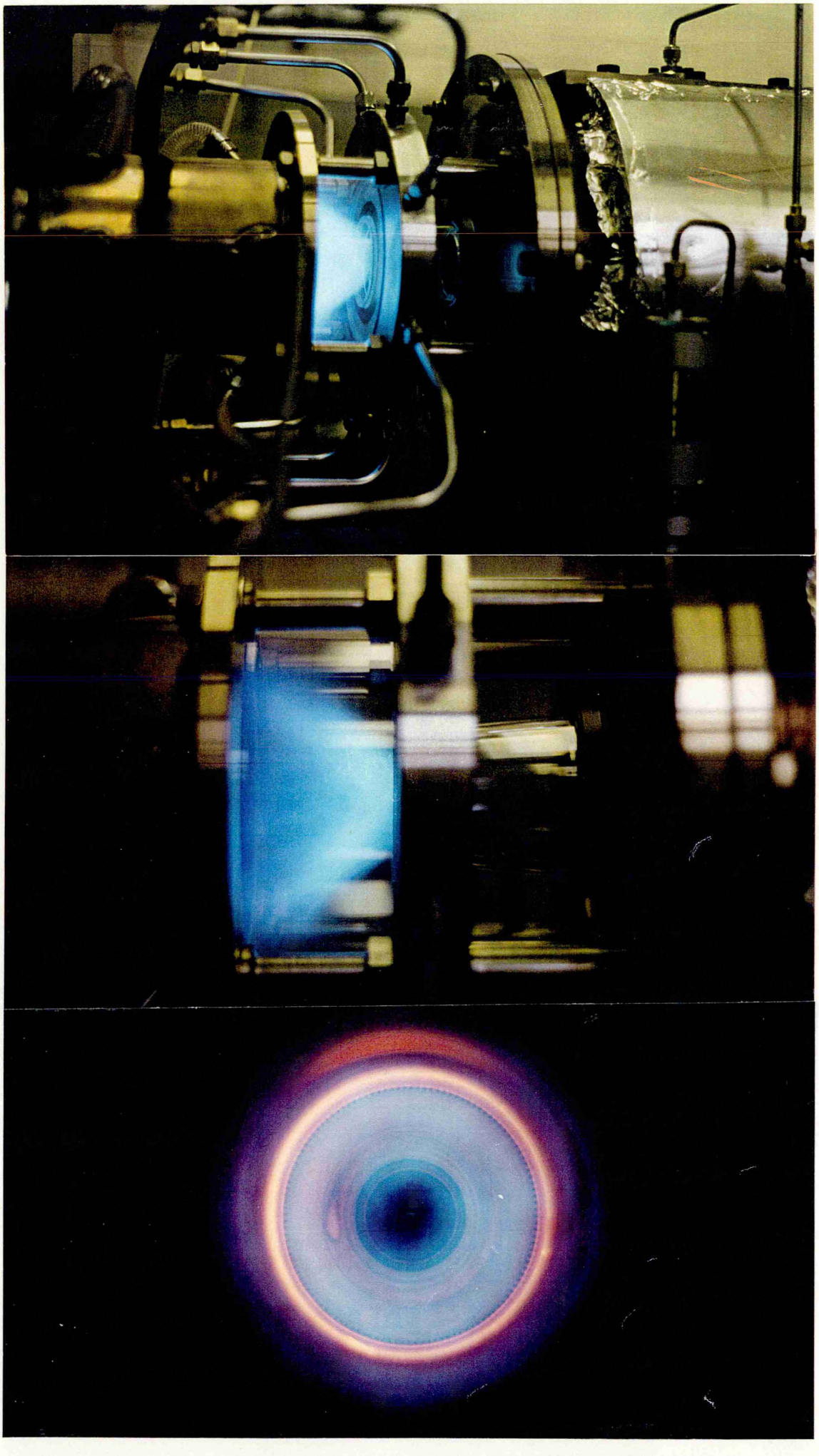

6. VELOCITY CHARACTERISATION OF THE PREMIXING DUCT

In order to understand the mixing processes, the autoignition and flashback tendency in an LPP gas turbine combustor, the velocity field in the premixer has to be studied and characterised. To this end, the velocity of the gas and liquid phases of the fuel-air mixture in the premixing duct have been measured in two components. This chapter deals only with the gas phase reactants, the liquid phase reactants being examined in chapter 7. The premixer consists of a slightly convergent duct, flared at the end to aid stabilisation of the primary zone recirculation. The flow field in the premixer consists primarily of a rotating, solid body of gas accelerating down the length of the premixing duct.

This chapter reviews the most useful techniques available to measure fluid velocities, evaluating their relative merits. This is followed by the results of measurements of axial and swirl velocity components made in the premixing duct using Laser Doppler Anemometry (LDA) and Phase Doppler Anemometry (PDA).

Velocities have been measured of air seeded with titanium dioxide without primary zone combustion using LDA. The premixer velocities with primary zone combustion have been measured using PDA tracking only the smallest droplets. The radial component of velocity in the premixing duct is small compared with the axial and swirl components and has been neglected.

6.1 Techniques for velocity measurement

Velocity measurement techniques may be divided into two categories; intrusive techniques and non-intrusive techniques. Non-intrusive techniques have the obvious advantage of not interfering with the flow field being measured but are usually more complicated. Most non-intrusive velocity measurement techniques rely on light

scattering off particles which have to be seeded into the flow and therefore require optical access to the measured fluid.

6.1.1 Pitot Probes

The mean velocity of a flow can easily be measured using a Pitot probe. With the Pitot probe pointed towards the direction of flow, the pressure measured is the sum of the flow's static pressure, P_S and the dynamic pressure, P_D. The dynamic pressure caused by the flow may be related to the fluid's main velocity, U using Benoulli's equation, knowing the gas density, ρ.

$$\text{Pitot probe pressure, } P_{probe} = P_S + \frac{1}{2}.\rho.\, U^2$$

The technique is limited to the spatial resolution of the probe dimensions but is capable of simultaneously measuring velocity in all three dimensions in turbulent and laminar flows with the use of multi-hole probes.

6.1.2 Hot Wire/Hot Film Anemometry

The mean and fluctuating components of velocity in a flow may be simultaneously measured using hot wire anemometry. The measurement probe consists either of an electrically heated fine wire held between two prongs, or a solid probe coated with a thin, electrically heated metal film deposited onto a non-conducting substrate. The velocity of the medium is calculated from the convective heat loss from the probe to the fluid. The probe heat loss is found from the heating voltage measured across a Wheatstone bridge required to maintain a constant probe temperature. Since the wire or film thickness is very small, very low fluctuations in flow velocity may be resolved. Hot wire probes have the advantage of quicker time response but are more vulnerable to damage from particulates in the flow. Mean and fluctuating velocities may be measured in two dimensions simultaneously in turbulent and laminar flows with a time response

of up to 90 Hz. Hot wire probes do not discriminate the intended measured component of velocity oriented to the probe from the actual resultant velocity component. This has to be resolved by taking multiple measurements. The spatial resolution is limited to the probe dimensions (approximately 4 mm).

6.1.3 Laser Doppler Anemometry

Laser Doppler anemometry (LDA) or Laser Doppler Velocimetry (LDV) is the only technique available for simultaneously measuring mean and fluctuating velocities non-intrusively in a flow. There are several configurations for employing LDA, but the fringe method is most common. In this method, two laser beams are intersected to form a measurement volume consisting of interference fringes.

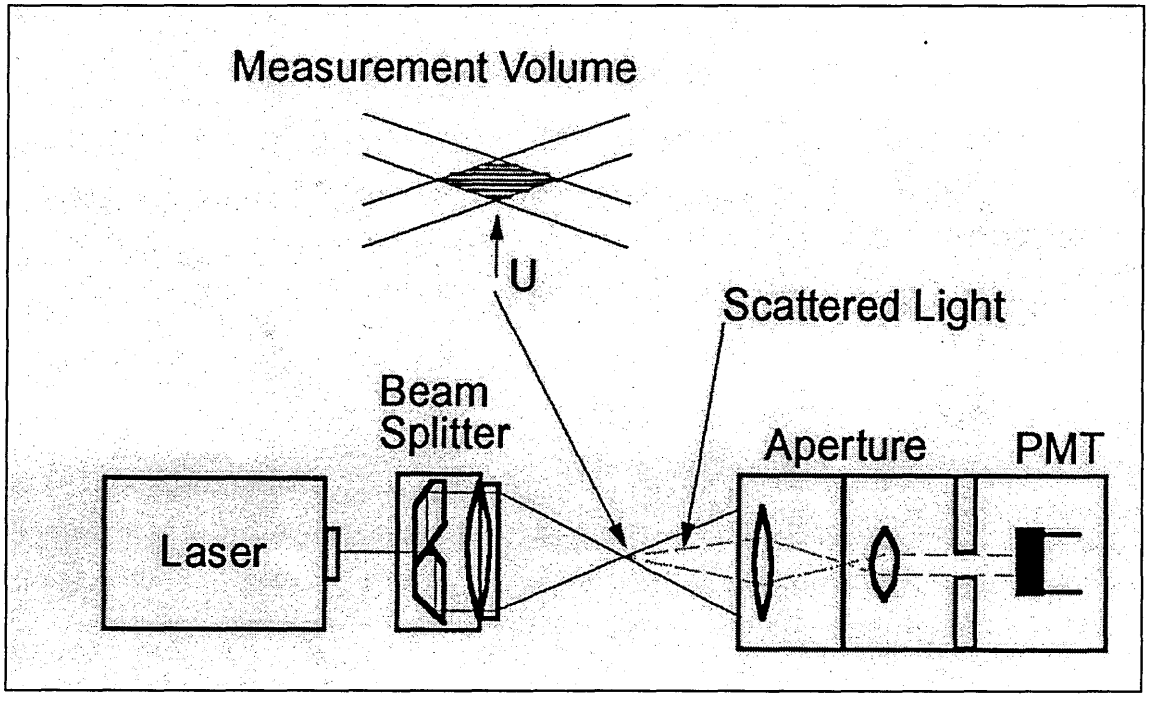

Figure 6.1 Schematic of the LDA Set-up.

As particles of seed pass through the fringes, they scatter intensity modulated light onto a photo detector via a spatial filter at the Doppler frequency, ν_D. Another LDA method measures the beat frequency between a reference beam and the scattered Doppler shifted

light by the particle velocity. The interference fringes are usually formed using light from an Argon Ion laser passed through prisms and lenses in the transmitting optics. By using more than one colour from the laser formed into overlapping measurement volumes in different planes, up to three components of velocity may be measured simultaneously.

The particle velocity can be found from the Doppler frequency ν_D, and the fringe spacing, λ_* knowing the transmitting half angle, θ and the laser wavelength, λ.

$$\text{Doppler Frequency, } \nu_D = \frac{U}{\lambda_*}$$

$$\text{and Fringe Spacing, } \lambda_* = \frac{\lambda}{2\sin\theta}$$

The size of the fringe spacing can be found since probe volume length, $d_x \approx d_y \approx d_f$ where $d_f = d_z.\sin\theta$ and d_z is the laser beam waist after expansion. The measurement volume dimensions are a compromise between spatial resolution, the maximum detectable Doppler frequency and the minimum focal length lens useable. The transmitting optics normally incorporate a beam expander with a large aperture to allow the beams to be focused onto a small spot.

A Bragg cell is normally used to add a wavelength shift to one of the beams so that the fringes move in the volume. If the Bragg shift is larger than the maximum measured Doppler shift then the velocity direction can be resolved.

The receiving optics consist of a pinhole spatial filter, a 45^o mirror, an interference filter matched to the laser wavelength and a photomultiplier. The signal current from the photomultiplier is proportional to the incident light intensity. The signal is low pass filtered to remove the Doppler pedestal and then high pass filtered to remove high frequency noise. This signal is passed to a Schmidt trigger to provide a rectangular wave

from which the Doppler frequency can be found when compared to a clock pulse. The particle velocity may then be calculated from the Doppler frequency.

LDA measurements can suffer from light signal to noise problems due to flame radiation and optical access. The measurement volume location can move due to beam steering through flame fronts and achieving a suitable seeding density at all points in a measured flow without coating windows is sometimes difficult.

6.1.4 Particle Imaging Velocimetry

Particle imaging velocimetry (PIV) is a technique for creating maps of two dimensional velocity vectors from a flow. A flow is seeded with particles and is illuminated with a laser sheet usually formed from a Nd:Yag or Argon Ion laser. The Mie scattered light is imaged onto a camera placed perpendicular to the sheet. The laser is double pulsed so that each particle illuminated by the laser sheet appears twice on the image. The distance between the particle scattered light images may be related to the particle's velocity and direction of motion. The images may be taken photographically and later illuminated with a laser source to form Young's fringes from which the velocity may be calculated. Alternatively, the images may be digitally stored on a CCD camera and processed by computer. Digital images can then be processed using fast Fourier transforms (FFT's) or using an autocorrelation method. A raw PIV image is usually divided up into separate regions processed individually to provide a single velocity vector in each region within the whole, measured flow field.

PIV techniques are limited by the range of velocities measurable which is determined by the resolution of the camera and the minimum laser illumination pulse spacing attainable. The flow needs to be seeded very densely and uniformly to achieve suitable particle scattering images. Conventional two pulse PIV suffers from problems of directional ambiguity of the velocity vector. This can be eliminated using three pulses unequally spaced pulses (Farrugia 1995) or by two image inter-correlation. The result of

using 3 pulse PIV is a better signal to noise ratio on each velocity vector with an increase in the minimum velocity measurable for a given minimum laser pulse spacing.

6.1.5 Doppler Global Velocimetry

Doppler global velocimetry is a technique for measuring velocity in a two dimensional flow field. A flow seeded with particles is illuminated with a laser tuned to be half way along an iodine absorption line. The scattered light from the particles is collected with a camera after passing through an iodine vapour cell. Stationary particles scatter light attenuated by 50% as they pass through the iodine vapour cell. As moving particles scatter Doppler shifted light through the cell, the change in collected intensity is apparent and can be related to the velocity. Three components of velocity could theoretically be measured using three detection systems. The technique is limited by the minimum detectable velocity determined by the laser wavelength and linewidth resulting in an accuracy of approximately +/-2 m/s.

6.1.6 Particle Seeding

In order to make measurements of velocity using scattering off particles, it is important that the particles accurately follow the flow and that they give off sufficient Mie scattered light. The accuracy with which a particle follows a turbulent flow can be estimated from its density, drag coefficient and its dimensions. The scattering efficiency of a particle can be estimated from Mie theory.

6.1.7 Mie theory

Mie scattering of light is the elastic scattering of photons from particulate matter, where the $d/\lambda << 1$ does not hold (for particle diameter, d and incident light wavelength, λ). The scattered light intensity I_{flux} collected from seed particles perpendicular to a light sheet can be estimated from

$$I_{flux} = I_o \cdot \int_{\Omega} \frac{\lambda^2 . |\sigma|^2}{4.\pi^2} d\Omega$$

Where the incident beam intensity is Io, the incident wavelength is λ, the Mie scattering coefficient of the particle is σ (Kerker 1969) and the solid cone angle is Ω. For particles which are small compared with the wavelength of light, the scattering goes as the cubic power of particle diameter. As the particles diameter reaches 10 to 20 microns, the scattering goes as the diameter squared.

Titanium dioxide, aluminium oxide and glass microballoons or microspheres provide the strongest scattering signal but will not survive flame temperatures. Water or oil droplets are easy to create but have low scattering cross sections and also do not survive at high temperature. Zirconia, zirconium fluoride, boron oxide and silicon dioxide are useful seeds for high temperature flows but can be hazardous by inhalation and through contact with skin and eyes.

6.1.8 Particles in Flows

An ideal particle has low density, a high drag coefficient and a large Mie scattering cross section. Large particles are more subject to lift forces across velocity gradients. The parameter, C can be used to determine how likely a particle is to follow a highly fluctuating or turbulent flow (Melling 1986).

$$C = \frac{18.\mu}{\rho_P . d_P^2}$$

For fluid viscosity, μ, particle density, ρ_P and particle diameter, d_P. A particle response in a turbulent flow with parameter, C is shown in figure 6.3. Another measure of particle response using Stoke's parameter is given by Buchhave (Lading 1993). The validity of this paramter is dealt with in chapter 7.

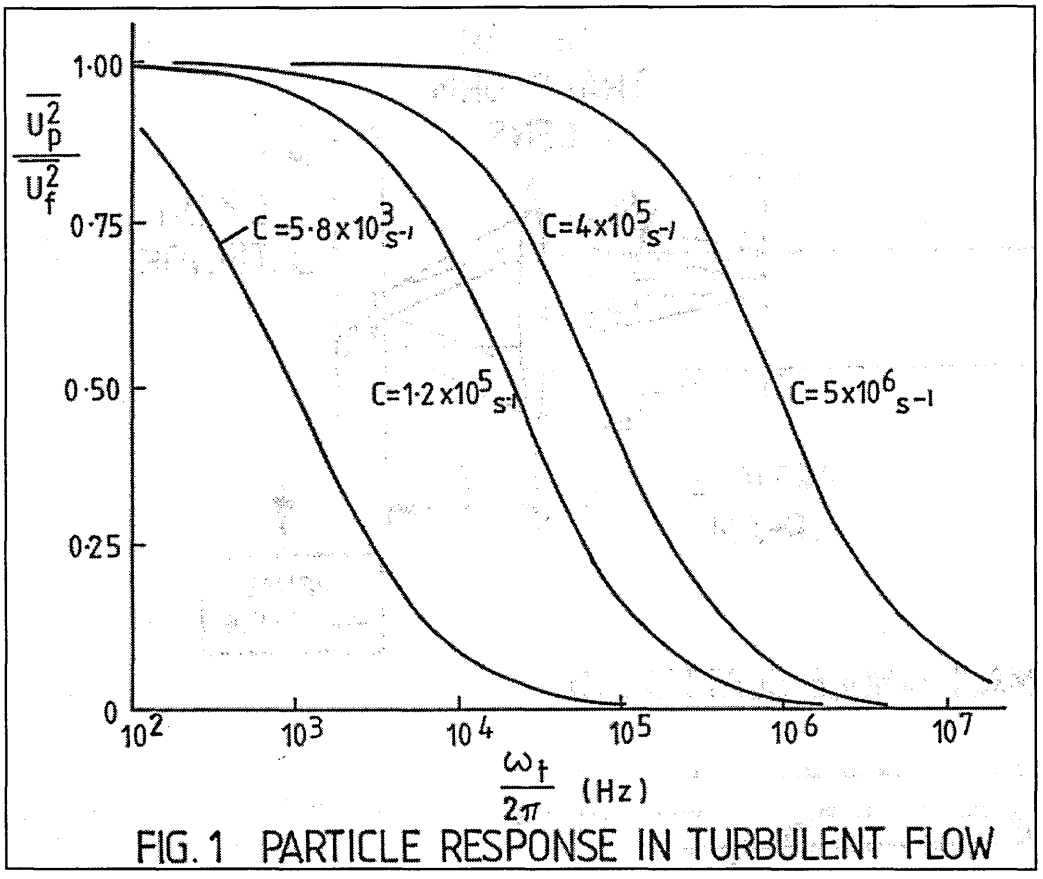

Figure 6.3 Particle Response to Turbulent Flow with Parameter C (Melling 1986).

The two most common methods of seeding particles into a flow are by using either a fluidised bed seeder or a brush type seeder. Fluidised bed seeders rely on an upward flow of gas in a chamber lifting or fluidising the solid particles in the seeder chamber. As the particles travel further up the chamber, gravity forces return most of the particles down to the bottom of the chamber. The remaining particles become entrained in the flow and continue to leave the seeder via an exit at the chamber top. This method is practical but suffers from the inability to control the seeding density independently of gas mass flow. This is normally tolerated by sending only a by-passed portion of the overall gas flow through the seeder.

Brush type seeders use a piston inside a cylinder full of particle seed to deliver the seed into a chamber containing a rotating brush. The gas to be seeded is forced through the brush chamber where it picks up the seed. The advantage of this method is the ability to

control the gas flow independently from the seeding density and to deliver much higher seeding densities. These devices are inherently mechanically complex and cannot be used with fragile, hollow seed particles such as microspheres.

6.2 Laser Doppler Anemometry Measurements in the Premixer

The axial and swirl components of velocity in the combustor premixing duct were measured non-intrusively using 2D laser Doppler anemometry. The equipment used was a three colour Dantec PDA kit with 310 mm lenses attached to the optics, fibre optically coupled to an Argon Ion laser and photomultiplier tubes. The equipment incorporated a Model 58N10 signal processing unit. The premixing duct is manufactured from transparent fused silica. The section of the premixer which is accessible with an LDA probe is between 28 and 80 mm from the injector tip.

The LDA optics were mounted on remotely controlled traverses to allow the measurement volume to be moved relative to the combustor premixer. The transmitting optics were mounted on one traverse which allowed the measurement volume to be raised above the fused silica premixing duct for beam alignment with a pinhole. The receiving optics were mounted on a separate traverse remotely controlled simultaneously with the transmitting optics traverse. Since both the optics were moved synchronously around the premixing duct, realignment was necessary to optimise the data collection rate due to distortion effects on the probe beam and the signal caused by the curved fused silica walls. The receiving optics were mounted at a 30^{o} forward scatter angle which maximises the signal data rate. Some of the measurements were made of droplet diameter simultaneously with two components of velocity but most were made by measuring one component of velocity at a time. By measuring the second velocity component later, the data rate and signal validation can be significantly improved allowing more measurement traverses to be made during a given testing period.

The flow was seeded upstream with particles of titanium dioxide using a piston fed, brush type seeder. The seed was injected close to the turbulent exit of the preheating

combustor using an injector comprising eight radially fired jets. The mean particle diameter was less than 0.2 microns which should accurately follow the flow at velocity fluctuations exceeding 10 kHz. Titanium dioxide was used as a seed since it is available in small particle sizes and provides a sufficiently strong scattering signal. As titanium dioxide becomes hot its scattering cross section reduces. This proved advantageous since any seed coating the duct wall became heated and maintained transparency, whilst the seed carried in the air scattered sufficient light.

The velocity in the premixer was originally measured using LDA with the combustor air preheated to 900 K, but with the primary zone unlit. This was due to the impossibility of discriminating between fuel droplets and particle seed when using LDA equipment. The premixing duct flow field with the combustor lit was found to be altered by the blockage effect of the combusting primary zone recirculation. In order to characterise the premixer velocity field with the combustor lit, subsequent measurements of droplet velocities in the premixer were reprocessed analysing only droplets sufficiently small to accurately follow the flow.

All the measurements were made at the same combustor operation condition listed in section 5.6.1. The effects of combustion on the premixer velocity field are discussed later in the chapter. The refracted light signal was collected at a 30° forward scatter angle. The set up conditions of the LDA equipment are listed as follows:

	Axial Component	**Swirl Component**
Probe Volume: delta x	0.0822 mm	0.0780 mm
delta y	0.0822 mm	0.0779 mm
delta y	2.0406 mm	1.9355 mm
Fringe Spacing	6.3849 nm	6.0561 nm
Number of fringes in volume	13	13
Wavelength	514.5 nm	488 nm
Focal length lens	310 mm	310 mm
Validation level:	0 dB	0 dB
Collection Optics Angle	30°	30°
Data Rate	> 2 kHz	> 2 kHz

Table 6.1 Set up Conditions of the LDA measurements

6.2.1 LDA Velocities - non-combusting

The velocity in the premixer has been characterised by taking 1D radial traverses down the length of the duct, 2D radial traverses at the start and end of the duct and a 2D axial traverse along the duct taken 10 mm off the premixer centreline. The 1D traverses only measure the axial component of velocity whereas the 2D traverses measure the axial and swirl components of velocity. Each measurement point consists of a minimum of 10,000 validated measurements.

The radial traverses of axial velocity were made at intervals of 5 mm down the whole accessible length of the premixing duct. A measurement was made at every 2 mm along each radial traverse. Velocities could not be measured within 5 mm of the fused silica duct walls since light scatter from the laser probe volume and reduced seed concentrations lowered the collected signal level. Profiles of mean axial velocity are shown in Figure 6.4. The fluctuating rms components of axial velocity are shown in figure 6.5. The rms data shows peaks in fluctuating velocity at random points in the premixer. These peaks do not correlate with PDA collection validation rate or data rate and are probably temporal fluctuations in the flow caused by instabilities in the flame tube recirculation. Graphs of all mean and axial velocities are shown at the end of the chapter to determine absolute measurements in figures 6.9 to 6.11.

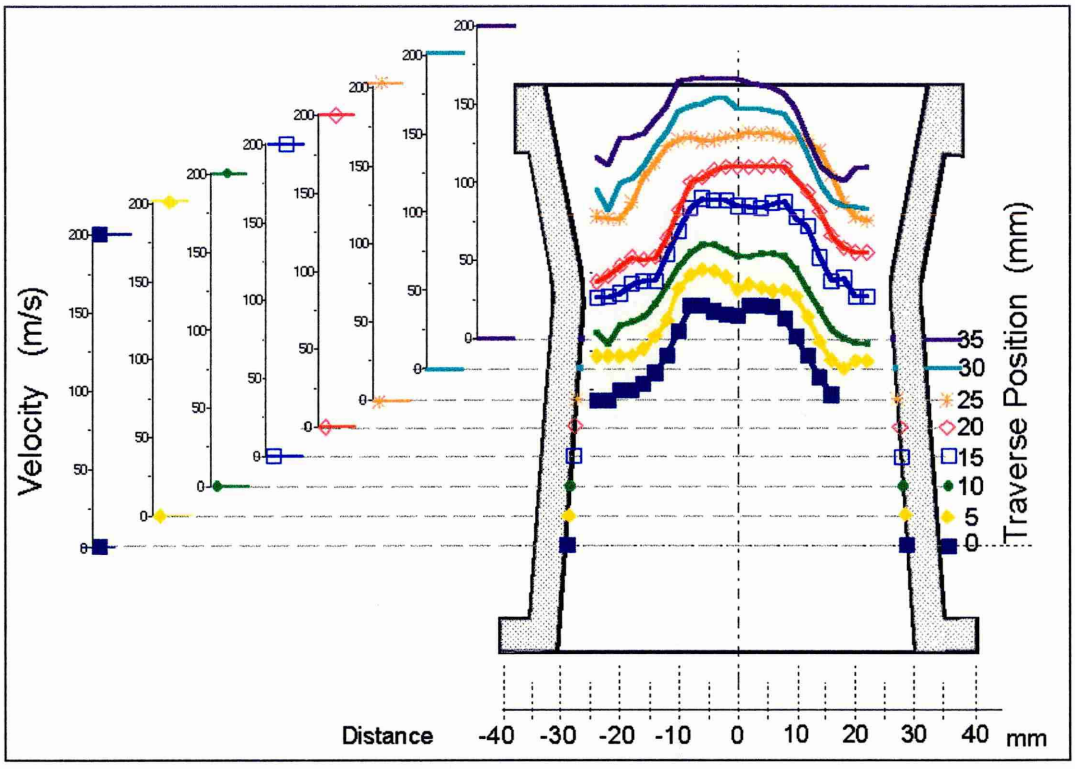

Figure 6.4 Mean Axial Velocity in the Premixing Duct - non-combusting.

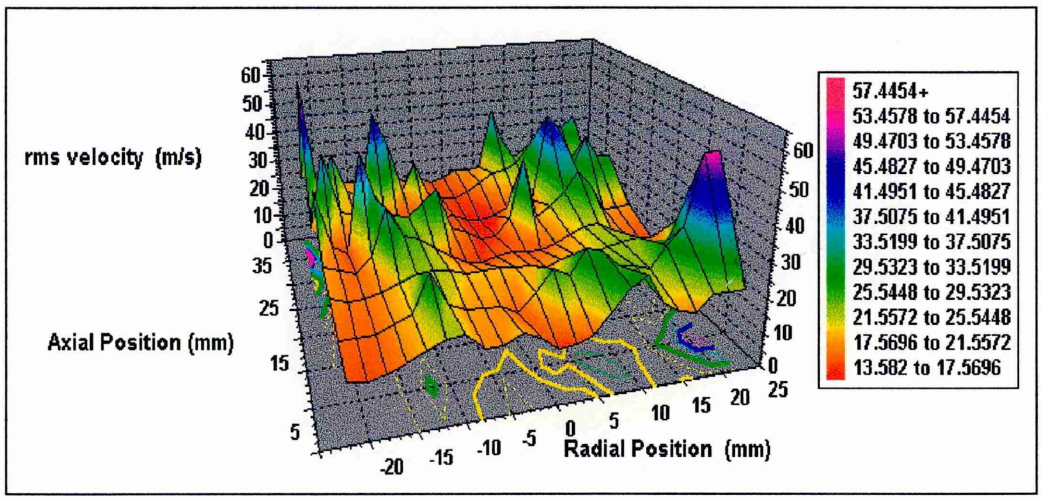

Figure 6.5 RMS Component of Axial Velocity in the Premixing Duct - non-combusting.

The levels of axial fluctuating (rms) velocity correspond to turbulence intensities of between 10% and 30%. The swirl turbulence intensities are in the range 30-40% and increase along the duct length.

The swirl velocity components were measured at the start of the duct and at the end of the duct. These are shown in figure 6.6. By ratioing the flow's swirl momentum to the axial momentum, the swirl number has been found. The swirl number decays from 0.746 at the start of the duct to 0.732 at the end. However, this variation is probably within the accuracy of the measurement since the velocity profiles had to be extrapolated to the duct walls to integrate the axial and swirl momenta. The variation in swirl velocity with axial distance is shown to be approximately constant from figure 6.7.

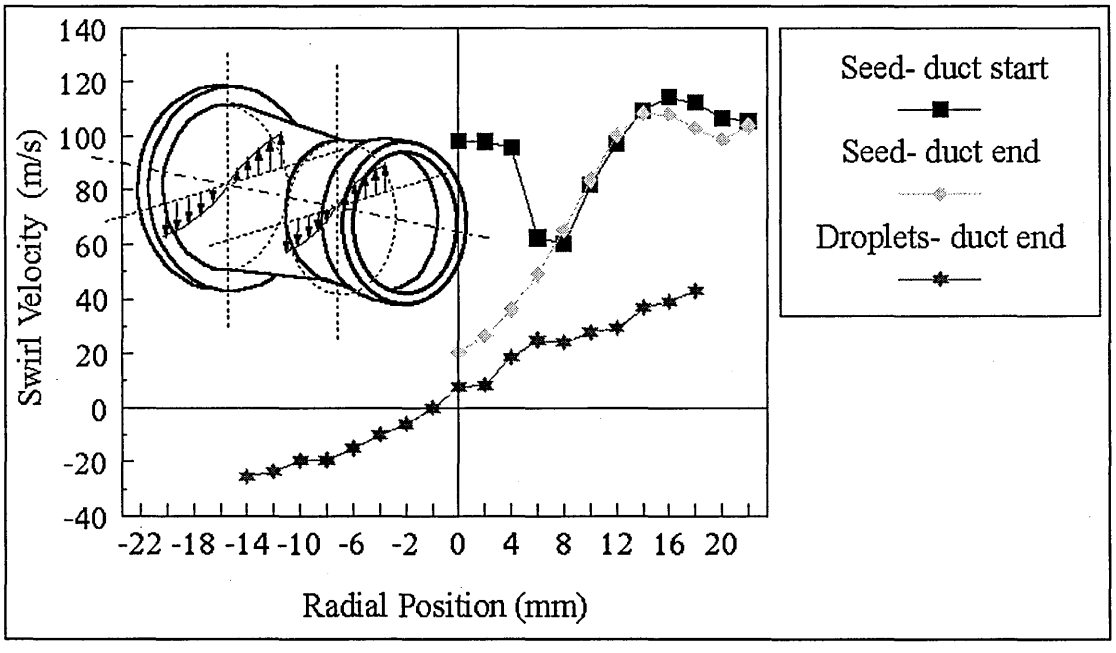

Figure 6.6 Mean Swirl Components of Velocity in the Premixing Duct- non-combusting (with seed) and combusting (with droplets).

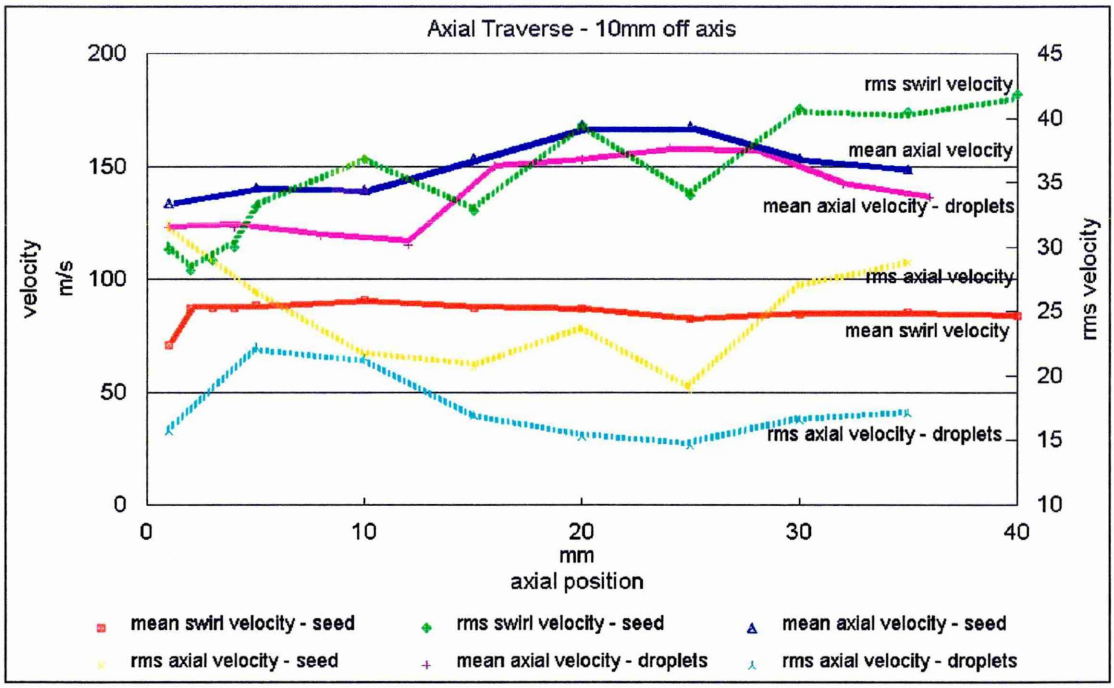

Figure 6.7 Axial Traverse of Swirl and Axial Components along the Premixing Duct- non-combusting (with seed) and combusting (with droplets).

The probability distribution of the velocities at each measurement is relatively broad. There is no dependence of mean velocity or measurement location on the shape or width of the velocity distribution. Typical velocity distributions made from 10,000 measurements at a single point in the premixing duct are shown below for axial and swirl velocities in figures 6.8 and 6.9.

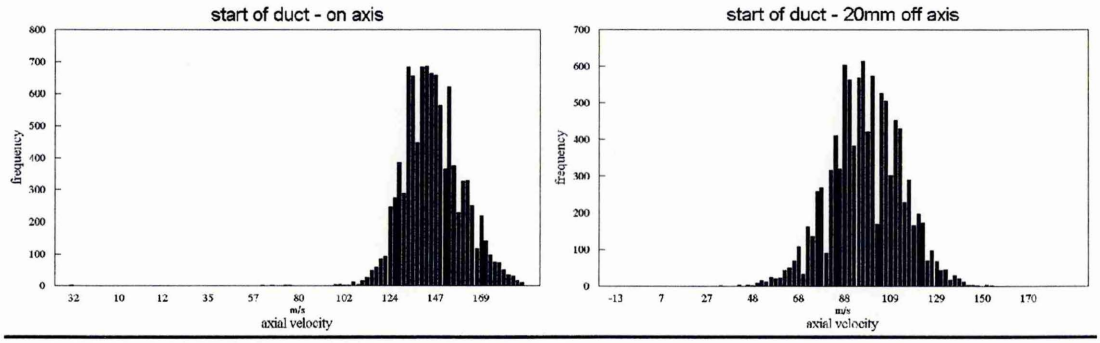

Figure 6.8 Distribution of Axial Velocities in the Premixing Duct at the origin.

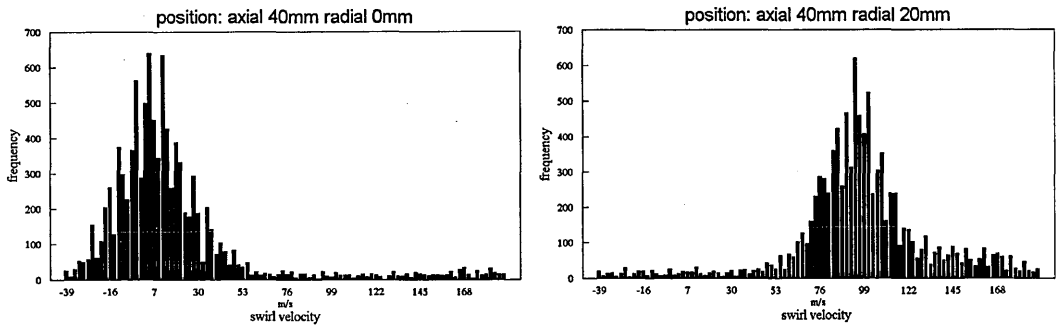

Figure 6.9 Distribution of Swirl Velocities Measured at the End of the Duct.

6.2.2 LDA Velocities - combusting

The velocity field in the premixing duct with the primary zone combusting was subsequently characterised by reprocessing the PDA data detailed in chapter 7 only sampling droplets less than 5 microns SMD. This data was taken in five radial traverses and one axial traverse. The droplets studied were mostly less than 1 micron SMD but includes some droplets up to 5 microns SMD where insufficient data was available. From Melling's criteria 5 micron droplets should follow the flow at 1000 K up to velocity fluctuation frequencies of 1 kHz. However, droplets less than 5 microns can lag the flow by up to 5 m/s (figure 7.13). The mean axial velocity profiles in the premixing duct are shown below in figure 6.10. The swirl components of velocity using droplets measured are shown in figure 6.6. The mean velocity component measured combusting are also shown at the end of the chapter for absolute measurements in figure 6.11.

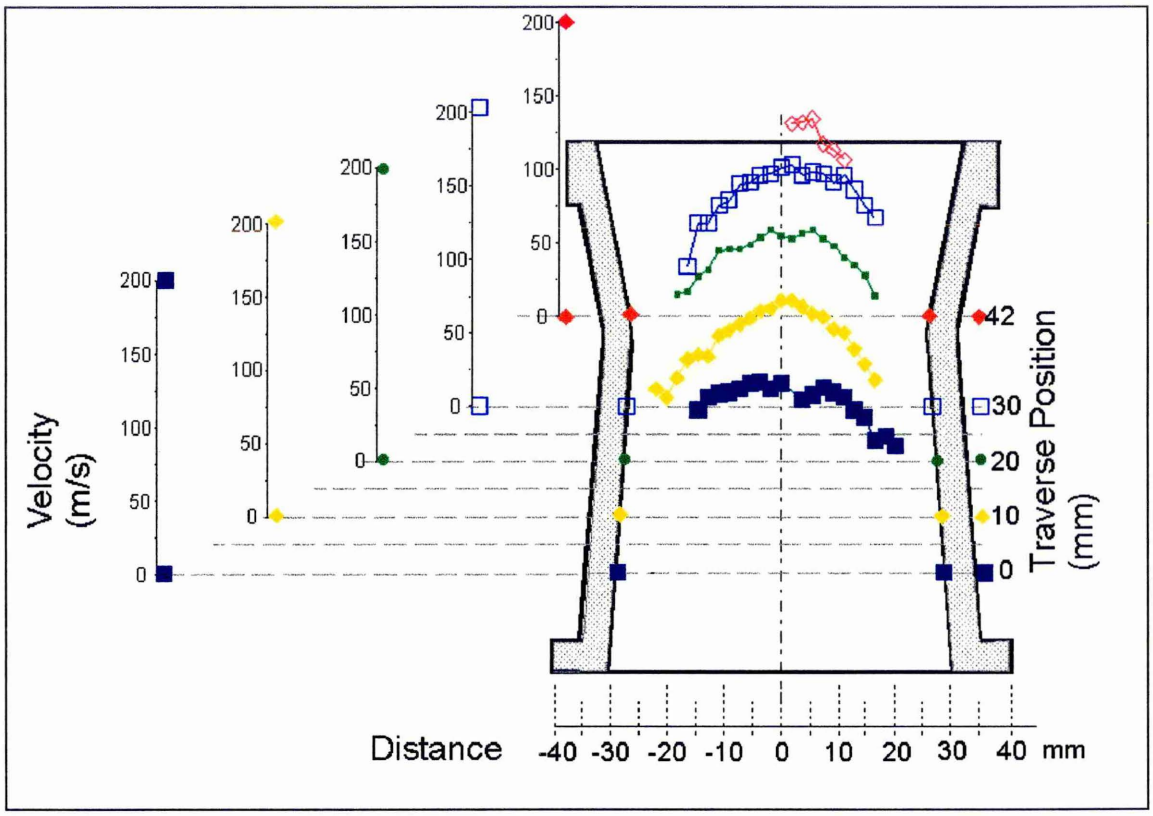

Figure 6.10 Profiles of Mean Axial Velocity in the Premixing Duct - combusting.

6.3 Discussion of Results

The flow field in the LPP premixer as measured by both LDA and PDA techniques, consists of a rotating solid body of gas travelling down the premixing duct. The axial component of velocity is predominantly in the range 100 to 150 m/s peaking at the centreline. The swirl velocity component is typically 105 m/s. The swirl at the start of the duct is asymmetric. The ratio of swirl to axial momentum is virtually constant along the length of the duct with a swirl number of 0.74.

These velocities give rise to a range of residence times between 0.51 ms at the core of the duct to 0.77 ms in the swirling outer flow in the duct. These values exclude the portion of residence time in the flow upstream of the fused silica section of the premixing duct.

The velocity field with combustion in the primary zone is different to the unlit case. The velocity profiles in the unlit case show a flat topped profile as opposed to the rounded profile for the combusting case. The core velocity accelerates as the duct converges and then decelerates as the fluid meets the effective blockage caused by the recirculation in the primary zone. The deceleration appears larger with combustion. This is because the recirculation is larger due to the expansion of the gases and presumably causes more blockage. As the flow leaves the duct, the gas will part around the core recirculation zone and accelerate into the dump combustor. The swirl angle when combusting is noticeably smaller with combustion. This is likely to be partly due to the differences in the seeds used. The differences in magnitude of velocity between the combusting to non-combusting case can be partly explained by the slip velocity of the droplets.

The velocity profile measured 58 mm from the injector tip has been integrated to find the volumetric flow. The profile had to be extrapolated to the wall of the duct assuming a flat boundary layer for the unknown region. The integrated velocity profile suggests a volumetric flow of 0.306 m^3/s (0.108 kg/m^3 at 1000 K inlet). This corresponds to a measured volumetric flow at 1000 K of 0.304 m^3/s. The effect of kerosene heating and evaporation was calculated to be responsible for a temperature reduction of 58 K. This reduction in temperature causes a discrepancy between the two measurements of 0.019 m^3/s.

The boundary layers could not be measured with LDA due to the low data rates close to the duct walls. This was due to flare from the laser beams as the measurement volume contacted the wall and low seed density. The velocity close to the wall is likely to be as high as the core velocity due to the final air guide nozzle. Some of the profiles show an increase in velocity approaching the wall suggesting that there is a high velocity region there. The modelled data in chapter 10 shows a high velocity region close to the duct walls. A high velocity boundary layer significantly reduces the LDA data collection rate since the seed concentration is lower.

The duct's turbulence intensity levels in the axial direction are mostly between 10 and 20% with combustion. The premixer Reynold's number is 29600. The axial turbulence is more intense in an annulus located between the premixer core and the region close to the wall. This is where most of the fuel is located and will be conducive to rapid mixing. Periodically, the axial turbulence intensity rises to 60% caused by primary zone instabilities. The effect of combustion in the premixer flow field is to change the overall mean velocity flow field and will also feed back combustion instabilities causing temporary rises in rms velocity.

The measurements of velocity from droplet data are consistently lower than LDA measured velocities. This suggests that sub 5 micron droplets do not follow a fast turbulent flow as often believed. This is further explore in the following chapter.

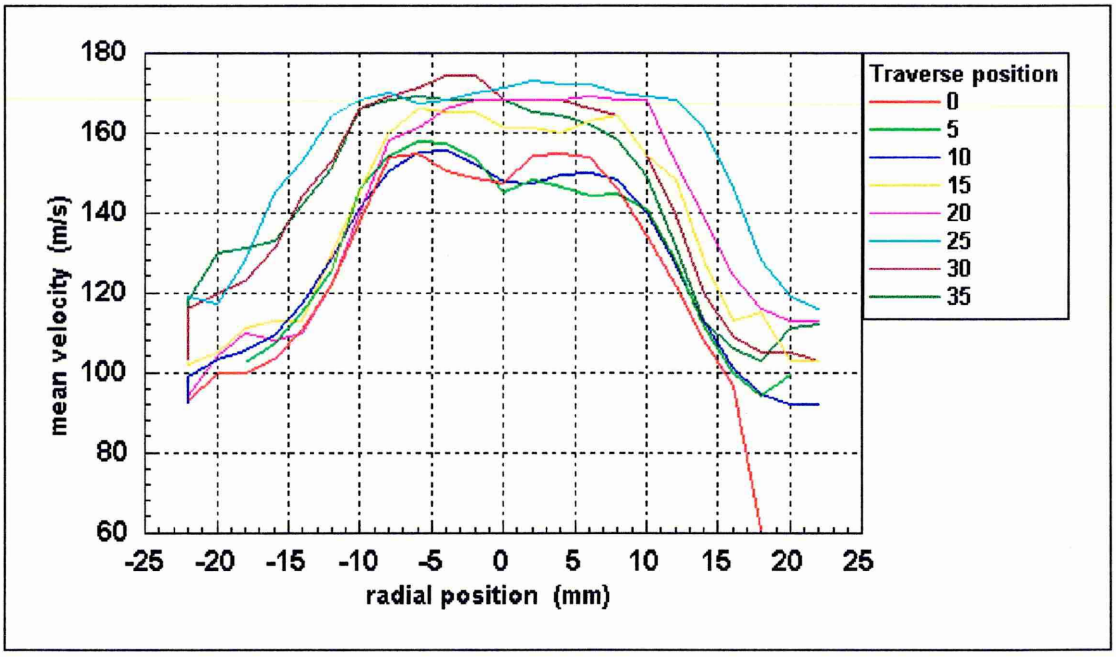

Figure 6.11 Mean Velocities - non-combusting

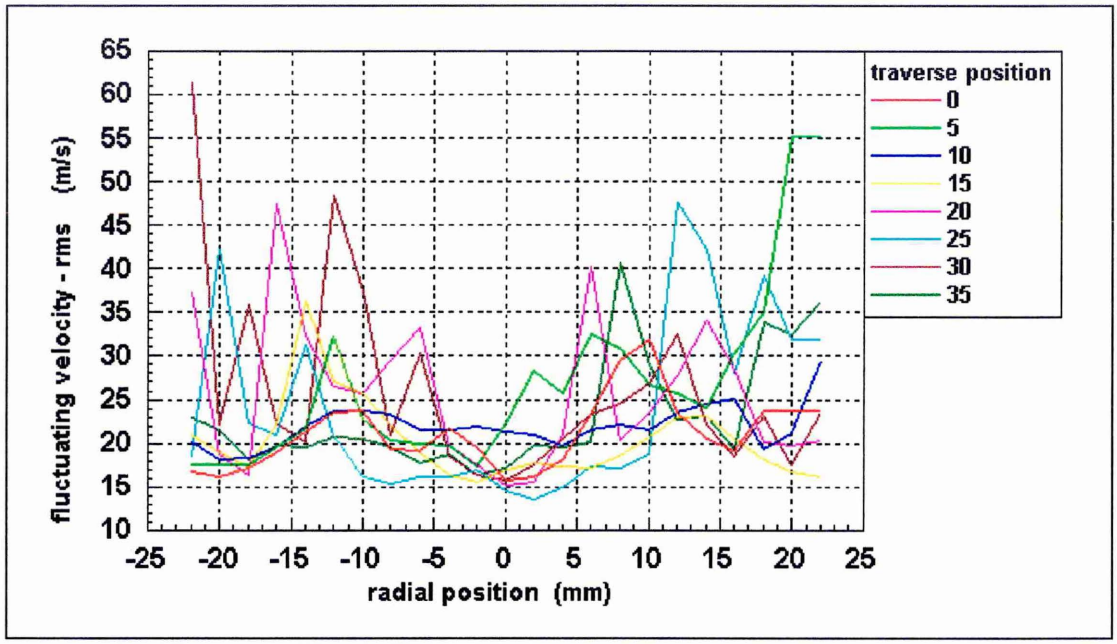

Figure 6.12 Fluctuating Velocities - non-combusting

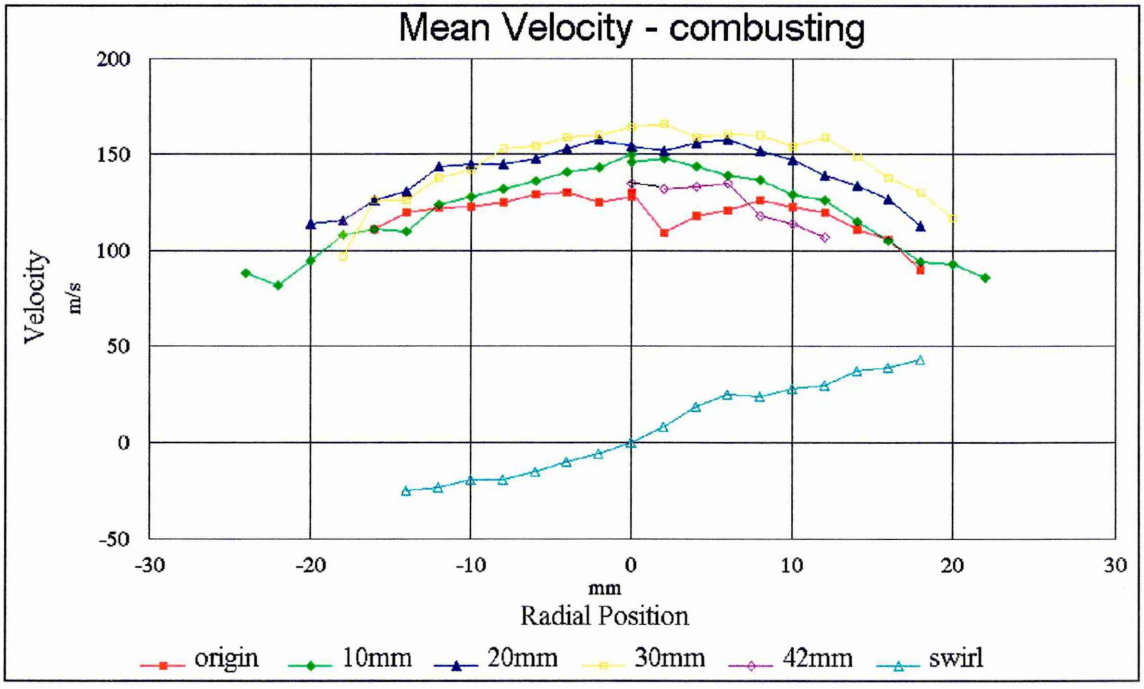

Figure 6.13 Mean Velocities - combusting

7. FUEL DROPLET CHARACTERISATION OF THE PREMIXING DUCT

The velocity, diameter and spatial distributions of the liquid phase fuel in the LPP combustor premixing duct has been studied using PDA and planar LIF techniques. These measurements provide information on the droplet size distributions, droplet motion, the instantaneous and mean liquid fuel spatial distribution. The fuel evaporation rate and the fuel-air mixing mechanism can then be inferred from the results. Measurements on liquid kerosene fuel have been made in the fused silica premixing duct between 28 and 80 mm from the injector tip.

This chapter reviews the PDA measurement technique used and details the measurements of two components of fuel droplet velocities and size distributions. Experiments to find a suitable fluorescent seed for the liquid phase LIF measurements are explained with the measurements and results. The results are interpreted in a final summary section.

7. 1 Phase Doppler Anemometry

Phase Doppler anemometry is regarded as the best available technique for simultaneously measuring droplet or particle velocities in up to three components simultaneously whilst measuring the droplet diameter. In this technique, droplets pass through measurement volume fringes as in LDA, scattering light onto a PMT detector. As the droplets pass through the volume, the fringes become magnified by lens effect of the transparent droplet. The refracted light is detected via receiving optics consisting of lenses, a spatial filter and two or three photodetectors placed apart to measure a phase shift on the signal.

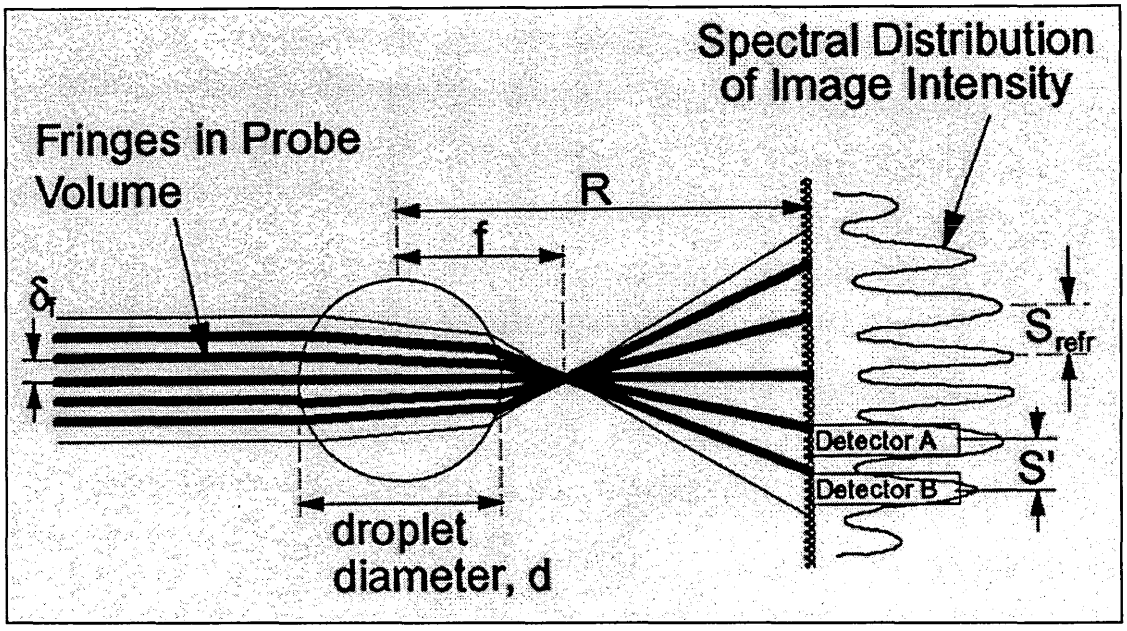

Figure 7.1 Schematic of Phase Doppler Anemometry Set-up.

The Doppler frequency of the intensity modulated light is related to the velocity as in LDA. The signal from each of the detectors is virtually identical except for a phase shift between the detectors which is proportionally related to the droplet diameter. The phase angle is given by:

$$\text{Phase Angle, } \theta = 2.\Pi.\frac{s'}{s_{refr.}} = 2.\Pi.s'.\ \frac{n}{n-1}.\frac{d}{4}.\frac{2.\sin\theta}{R.\lambda} \quad \alpha \quad \text{diameter, d}$$

The sphere focal length is given by $f = \frac{n}{n-1}.\frac{d}{4}.$

for a detector spacing s', imaged fringe spacing s_{refr}, droplet refractive index n, detection optics angle θ, and a laser beam wavelength λ. The detector spacing s' must be less than the image's fringe spacing s_{refr} to avoid phase angle ambiguity. The maximum diameter that can be measured is increased by minimising the detector spacing s', decreasing the beam intersection angle and maximising the distance between the image

plane and the probe volume R. The maximum velocity measurable may be extended by using a smaller intersection angle or a higher Bragg shift.

PDA measurements suffer from the same problems of collection signal noise interference from flames and errors due to beam steering. The droplets must remain spherical and the refractive index must be known to accurately measure the diameter. The effective droplet refractive index of multi-component fuels is difficult to determine in hot flows as lighter fractions vaporise from the droplet. To estimate the remaining droplet refractive index the temperature time history of the droplet needs to be known.

7.1.1 The Refractive Index of Kerosene

The refractive index of kerosene can easily be measured at 273 K to be 1.45. All hydrocarbon fuels have refractive indices between 1.4 and 1.5. Aromatics such as benzene have refractive indices of between 1.5 and 1.6. In order to estimate the refractive index of kerosene at higher temperature an empirical correlation from Eykman was used for refractive index, n and liquid density,ρ.

$$\left(\frac{n^2 - 1}{n + 0.4}\right) = \rho \,.\, \text{constant}$$

The droplet temperature history and aromatic content is unknown so a refractive index of 1.45 was used. An increase in refractive index from 1.4 to 1.6 would change a measured droplet's diameter from 25 microns to 32.8 microns. The droplet velocity would be unaffected.

7.2 PDA Measurements in the Premixing Duct

The droplet field in the premixing duct has been characterised with PDA radial traverses taken at five positions down the length of the duct and with two axial traverses along the length of the duct. One axial traverse was taken on the duct centreline and one 10 mm

off the centreline. The PDA equipment used is the same DANTEC kit described in chapter 6. The set-up included a 30° forward scatter angle. The set-up parameters are detailed in Table 7.1.

	Axial Component	Swirl Component
Probe Volume: delta x	0.0822 mm	0.0780 mm
delta y	0.0822 mm	0.0779 mm
delta y	2.0406 mm	1.9355 mm
Fringe Spacing	6.3849 nm	6.0561 nm
Number of fringes in volume	13	13
Wavelength	514.5 nm	488 nm
Focal length lens	310 mm	310 mm
Validation level:	-2 dB	-2 dB
Data Rate	100-2000 Hz	100-2000 Hz
Collection Optics Angle	30°	30°
Refractive Index of Kerosene	1.4	1.4

Table 7.1 PDA Set up Conditions

The PDA optics were mounted on two remotely controlled, synchronous traverses as described in section 6.2. All the measurements were taken at the combustor operation condition detailed in section 5.6.1.

The diameter of a droplet measured with PDA through a curved window may be altered by the change in measured phase angle caused by the refraction of the collected light signal through the window (Graziadio 1991). For these measurements, this effect would be large if the droplet diameters were measured through the curved surface of the premixing duct from refraction of the swirl component fringes. Since the diameter is measured from the axial component fringes, only the tapering of the conical duct is likely to affect the measurement. This effect on the measured phase angle is estimated to be small.

7.2.1 PDA Results

Each measurement point consists of 10,000 validated samples of droplet velocity and diameter. The mean velocities and diameters are shown in the following figures for both the radial and axial traverses. The radial traverses do not reach the duct walls due to the low data collection rate in this region. This is due to a combination of high air velocities resulting in low droplet concentrations and light signal interference from scattering off the duct wall. All the PDA measurements were taken with the LPP combustor lit.

7.2.2 PDA Traverses

Radial PDA measurement traverses of mean axial droplet velocity were taken 0, 10, 20, 30 and 42 mm down the length of the duct. Each traverse consisted of measurements made at intervals of every 2 mm. These are shown below in figure 7.1. The axial and swirl components of velocity taken on a simultaneous 2D traverse at the start of the duct are shown in figure 7.2. The absolute mean axial velocities can be read off figure 7.3.

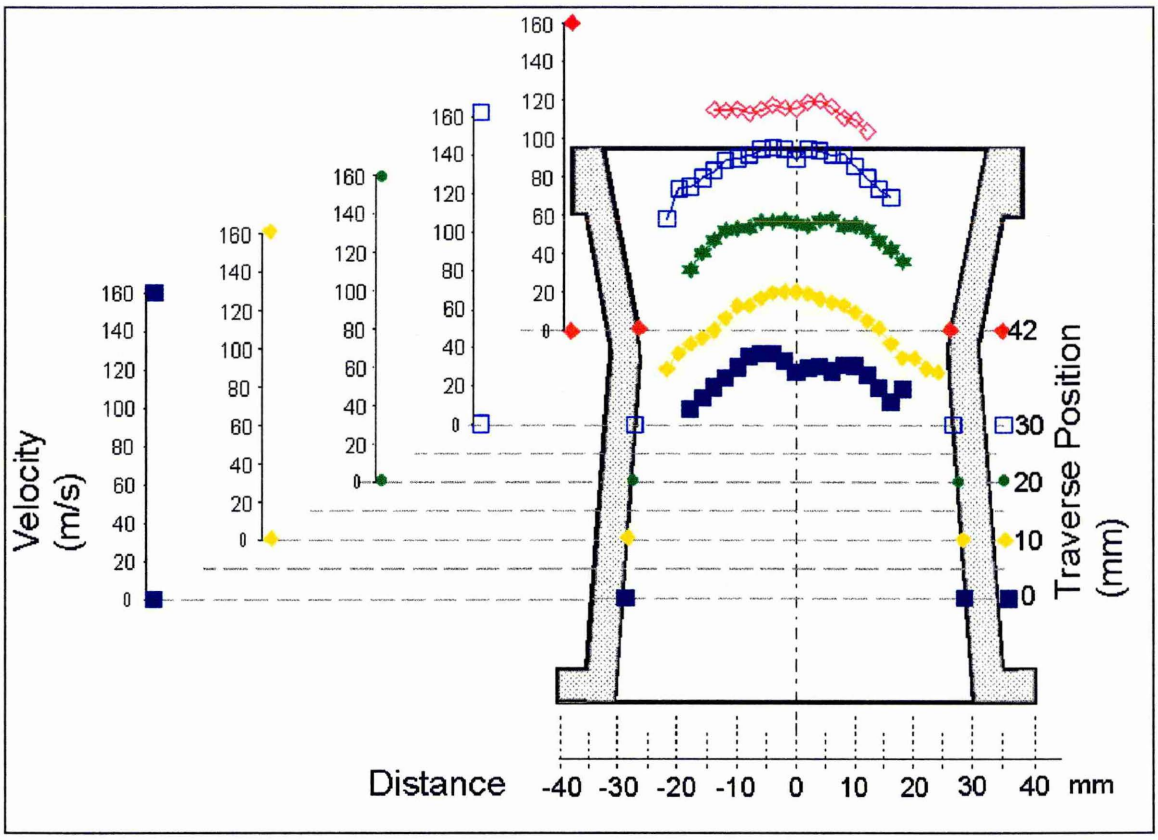

Figure 7.2 Mean Axial Droplet Velocities in the Premixing Duct.

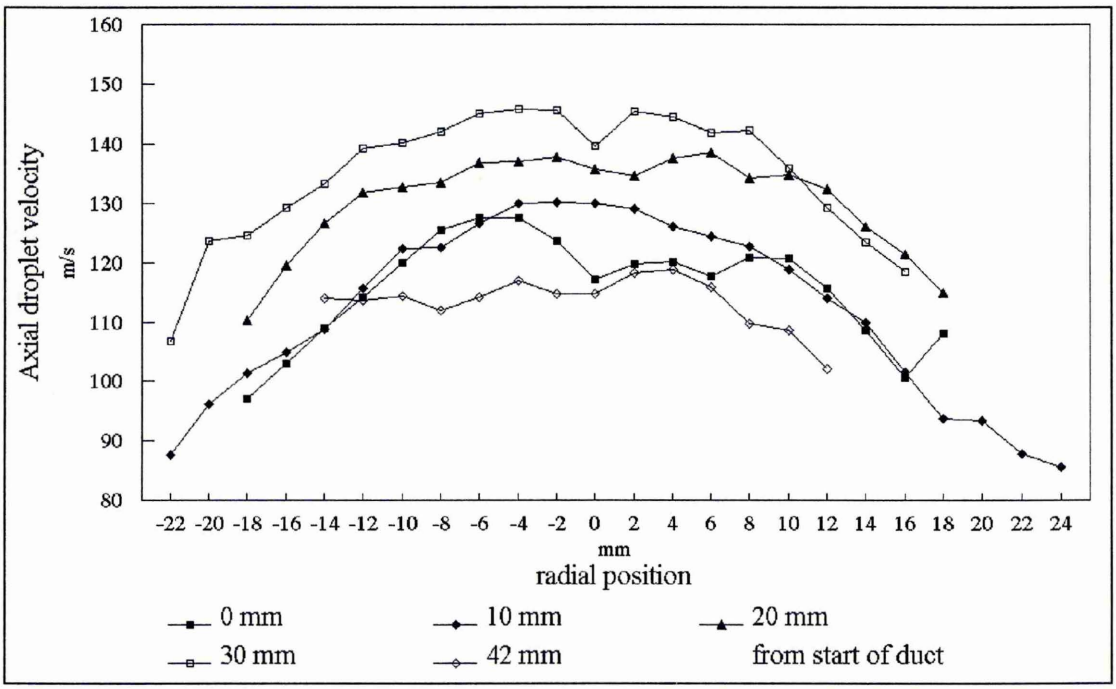

Figure 7.3 Mean Axial Droplet Velocities in the Premixing Duct.

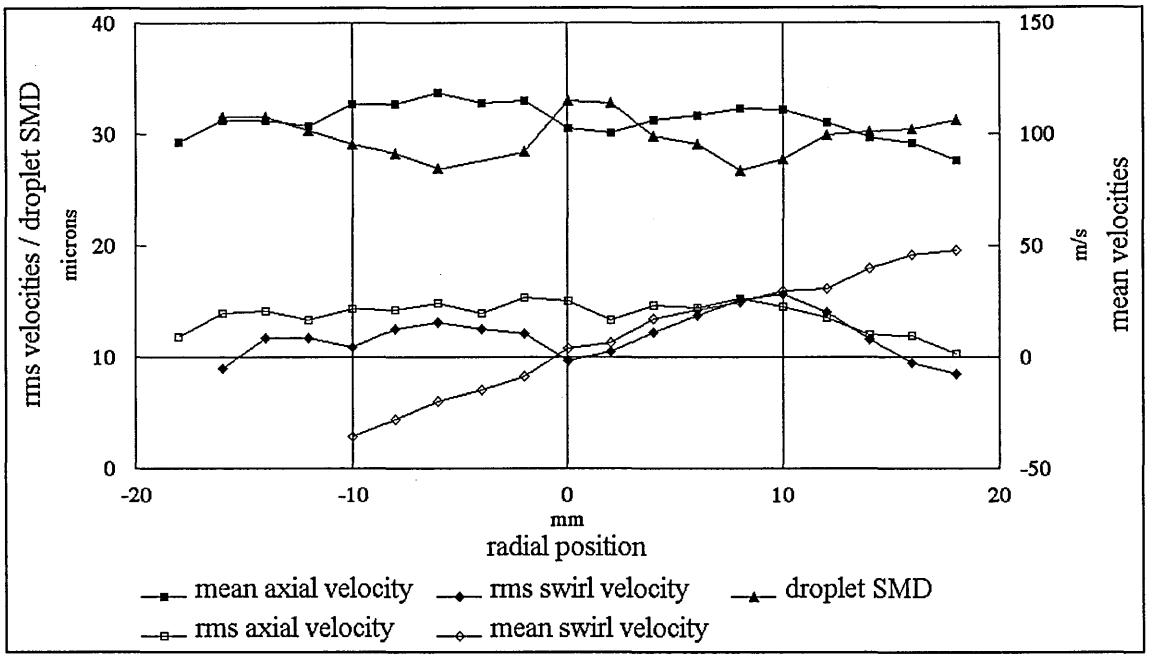

Figure 7.4 2D Radial Traverse of Droplet Axial and Swirl Velocity and Diameter at the Start of the Duct.

The variation of droplet velocity and diameter with distance down the length of the duct can be observed in figures 7.5 and 7.6, taken on the axis centreline and 10 mm off axis respectively. The distance quoted in all the figures is the distance from the origin which is the closest position to the injector that it is possible to measure. This origin is located 28 mm from the tip of the injector.

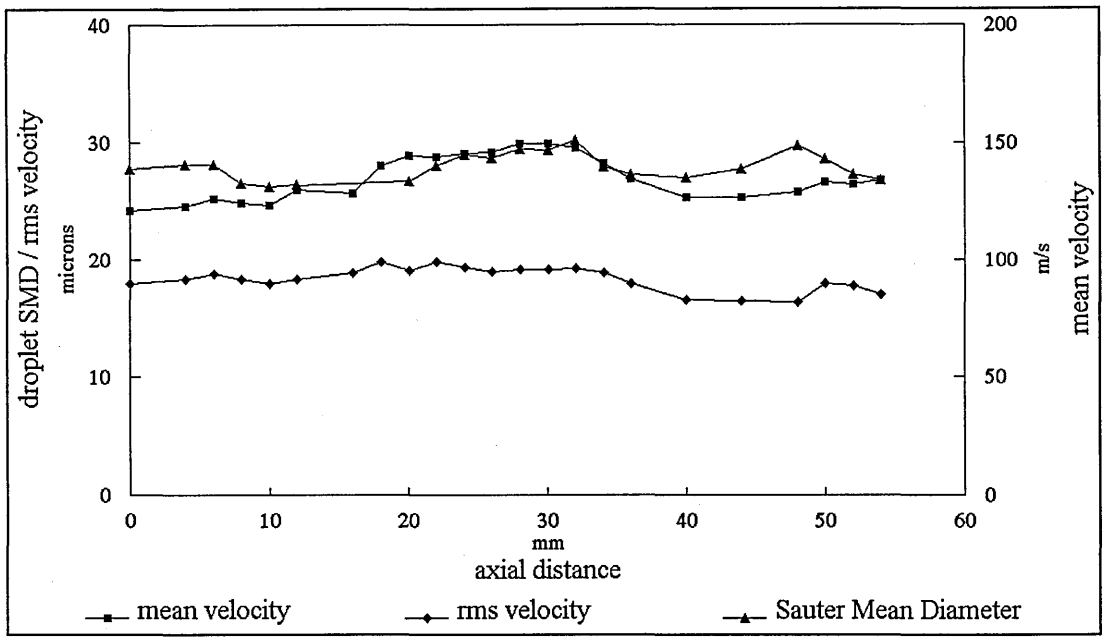

Figure 7.5 Axial Traverse of Mean Axial Velocity and Diameter of Droplets along the Axis of the Premixing Duct.

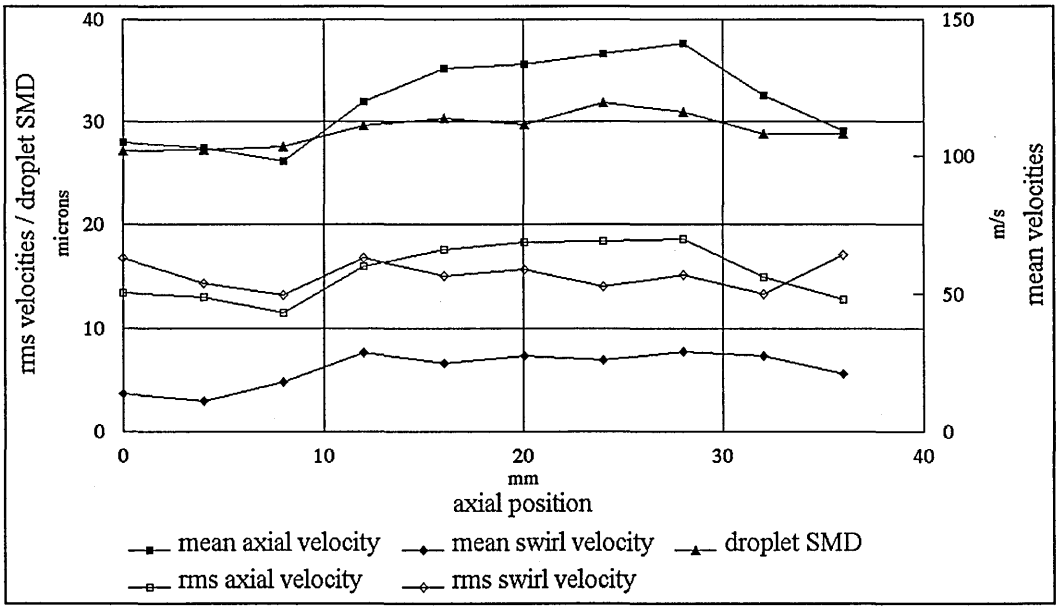

Figure 7.6 Axial Traverse of Axial and Swirl Velocities and Diameter of Droplets 10 mm off the Axis centreline in the Premixing Duct.

7.2.3 Droplet Diameter Dependence on AFR

To determine the effect of overall air fuel ratio on mean droplet diameter, the transmitting and receiving optics were angled to point the measurement volume as close to the injector as possible. Measurements of droplet diameter distribution at each AFR are shown in figure 7.7. The droplet diameter is quoted as the arithmetic mean diameter not the Sauter Mean Diameter (SMD).

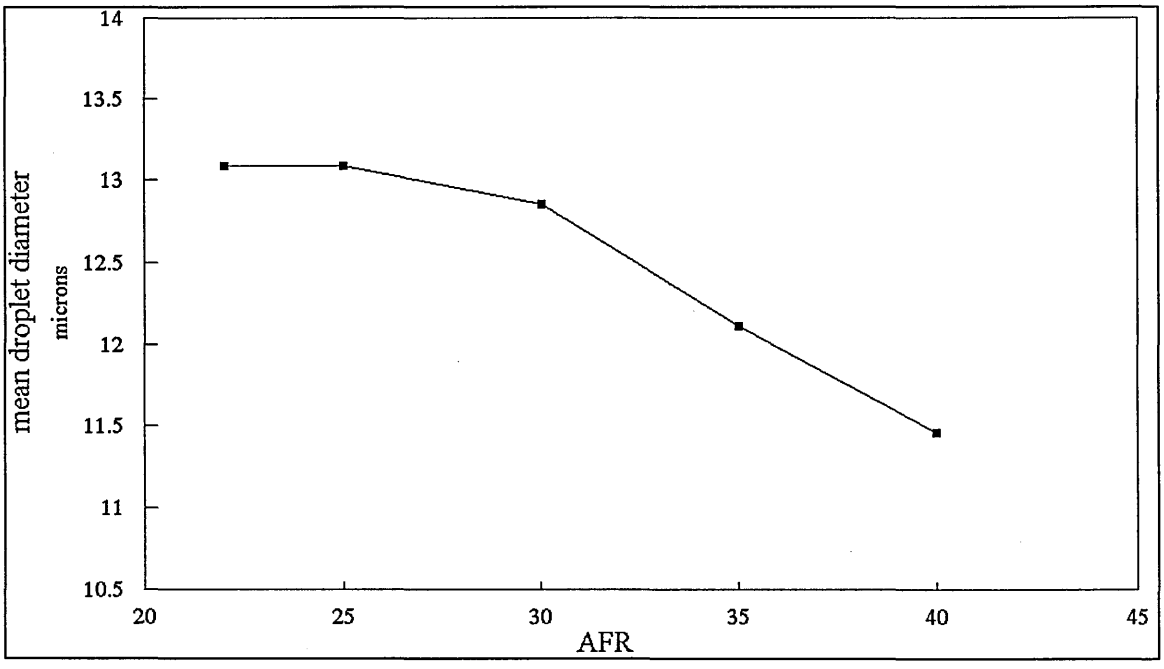

Figure 7.7 Dependence of Droplet Diameter on Overall AFR.

7.2.4 Distributions of Diameter and Droplet Velocities

The distribution of the diameter of the droplets is consistent at all the points measured in the premixing duct. The actual droplet diameters varied from 0.3 micron to 60 micron with a consistent SMD of 25 - 32 micron. Figure 7.8 shows a typical diameter distribution taken from a single point PDA measurement on the premixer centreline 28 mm from the injector. The distribution is made up from 50,000 validated measurements.

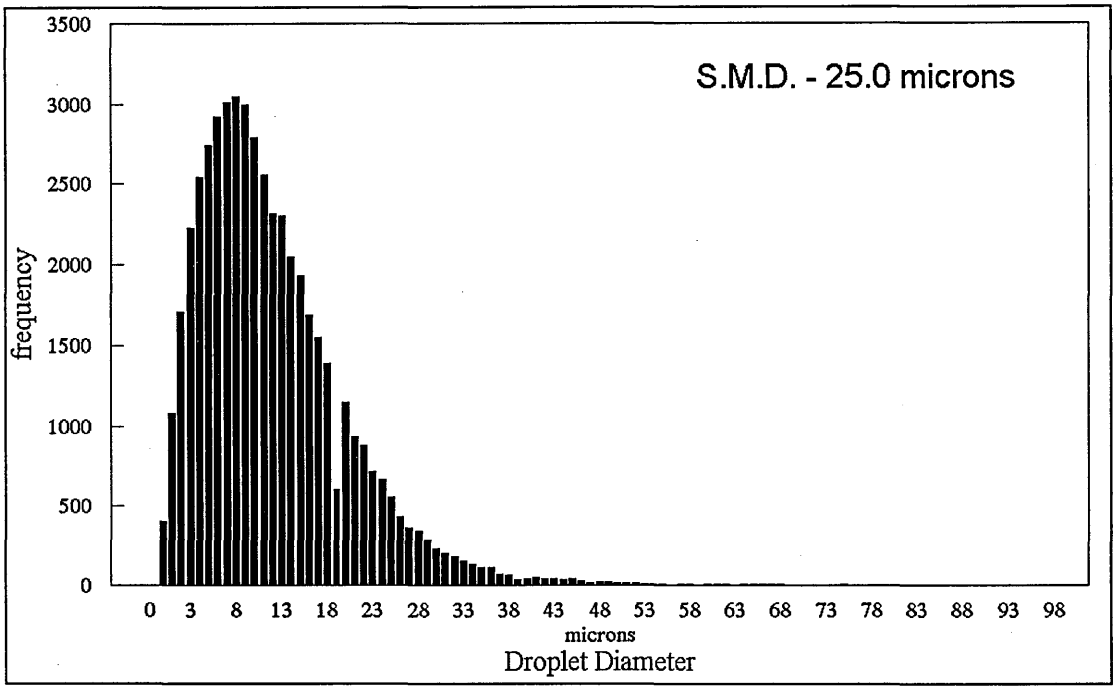

Figure 7.8 Diameter Distribution taken at the Start of the Premixing Duct on the Centreline.

The velocity distributions in the premixing duct vary depending on which component of velocity is being measured and the mean velocity. For a given polydisperse distribution of droplets in a flow, the velocity distribution will broaden as the mean velocity increases. This is because the larger droplets will travel increasingly slower relative to the air as the air velocity rises. Conversely, at lower mean velocities a larger percentage of the droplets are capable of keeping up with the main air flow and resulting in smaller slip velocities between the droplets and the air causing a narrower distribution. Figure 7.9 shows the droplet axial velocity distributions at different points down the duct. The distribution width correlates well with the mean velocity. The dependence of distribution width on mean velocity is further shown in figures 7.10 and 7.11 for measurements taken at the ends and middle of all the radial PDA traverses in the premixing duct. There is a strong correlation between the width of the diameter distribution and the mean droplet velocity.

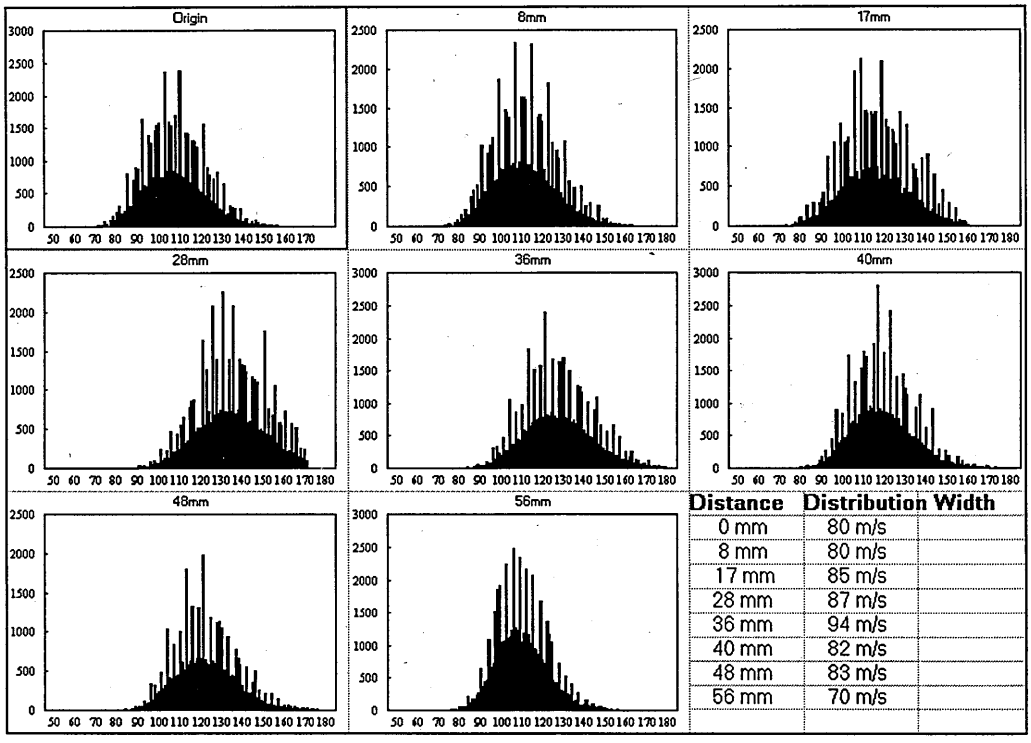

Distance	Distribution Width
0 mm	80 m/s
8 mm	80 m/s
17 mm	85 m/s
28 mm	87 m/s
36 mm	94 m/s
40 mm	82 m/s
48 mm	83 m/s
56 mm	70 m/s

Figure 7.9 Droplet Axial Velocity Distributions along the Centreline of the Premixing Duct.

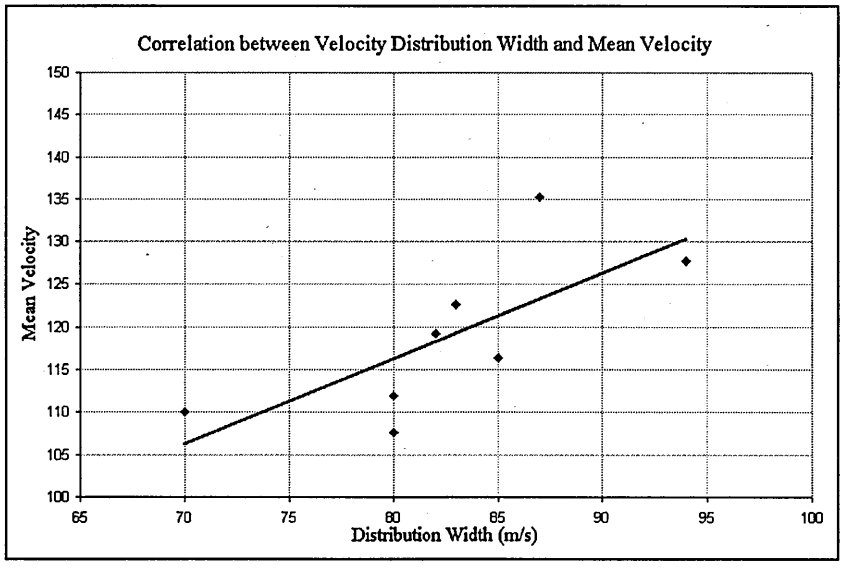

Figure 7.10 Correlation of Distribution Width to Mean Velocity of PDA Data

Figure 7.11 Droplet Axial Velocity Distributions for Three Radial Locations: Near the Duct Walls and on the Centreline at 5 Positions along the Length of the Duct.

(overleaf)

rad. -14 ax. 42mm

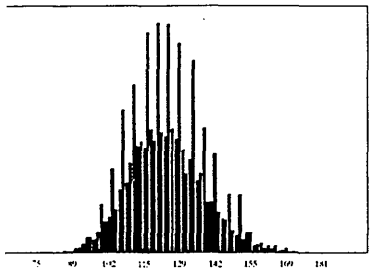

rad. 0 ax. 42mm

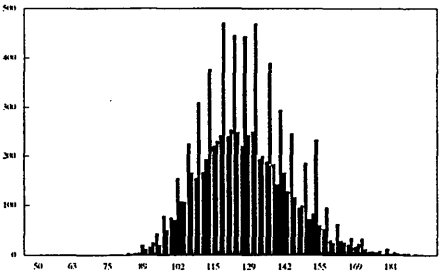

rad. +12 ax. 42mm

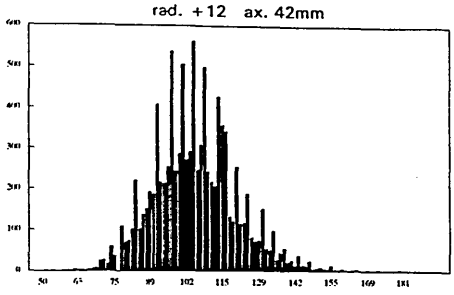

rad. -18 ax. 30mm

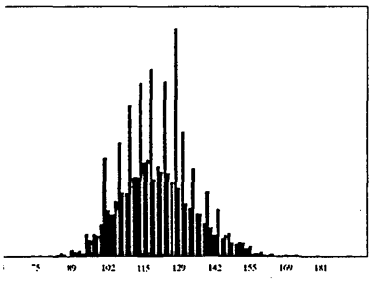

rad. 0 ax. 30mm

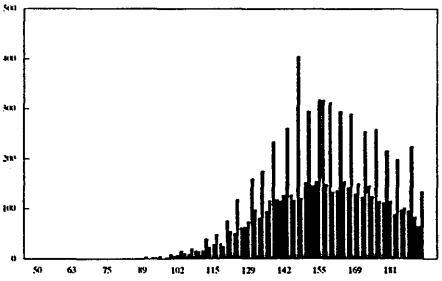

rad. +20 ax. 30mm

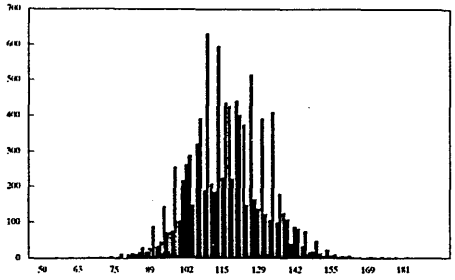

rad. -20 ax. 20mm

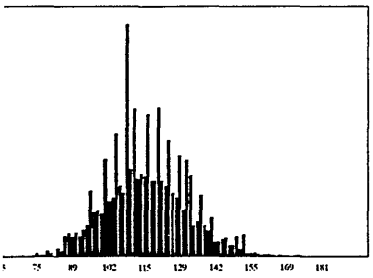

rad. 0 ax. 20mm

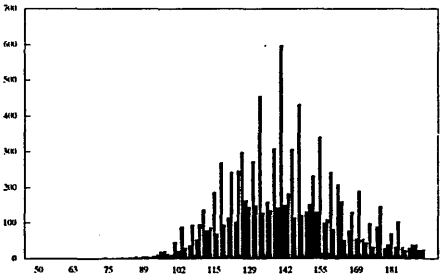

rad. +20 ax. 20mm

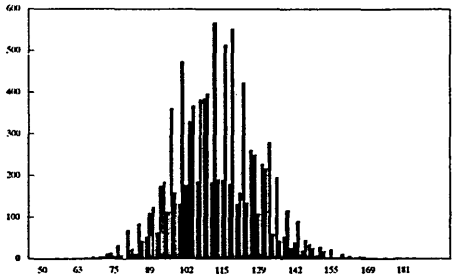

rad. -20 ax. 10mm

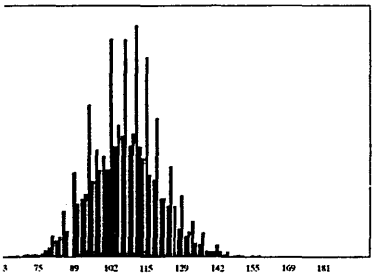

rad. 0 ax. 10mm

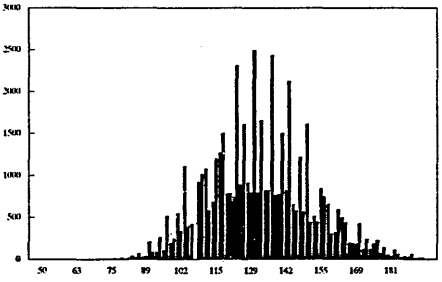

rad. +20 ax. 10mm

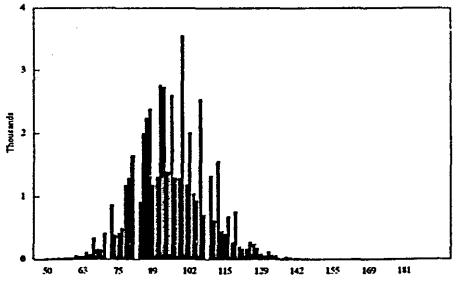

rad. -18 ax. 0mm

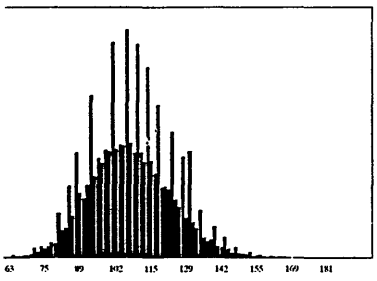

rad. 0 ax. 0mm

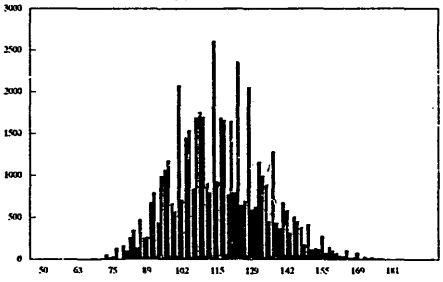

rad. +16 ax. 0mm

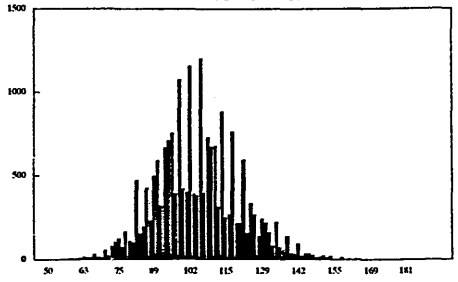

7.2.5 Droplet Slip Velocity

The velocity of the fuel droplets in the premixer will always lag behind that of the gaseous flow. The accuracy to which small droplets follow turbulent fluctuations in a flow is dealt with in section 6.1.6. These criteria suggest that droplets below 5 microns will follow turbulent fluctuations up to 1 kHz. However, the slip velocity of droplets from 0.3-60 microns is shown in figure 7.12 for a mean air velocity of 142 m/s. The slip velocity of the droplets at the start of the duct (60.5 mm from the point of injection) is higher than that at the end (102.5 mm from the injection point) suggesting that the droplets are still accelerating at the beginning of the duct. The curve does not show a flat topped profile which would indicate that the slip velocity of sub micron droplets was negligible. Figure 7.13 shows the size velocity correlation for droplets up to 10 microns for three points of similar maximum velocity at the end of the duct. The graph clearly shows that droplets of 5 microns are travelling about 5 m/s slower than the smallest droplets. Since the value of 1/diameter^2 appears to plateau below 5 micron droplets in figure 7.12, the Melling parameter may not to be accurate at this condition.

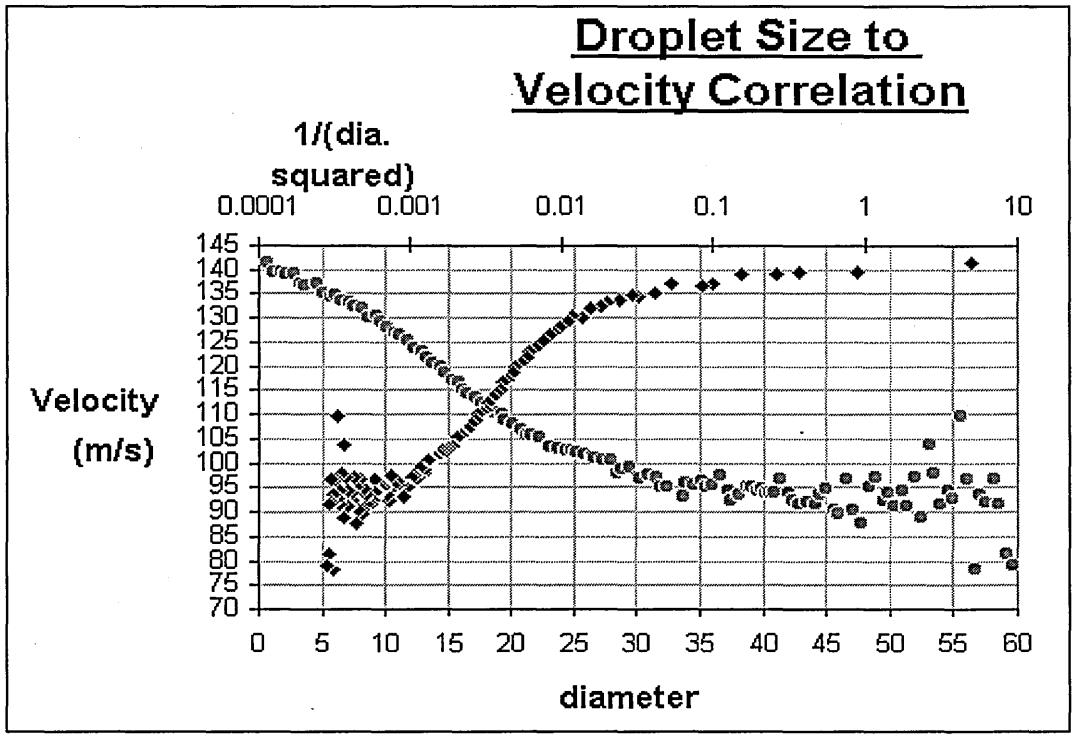

Figure 7.12 Droplet Velocity for 0.3 - 60 micron Diameter Droplets.

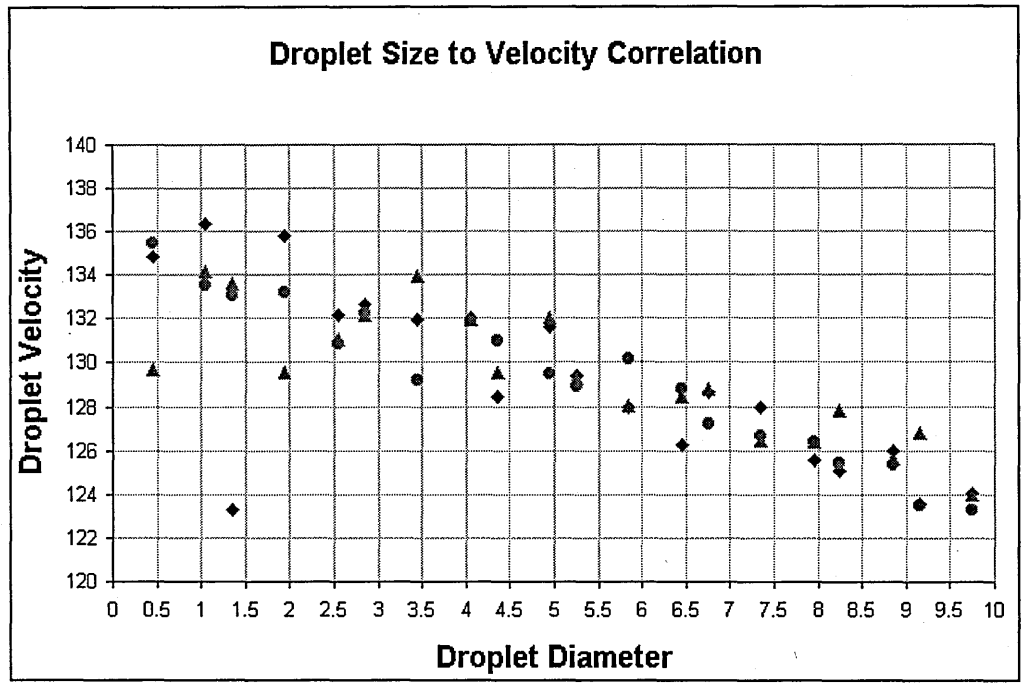

Figure 7.13 Droplet Size Velocity Correlation for Small Droplets (102.5 mm from the point of injection)

7.3 Laser Induced Fluorescence Imaging of Liquid Phase Fuel

The instantaneous distribution of droplets in the premixer can be visualised by using LIF images that discriminate only the liquid phase of the fuel. Conventional PDA measurements cannot under most conditions reliably measure droplet concentration. This is because the PDA collection signal data rate is a function not only of the droplet concentration but also of the signal collection efficiency, the droplet sphericity, the other validation criteria used in the signal processing and the maximum number of droplets measurable in the measurement volume at any one time. The fuel droplet concentration in the premixing duct was qualitatively measured using LIF. Using mineral spirits seeded with 2,5 Diphenyloxazole (PPO) as a fuel and exciting with an excimer laser, LIF images representing only liquid fuel were taken. These images provide a qualitative indication of the fuel droplet concentration in the premixer. The droplet size cannot be inferred from these images since droplet scattering is a function of many factors such as droplet position in the sheet thickness. However, the location of the droplets can easily be identified.

7.3.1 Fluorescent Compounds

Preliminary work was undertaken to find suitable fluorescing compound that could be used as a seed in the fuel. It was known that kerosene provides significant fluorescence in both its liquid and vapour phase (Tait and Harding 1992). Kerosene contains approximately 20 % by mass of aromatic compounds many of which are likely to fluoresce in the liquid and gaseous phase. In a typical kerosene there are approximately 0.05 % three ring compounds, 2.0 % two ring compounds and 18 % single ring compounds.

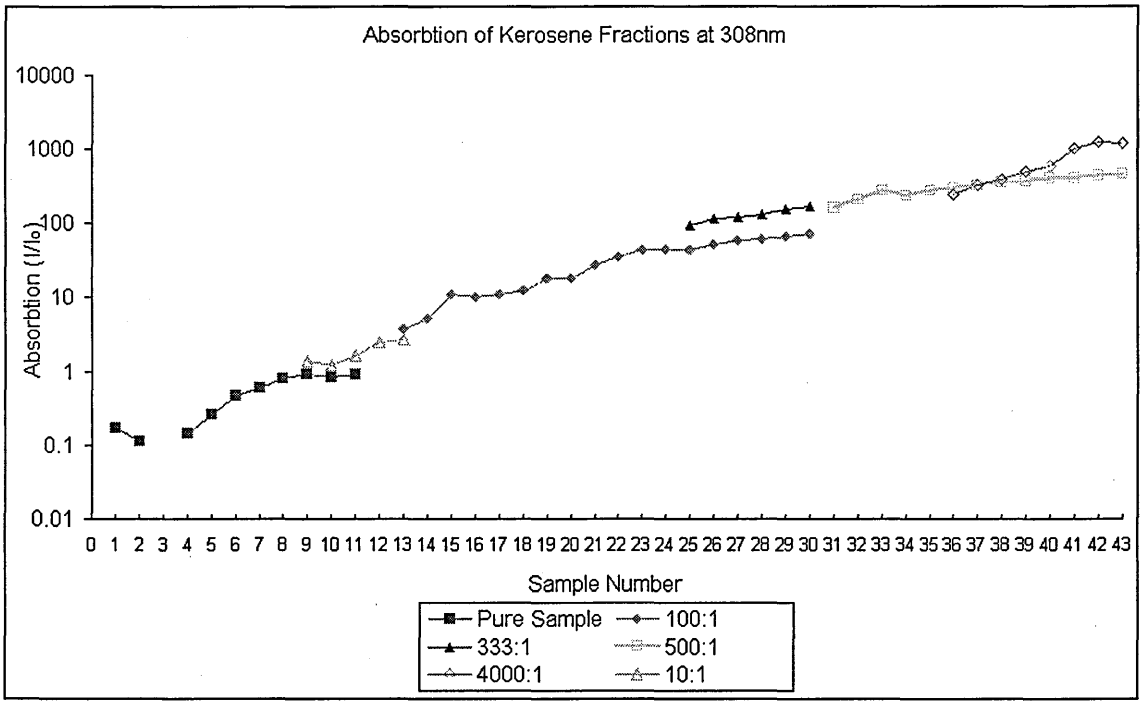

Figure 7.14 Absorption at 308nm of Fractionated Kerosene Samples.

To attempt to identify which aromatic constituents of kerosene fluoresce a sample of kerosene was carefully fractionated. The kerosene samples were fractionated into small intervals of between 1 and 5 °C. The liquid phase absorption and fluorescent spectra of each kerosene fraction was then found using a spectrometer. The absorption and fluorescent spectra were almost identical for each fraction suggesting that the same fluorescing or absorbing compounds were present in all fractions (see figure 7.14). A graph of absorption verses boiling fraction shows a logarithmic increase in absorption

with fraction boiling point. This further indicated that the same absorbing aromatic compounds contaminated all the lower boiling fractions but to predictably lesser degrees. This suggests that any droplet in the premixing duct is also likely to be contaminated with traces of aromatics originating from all boiling points.

It is likely that a compound in kerosene of very low concentration could be responsible for a very high fluorescent yield due to the wide variation in molecular excitation efficiency and collisional quenching efficiency. In order to find likely aromatic fluorescent seeds, a number of two and three ring aromatic compounds were investigated.

Once useful fluorescent compounds have been identified they can potentially be used as fluorescent seeds or markers. By using fuel void of any fluorescent compounds in the LPP combustor suitable fluorescent seeds or markers may be then added for LIF measurements on unburnt fuel. This allows the progress of the fluorescent seed to be traced in the premixing duct or primary zone without any of the uncertainties in the boiling point of the fluorescent compounds in kerosene LIF.

By adding small quantities of samples into a non-fluorescing solvent (pentane), the fluorescent spectra of various aromatics were found. The spectrum of PPO shows that significant ultra violet and visible fluorescence is apparent when excited at 308 nm in the liquid phase. Once the fuel has been vaporised in the premixer the PPO fluorescence is too small to measure. This could either be due to high oxygen quenching or molecular break-up of the PPO. PPO is a large molecule very susceptible to fragmentation in its gas phase. It is possible that the PPO molecules may break up and cease to fluoresce whilst still in the liquid phase. This would lead to the under estimation of liquid fuel fraction. The result is that the liquid phase PPO fluoresces extremely strongly whilst discriminating effectively from the vapour phase. The intensity of the LIF signal from PPO is not necessarily linear with PPO concentration. This means that PPO LIF measurements only provide qualitative data on liquid fuel concentration. PPO LIF is

however a useful technique for spatially marking the presence of liquid fuel in two phase mixtures.

The spectra of kerosene, 2,5 Diphenyloxazole (PPO), naphthalene and fluoranthene are shown in the Appendix II.

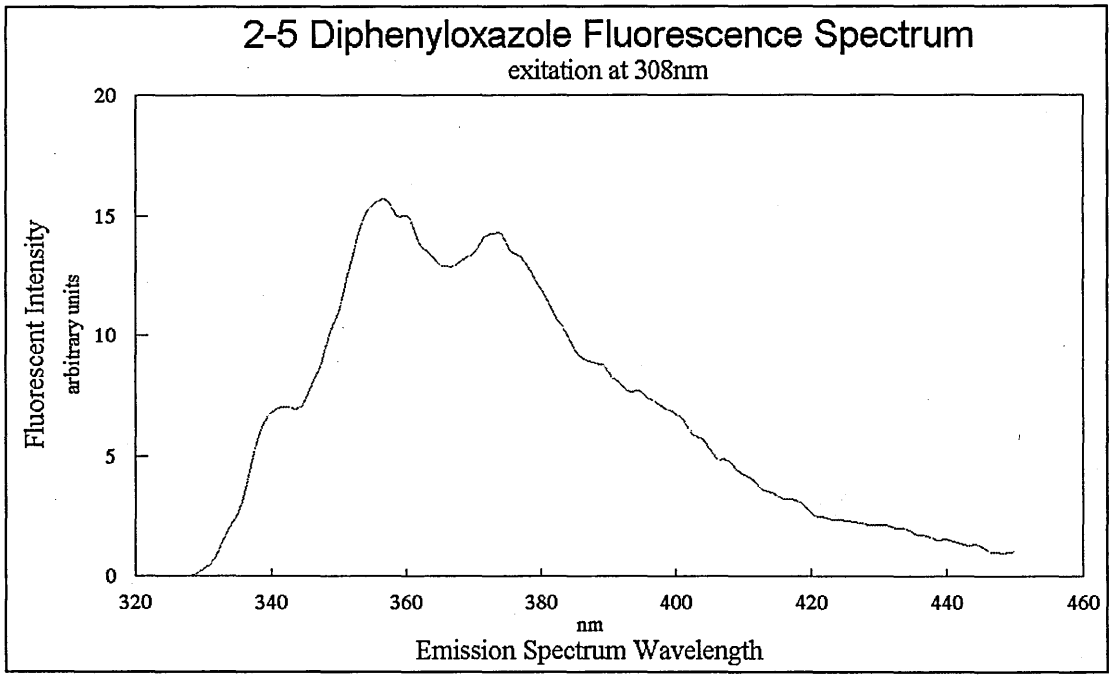

Figure 7.15 Fluorescent Spectra of Liquid Sample of 2,5 Diphenyloxazole (PPO)

7.3.2 Liquid Fuel LIF Measurement Results

LIF images were taken using mineral spirits seeded with 0.3% by mass PPO as a fuel. Mineral spirits is very similar to kerosene without aromatics and therefore has no significant natural fluorescence. The laser used was a Lambda Physik EMG-15-MSC excimer filled with a xenon chloride mix to give emission at 308 nm. This was formed into a laser sheet 60 mm wide and approximately 250 microns thick using a pair of cylindrical lenses and a 2 m spherical lens and passed into the premixing duct.

The powerful PPO fluorescence was collected onto an intensified CCD camera synchronised to the laser pulse. The camera used was a fibre optically coupled, intensified Princeton Instruments camera controlled from a Pentium PC. The intensifier

duration or gate was set to 100 ns and synchronised with an output trigger pulse from the laser. This discriminates most of the background from the LIF images. The images were stored on the PC's hard drive and then transferred to a DEC workstation for image processing. The images were processed to remove background contribution and flatfielded to normalise for laser sheet intensity variations. The experiment was also run without PPO in the fuel to ensure that no fluorescence was detectable from other sources such as minor constituents in mineral spirits or contamination. Instantaneous LIF images of PPO fluorescence are shown on the following pages.

7.4 Discussion of Results

The PDA measurements made in the combustor's premixing duct show that the fuel droplet velocities increase towards the neck of the duct and decelerate at the end. The droplet axial velocity components are in the range 100 to 150 m/s. The fluctuating rms velocity components are typically between 12 and 20 m/s. This compares with rms velocities of 20 to 30 m/s of the seeded air. The droplet motion is similar to the motion of the air in the premixing duct subject to slip velocities. The swirl velocity component of the droplets are conserved along the length of the duct similarly to the air. It likely that there is only a very small fraction of fuel left unevaporated in the premixing duct.

The diameter of the droplets remain between 25 and 32 micron SMD at all locations in the duct. The diameter distribution consistency and droplets diameter suggests that most of the fuel evaporation has taken place before entering the transparent section of the premixing duct.

There is a strong correlation between the overall AFR and the mean droplet diameter.

The velocity distributions of the droplets changes in the premixing duct, depending on the mean velocity. For a given polydisperse distribution of droplets, the velocity distribution will broaden as the mean velocity increases. This is because as the mean velocity is increased, an increasingly higher proportion of the droplets will lag behind

the velocity of the air carrying the droplets. The velocity distributions in the duct show a predictable mean velocity dependence on distribution width for all the radial traverses and axial traverses.

The slip velocity of the droplets between the air and the liquid is as much as 50 m/s for droplet diameters of 60 microns. Droplets below 5 microns in diameter do not attain the carrier gas velocity by up to 5 m/s..

PPO seeded into mineral spirits of the fuel provides an excellent marker for the liquid phase of the fuel since it is an extremely powerful fluorescence source and yields no measurable fluorescence in its gaseous phase. The LIF images of PPO representing liquid fuel provide a useful qualitative indication of the droplets in the premixing duct. There is a very large temporal and spatial fluctuation of droplet concentration in the premixer. The droplets are most often caught in clusters on the centreline of the duct. There is a high variation in droplet location in the duct with respect to time and droplet clusters can at times be observed at all locations in the duct.

The fact that the average droplet location in the duct does not correspond with the location of the vapour phase fuel, further suggests that the vast majority of the droplets have evaporated before entering the premixing duct.

Subsequent measurements using mineral spirits and a new batch of kerosene as fuels revealed that virtually no droplets were present in the duct. The new batch of kerosene and mineral spirits presumably has a low content of high boiling point aromatics which are not detectable with PDA. This further suggests that only high boiling fractions of kerosene are capable of surviving unevaporated into the duct. Given that the concentration of fuel droplets in the premixer appears to be very low, it seems unlikely that the PPO is breaking up prematurely in the liquid phase. This gives confidence to any measurements of liquid fuel made by PPO LIF.

Figure 7.16 Mean LIF Image and Instantaneous LIF Images of PPO in Mineral Spirits Representing Liquid Fuel.

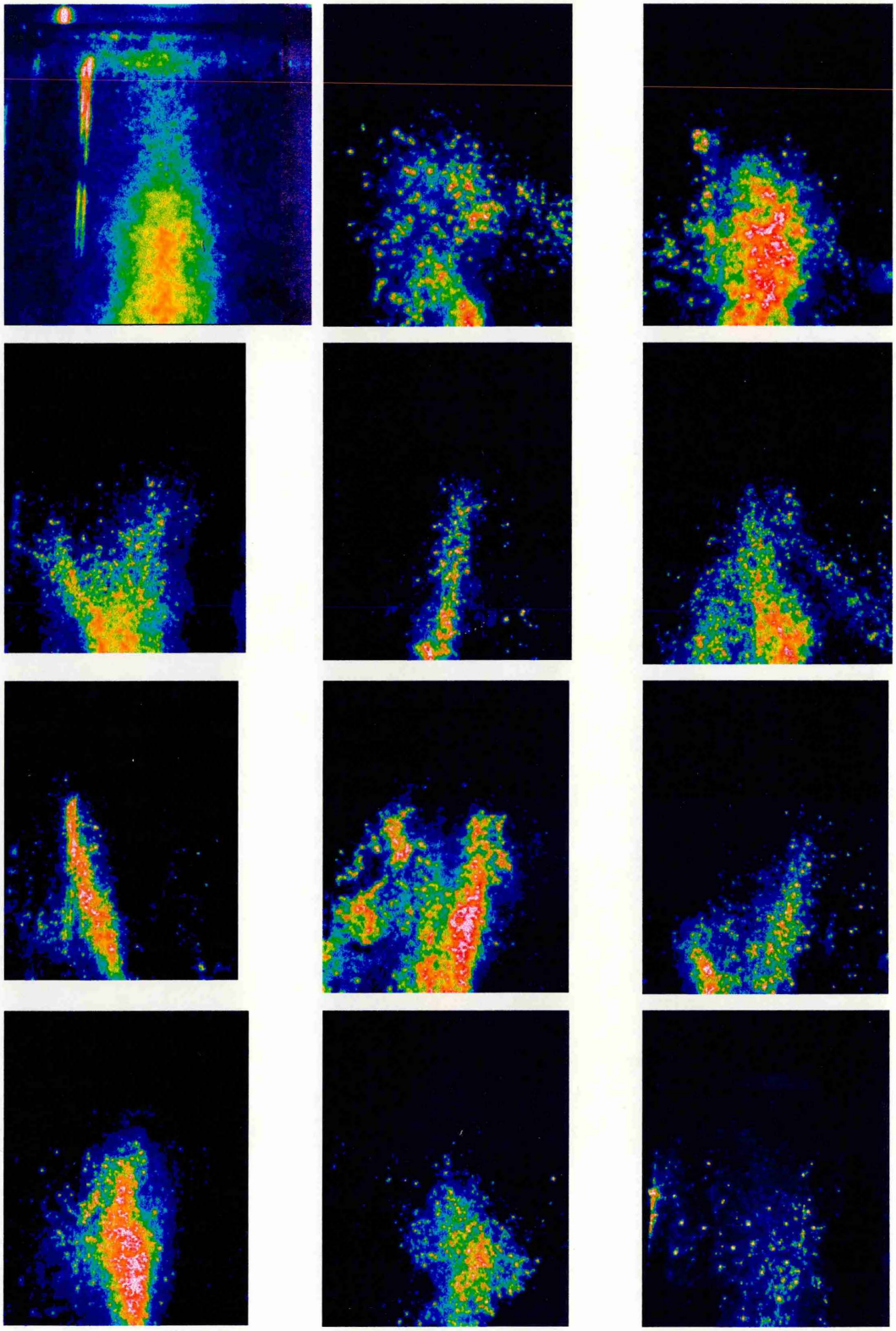

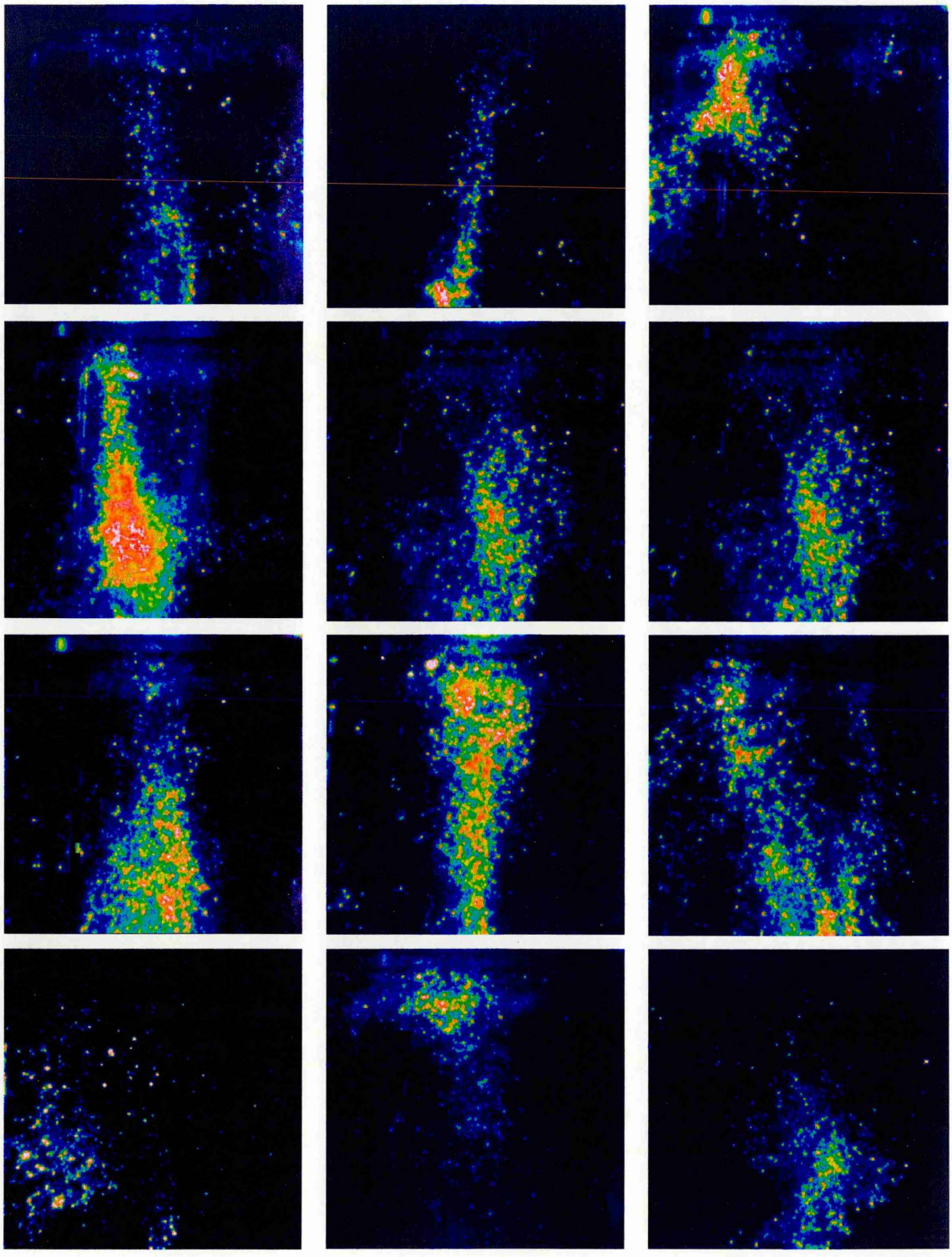

8. FUEL VAPOUR CHARACTERISATION OF THE PREMIXING DUCT

The fuel in a combustor premixer needs to be characterised before the mixing processes can be studied and understood. The vapour phase fraction of fuel in the LPP premixing duct has been studied using Laser Induced Fluorescence (LIF). The aromatics naturally present in kerosene or the fluorescent marker seeded into a non-fluorescing fuel can be excited with an excimer laser and made to fluoresce. Images of this fluorescence have been collected on a CCD camera resulting in two dimensional measurements representing fuel vapour concentration. These images can be post calibrated to absolute levels of fuel concentration or AFR knowing the inlet conditions to allow a detailed study of the fuel-air mixing processes in the premixing duct to be made. The images have been interpreted to study fuel-air mixing rates, calculate the mean and standard deviation in fuel concentration and find the unmixedness parameter. The proportion of temporal to spatial fluctuation in fuel concentration has been estimated. The effect of the boiling point of a particular fraction of fuel on the fuel placement and the fuel-air mixing rate can easily be observed.

A review of laser induced fluorescence is given in section 4.1. The choice of fluorescent marker is explained in the experiments completed to study aromatic compounds and their spectra. The LIF measurement technique and the image processing applied are also detailed. Finally, the results are shown and later interpreted in the discussion section at the end of the chapter.

8.1 Fluorescent Seeds

Both the liquid and the vapour phases of kerosene fluoresce strongly when excited with UV light. This fluorescence is from aromatic compounds naturally present in the fuel. However, LIF images of kerosene fluorescence can only give qualitative data on fuel concentrations due to uncertainties in kerosene's fluorescent behaviour. It is likely that

there are a multitude of compounds in kerosene which fluoresce strongly when excited in the UV. Most of these compounds have unknown fluorescence dependencies with respect to temperature. The boiling point of the fluorescence source in kerosene is likely to be weighted to the higher boiling fractions. Kerosene boils at between 150 °C and 325 °C with a very small volume percentage of aromatics boiling at still higher temperatures.

To eliminate the uncertainty of which boiling fractions in kerosene fluoresce, other fluorescent seeds had to be found. These seeds can be added to a non-fluorescing fuel and used as a marker representative of a particular boiling point in the fuel. Mineral spirits is a fuel similar to kerosene but with the aromatics removed. The seed or fluorescent marker added to the mineral spirits will then fluoresce allowing the fuel to be tracked in the premixing duct. Any laser induced fluorescence from pure mineral spirits is too weak to be detectable in the concentrations present in the premixing duct. Mineral spirits can be used as a non-fluorescing fuel carrier for fluorescent seeds or markers without causing noticeable effect on combustion or mixing. The experiments completed to find suitable fluorescent seeds are detailed in section 7.3.1. Two useful fluorescent seeds for marking vapour phase fuel were identified. One of these is naphthalene which has a boiling point of 218 °C, and can be said to be representative of the middle boiling range of kerosene. The second fluorescent seed is fluoranthene which boils at 384 °C and represents the highest boiling fractions of kerosene. The fluorescence spectra of liquid kerosene, naphthalene and fluoranthene seeded into a non-fluorescing solvent (pentane) are shown in figure 8.1 for excitation at 308 nm.

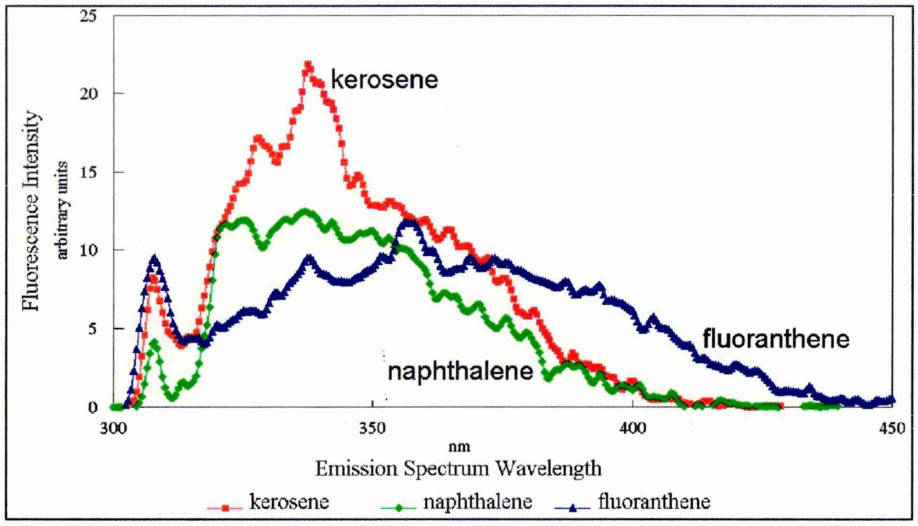

Figure 8.1 Fluorescence Spectra for Kerosene, Naphthalene and Fluoranthene in the Liquid Phase Excited at 308 nm.

There remains an uncertainty in the LIF measurements whether using kerosene, or seeded mineral spirits caused by their unknown behaviour relative to temperature and oxygen concentration. For the purposes of this experiment it is assumed that the low gradients of temperature and oxygen concentration present in the premixer have a negligible effect on the final fluorescent yield. The fluorescence dependence of oxygen quenched naphthalene is highly non-linear with temperature (Smith A.) However at the temperatures experienced in the premixing duct, the fluorescence temperature dependence is likely to be relatively flat.

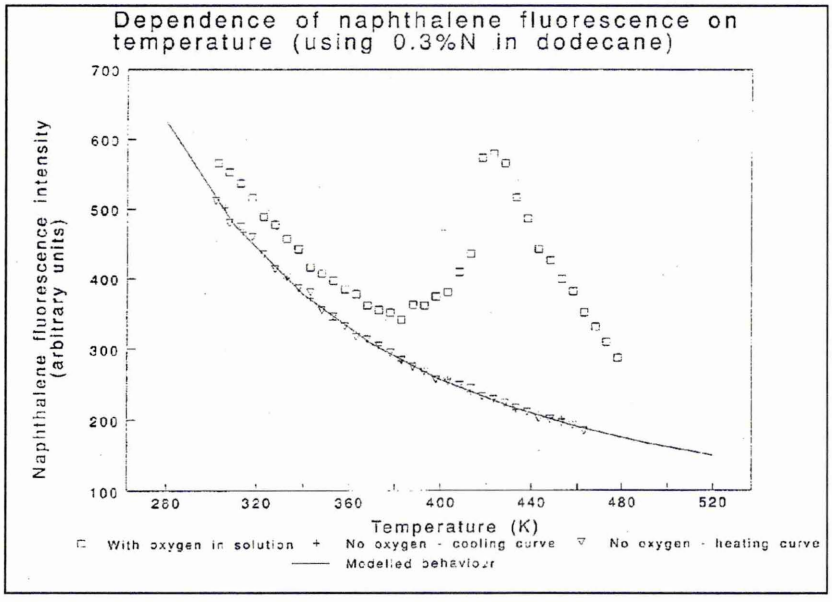

Figure 8.2 Effect of Temperature on Naphthalene Fluorescence - Smith.

8.2 Experimental Set-up

The experimental set up consisted of a laser sheet introduced into the measurement volume to excite the fuel fluorescence. This was then collected perpendicular to the sheet and imaged onto an intensified CCD camera.

The laser sheet was formed with light emission from a Lambda Physik EMG-150-MSC excimer laser filled with a xenon chloride gas mixture. The laser emits ultra-violet light at a wavelength of 308 nm with pulse energies of up to 200 mJ. Using a combination of a plano-convex, a plano-concave and a 2 m focal length spherical lens, the laser's rectangular section beam was formed into a thin sheet approximately 60 mm wide and 250 microns thick. This sheet could be introduced into the premixer or primary zone radially or axially in the configurations shown in figure 8.3.

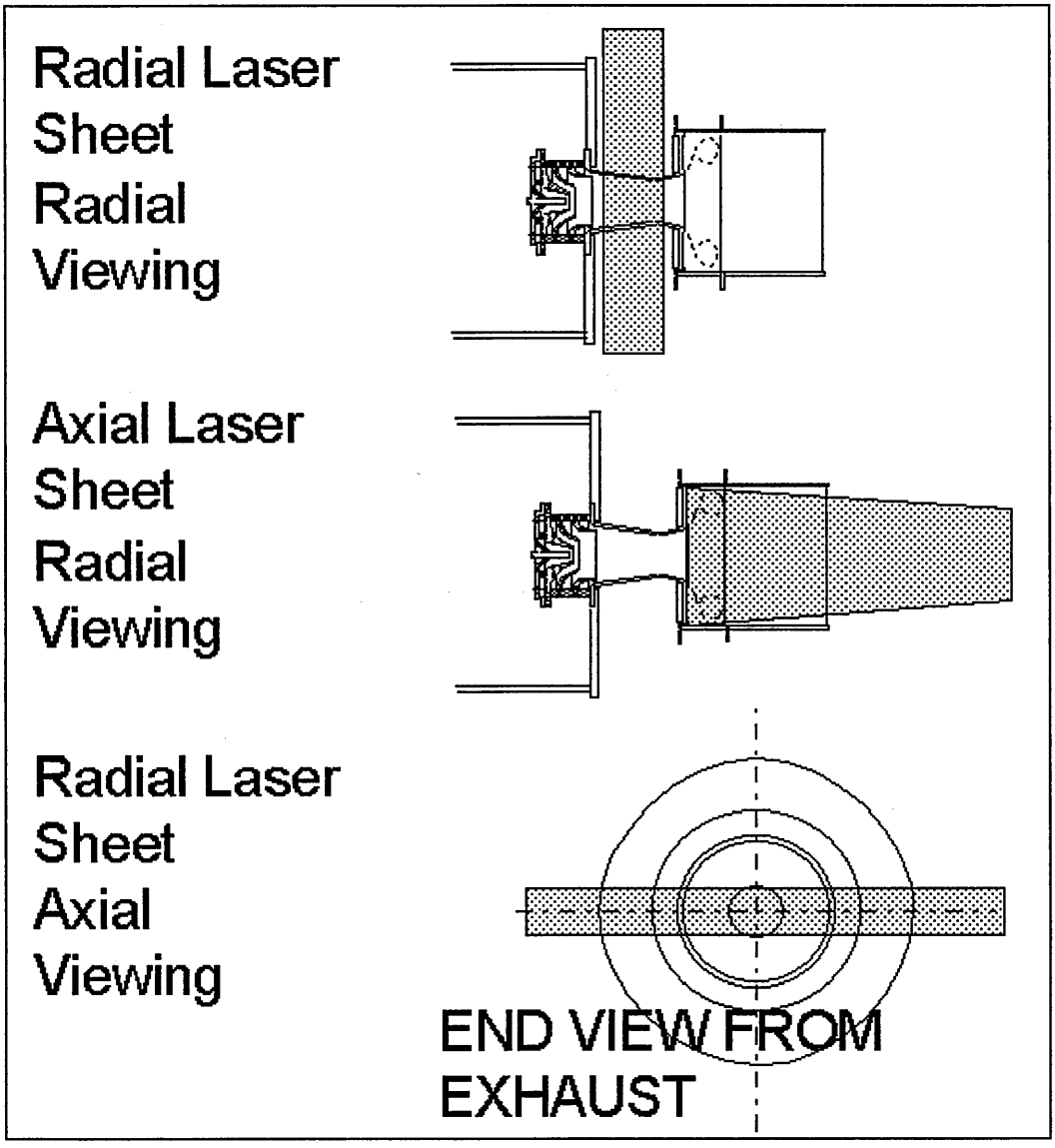

Figure 8.3 LIF Configurations used on the LPP Combustor Premixer and Primary Zone.

A CCD camera collected the fluorescent signal with a Nikon f/2.8 60 mm macro lens. The camera collected and amplified the signal with a composite fibre optically coupled intensifier tube. The camera employed was a Princeton Instruments ST-130/135 camera with a chip resolution of 576 X 384 pixels. The intensifier tube was powered by an HV pulse from a Princeton Instruments PG-200 digital power supply incorporating an MCP-100 high voltage unit. The intensifier power supply was triggered from an attenuated CMOS pulse from the excimer laser power supply to gate the intensifier with a 100 ns duration tightly surrounding the laser pulse. The laser pulse duration is typically 20 ns

and the compound fluorescing lifetime typically lasts less than 20 ns from the molecule's excitation.

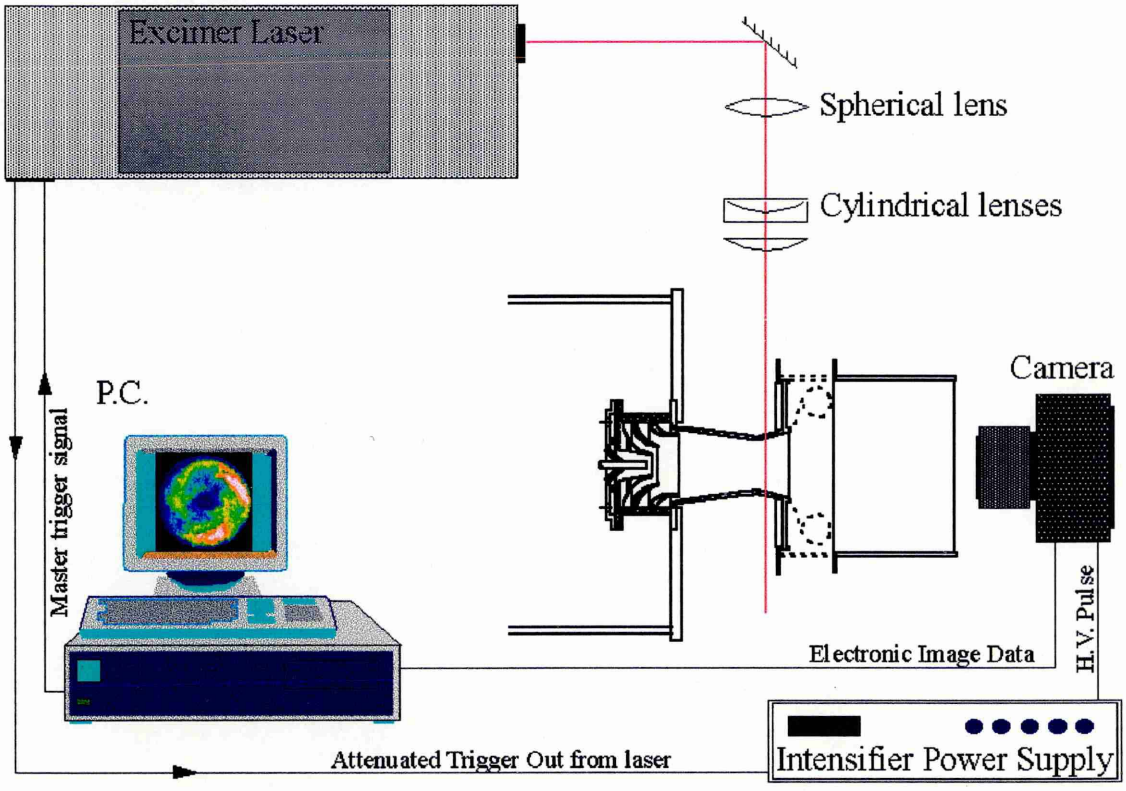

Figure 8.4 Experimental Set up of Planer LIF Experiment

The camera was controlled from a Pentium PC which instigated each LIF image collection by sending a start trigger pulse to fire the laser 80 ms after the camera shutter was opened. The camera digital readout time was approximately 10 seconds which limits the maximum frequency of LIF data collection. Mean images of fuel fluorescence were collected by averaging between 20 and 200 images on the camera controller. By averaging images onto the camera, the laser can be fired at a high repetition rate raising the data collection rate. The collected fluorescence signal was filtered by both the glass lens filtering out light of wavelength shorter than 360 nm and by a 310 nm long pass filter. This should eliminate all the UV light scattered from the sheet. The excimer laser gives off a small portion of visible light which can be removed from the final processed images along with any residual UV light by background subtraction. The images were stored on the PC hard disk and then transferred to a workstation for image processing.

8.3 Image Processing

The raw images of fuel vapour fluorescence were processed to yield a final calibrated image of fuel fluorescence only using Cranfield's laser image processing software CLIPS (by Tait 1994). The intensity at each pixel on the final image will then be proportional to the concentration of the fluorescent species in the fuel vapour independent of any contribution from background sources and spatial variations in laser sheet intensity subject to certain assumptions. These are :

- the fluorescent signal collected is unaffected by any spatial or temporal variations in temperature or oxygen concentration
- the background light is the same during LIF image measurement as during subsequent background image measurement
- the laser sheet intensity profile is the same during LIF image measurement as during subsequent flat-fielding image measurement
- there is no attenuation of the laser sheet intensity due to absorption through the measured medium
- the fluorescence signal is in a linear, non-saturated regime relative to laser sheet fluence
- any interference from the liquid phase fuel is negligible
- no significant amounts of fluorescence are trapped (absorbed) on their path from the laser sheet plane to the camera.
- and all the fuel is in its vapour form.

The images were processed by removing a background image and dividing by a flatfielding image to normalise for variations in laser sheet intensity. The background images were created by averaging 50 images of pure air in the premixer. The flatfielding images were taken by flooding the measurement volume with acetone vapour. Acetone is volatile and easily diffuses to form a uniform concentration in the measurement volume. Fluorescence from acetone can be shown to be directly related to concentration and laser fluence in an isothermal field (Tait 1994). The acetone fluorescence was recorded on the

camera and had a background subtracted to provide the flatfielding image for image processing.

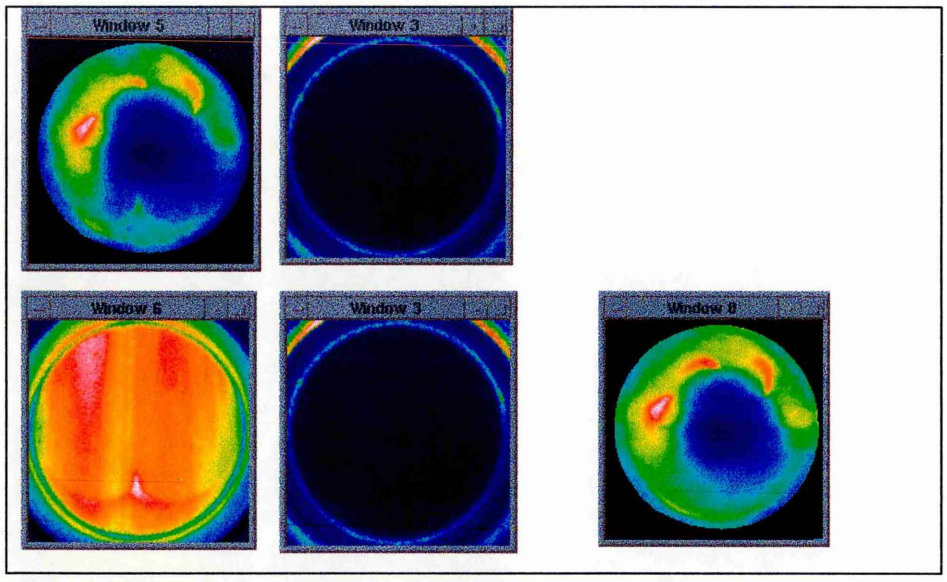

Figure 8.5 Image Processing by Background Removal and Flatfielding - raw image, background image, flatfielding image, background image, final image

8.4 Calibration and Accuracy of LIF Measurements

Kerosene and naphthalene LIF images have been calibrated to an absolute AFR scale. This calibration is based upon integrating the concentration of fluorescent material in a mean processed image and correlating against the known inlet conditions or overall AFR. The imaged fluorescing compound is assumed to be representative of all of the liquid and vapour fuel. The fuel is assumed to be entirely vaporised and travelling at the same velocity as the air. The AFR is defined as

$$\text{Overall AFR} = \frac{\text{Air Mass Flow}}{\text{Fuel Mass Flow}} = \frac{\int 2.\Pi.r.U_{air}.[air]\,dr}{\int 2.\Pi.r.U_{fuel}.[fuel]\,dr} \propto \frac{1}{I_{fluor.}}$$

For the premixing duct radius r, velocity U, air concentration per sectional element in units of m^2 [air], fuel concentration per m^2 [fuel] and fluorescence signal per pixel $I_{fluor.}$ If the fuel and air have the same density and the fuel concentration is proportional to the

collected fluorescence signal, then the overall AFR may be related to mean fluorescence signal spatially averaged across a processed image. An image representing the integral $\int 2.\pi.r.U.[fuel]dr$ was calculated for an axial section in the premixing duct to observe the change in gross fluorescent flux (fuel) along the length of the premixer. The velocity, U was taken from the measurements detailed in chapter 6. The flux of fluorescent material can be seen to decline along the length of the duct. This is possibly caused by the rich zone at the start of the duct being out of the plane of the laser sheet further down the duct and asymmetry of the fuel vapour at the duct exit. The variation in fuel flux is shown in figure 8.6 and is an approximate indication of the absolute accuracy of the AFR measurements. The maximum variation of fluorescent flux is approximately 25 %. The repeatability of each mean LIF is within only a few percent and is probably a better indication of the true measurement accuracy.

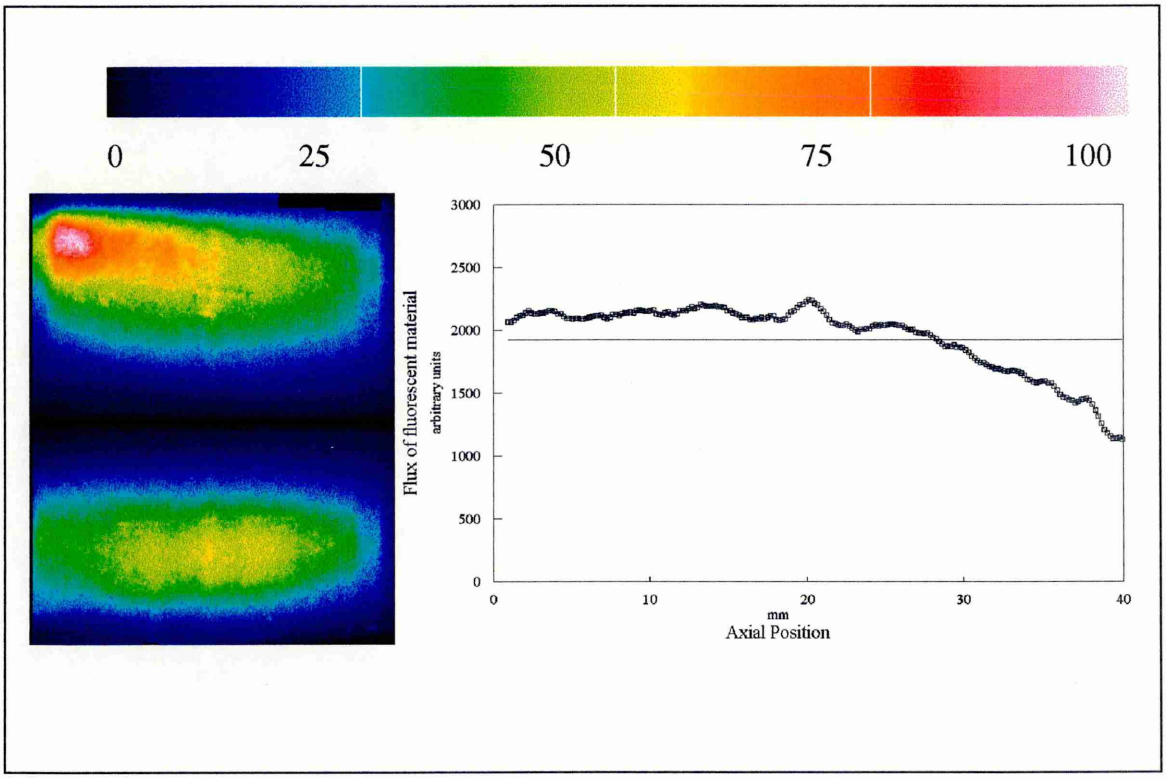

Figure 8.6 Image Representing Flux of Fluorescent Material in the Premixer (arbitrary units).

The absolute accuracy of planar LIF measurement technique can be inferred from a comparison made with gas analysis measurements. LIF measurements have much improved temporal and spatial resolution over gas analysis measurements. However, gas analysis is a widely accepted, reliable method for measuring concentration. The gas analysis instruments are calibrated to a known span gas whereas the LIF measurements were post calibrated to the known inlet conditions. The LIF technique has the advantage of providing an instantaneous measurement freezing the motion of the fluid and a high spatial resolution. Gas analysis has a time response of order seconds before the sample reaches the gas analyser and takes time to react to the change in concentration. The spatial resolution of the gas analysis measurement is limited to the dimensions of the probe. The comparison of LIF measurements with gas analysis measurements is shown in figure 8.7. The poor resolution of the gas analysis measurement and interference from the probe appears to have had the effect of blurring out much of the structure in the concentration profile. This could be improved by the use of a smaller diameter more aerodynamic probe. However, the gas analysis measurements will always suffer from inaccuracies due to the intrusive nature of the probe. The comparisons with LIF measurements highlight the inaccuracies of probe sampling measurements. The difference between the kerosene and naphthalene LIF measurement profiles shows that the kerosene LIF is weighted towards higher boiling fractions which survive longer unevaporated and end up further outboard.

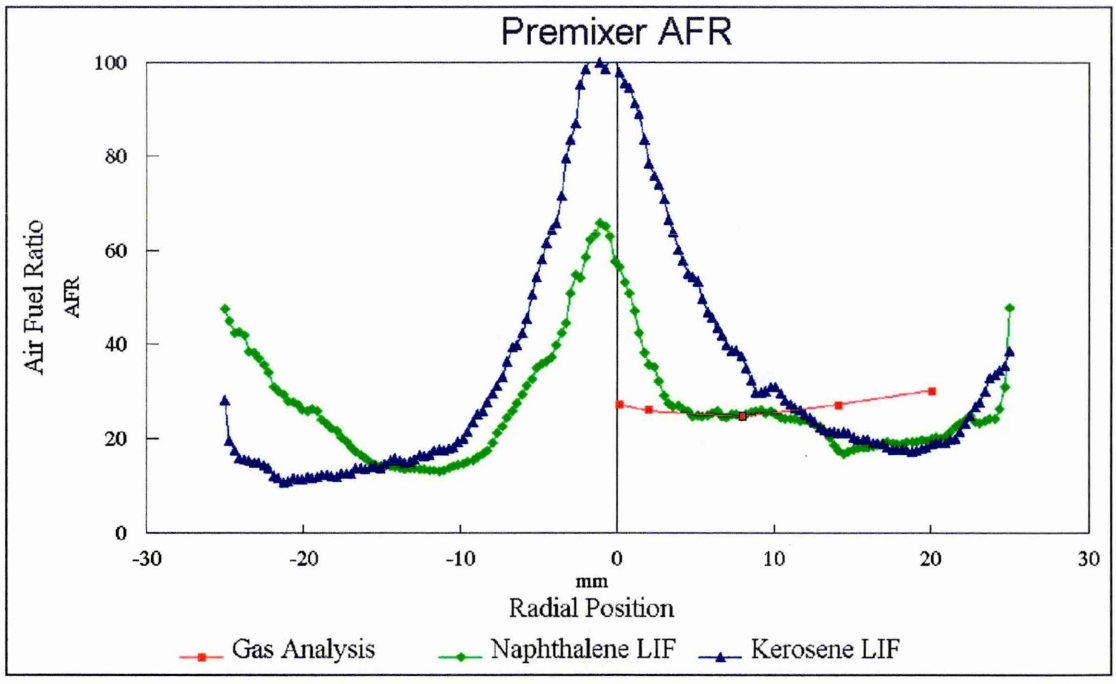

Figure 8.7 Comparison of Premixer AFR Measured with Planar LIF and Gas Analysis.

8.5 LIF measurement results

The following three sections detail vapour phase fuel LIF measurements in the premixing duct using either kerosene as a fuel, naphthalene in mineral spirits as fuel or fluoranthene in mineral spirits as fuel. Tests were conducted using pure mineral spirits before and after each batch of fuel to check that no fluorescence was detectable. This ensured that no contamination of fluorescence either from mineral spirits or from residues of previous fuels contributed to the measurement. The entire fuel system and pipework had to be flushed with methanol between each change of fuel to efficiently remove any such contamination.

8.5.1 Kerosene LIF measurements

Measurements of LIF from the aromatics in kerosene were made in axial sections of the premixing duct and in five radial sections down the length of the duct. For the axial measurements, the laser sheet was passed horizontally through the side of the duct with the camera placed perpendicular to the laser sheet. For the radial measurements, the laser

sheet was sent vertically through the duct with the camera placed looking up through the exhaust. It is apparent from the radial fluorescence images that there is no noticeable image distortion due to refraction effects across the high temperature gradients in the exhaust. This effect can be qualitatively estimated by comparing a background image collected non-combusting with a LIF image collected with combustion. These images are shown in Appendix II.

8.5.1.1 Axial Sections

The axial section mean LIF image was calculated from 88 instantaneous images of fuel fluorescence. The axial mean and instantaneous images of kerosene LIF are shown below in figure 8.8. These images are scaled to an absolute AFR. An image of the rms or standard deviation in the fuel fluorescence normalised by the mean has been calculated and is shown in figure 8.9. The rms image is scaled from 0 to 100% of the mean. Regions showing a high variance in fuel concentration are likely to be areas of rapid mixing.

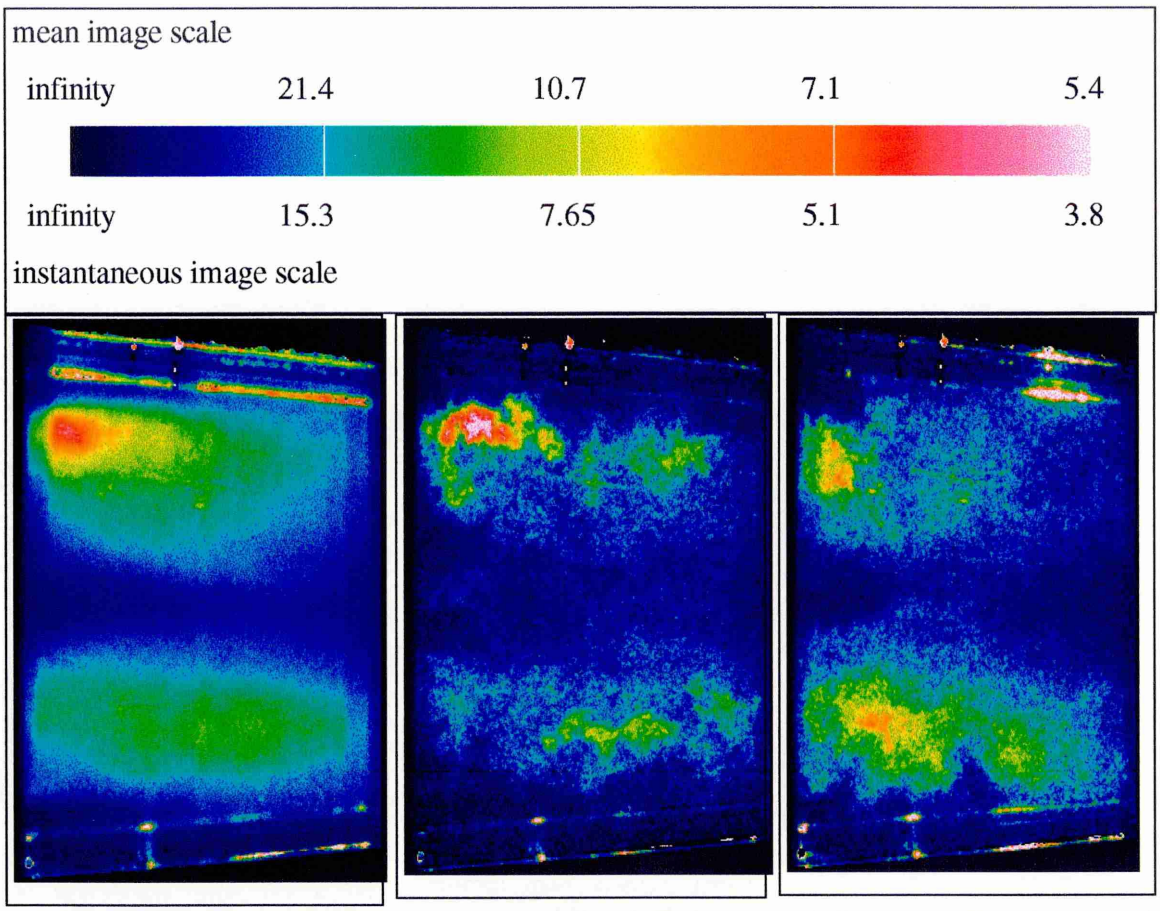

Figure 8.8 Mean and Instantaneous Axial LIF Images of Kerosene Fuel Vapour in the Premixing Duct Scaled in AFR.

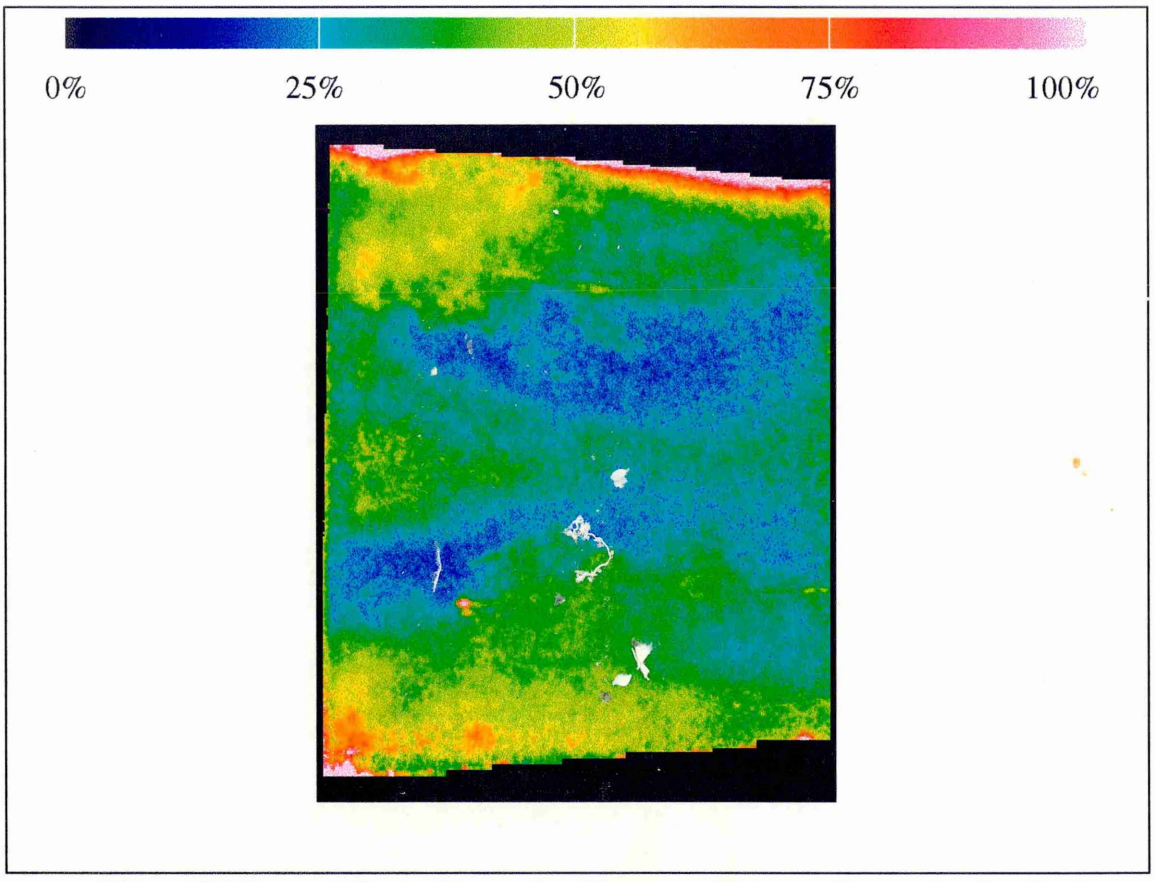

Figure 8.9 Image of rms / mean for Kerosene Vapour Concentration in the Premixing Duct Scaled in %.

8.5.1.2 Radial Sections

Radial images of kerosene fuel LIF were taken at five positions down the length of the duct 30, 42.5, 55, 67.5 and 80 mm from the tip of the injector. The 80 mm position corresponds to the neck of the duct. A mean, instantaneous and normalised rms LIF image is shown for each position in figure 8.10. One hundred instantaneous LIF images were taken at each position and were used to calculate the mean and normalised rms images.

Figure 8.10 Mean, Instantaneous and Normalised rms Images of Kerosene LIF in the Premixing duct at 30, 42.5, 55, 67.5 and 80 mm from the Injector Tip.

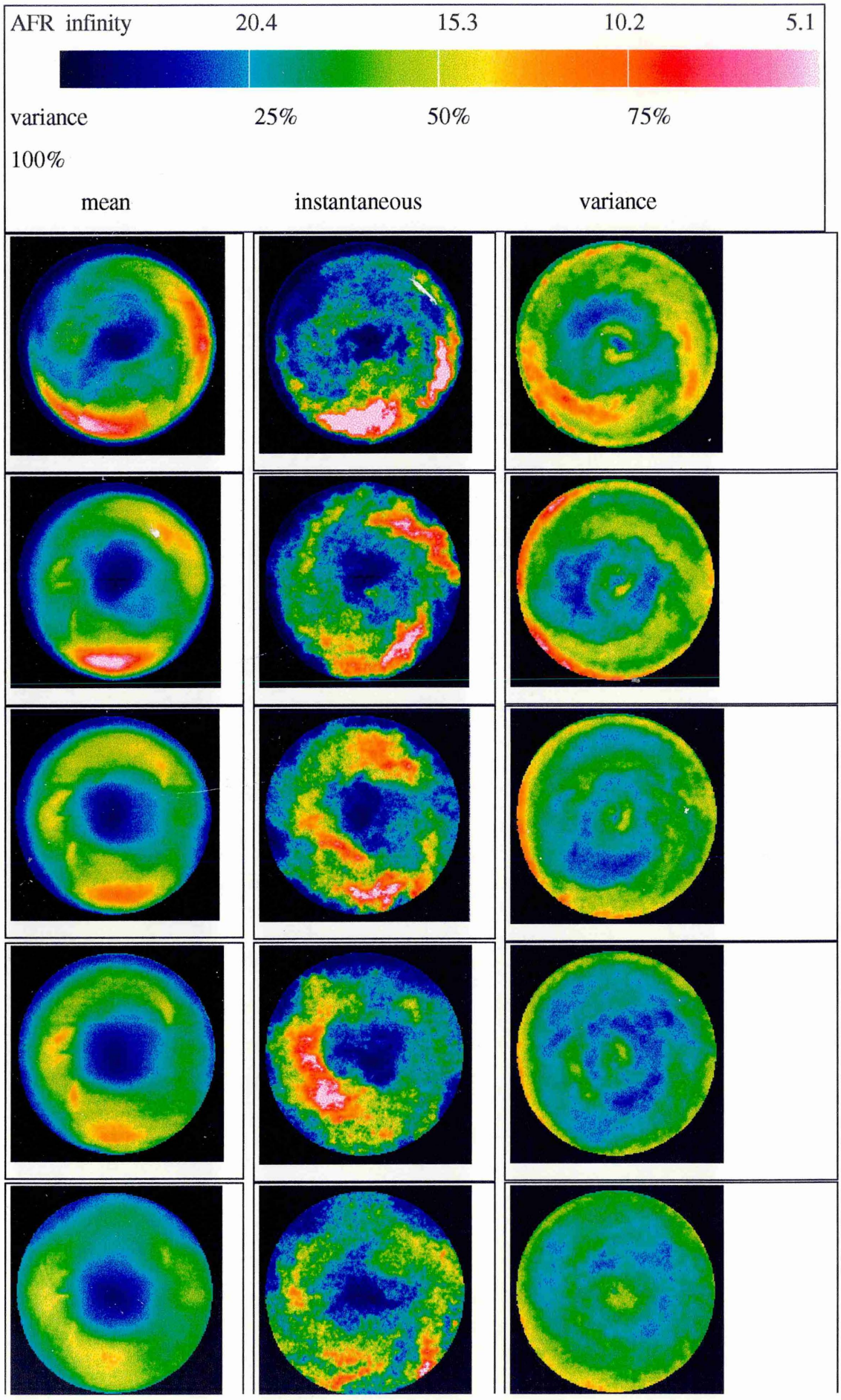
AFR infinity
20.4
15.3
10.2
5.1
variance
25%
50%
75%
100%
mean
instantaneous
variance

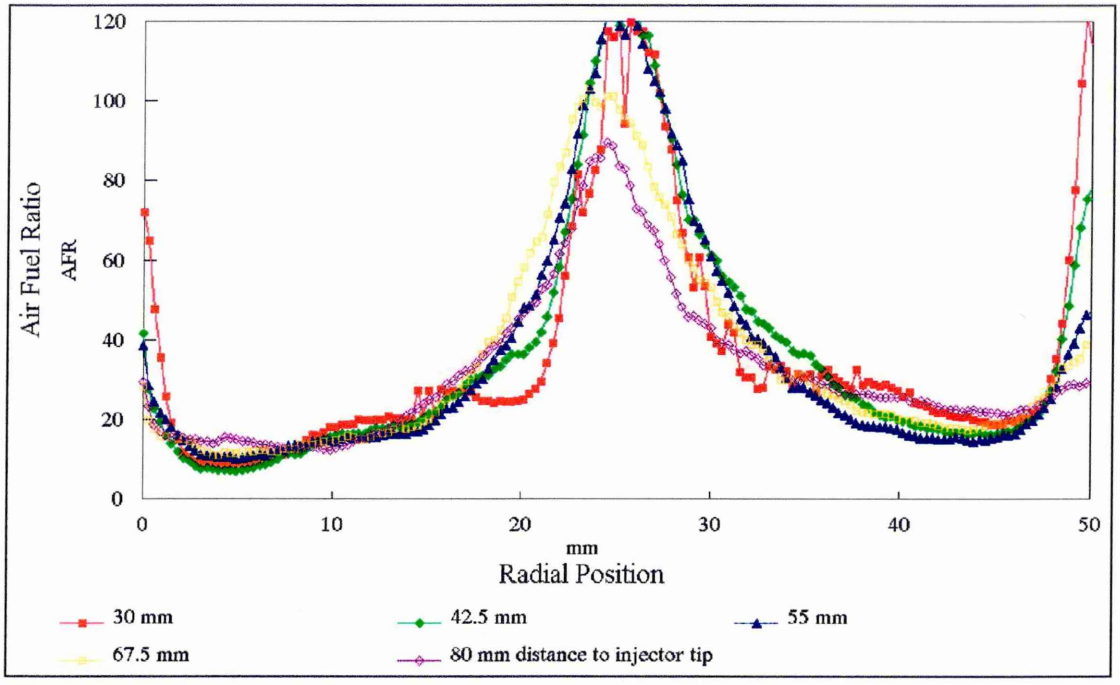

Figure 8.11 Profiles across Mean Kerosene LIF Images down the Length of the Premixing Duct Scaled in AFR.

Profiles of AFR across the duct for each radial section are shown in figure 8.11. The profiles show a fuel lean region in the core of the duct and at the edge of the duct. The profiles become flatter indicating better mixing along the length of the duct.

8.5.1.3 Fluctuating Components of Fuel Concentration

The spatially averaged value of normalised rms for kerosene fuel vapour concentration at each position along the length of the premixing duct can be observed to decrease with axial distance up to the end of the duct where there is a slight increase. The absolute values of fuel concentration rms are similar in both the radial and axial measurements as shown in figure 8.12.

This increase in fuel concentration rms is probably partially due to the effect of the flow field being altered by the primary zone. The fuel-air mixture becomes split into an annulus before entering the primary zone. The core hole present in the axial images is

due to the absence of fuel in the premixer core. The region inside the annulus at the duct exit is most likely filled with hot combustion products and combusting fuel-air mixture. This core will widen at the exit of the premixing duct due to the effect of the primary zone recirculation. The fluctuation of fuel concentration is naturally high where there is virtually no fuel. High turbulence levels near the primary zone are likely to increase the temporal component of fuel concentration fluctuation. These effects could explain the increase in the measured normalised rms of fuel concentration at the end of the premixing duct. The exit of the premixing duct is 109 mm from the tip of the injector.

In order to quantify the relative contribution of temporal fluctuation in fuel concentration to total fluctuation (spatial and temporal) further analysis was completed. The temporal component of fluctuation can be estimated by integrating the total fuel present in each instantaneous image and then calculating an image spatially averaged rms value. Ideally, a more accurate method would have been to calculate the rms value averaged over a smaller region. However, due to the limited number of measurement images which it is practical to measure and store, the rms value was averaged across a whole image. This will result in a small underestimation of the temporal component of fluctuation. This shows the variation in total fuel present at each measurement location independent of the spatial distribution of fuel. The contribution to fuel concentration rms was calculated to be approximately 27 % temporal and 73 % spatial with an increase in the temporal component towards the duct end. This is also shown in figure 8.12.

The rate of fuel-air mixing in the premixing duct has been quantified by calculating the unmixedness of the mixture. The unmixedness parameter defined below ranges from zero to one, with zero for a perfectly mixed system and 1 for a badly mixed system or a system with maximum variance in fuel concentration (Fric 1993).

$$\text{Unmixedness Parameter, } U = \frac{c'^2}{\bar{c}.(1-\bar{c})}$$

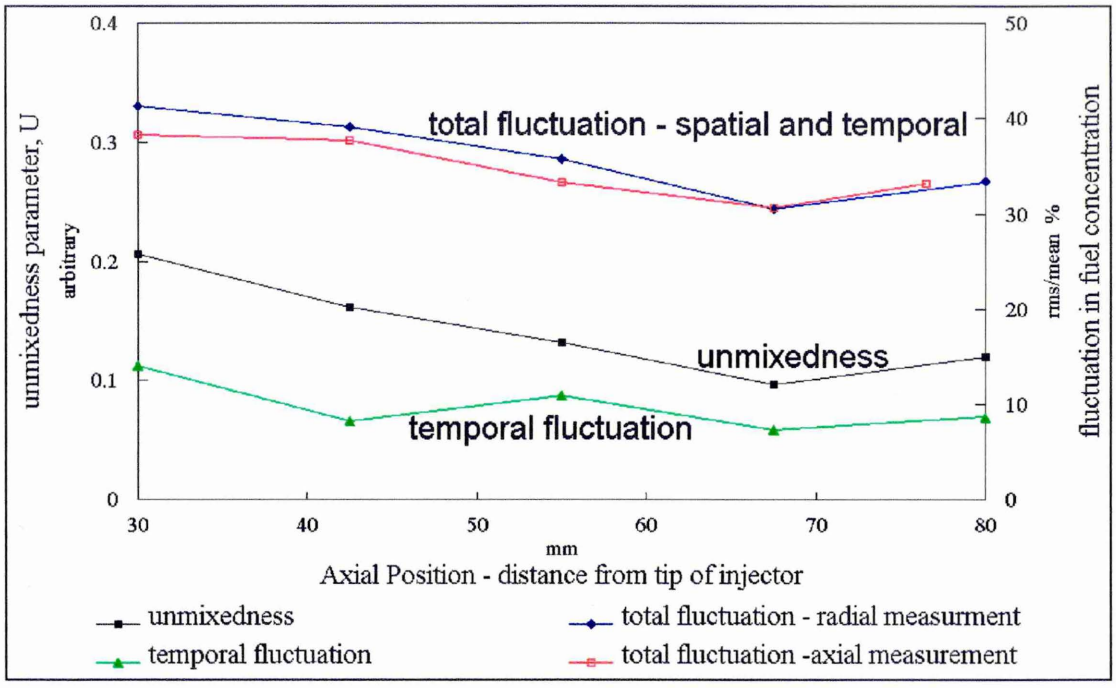

Figure 8.12 Unmixedness Parameter, U and Spatially Averaged Values of Normalised Fluctuation (rms) in Kerosene Fuel Concentration.

where c'^2 is the variance in fuel concentration and $\bar{c}$ is the time averaged mean. This parameter was calculated for each of the sectional kerosene LIF images and averaged across the whole image. The value unmixedness declines along the length of the duct indicating that the fuel-air mixture is becoming more uniform.

8.6 Naphthalene LIF Measurements

A further set of LIF images using mineral spirits seeded with naphthalene for a fuel were collected in the same configurations as with the kerosene LIF. Naphthalene boils at 218 °C and is therefore representative of a typical middle boiling fraction of kerosene. Naphthalene was seeded at a concentration of 2.8 - 4.0 % by mass in mineral spirits. During the LIF measurement the premixer suffered periodical premature ignition when using naphthalene as a seed. This occurred more frequently when using a higher seed concentration. This could either be flashback or autoignition. An enhanced flame speed of seeded mineral spirits and air mixture relative to kerosene could increase flashback tendency. The autoignition delay time may equally have been reduced by altering

preignition chemistry by the addition of naphthalene. The effect of the addition of aromatics is normally to extend autoignition delay time. The preignition occurred approximately once every two minutes and did not affect the ability to take measurements. It is highly unlikely that any of the LIF images were recorded during such a preignition event. None of the images recorded show any fuel distribution noticeably different from the normal.

8.6.1 Axial Sections

The axial naphthalene LIF measurements comprise of mean and rms images calculated from 40 instantaneous images. The mean and instantaneous LIF images are scaled to an absolute AFR and are shown below in figure 8.13.

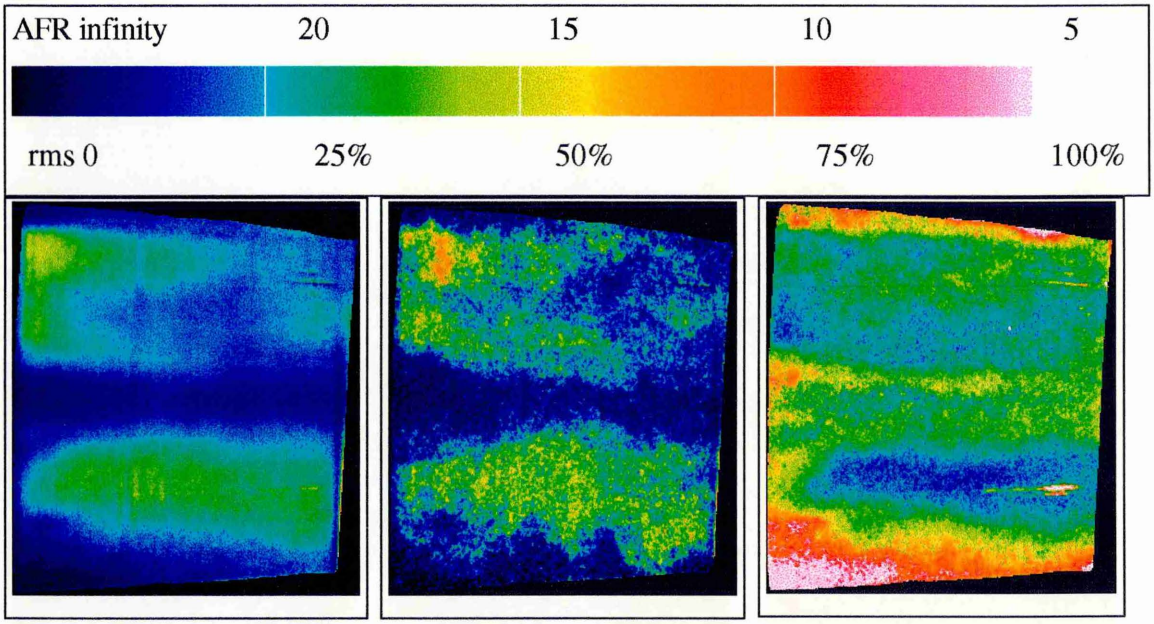

Figure 8.13 Mean, Instantaneous and Normalised rms Axial LIF Images of Mineral Spirits Seeded with Naphthalene as Fuel in the Premixing Duct Scaled in AFR and %.

8.6.2 Radial Sections

Radial section LIF images of naphthalene seeded fuel were taken at three sections along the length of the premixing duct. These were at 30, 55 and 80 mm from the tip of the injector. The radial mean image was averaged from 50 instantaneous images. The mean and instantaneous images are AFR scaled and are shown in figure 8.14.

Figure 8.14 Mean and Instantaneous Radial LIF Images of Mineral Spirits Seeded with Naphthalene as Fuel at 30, 50, and 80 mm along the Premixing Duct.

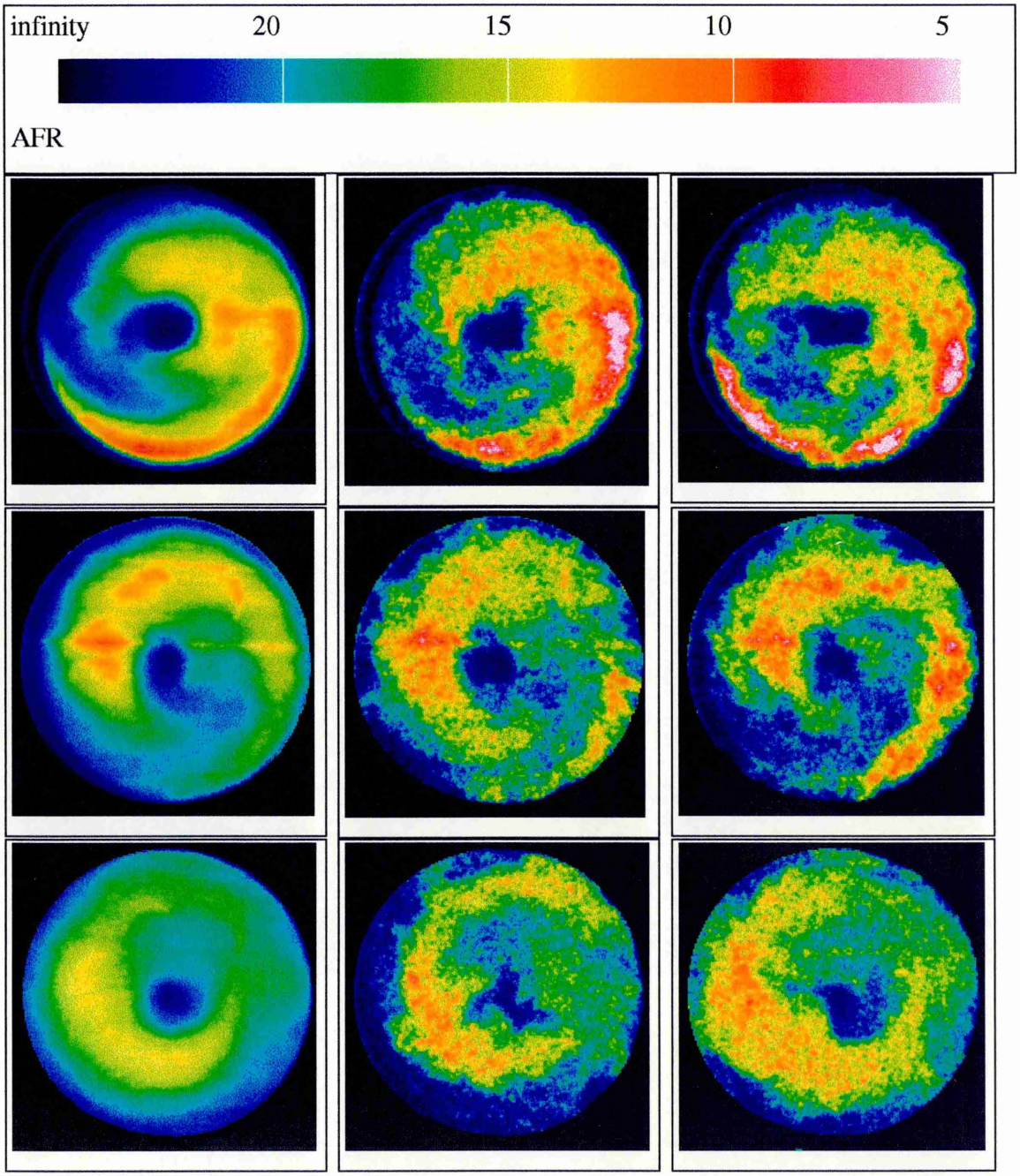

The mixture can be observed to become better mixed along the premixing duct's length from the mean image profiles of naphthalene LIF. These were taken from the mean radial images and shown below in figure 8.15. The profiles become increasingly flat for measurements further along the length of the premixer.

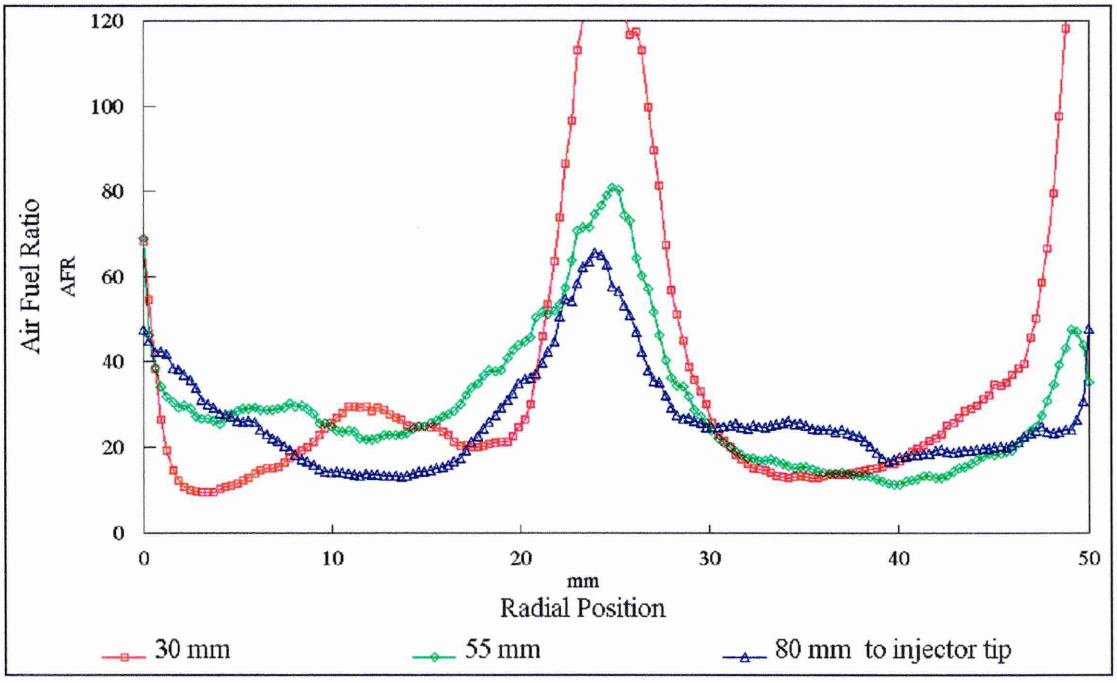

Figure 8.15 Profiles of Naphthalene LIF from Mean, Radial Images Scaled in AFR.

8.7 Fluoranthene LIF Measurements

The final set of fuel vapour LIF was made using fluoranthene seeded into mineral spirits as the fuel. Fluoranthene boils at 384 °C and is therefore representative of the highest boiling fractions present in kerosene. The axial measurements show a different placement of fuel from the naphthalene LIF images caused by the slower vaporisation in the duct and the consequent longer droplet trajectory. No preignition in the premixer occurred during the fluoranthene LIF measurements.

Mean, instantaneous and normalised rms axial section images of fluoranthene LIF were calculated from 50 instantaneous images. These are shown in figure 8.16. The scale for all the fluoranthene LIF images is equivalent to half the AFR shown in the naphthalene

data set for comparison but is not useful as an indication of AFR since the boiling fraction measured is not representative of most of the fuel.

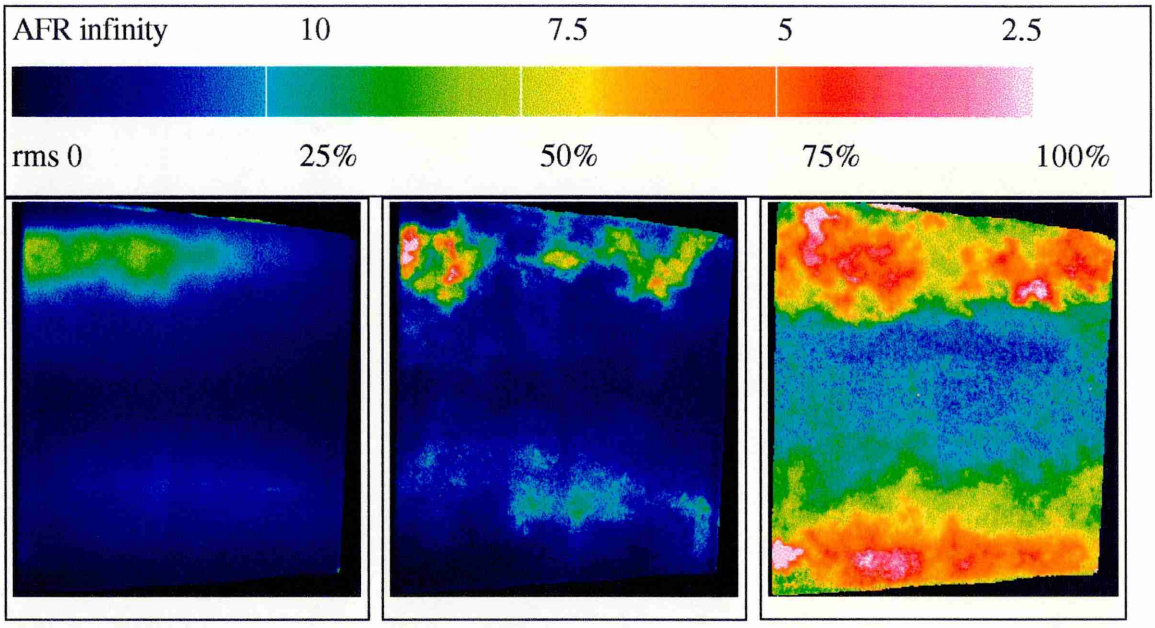

Figure 8.16 Mean, Instantaneous and Normalised rms Axial LIF Images of Mineral Spirits Seeded with Fluoranthene as Fuel in the Premixing Duct.

Radial sections of fluoranthene LIF were made at three locations down the length of the premixing duct similarly to the naphthalene LIF measurements. The mean values were calculated from a set of 50 images. Figure 8.17 shows mean and instantaneous images of fluoranthene LIF 30, 55 and 80 mm from the tip of the injector on the same scale as in figure 8.16. The mean image of fluoranthene fluorescence contains visible laser structure. This could either be caused by saturation of the seed fluorescence excitation or saturation of the flatfielding image due to non-linearities in the camera. The mean image is shown has not been flatfielded since it better represents the fuel concentration. The flatfielded image is shown in the Appendix II.

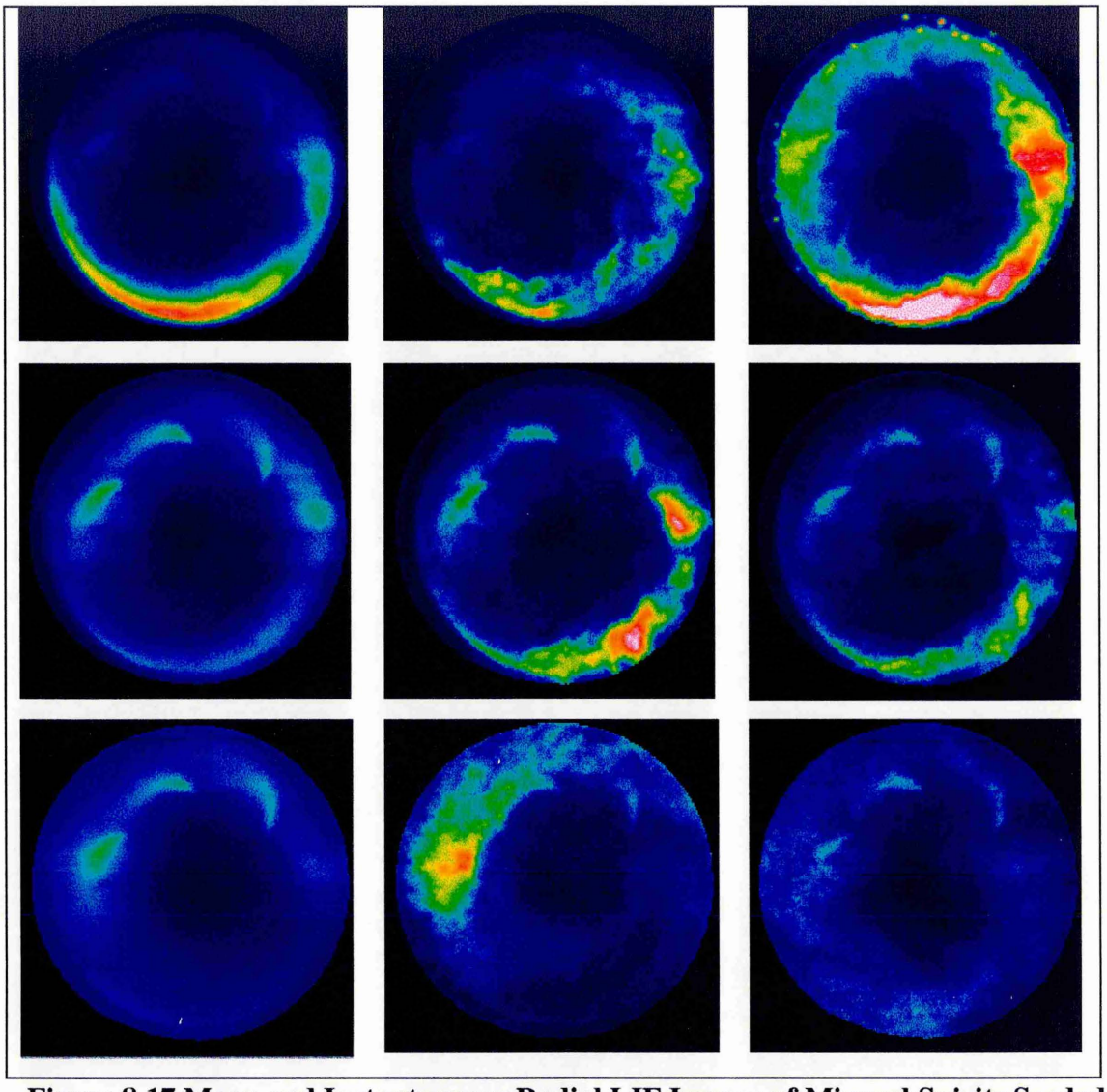

Figure 8.17 Mean and Instantaneous Radial LIF Images of Mineral Spirits Seeded with Fluoranthene as Fuel at 3 Axial Locations in the Premixing Duct.

8.8 Discussion of Results

The fuel vapour concentration field has been characterised using LIF measurements in the premixing duct. The fuel is distributed in a thick annulus in the premixing duct with a small diameter fuel lean core. The lean core becomes smaller along the duct as turbulent and diffusive mixing processes homogenise the mixture. The fuel-air mixture can be observed to become better mixed as it progresses along the length of the premixer. The fuel-air mixture finally diverges into a wider radius annulus as it leaves the premixing duct to enter the toriodal, primary zone recirculation.

The fuel distribution is asymmetric at the start of the duct. As the mixture moves down the duct, the swirl velocities can rotate fuel rich zones in and out of the laser sheet measurement plane. The high boiling point fraction rich regions are rotated and conserved down the length by the solid body rotating gases despite high turbulence levels. This is not the case for the lower boiling point fraction since this fraction is better mixed.

The fuel distribution in the premixing duct varies considerably from one measured image to the next. This indicates that the fuel is distributed with high levels of fluctuations in concentration. The measured fluctuating fuel concentration rms declines typically from 40 to 30% of the mean from the start of the duct to the end of the duct taken from both axial and radial section kerosene LIF images. Since the fuel air mixture can easily be seen to become better mixed along the length of the duct and the values of the spatially averaged fluctuating fuel concentration are reduced slowly along the premixing duct's length it is evident that a component of the fuel concentration fluctuation is temporal. The relative contribution on total fluctuation has been estimated to be 27 % temporal and 73 % spatial. The total fluctuation in fuel concentration becomes slightly more temporal at the duct exit presumably partly due to higher turbulence levels caused by the influence of the primary zone. The fluoranthene LIF images representing the high boiling fraction of fuel show highly fluctuating fuel concentrations levels from 100 to 50% of the mean along the duct length in the fuel richest regions. These levels are likely to be higher since high boiling fractions are lower in concentration and therefore inevitably have a lower probability of being present at a particular location.

The degree of fuel-air mixing in the premixing duct has been quantified using calculations of the unmixedness parameter. This parameter declines along the length of the duct from 0.207 to 0.097 indicating that the mixture is becoming more uniform as the mixture progresses down the premixing duct.

The middle boiling fractions of kerosene represented in the naphthalene LIF images are likely to be well mixed prior to combustion. These images show a uniform fuel

distribution across the whole diameter of the duct. The mixture is already quite uniform on entry to the duct and becomes noticeably more uniform by the duct exit.

The regions of high levels of variance in fuel concentration are indicative of rapid mixing zones. However, care must be taken when interpreting these images since the variance is also high where the fuel concentration is very low. Figure 8.10 shows an inner ring of higher fuel concentration rms where the mean level is also high suggesting fast mixing. This region corresponds to a region of high fluid velocity rms measured with LDA shown in figure 6.5.

The highest boiling fractions of kerosene represented in the fluoranthene LIF images show much poorer mixing on entry to the duct. The mixing is noticeably slower and the fuel concentration gradients are much higher. The middle boiling fractions can confidently be said to mix much quicker than the high boiling fractions. The effect of swirl on the mixing processes is to rotate the rich regions from the injection points as the mixture travels down the premixer. The fuel appears to be located in a spiral down the length of the duct. The rich zones in the naphthalene LIF images appear to rotate by 3/4 of one rotation per diameter. This is in agreement with the measured swirl number of 0.74.

The fuel placement in the premixing duct is noticeably different between the high boiling fractions and the middle boiling fractions. The middle boiling fractions are distributed evenly across the duct diameter. The high boiling fractions are located in regions of very high concentration close to the outer diameter of the duct. The high boiling fractions appear to survive a longer droplet trajectory and impinge upon the outer prefilming lip. The fluoranthene LIF images show more asymmetry than the naphthalene LIF images. The individual injection points are clearly resolved in the fluoranthene LIF images and are conserved along the length of the premixer. The effect on fuel placement of boiling point fraction is partly exaggerated by the use of fluoranthene as a marker. The volumetric proportion of such a high boiling point fraction in kerosene is small.

The addition of naphthalene into the fuel caused periodic ignitions in the premixer. This could be caused by naphthalene enhanced flashback or autoignition in the premixing duct.

The AFR measurements with gas analysis and the axial profile of fluorescent flux do not convincingly confirm the accuracy of the LIF technique. However, there are likely reasons for these discrepancies. The absolute accuracy of the LIF measurements is likely to be good since the measurements show excellent repeatability. Also the measured rms component of fuel concentration is very similar averaged across all radial profiles from the axial section images, compared to the rms averaged across a radial section image at the same location. This indicates that the technique is consistently measuring the same quantity.

The kerosene LIF image sections in figure 8.7 show a fuel leaner core compared to the naphthalene LIF. This is intuitive with kerosene LIF being weighted to heavier, higher boiling point fractions. Higher boiling point fractions of fuel are placed further outboard relative to lower boiling point fractions as demonstrated by the fluoranthene LIF.

9. LPP COMBUSTION

Combustion stabilises in the primary zone of the LPP combustor in the recirculation formed as the mixture is dumped into the flame tube. This region has been studied using LIF and thermocouple measurements. The first section of the LPP combustor flame tube is constructed from fused silica to allow optical access for studying primary zone combustion. This section of the combustor is film cooled to ensure the survival of the fused silica section and the remaining section comprises a double skin of water cooled stainless steel. Measurements of temperature and on unburnt fuel concentration have been made in the primary zone using thermocouple measurements and kerosene LIF respectively. The kerosene LIF images have been processed to yield images of reaction progress variable indicating the thickness and location of the turbulent flame brush and qualitative pdf's of parent fuel fraction through the flame front.

9.1 Temperature Measurements

The temperature in the primary zone was measured using a traversing thermocouple. The thermocouple was insulated with a ceramic sheath to eliminate the necessity of making corrections for radiation loss from the thermocouple bead. The mean temperature measured was found for a traverse through the primary zone at the head of the combustor. This is shown in figure 9.1.

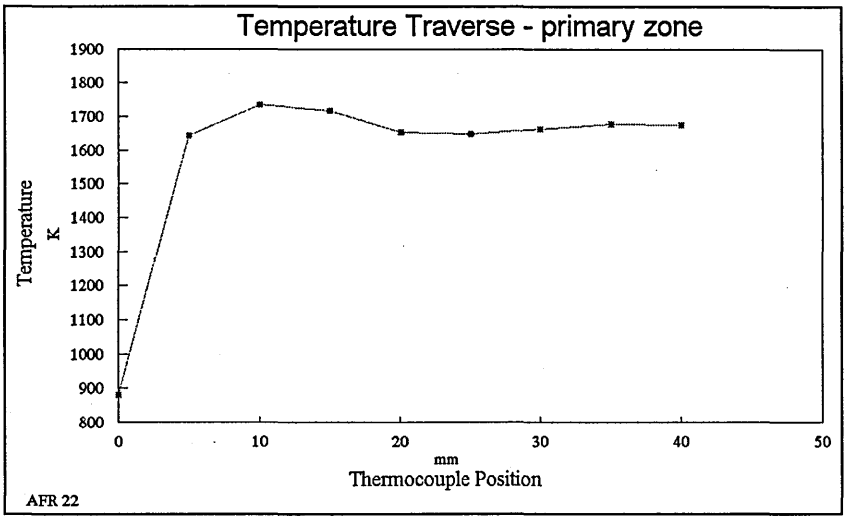

Figure 9.1 Temperature Traverse through the Primary Zone.

The absolute values of temperature measured in the primary zone are lower than the calculated adiabatic flame temperature. The combustion at the point of measurement is incomplete due to the inadequate residence time at this location. This could reduce the adiabatic flame temperature by 3-4 K assuming a typical post primary zone concentration of 1000 ppm CO and 100 ppm UHC (C_3H_8). The primary zone is heavily quenched by cold film cooling air and the combustor water cooling. The dilution effect of the film cooling will bring the flame temperature down by 80 K. The latent heat of vaporisation of the fuel will cool the inlet temperature by approximately 60 K. However, this amounts to a total of 145 K below the adiabatic flame temperature. The remaining discrepancy between the calculated and measured is still temperature 255 K. This is presumably due to further incomplete combustion, heat losses from the flame through the fused silica duct and to the water cooled flame tube walls. The underestimation of CO and UHC at the exit of the primary zone by gas analysis could cause a significant reduction in primary zone flame temperature. (see page 51).

9.2 Primary Zone LIF Measurements

Planer LIF measurements of fluorescence from the aromatics naturally present in kerosene were made using the same experimental set-up described in detail in chapter 8. An excimer laser sheet was introduced radially into the primary zone. An intensified CCD camera collected the fluorescence perpendicular to the laser sheet with a Nikon f/2.8 105 mm macro lens viewing radially into the combustor. The LIF measurement images had the background contribution removed and were flatfielded to normalise out variations in laser sheet intensity. The final processed images have not been calibrated to an absolute scale and the intensity at each pixel can only be said to be approximately proportional to the kerosene vapour concentration. The fluorescing species in kerosene will vary from batch to batch as the aromatic content changes. The boiling fraction of these fluorescing species and their fluorescence behaviour relative to oxygen concentration and temperature are unquantified. This means fuel concentration measurements using kerosene LIF are only qualitative. However, the kerosene LIF measurements detailed in Chapter 8 compare favourably with the quantitative

naphthalene measurements. For these measurements, it is assumed that the effects of the boiling fraction of the kerosene's fluorescing species and their oxygen quenching and temperature dependent behaviour result in fluorescence which is approximately proportional to kerosene vapour concentration. The LIF images show the unburnt vapour fuel that surrounds the combustion recirculation.

9.2.1 Kerosene LIF

Mean and instantaneous planar LIF images of kerosene fluorescence were made with combustion at the operating condition detailed in section 5.6.1. A mean image calculated from 100 instantaneous images is shown in figure 9.2 and sample instantaneous images are shown in figure 9.3.

The unburnt, intact fuel or parent fuel fraction (PFF) can be seen to begin to become entrained upstream by the recirculation. by the time the mixture has turned fully upstream into the recirculation the pff has presumably been broken up into smaller fuel fragments and is partially burnt. Some unevaporated droplets are visible entering the flame tube.

The laser sheet was introduced from the bottom of the image to the top. The asymmetry in the fuel concentration is therefore undoubtedly real.

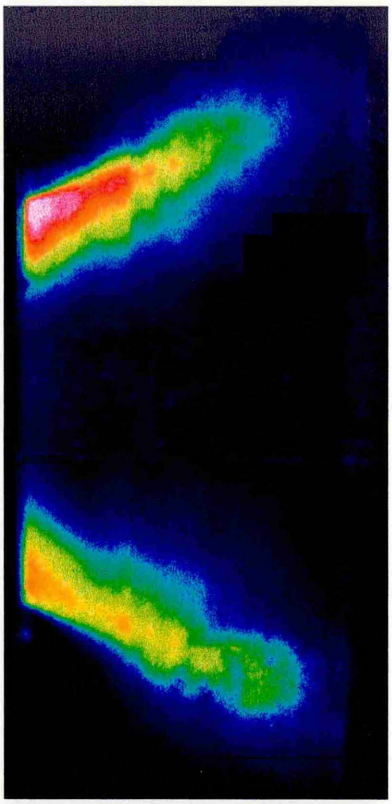

Figure 9.2 Mean LIF Image and Instantaneous LIF Images of Unburnt Fuel in the Combustor Primary Zone.

Scale : arbitrary units

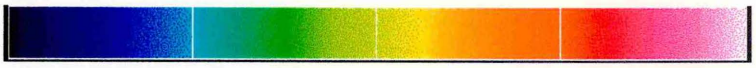

0 25 50 75 100

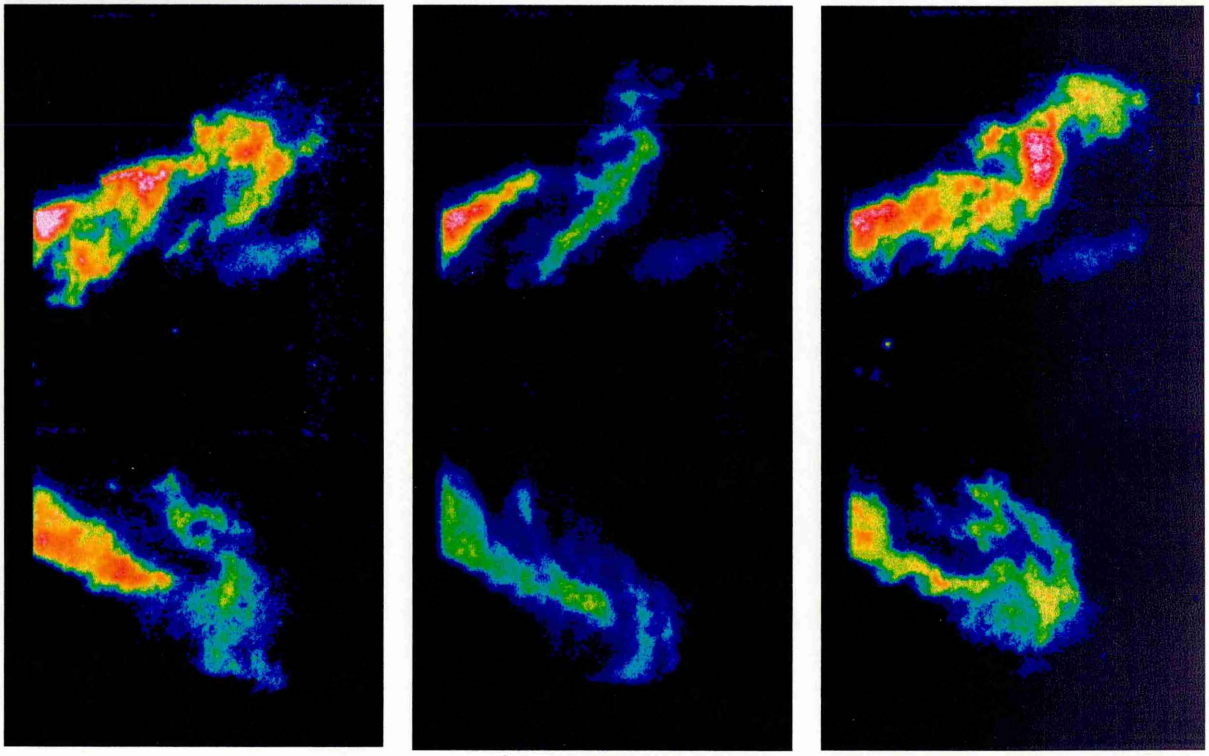

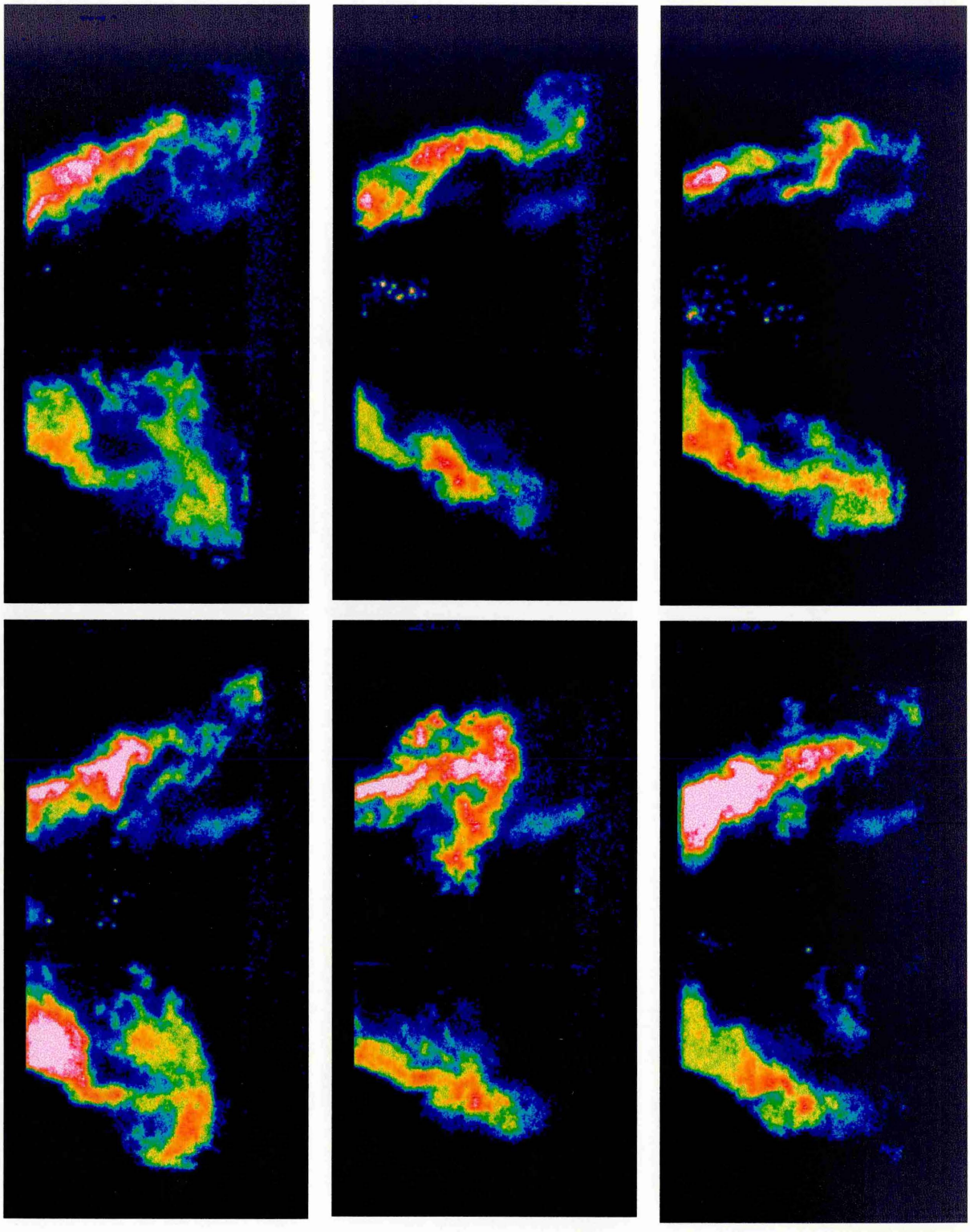

By assuming that the presence of fuel indicates a reaction progress variable of zero and the absence of fuel indicates a reaction progress variable of one, the data set may be

used to accurately calculate the spatial distribution of flame front location. Each instantaneous image was binarised and then summed to provide the final image representing reaction progress variable spatial distribution. A section of this image perpendicular and across the flame front is shown below in figure 9.3.

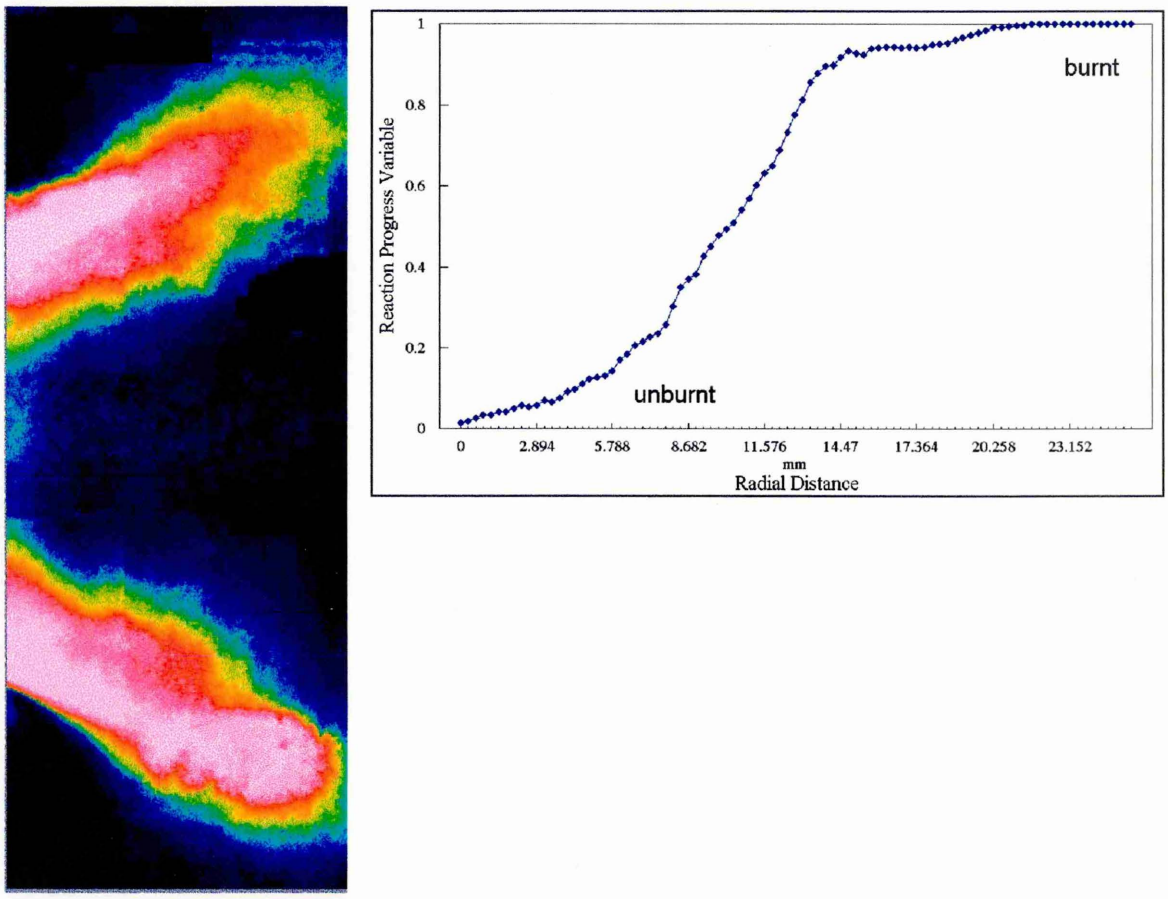

Figure 9.3 Image Representing Combustion Reaction Progress Variable and Radial Section across the Flame Front (from Region of Pure Unburnt Mixture to no Parent Fuel Fraction).

The radial thickness of the flame brush in the combustor is measured as 22 mm. This is an accurate measurement despite the lack of quantifiability of the fuel concentration in the LIF images since the images are binarised.

9.2.2 Probability Density Functions of Parent Fuel Fraction

Probability density functions (pdf's) of parent fuel fraction measured by kerosene LIF have been made at several points through the flame front. These measurements are subject to the same uncertainties in fuel concentration mentioned earlier. The pdf's were constructed from a bin of 20 X 20 pixels in 100 images. Each bin represents an area 5.8 mm square. The location of the pdf's are from the unburnt fuel region moving axially downstream to the burnt region. The pdf profiles show the probability of a particular fuel concentration at each location.

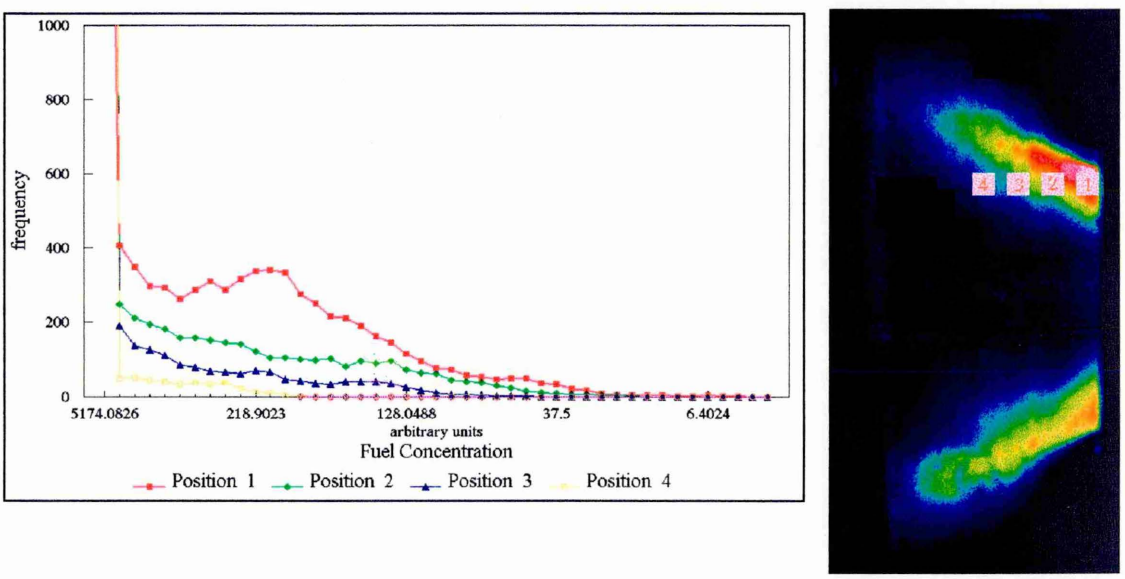

Figure 9.4 PDF Profiles of Fuel Concentration through the Flame Front.

9.3 Conclusions

The temperature and fuel concentration in the LPP combustor primary zone has been measured with thermocouples and qualitative planar LIF. The primary zone temperature profile shows a peak temperature of 1735 K. The mean temperature differs from the adiabatic flame temperature by 400 K. 145 K of this can be accounted for by airstream cooling due to the latent heat of the fuel, the dilution effect of the film cooling and the incompleteness of combustion of 100 ppm UHC and 1000 ppm CO.

The remaining difference is presumably due to further incomplete combustion, heat losses to the water cooled flame tube and surroundings.

The mean kerosene LIF measurements show the location of the unburnt fuel surrounding the primary zone recirculation. The instantaneous LIF images indicate a large shot to shot variation in fuel concentration and location around the turbulent primary zone recirculation. The degree of survival of the pff can be observed.

The reaction progress variable distribution in space has been quantified by binarising fuel LIF images. These show that the flame front brush thickness is 22 mm.

Probability density functions of fuel concentration at several locations through the flame front have been constructed from 40,000 measurements in areas 5.8 mm square. These show the trend of fuel concentration pdf's as fuel is consumed in the flame.

10. CFD MODELLING COMPARISONS

10.1 Introduction

The LPP combustor has been modelled using the 'FLUENT 3D' CFD code in order to provide further understanding of the entire combustor velocity field. The CFD results presented in this chapter were created by F. Monmont (1999) and have been interpreted by the author. The combustor velocity field has been modelled in two dimensions, under the same conditions as for the measurements but neglecting liquid fuel injection and primary zone combustion. The CFD solution provides a useful insight into the velocity field outside the regions where it is difficult to measure. The distribution of turbulence within the premixer and combustor show the likely areas of rapid turbulent mixing.

10.2 CFD Model Boundary Conditions

The CFD model solution was solved on a grid encompassing the premixer and the first section of primary zone. The inlet boundaries are located at the exit of the premixer swirlers. The relative mass flow splits between each of the swirlers was estimated from calculations of pressure drop across each air inlet and is shown in Table 10.1. The CFD solutions were very sensitive to the proportion of air shared between the two outer swirlers. The final boundary condition at the exit of the flame tube or dump combustor was provisionally set as a uniform static pressure. The modelled results are likely to differ from the measured data mainly due to the effect of the added volume of the vaporised fuel, the cooling effect of heating and vaporising the fuel and due to the heat release from the primary zone combustion.

Air Inlet	Axial Velocity	Swirl Velocity	Mass Flow
Radial inlet	16 m/s	9.23 m/s	2.13×10^{-3} Kg/s
58° swirler	25 m/s	41 m/s	3.834×10^{-3} Kg/s
68° swirler	25 m/s	63.41 m/s	4.233×10^{-2} Kg/s
Injector Hole	80 m/s	0 m/s	7.986×10^{-3} Kg/s

Table 10.1 Boundary Conditions for CFD Model

10.3 CFD Model Results

10.3.1 The Velocity Field

The resultant velocity vector calculated from all three components of the LPP combustor velocities modelled are displayed in the combustor in figure 10.1. The radial component of velocity is close to zero at all points in the combustor except in the region of the recirculation. All the main features of the flow field in the combustor are present in the CFD results. The flow accelerates into and along the premixing duct until it encounters the recirculation caused by vortex breakdown as the swirling fluid diverges into the primary zone. The highest velocities are shown where the reactants squeeze past the recirculation and into the combustor flame tube.

There are several discrepancies between the modelled results and the measured results. Firstly, the recirculation is small due to the absence of combustion and the consequent lack of volumetric expansion. This allows the modelled recirculation to penetrate much further into the premixing duct. There is a wake behind the final prefilmer caused by the dimensions of the CFD grid which would not appear behind the actual sharp tipped prefilmer. The core velocity is lower than the peak velocity only on the modelled data. The velocity measurements made with and without combustion show the maximum velocities along the core of the premixer.

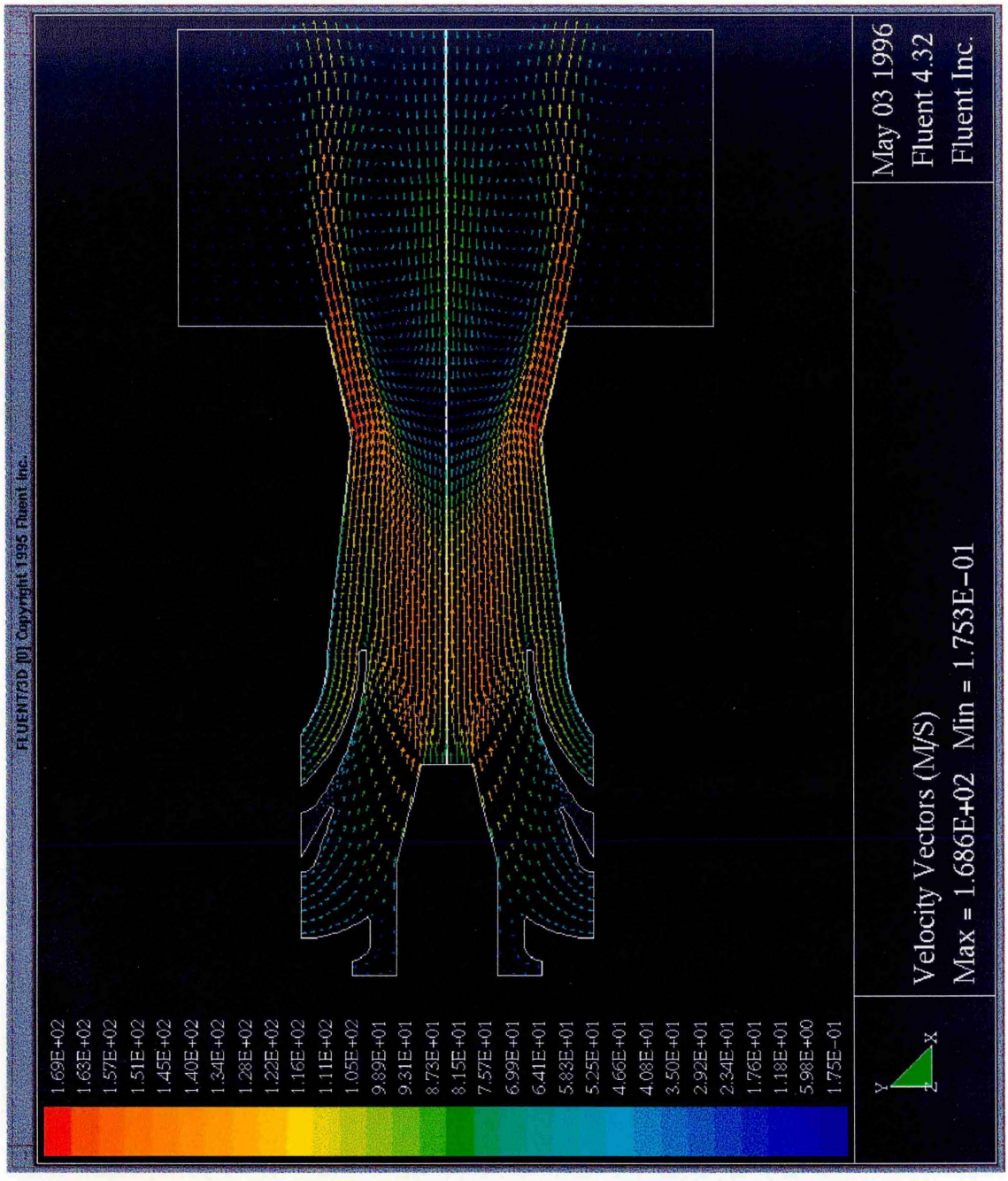

Figure 10.1 CFD Modelled Velocity Vectors in the LPP Combustor.

A comparison between the measured and modelled velocity profiles at the neck of the duct and 42 mm upstream of the neck are shown in figures 10.2 and 10.3. The measured profiles are for the non-combusting condition. Both the axial and swirl velocity profiles differ greatly between the modelled data and measured data at the neck of the duct. This is largely caused by the inaccurate size and location of the recirculation in the CFD modelled results.

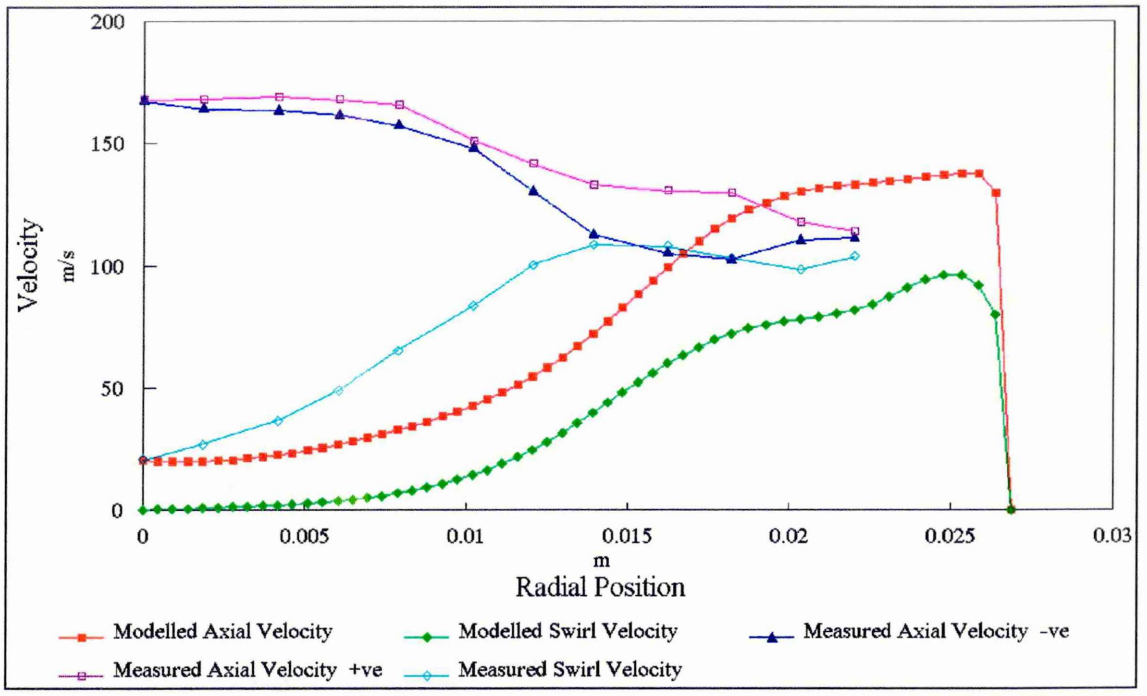

Figure 10.2 Comparison Between Modelled and Measured Velocity Profiles at the Neck of the Duct. (-ve and +ve refer to radii above and below the centreline)

The profiles of velocity measured and modelled 42 mm further upstream in the duct compare much more favourably. The axial velocity profiles show very similar trends. The absolute value of velocity is higher for the measured velocity values. The modelled data shows a high velocity region right up to a thin boundary layer which was not measured with LDA. The swirl velocity profiles also compare very favourably except in the region of asymmetry in the measured data.

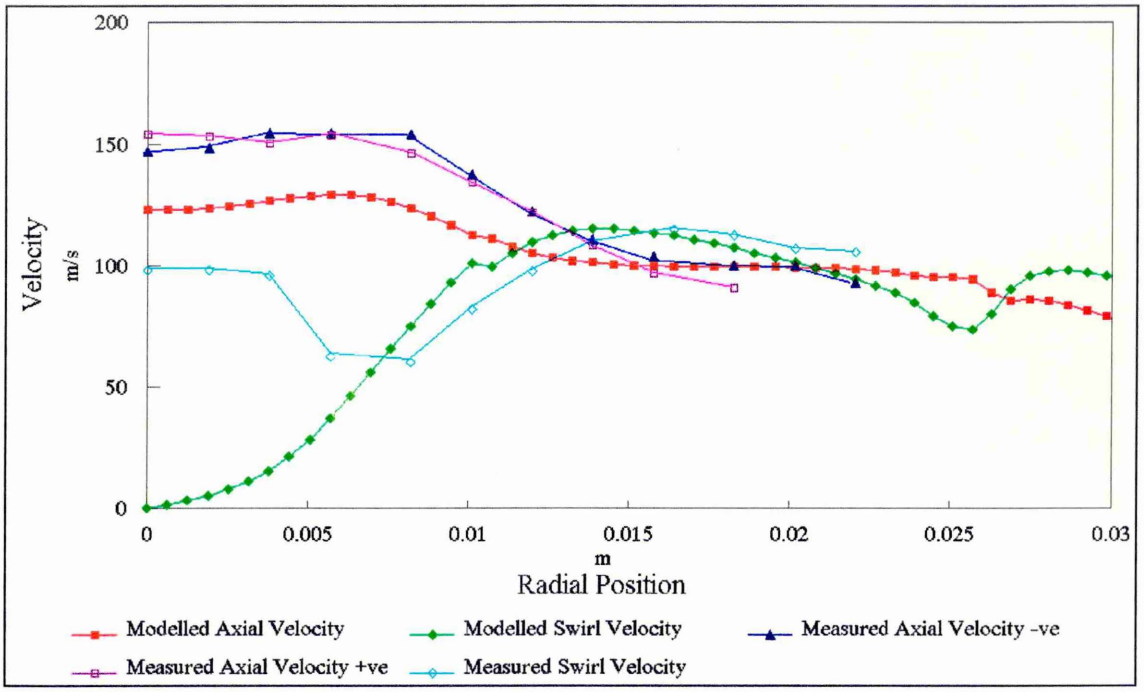

Figure 10.3 Comparison Between Modelled and Measured Velocity Profiles 42 mm Upstream of the Neck of the Duct.

10.3.2 The Turbulence Field

The CFD modelled solution also provides information on the distribution of turbulent kinetic energy. This is related to the fluctuating rms. component of velocity measured with LDA in chapter 6 by the following expression.

$$\tilde{U} = \sqrt{\frac{2}{3}.k}$$

For fluctuating velocity, $\tilde{U}$ and turbulent kinetic energy, k (Scheistel 1991). The modelled turbulent kinetic energy distribution is shown in figure 10.4.

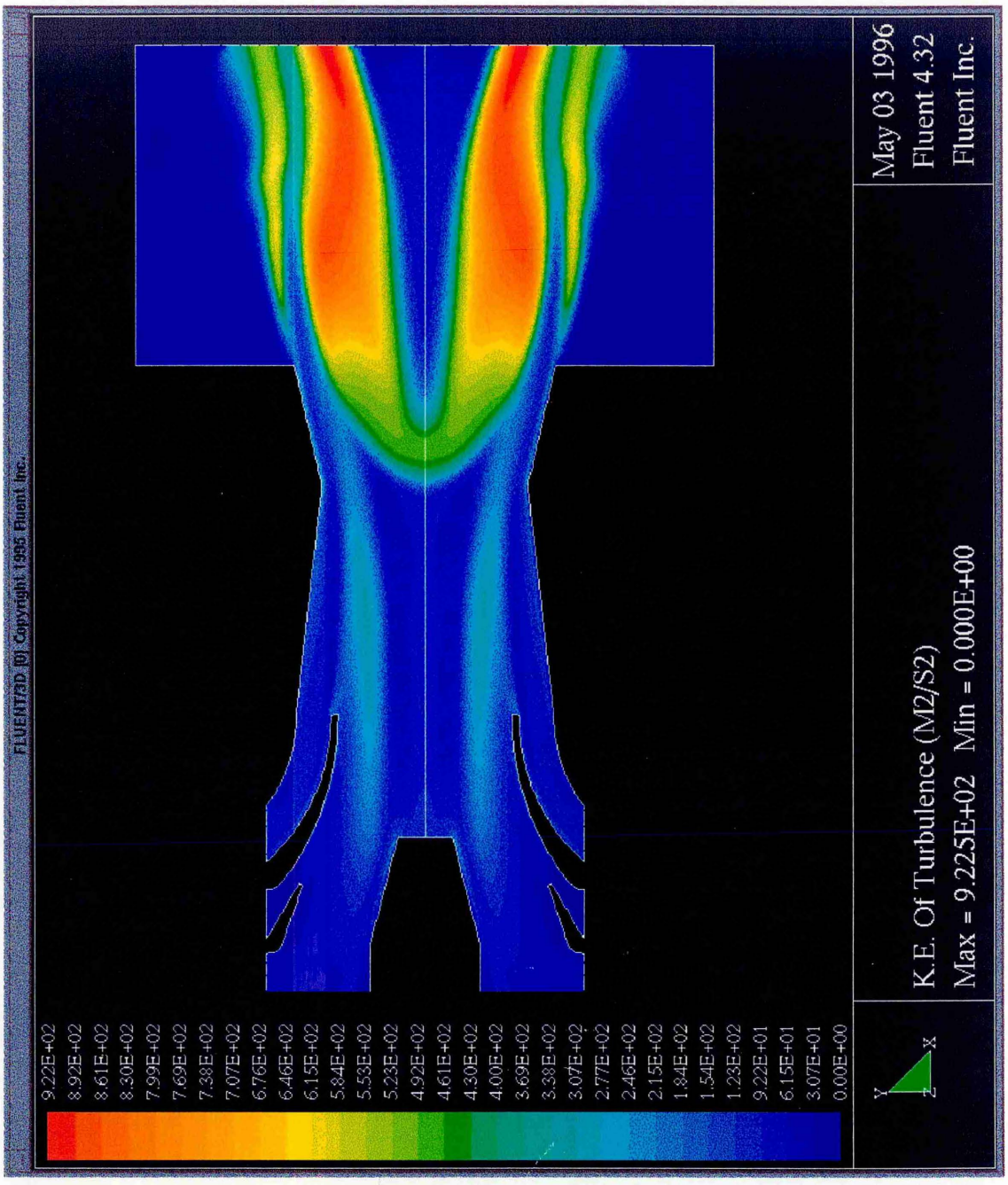

Figure 10.4 CFD Modelled Turbulent Kinetic Energy in the LPP Combustor.

The highest regions of turbulent energy are naturally in the recirculation zone where shear between the air motions is high. This is likely to be replicated in the real case but since the modelled recirculation zone size and location are unrealistic, the modelled turbulence distribution in this region is inaccurate. The modelled distribution of turbulent energy in the premixing duct compares quite favourably with the measured

rms values shown in figure 6.5, chapter 6 in terms of magnitude and location. There is a region of elevated turbulence in a thick annulus located away from both the premixer core and wall. This extends from the injector tip right up to the recirculation and will be conducive to rapid fuel-air mixing. The turbulence intensity in this region is approximately 11 %. This compares a measured value in the same region of 16 % (+/- 2%.

10.4 Discussion of Results

The LPP combustor velocity field has been modelled in two dimensions using a CFD code. The solution to the model provides useful information on the flow field in the regions where it is impossible to make non-intrusive measurements. The modelled results show all the important features present in the measured data set, ignoring fuel injection and primary zone combustion. For this reason, the modelled data has only been compared with velocity measurements made non-combusting.

The modelled velocity vectors in the premixer show the gases are constantly accelerating down the duct until the flow reaches the recirculation. The modelled axial velocity remains high right up to the wall where there is a thin boundary layer. The highest velocities are at the neck of the duct where the flow squeezes past the recirculation.

The CFD model results predict the onset of vortex breakdown and the consequent formation of a recirculation to be too early in the premixer. This could be a feature of the inlet mass flow split boundary conditions employed, since the core velocities are slightly lower than the measured profiles. The model results were very sensitive to the mass flow splits incorporated.

Comparisons of axial velocity profiles made upstream at the start of the transparent section of the premixing duct are favourable. The axial velocity profiles are similar in

shape but differ in magnitude. The measured and modelled swirl velocity profiles are also similar except for the measured asymmetry at the start of the duct.

The regions of high turbulent energy modelled on the CFD code are located in a thick annulus away from the premixer core and wall. This is also the case in the measured results. The CFD model has predicted a turbulence intensity of 11 % in this area compared to 16 % measured with LDA.

A CFD modelled solution has not yet been made incorporating combustion in the primary zone. Since the measured data shows a noticeable difference between the combusting and non-combusting cases, a modelled combusting solution would provide more realistic results.

11. CONCLUSIONS

An experimental rig has been designed and commissioned to operate a full scale, realistic lean, premixed, prevaporised (LPP) combustor. The combustor clearly operates in the lean, premixed mode emitting 1-1.7 EINOx at 200-400 ppm CO. The combustor has wide optical access to the premixer, primary zone and up the exhaust. A series of measurements have been completed on the combustor to attempt to identify the processes fundamental to LPP combustion which govern its performance and to further current understanding of LPP combustion. The measurements completed characterise the velocity field, the distribution of size, velocity and concentration of droplets and the fuel vapour concentration in the premixer. Measurements on unburnt fuel in the primary zone provide indications of flame brush thickness, flame location and qualitative fuel concentration. The flame temperature is also measured. These measurements can be interpreted to learn much about the mixing and combustion processes in the LPP combustor and provide a comprehensive data set for CFD model validation. A number of conclusions relevant to LPP combustion have been drawn and are summarised in the sections below.

Measurements have also been made on a counterflow triple flame and compared with one dimensional modelled data. The investigation demonstrates that triple flames will stabilise in regions of partially premixed reactants. A number of deficiencies are evident if the model is to adequately simulate this complex flame structure. The model requires a higher grid density, improved chemistry and a better model for the physical flow field. Parallel work on the triple flame stability limits confirms evidence that diffusion flames suffer strain extinction prior to premixed flames. This will have a favourable effect in LPP combustors by extinguishing some of the non-premixed combustion.

The velocity field in the premixer has been characterised with and without primary zone combustion by using LDA and PDA techniques. The velocity field consists of a solid body rotation of gases with a peak axial velocity of 150 m/s and swirl velocity of 105 m/s. The swirl number defined as the ratio of swirling momentum to axial momentum is approximately

constant along the length of the premixer at 0.74. The range of residence times in the premixer section vary from 0.51 to 0.77 ms. The axial velocity accelerates along the converging duct and then decelerates at the end due to the duct divergence and blockage caused by the primary zone recirculation. The premixer velocity field is different with combustion to that without combustion due to the effect of the increased blockage caused by the enlarged primary zone with combustion. The turbulence intensity levels in the premixing duct are typically 10 to 20% but periodically increase to 60% due to instabilities in the flame tube. This suggests that primary zone oscillations are capable of feeding back into the combustor premixer where they could effect the preparation of the fuel-air mixture.

The liquid fuel droplets in the combustor premixing duct were studied using PDA and planar LIF. The droplets follow the flow of the gaseous field, subject to a slip velocity dependent on droplet size. The droplet slip velocities are up to 50 m/s for 60 micron droplets and correlate well with diameter. The mean droplet velocities are in the range 100 to 150 m/s. The swirl velocity components of the droplets are also conserved along the length of the duct. The fluctuating component of velocity is between 12 and 20 m/s. This compares with 20 to 30 m/s for air without combustion. The velocity of sub 5 micron droplets are slower than the gas velocity by up to 5 m/s at the end of the premixing duct. This suggests that small droplets do not reach the full carrier gas velocity in high speed, high temperature, turbulent flows. There is much evidence suggesting that only a very small fraction of fuel survives unevaporated into the transparent section of the premixing duct.

Droplets were measurable at all points in the duct with the first batch of kerosene fuel but were more scarce towards the end of the duct. Subsequent PDA measurements with mineral spirits (kerosene without aromatics) and a new batch of kerosene showed virtually no droplets in the duct. This is probably because only very high boiling point fractions in the fuel survive unevaporated to the end of the premixing duct and no high boiling fractions were present in these particular batches of fuel. This theory is backed up since the available droplet diameters measurement data remained constant between 25 and 32 micron SMD along the length of the duct. LIF images of liquid fuel in the duct show a tendency for the droplets to stay on the axis. This is away from the bulk of the fuel vapour suggesting that any of the remaining evaporation

of liquid droplets only constitutes a negligibly small proportion of the total mass of fuel. The vapour LIF measurements also show no increase in fuel vapour flux along the length of the duct. The droplet distribution measured by liquid phase LIF varies largely from shot to shot and the droplets can reach all parts of the duct. This is consistent with the design principle of achieving the desired fuel distribution whilst in the liquid phase, since once the fuel is vaporised, it is much more difficult to disperse the fuel.

The mean droplet diameter correlates well with overall AFR even though the mean diameter changes by only 1.5 microns. The velocity distributions broaden predictably as the mean velocity increases, consistent with a understanding of polydisperse distribution of droplets in a flow.

The vapour phase fuel concentration in the premixing duct was initially measured using planar LIF on kerosene's natural aromatics. These were followed by PLIF measurements tracking seeded markers in a non-fluorescing fuel (mineral spirits). Measurements of fuel vapour were made tracking two representative boiling points in the fuel. By seeding with naphthalene the fraction of fuel of boiling point 218 ^{o}C could be studied. High boiling point fractions of fuel were measured using fluoranthene as a marker which boils at 384 ^{o}C. The seeded PLIF images show the fraction of fuel relating only to these precise boiling points.

The LIF images show that the fuel is located in the premixer in a thick annulus with a small diameter lean core which becomes smaller as turbulent mixing and diffusion homogenise the mixture. The fuel air mixture becomes measurably better mixed as it progresses down the duct. This is shown clearly on the mean and instantaneous LIF images and by the calculated unmixedness parameter. The mixture finally diverges into the primary zone where it is swept around the toroidal primary zone recirculation.

The fuel air mixture is asymmetric at the start of the duct. The LIF images show discrete rich fuel jets representative of high boiling point fractions of fuel in the mixture that can be observed to rotate with the swirling air, conserving their structure along the length of the duct at the same swirl angle as measured with LDA. The injection points can still be clearly observed in images

of high boiling point fuel fraction at the end of the duct. The middle boiling fractions in the fuel are much better mixed at the start of the duct and become even better mixed at the end of the duct.

The images representing the middle boiling fraction show that the rate of mixing is fast and the fuel is well distributed in the duct. This contrasts with the images representing high boiling fractions where the fuel is concentrated in a thin annulus. This is caused by the longer droplet lifetime (and trajectory) of higher boiling point fractions. As the droplets are spun outwards they evaporate leaving the light fractions in the core of the duct. Consequently, only the highest boiling point fractions will be present in the outer radii of the duct. The rate of mixing of the high boiling fractions is noticeably slower than the middle boiling fractions. The middle boiling fractions of kerosene are likely to be well mixed prior to combustion. The high boiling fractions however are poorly mixed on exit from the duct and show high gradients in concentration. This will have an effect on primary zone combustion since different fractions of fuel will be separately distributed and mixed at different rates. This effect is slightly exaggerated by the choice of a very high boiling point fuel marker. The differential fuel placement of fuel fraction dependant on boiling point and differential fuel mixing rate dependant on boiling point will have an important impact on the combustion of multi component fuels in all applications. For instance, the effect of additives to fuels in piston engines and gas turbines may be impaired by its selective placement in the combustion zone and possible inadequate mixing. Different fractions of fuel will experience different conditions such as temperatures, turbulence levels, quenching rates and residence times.

The fuel distribution in the duct fluctuates from one measurement image to the next. The fluctuation in kerosene concentration declines from 40 to 30% of the mean from the start to the end of the duct. The fluctuating component of fuel concentration has been estimated to be 27% temporal and 73% spatial. The temporal component of fluctuation increases at the end of the duct partly due to the effect of the primary zone. The sparser distributed high boiling fractions of fuel show a higher fluctuation in concentration.

The regions of high fuel concentration variance in the premixing duct indicate where the fuel air mixing will be fastest. This area corresponds to the measured regions of high fluctuating velocity components and agrees with the modelled velocity rms location.

LIF images of fluorescence from kerosene vapour were collected in the primary zone of the combustor. The instantaneous images show a large variation in unburnt fuel location in the flame tube. However, the apex of the cone shaped visible flame is stable in space when observed with the naked eye. The mean unburnt fuel location surrounds the first part of the primary zone recirculation. The spatial distribution of reaction progress variable has been accurately found and indicates the flame brush thickness to be 22 mm. Probability density functions of fuel concentration at several locations through the flame front have been constructed from qualitative images of kerosene concentration.

The temperature in the combustor was measured by traversing a thermocouple through the primary zone. The temperature profile is fairly flat, peaking at 1735 K. This is lower than the predicted adiabatic flame temperature due to incomplete combustion at the point of measurement, dilution from the film cooling and the wide use of water cooling in the combustor.

The choice of measurement techniques used has been shown to provide useful information for all the measurements. LDA and PDA techniques provide accurate quantitative data. The liquid phase fuel can be studied in isolation to provide a useful qualitative indication of liquid fuel spatial distribution in the duct by using LIF on mineral spirits seeded with PPO. This effectively discriminates the liquid phase fluorescence from vapour phase in the premixing duct. Fuel vapour LIF measurements using naphthalene and fluoranthene as seeds are useful for studying specific boiling fractions in a multi-component fuels such as kerosene. These measurements can be post-calibrated to provide absolute measurements of AFR. The accuracy of the absolute AFR measurement has yet to be convincingly proven since the comparative techniques such as gas analysis suffer from errors due to the effects of the probe. The LIF measurements on fuel reveal highly detailed variations in fuel concentration. A large data set is therefore required to smooth out spatial and temporal fluctuations to generate a mean image. LIF provides useful 2D

information on vapour fuel concentration and fuel distribution in practical LPP combustors. The LIF measurement profiles of AFR highlight the errors of taking gas sampling measurements. Gas sampling techniques cannot measure short time scale fluctuations in concentrations.

The effect of interference from soot or high droplet number density in non-premixed systems needs to be evaluated.

The preliminary CFD modelled data agrees well with the measured data excepting its limitations of using a non-combusting model and employing gaseous fuel. The highly turbulent regions in the combustor agree well with the measured data of fuel concentration variance (by LIF) and gas velocity rms component (by LDA).

A data set measuring a wide variety of separate quantities has been comprehensively measured on the LPP gas turbine combustor. This provides a cohesive picture of the operation of the combustor. The measurement of separate quantities agree convincingly. For example, the rapid mixing regions of high turbulence in the premixer measured with LDA on gas as fluctuating velocity, by LIF measurements of high variance in fuel concentration all agree with the zones of high turbulent energy predicted in the CFD modelled data. Similarly, the rotation of the high boiling point fuel jets in and out of the plane of laser sheet measured by LIF is in agreement with the LDA measured swirl angle. This demonstrates that laser diagnostics are now capable of making accurate though not necessarily absolute measurements in realistic devices such as gas turbine combustors. The choice of measurement techniques has been vindicated by the successful production of a comprehensive and cohesive data set. Laser diagnostic measurements have obvious advantages over non-intrusive methods but still require further development to allow their easy, accurate and quantifiable implementation.

APPENDIX I

This appendix contains the specification, instrumentation, light-up and shut down procedure, flow diagrams, calibrations, calculations and drawings of the experimental combustion rig.

A1. Design Specification and Instrumentation

Combustor:	
Mass flow air	0.107 kg/s
Fuel Flow (AFR 22)	4.86 g/s
Power	225 kW
M√T/P	3.21 kg K/s atm
Mass flow film cooling air	0.005 kg/s
Inlet Air Temperature	900 K
Inlet Air Pressure	1 atm (nominal)
Service Rig:	
Turbotron Blower:	
Mass flow range	0.05 - 0.45 kg/s
Pressure range	0.1 - 1 bar
Exit Temperature	328 K
Oxygen Enrichment: mass flow oxygen	5.0 g/s
Preheater: vitiating combustor	
Mass flow propane	2.4 g/s
Overall AFR	45
Primary Zone equivalence ratio	0.62
Power	112 kW
Mean Exit Temperature	900 K

Instrumentation:	
Inlet Air Mass Flow	Inlet Venturi nozzle static pressure with Druck pressure transducer.
Oxygen Mass Flow	Rotameter and pressure gauge.
Propane Mass Flow	Rotameter and pressure gauge.
Kerosene Mass Flow	Turbine meter and digital readout.
Oxygen Sample Flow	Rotameter.
LPP Combustor Inlet Oxygen Concentration.	Servomex Paramagnetic Gas Analyser.
Test Cell Ambient Oxygen Concentration.	Scottish Anglo Ambient Oxygen Meter (electrochemical).
Inlet Air Temperature	Type K thermocouple and bi-metallic strip indicator.
Oxygen Temperature	Type k thermocouple.
Propane Temperature	Type K thermocouple.
Preheater Exit Temperature	Type K thermocouple.

LPP Combustor Inlet Temperature	Type K thermocouple.
Fused Silica Temperatures	Type K thermocouple.
LPP Combustor Temperature	Type R thermocouple.
Propane Regulator Air Pressure	Pressure Gauge.
Kerosene Regulator Air Pressure	Pressure Gauge.
Film Cooling Upstream Pressure	Mercury Manometer.

A2. Light up Procedure

Switch on propane water heater 1 hour before running.
Switch on power to control equipment 1 hour before running to warm up oxygen meter.
Calibrate oxygen meter when warm.
Place barrier across road with laser warning signs if necessary.
Turn on oxygen sample line cooling.
Turn on shop air compressor.
Turn on both water manifold cocks and check drains are functional.
Turn on both propane gas tanks and adjust regulator to 15 psi. on rig gauge.
Turn on and zero Druck pressure transducer.
Check Turbotron throttle valve is open and switch on.
Turn on fan for elbow window purge air and film cooling.
Adjust air throttle for inlet nozzle static pressure of 1.00 kpa. (Druck pressure transducer)
Switch on Igniter 1 for preheater.
Switch on propane.
Adjust propane to 3-15 psi. on propane controlling regulator and to 3.5 psi. on injector pressure gauge.
** If rig does not light in 10 seconds, switch off propane and igniter, purge line and retry.
On ignition, turn off Igniter 1, adjust regulator to stabilise temperature to 627 °C on thermocouple 3, (propane pressure +/- 2 psi.).
Turn on nitrogen supply to dome loader for oxygen control.
Open rig oxygen shut off valve.
Check DC power supply voltage to oxygen control valve is set at 24 V.
Turn on oxygen supply at bottle crate.
Switch on oxygen.
Adjust domeloader pressure controller to achieve 21 % oxygen in rig (oxygen meter).
Turn on nitrogen supply to liquid fuel system and adjust controller to 20 Bar in tank.
Switch on Igniter 2.
Switch on kerosene supply.
Adjust kerosene controlling regulator to achieve 6-7 g/s on fuel flow meter. (see **)
On ignition, switch off Igniter 2 and adjust regulator to achieve 4.86 g/s.

A3. Running Condition Indicator Settings

Air inlet nozzle static pressure - 1.00 Kpa.
LPP combustor inlet temperature (thermocouple 3) - 627 °C (900 K).
Oxygen level - 21 %.
Kerosene - 4.86 g/s. (Equivalent to overall AFR 22).

A4. Shut Down Procedure

Switch off kerosene.
Switch off oxygen.
When oxygen supply gauge reads zero, switch off propane supply.
Purge kerosene.
Purge oxygen.
Purge propane.
Open air control valve to maximum.
Turn off nitrogen supply to oxygen and kerosene systems.
Turn off oxygen rig shut off valve.
When rig temperature reduces to below 100 °C, turn off Turbotron fan.
Turn off fan for elbow window purge air and film cooling.
Turn off shop air compressor.
Close bottle valves on propane and oxygen.
Switch off propane water heater.
Switch off Druck pressure transducer.
Turn off oxygen sample cooler.
Empty oxygen sample cooler water trap and air compressor traps.
Turn off all water cooling except to manifold flange.
Relieve pressure inside kerosene system (to prevent nitrogen diffusing into fuel).
Turn off power to control equipment.
When mounting flanges are cool, turn off manifold flange cooling water.

A5. Thermocouple Temperatures

Type 1 thermocouples:

Thermocouple		Temperature measured
Type K:	1	Not - connected
	2	Preheater outlet
	3	LPP combustor inlet
	4	Loose thermocouple
	5	Loose thermocouple
Type R:		Primary zone temperature

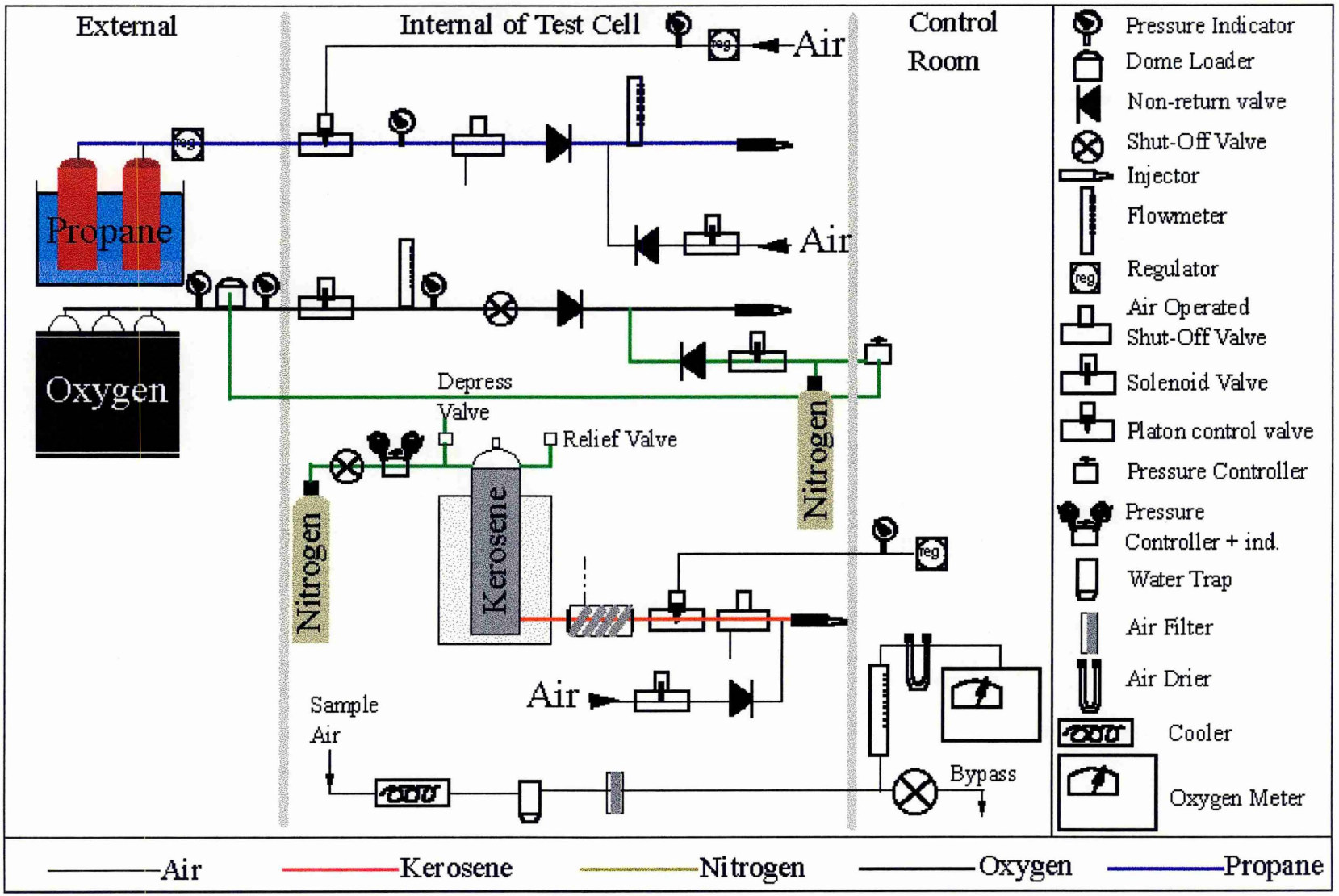
External
Internal of Test Cell
Control Room
Air
Air
Propane
Oxygen
Depress Valve
Relief Valve
Nitrogen
Nitrogen
Kerosene
Air
Sample Air
Bypass
Pressure Indicator
Dome Loader
Non-return valve
Shut-Off Valve
Injector
Flowmeter
Regulator
Air Operated Shut-Off Valve
Solenoid Valve
Platon control valve
Pressure Controller
Pressure Controller + ind.
Water Trap
Air Filter
Air Drier
Cooler
Oxygen Meter
Air
Kerosene
Nitrogen
Oxygen
Propane

A7. Calibrations

Calibration graphs for air mass flow, kerosene mass flow, propane mass flow and pressure drop across the LPP premixer are shown below.

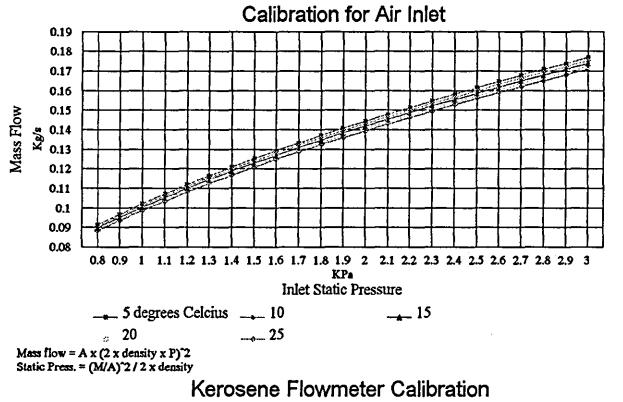

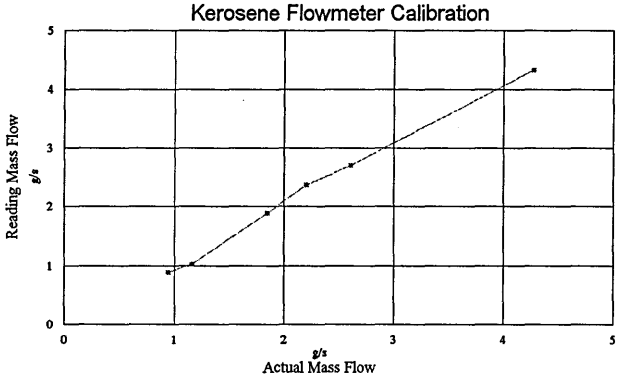

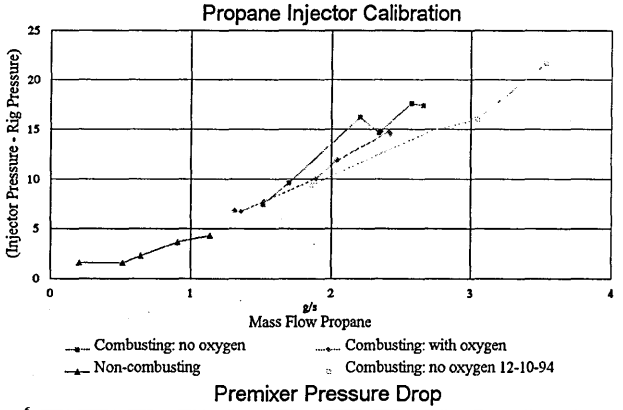

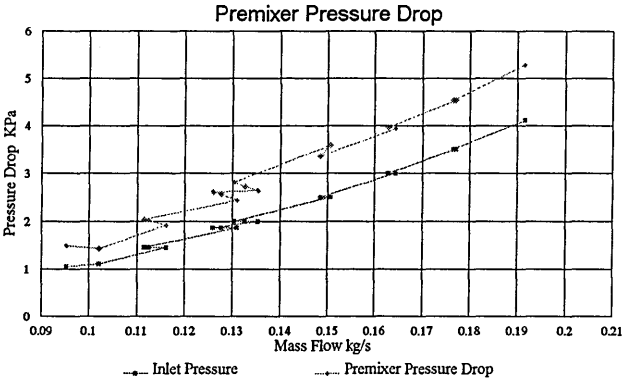

A8. Species Concentrations through Autoignition Modelled on HOMREA (Ch.5.)

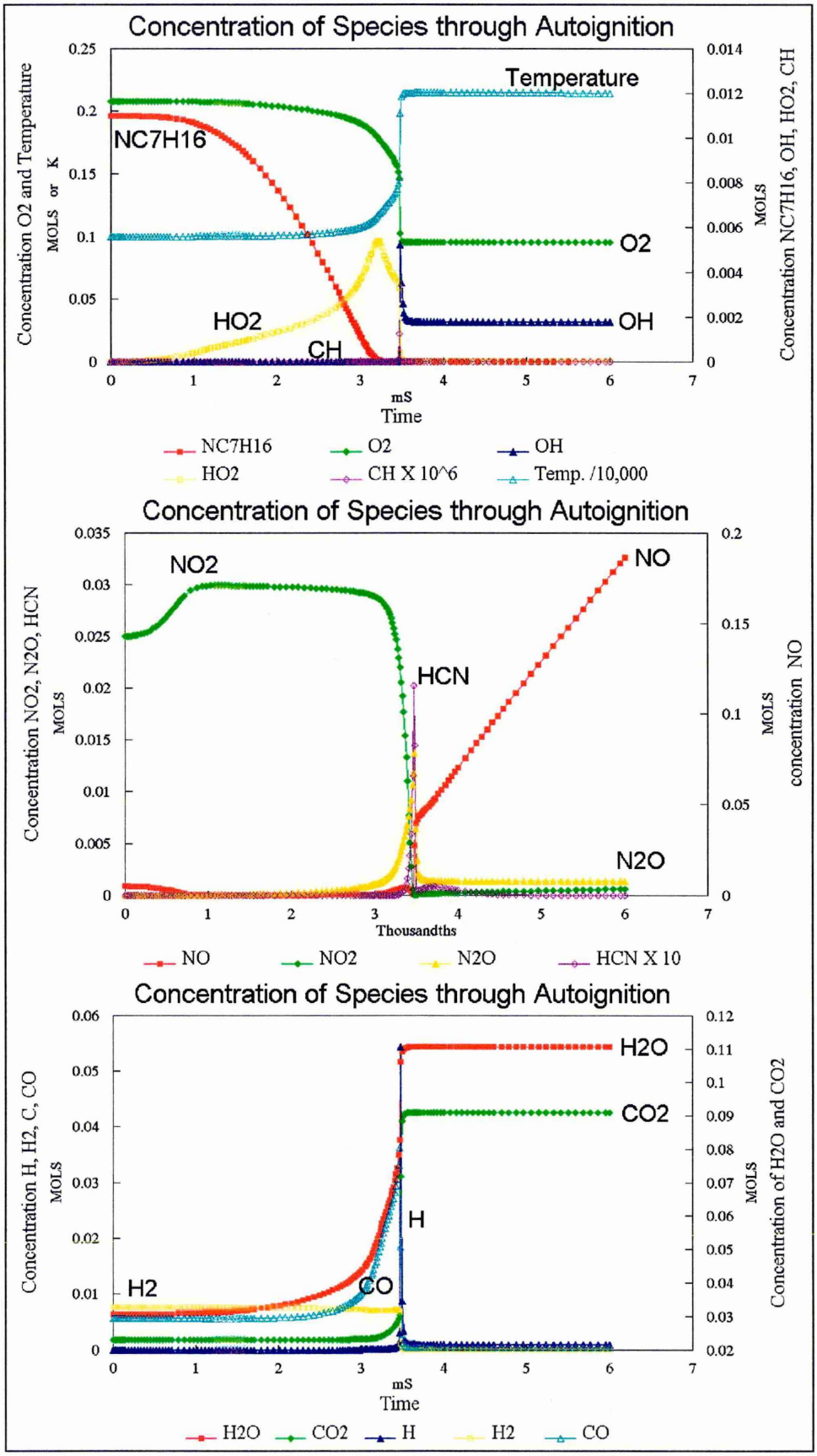

A9. The Pressure Loss Factors and Mass Flow Splits for the Preheating Combustor

The mass flow to each part of the preheating Snecma combustor has been calculated by summing the pressure loss factors across each flow entry. The pressure loss factors were calculated from the following formulae.

$$\text{Total Mass Flow } \alpha \frac{1}{\sqrt{\phi_1}} + \frac{1}{\sqrt{\phi_2}} + \frac{1}{\sqrt{\phi_3}} + \ldots\ldots$$

Where ϕ represents the pressure loss factor across each entry. The pressure loss factor across a curved vane swirler can be found from

$$\text{Pressure Loss Factor} = 1.15 \cdot \left(\frac{A_l}{A_{sw}}\right)^2 \cdot \sec^2(\alpha) - 1$$

Where A_l is the area of the combustor liner, A_{SW} is the swirler and α is the swirl angle. The prefix constant should be changed to 1.3 for straight vane swirlers.

A10. Turbulence Behind a Grid

The turbulence intensity a specific distance downstream of a grid or screen has been correlated to the characteristic dimension of the grid by Baines and Peterson. The turbulence intensity can be read of the following graph for a number of bar widths downstream.

$$\text{Bar widths}, \; b = M - 0.952.D$$

for bar or mesh spacing, M and hole diameter, D. The turbulence intensity in the graph is denoted v_x' and the distance from the grid is x.

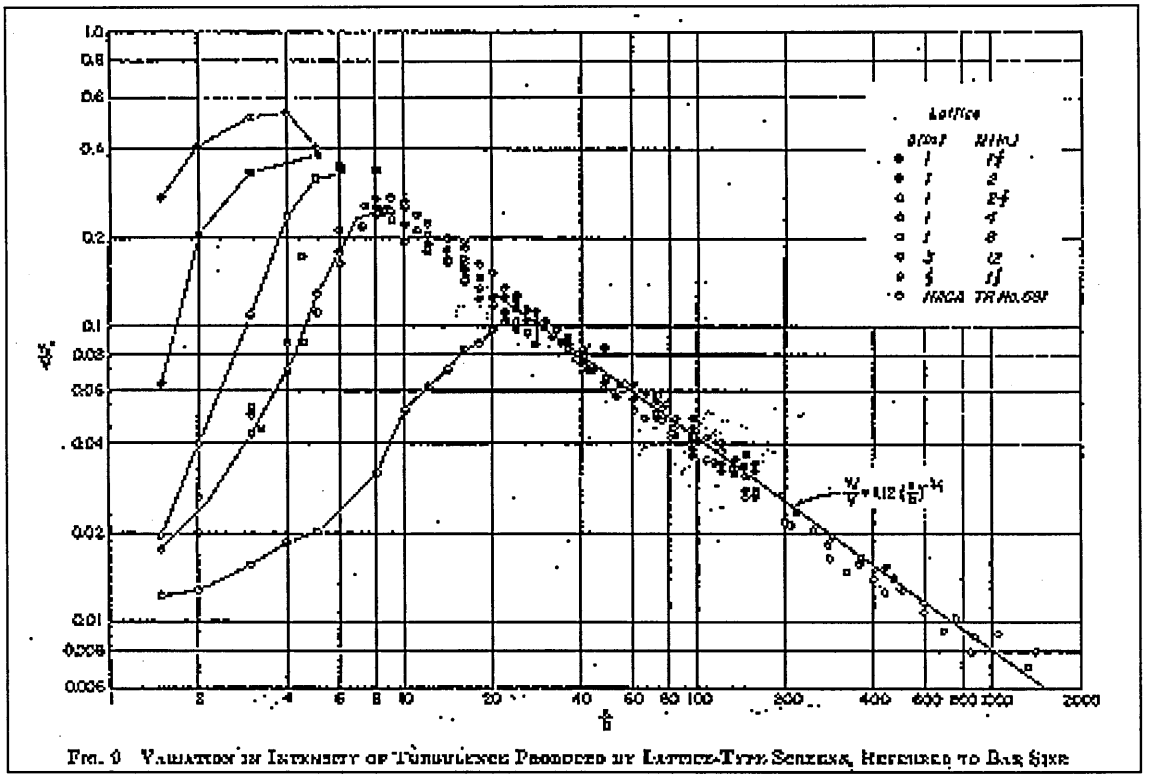

A11. Displacement of Light Paths through the Wall of a Fused Silica Duct

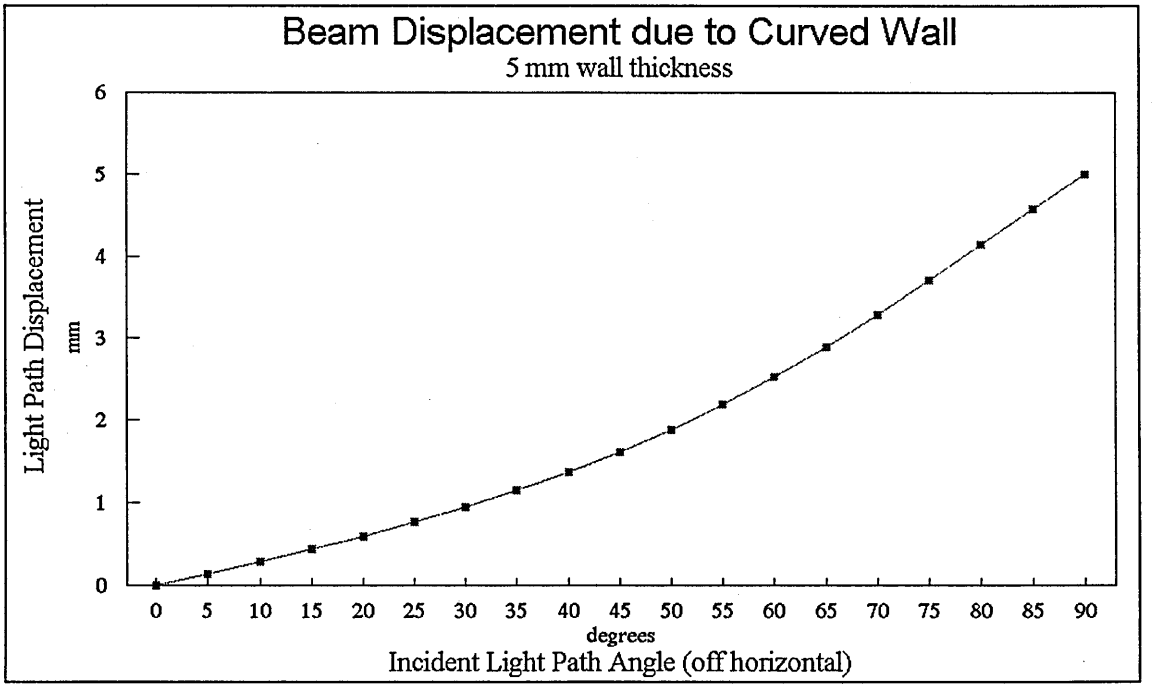

A12. The Adiabatic Flame Temperature of Kerosene-Air Mixtures for AFR 20 to 40

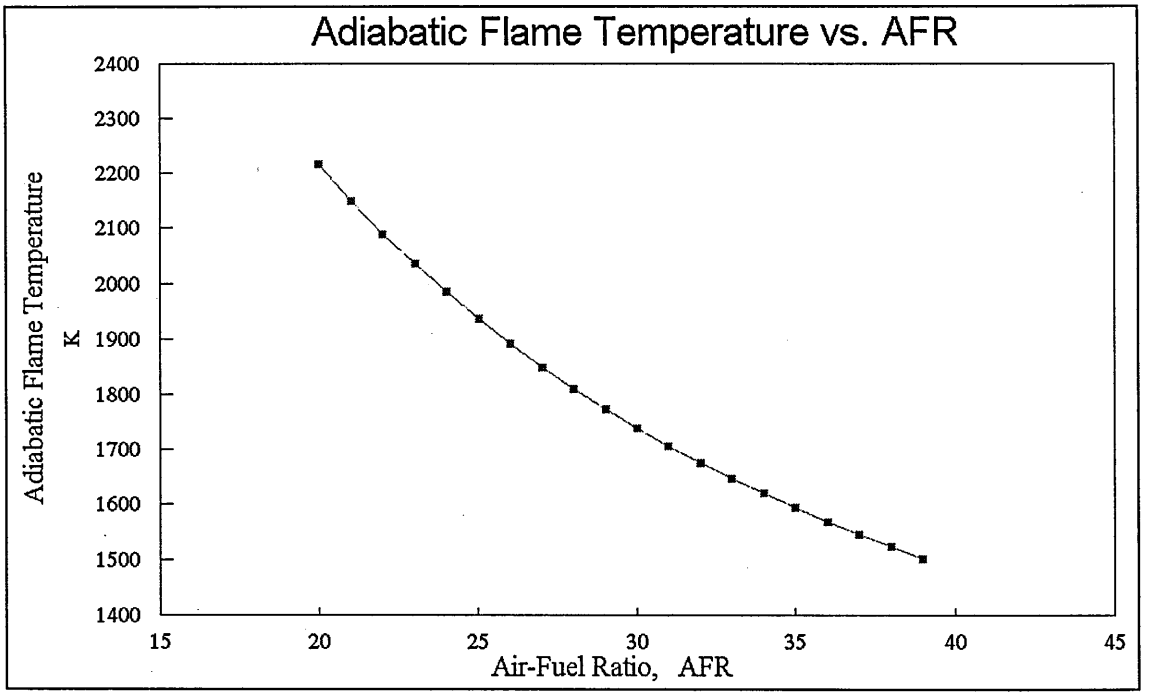

A13. Turbotron Fan Characteristic

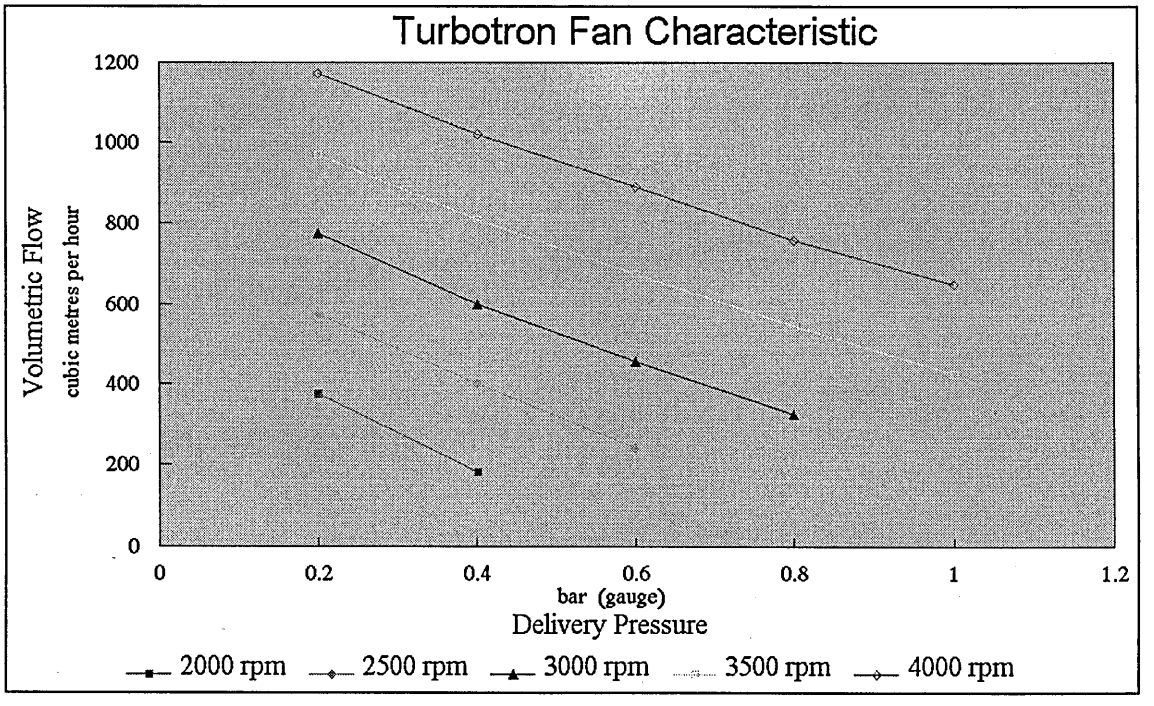

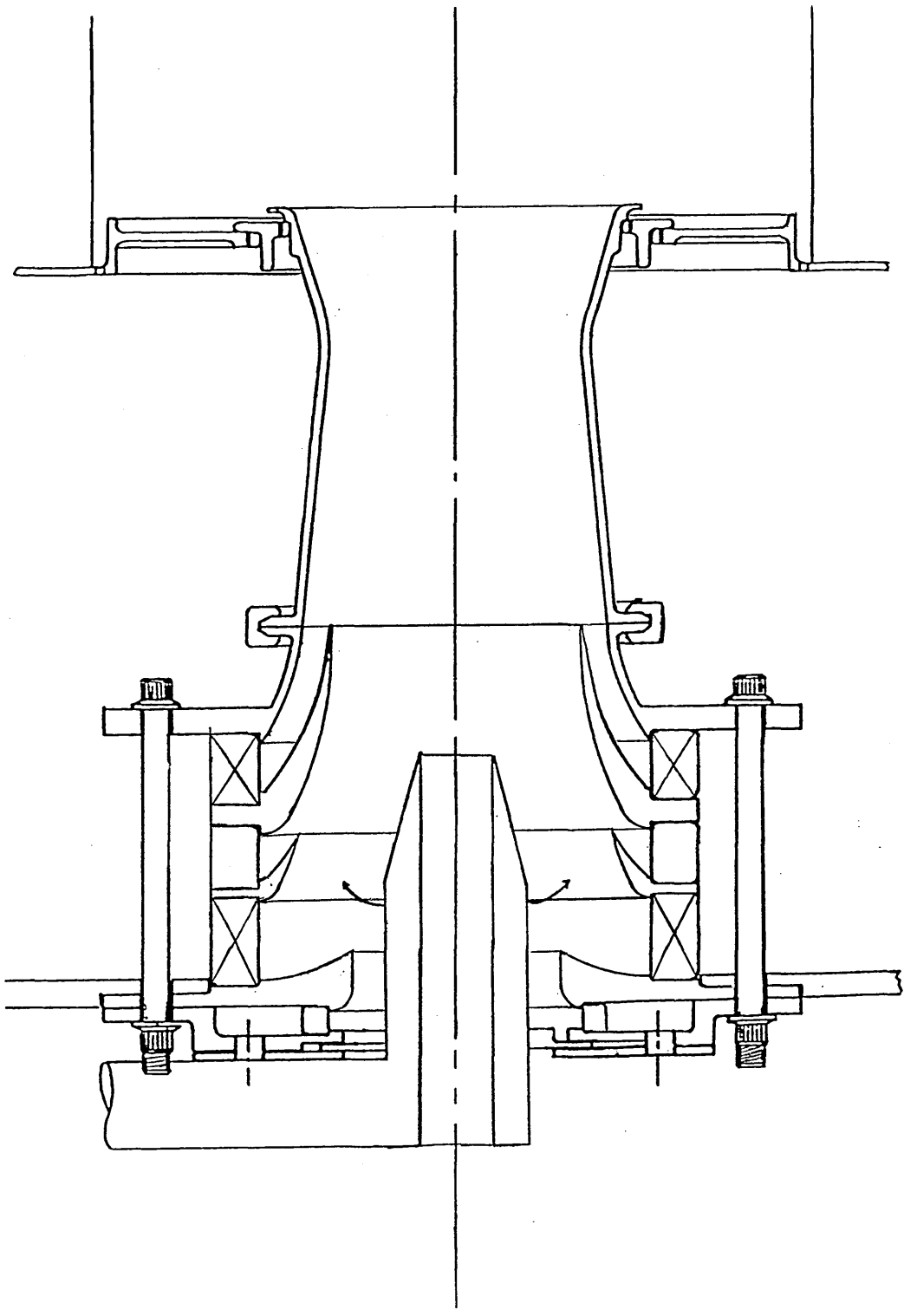

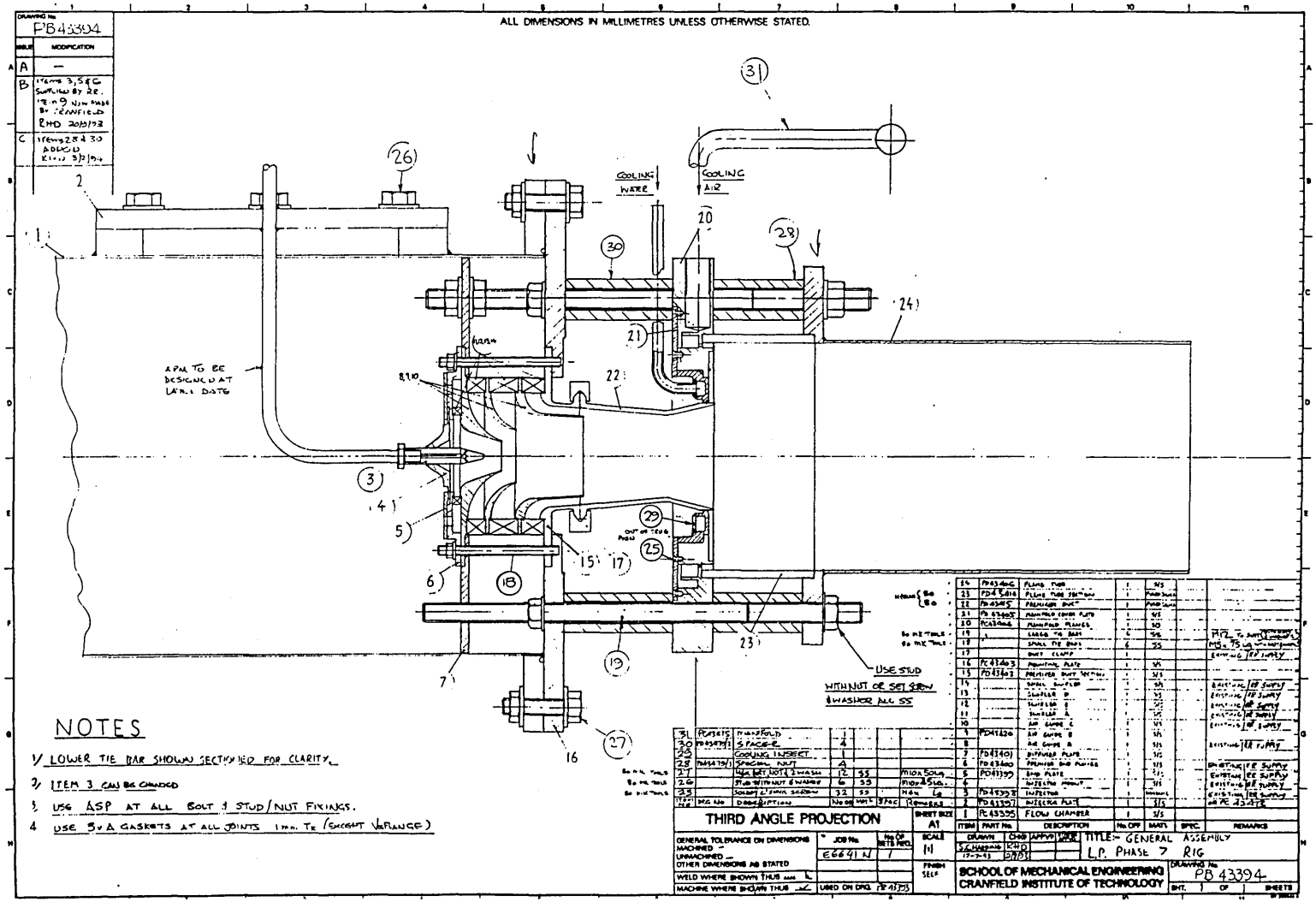
ALL DIMENSIONS IN MILLIMETRES UNLESS OTHERWISE STATED.
PB43394
COOLING WATER
COOLING AIR
RPM TO BE DESIGNED AT LATER DATE
USE STUD WITH NUT OR SET SCREW & WASHER ALL SS
NOTES
1/ LOWER TIE BAR SHOWN SECTIONED FOR CLARITY.
2/ ITEM 3 CAN BE CHANGED
3/ USE ASP AT ALL BOLT & STUD/NUT FIXINGS.
4 USE 5v A GASKETS AT ALL JOINTS 1mm. TK (EXCEPT VANFLANGE)
THIRD ANGLE PROJECTION
SCALE 1:1
SCHOOL OF MECHANICAL ENGINEERING
CRANFIELD INSTITUTE OF TECHNOLOGY
TITLE:- GENERAL ASSEMBLY L.P. PHASE 7 RIG
DRAWING No. PB 43394

DRAWING No. PB43483

ISSUE	MODIFICATION
A	—

ALL DIMENSIONS IN MILLIMETRES UNLESS OTHERWISE STATED

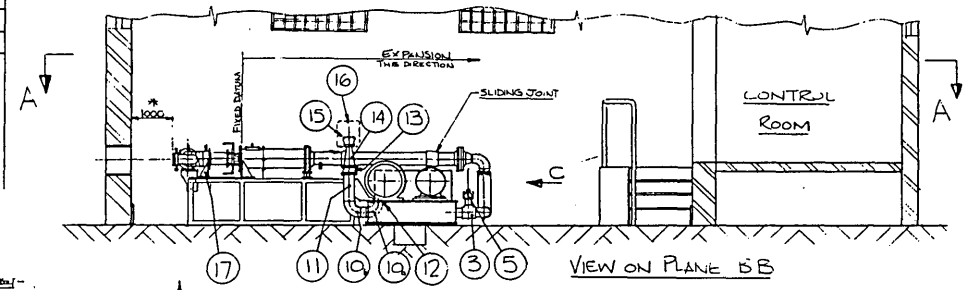

VIEW ON PLANE BB

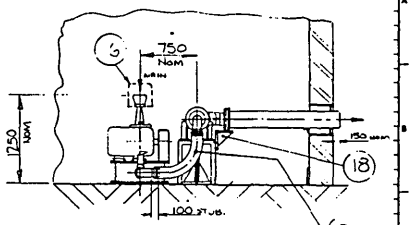

VIEW ON ARROW 'C'

ANGLE STRIP RAILING — TO WALL TO KEEP PIPE ON. (USE 40 x 40 ANGLE) WITH 16 SWG ALUM. DISC (2 HOLES) TO KEEP OUT BIRDS

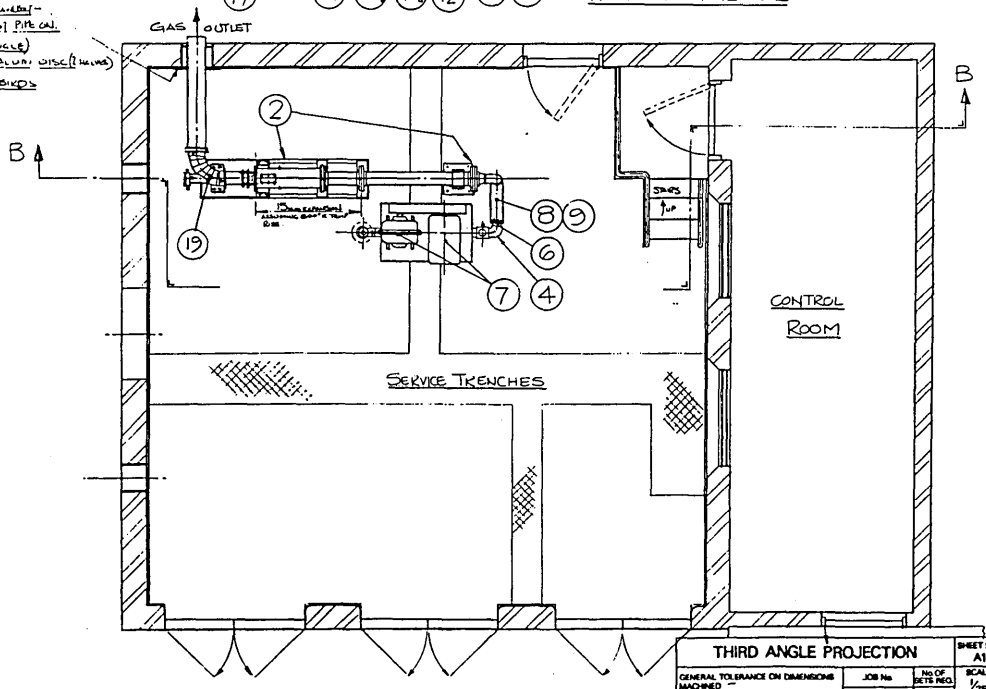

VIEW ON PLANE AA

NOTES

1. DIMENSION MARKED * IS VARIABLE — CAN BE ADJUSTED TO SUIT RIG SUPPORT STANDS, FAN POSITION, BOLTING DOWN HOLES, AND SERVICE TRENCH.
2. RIG AND FAN POSITIONS ARE NOMINAL.
3. BOLT STANDS & FAN DOWN USING RAWLBOLTS.
4. PIPEWORK TO BE OF SCREWED & WELDED CONSTRUCTION. JOINTS TO BE LEAKPROOF.
5. REMOVE EXISTING FAN INLET, THEN REPLACE WITH ITEMS 10 & 12.

ITEM	PART No.	DESCRIPTION	No. OFF	MATL	SPEC.	REMARKS
19	PA43485	WATER COOLED ELBOW	1			
18	PC43496	BRACKET	1			
17	PB43495	BRACKET	1			
16		FILTER SCREEN	1			R.J.L.
15		BELL MOUTH INLET	1	ASTM		EXISTING
14		TRANSITION	1			R.J.L.
13		VALVE (BUTTERFLY)	1			EXISTING MOTORISED
12		FLANGE	1	MS	BS4504 PN16	SPECIAL TO SUIT FAN INLET
11		PIPE	As Reqd	MS	BS 1600 4" NOM BORE	4" NB EXISTING
10		90° ELBOW	2		BS 1640	
9		TUBE CLAMP	2	MS		TO SUIT ITEM 8
8		FLEXIBLE TUBE	1	RUBBER		12 REINFORCED 4" DIA
7		FAN	1	—		CONSISTING OF IMPELLER, SHAFT, BEARINGS, FRAME AND MOTOR
6		STUB PIPE	2	MS	BS 1387	4" NB SCREWED
5		RELIEF VALVE	1			SUPPLIED WITH FAN
4		90° BEND	1	MS	BS 1256	4" NB MAX. RADIUS
3		UNEQUAL TEE	1	MS	BS 1256	4" x 4" x 2½"
2	PB43393	LP PHASE 7 RIG GA	1			
1	PB43494	LAYOUT OF PH 7 RIG	1			

THIRD ANGLE PROJECTION

GENERAL TOLERANCE ON DIMENSIONS MACHINED — UNMACHINED — OTHER DIMENSIONS AS STATED

WELD WHERE SHOWN THUS

MACHINE WHERE SHOWN THUS

USED ON DRG. —

JOB No. E6G4IN

No OF SETS REQ. 1

SHEET SIZE A1

SCALE 1/25

FINISH SELF

DRAWN	CHKD	APPVD	DATE
R.H. BENNE 7-FEB-24			

TITLE:- LAYOUT OF LP PHASE 7 RIG IN TEST HOUSE N° 1

SCHOOL OF MECHANICAL ENGINEERING
CRANFIELD INSTITUTE OF TECHNOLOGY

DRAWING No. PB43483

SHT. | OF | SHEETS

DRAWING No. PC4395S3	
ISSUE	MODIFICATION
A	—

ALL DIMENSIONS IN MILLIMETRES UNLESS OTHERWISE STATED.

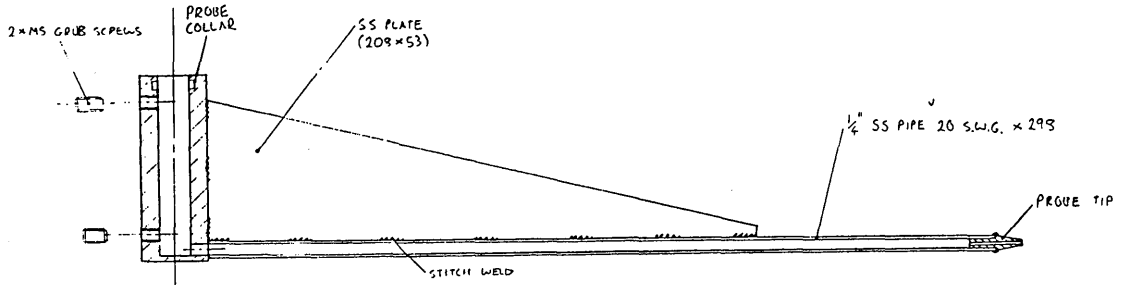

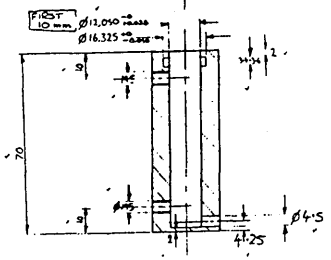

PROBE COLLAR-NOTES

1/ DRILL & REAM CENTRAL HOLE Ø12,2 × 63

2/ 2 HOLES DRILLED AND TAPPED M5.

3/ Ø6 HOLE OPPOSITE SIDE TO M5 HOLES.

4/ REMOVE ALL SHARP EDGES.

5/ MATERIAL S S.

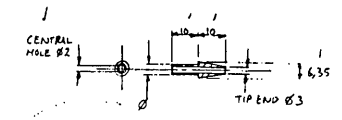

PROBE TIP-NOTES

1/ MATERIAL: SS.

2/ Ø4.52 TO FIT ¼" SS TUBE BORE.

REMOVE SHARP EDGES

THIRD ANGLE PROJECTION	JOB No.	No. OF SETS REQ.	SHEET SIZE A2	ITEM	PART No.	DESCRIPTION	No. OFF	MAT'L	SPEC.	REMARKS
GENERAL TOLERANCE ON DIMENSIONS MACHINED ± 0,25 UNMACHINED	E6641N	1	SCALE 1:1	1	PC4353	SAMPLE PROBE	1	SS		
OTHER DIMENSIONS AS STATED			FINISH SELF	DRAWN S.C. HARDING 15/12/25	CHK'D RH-D 15/12/25	APPV'D	STRESS APPV'D	TITLE:- SAMPLE PROBE EXTENSION - LPP PHASE 7 RIG		
WELD WHERE SHOWN THUS				SCHOOL OF MECHANICAL ENGINEERING CRANFIELD UNIVERSITY				DRAWING No. PC4353		
MACHINE WHERE SHOWN THUS	USED ON DRG.							SHT. 1 OF 1 SHEETS		

DRAWING No. PD 43406

ISSUE	MODIFICATION
A	—
B	△ NOTE TO SUIT FUSED SILICA TUBE ADDED RHD 13/5/93
C	WATER COOLING ADDED: ¼" SS TUBE DIVIDERS. IGNITER BOSS ADDED (AS CLOSE TO FLANGE AS POSSIBLE.)

ALL DIMENSIONS IN MILLIMETRES UNLESS OTHERWISE STATED.

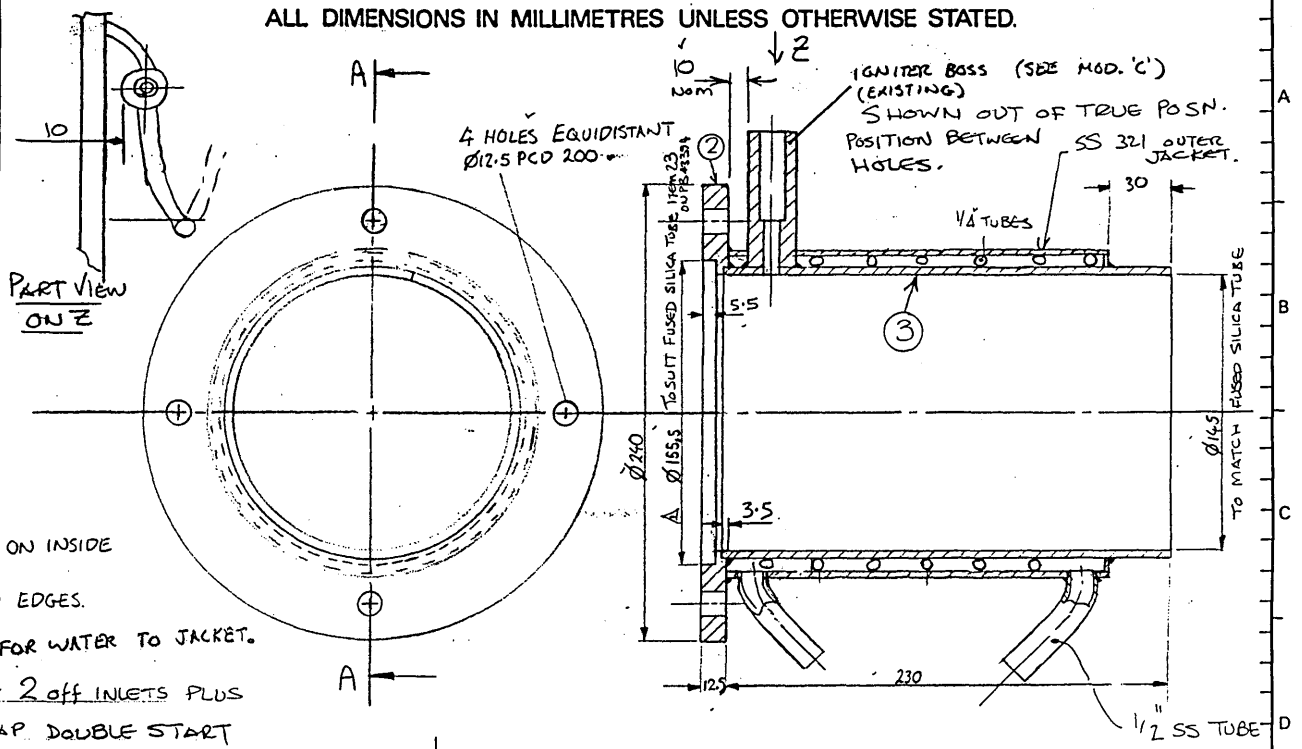

NOTES

1/ SMOOTH SEAM WELD ON INSIDE

2/ REMOVE ALL SHARP EDGES.

3/ ½" B.S.P. FITTINGS FOR WATER TO JACKET.

4/ WATER COOLING:- 2 off INLETS PLUS 2 off OUTLETS, WRAP DOUBLE START HELIX EACH WITH SEPARATE INLET & OUTLET.

ITEM	PART No.	DESCRIPTION	No. OFF	MAT.	SPEC.	REMARKS
3		DUCT	1	SS	321	16 SWG
2		FLANGE	1	SS	321	250 o/D x 130 i/D x 5/8" TK
1	PD43406	FLAME TUBE ASSY	1			

BO PHILLIPCORNES
BO PHILLIPCORNES

THIRD ANGLE PROJECTION

SHEET SIZE A3

GENERAL TOLERANCE ON DIMENSIONS	JOB No.	No. OF SETS REQ.
MACHINED ±0·1	E6641N	1
UNMACHINED		
OTHER DIMENSIONS AS STATED		
WELD WHERE SHOWN THUS		
MACHINE WHERE SHOWN THUS	USED ON DRG. PB 43394	

SCALE 1:2

FINISH SELF

DRAWN	CHK'D	APPV'D	STRESS APPV'D
S.C. HARDING	RHD		
13 JUN 93	21/7/93		

TITLE:- FLAME TUBE
L.P. PHASE 7 RIG

SCHOOL OF MECHANICAL ENGINEERING
CRANFIELD INSTITUTE OF TECHNOLOGY

DRAWING No. PD 43406

SHT. 1 OF 1 SHEETS

MY 220837 R

DRAWING No. PD 43415

ISSUE	MODIFICATION
A	—

ALL DIMENSIONS IN MILLIMETRES UNLESS OTHERWISE STATED.

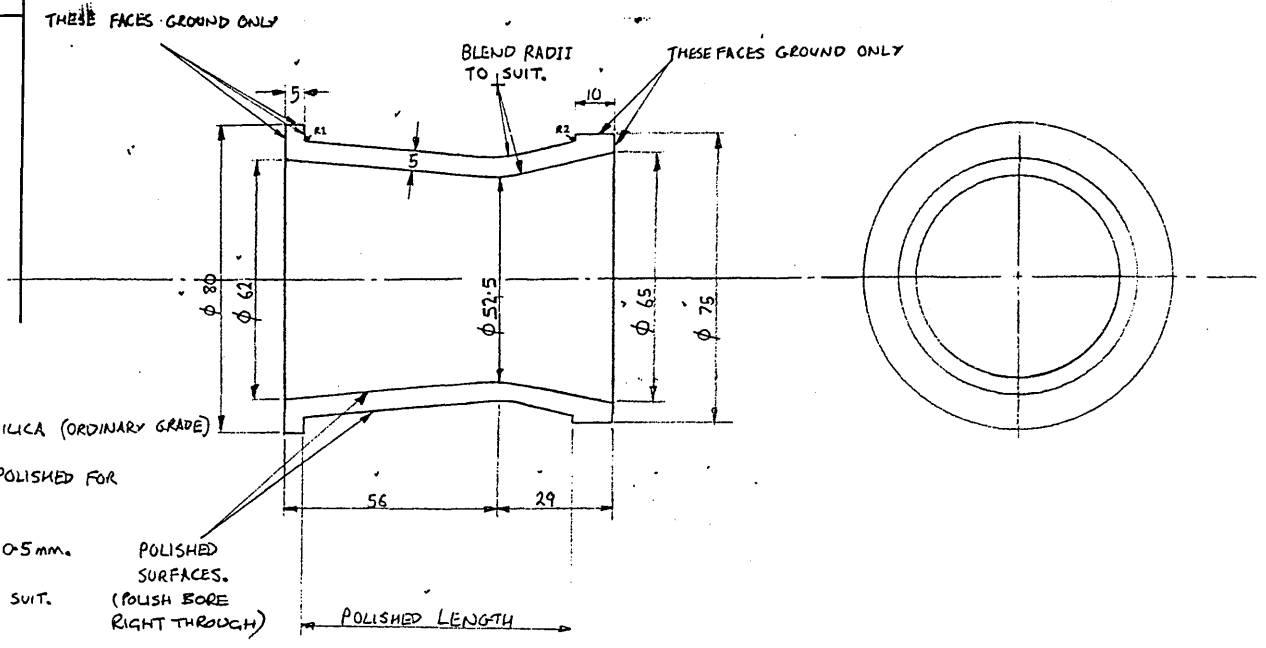

NOTES

1/ MATERIAL : FUSED SILICA (ORDINARY GRADE)

2/ SURFACES INDICATED POLISHED FOR TRANSPARENCY ONLY

3/ ALL TOLERANCES ± 0·5mm.

4/ RADII R1 AND R2 TO SUIT.

ITEM	PART-No.	DESCRIPTION	No. OFF	MATL	SPEC.	REMARKS
1	PD 43415	PREMIXING DUCT	1	FUSED SILICA		

THIRD ANGLE PROJECTION

SHEET SIZE A3

GENERAL TOLERANCE ON DIMENSIONS
MACHINED SEE NOTE 3
UNMACHINED
OTHER DIMENSIONS AS STATED

WELD WHERE SHOWN THUS

MACHINE WHERE SHOWN THUS

JOB No.	No. OF SETS REQ.
E6641N	
USED ON DRG. PB43394	

SCALE 1:1

FINISH SEE NOTE 2

DRAWN	CHK'D	APPV'D	STRESS APPV'D
S.C. HARDING	RHD		
30 JULY 93	13/9/93		

TITLE:- PREMIXING DUCT LP PHASE 7 RIG

SCHOOL OF MECHANICAL ENGINEERING
CRANFIELD INSTITUTE OF TECHNOLOGY

DRAWING No. PD 43415

SHT. 1 OF 1 SHEETS

MY320637R

DRAWING No. PD 43414

ISSUE	MODIFICATION
A	-

ALL DIMENSIONS IN MILLIMETRES UNLESS OTHERWISE STATED.

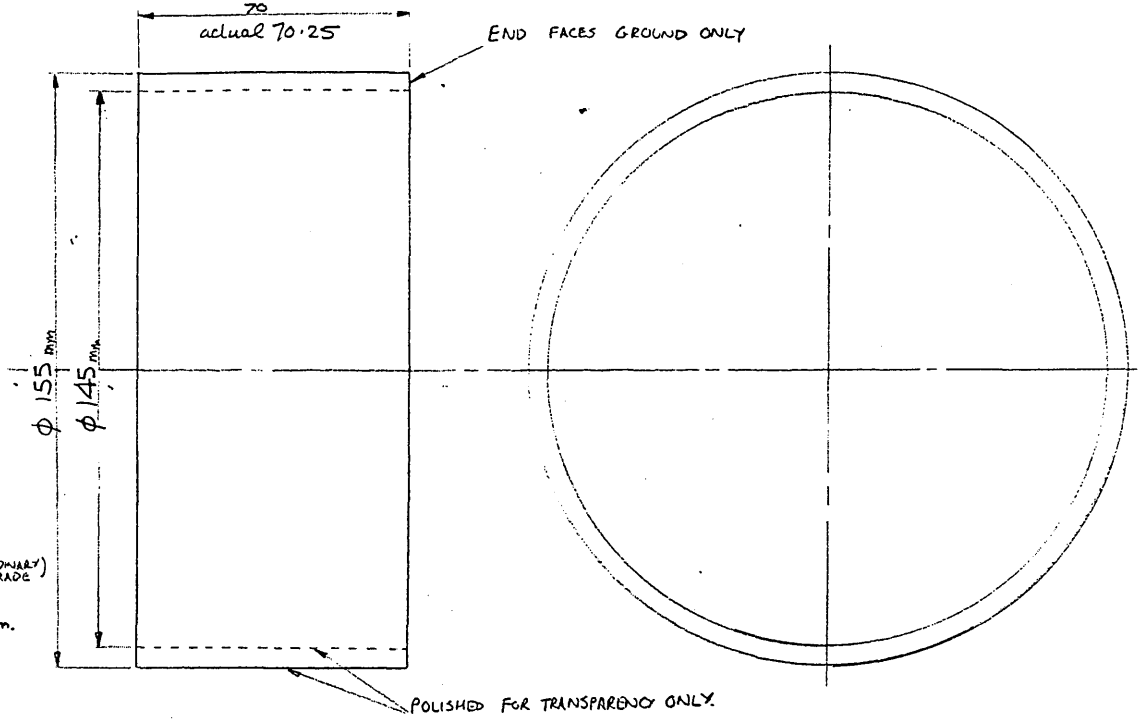

NOTES

1/ MATERIAL: FUSED SILICA (ORDINARY GRADE)

2/ ALL TOLERANCES ± 0·5mm.

3/ SURFACES POLISHED FOR TRANSPARENCY ONLY.

THIRD ANGLE PROJECTION			SHEET SIZE	ITEM	PART No.	DESCRIPTION	No. OFF	MATL	SPEC.	REMARKS
GENERAL TOLERANCE ON DIMENSIONS	JOB No.	No. OF SETS REQ.	A3	1	PD 43414	FLAME TUBE	1	FUSED SILICA		
MACHINED SEE NOTE 2	G6641N		SCALE 1:1	DRAWN	CHK'D	APPV'D	STRESS APPV'D	TITLE:- FLAME TUBE		
UNMACHINED				S.C. HARDING 30 JULY 93	RHD 13/8/93			LP PHASE 7 RIG.		
OTHER DIMENSIONS AS STATED			FINISH	SCHOOL OF MECHANICAL ENGINEERING				DRAWING No. PD 43414		
WELD WHERE SHOWN THUS			SEE NOTE 3.	CRANFIELD INSTITUTE OF TECHNOLOGY				SHT. 1 OF 1 SHEETS		
MACHINE WHERE SHOWN THUS	USED ON DRG. PD 43394									

MY 230637 R

APPENDIX II

This appendix contains the fluorescence spectra of kerosene and various aromatics, a background and fluorescence image of the LPP combustor and the flatfielded fluoranthene LIF image.

A1. Fluorescence Spectra of Liquid Samples

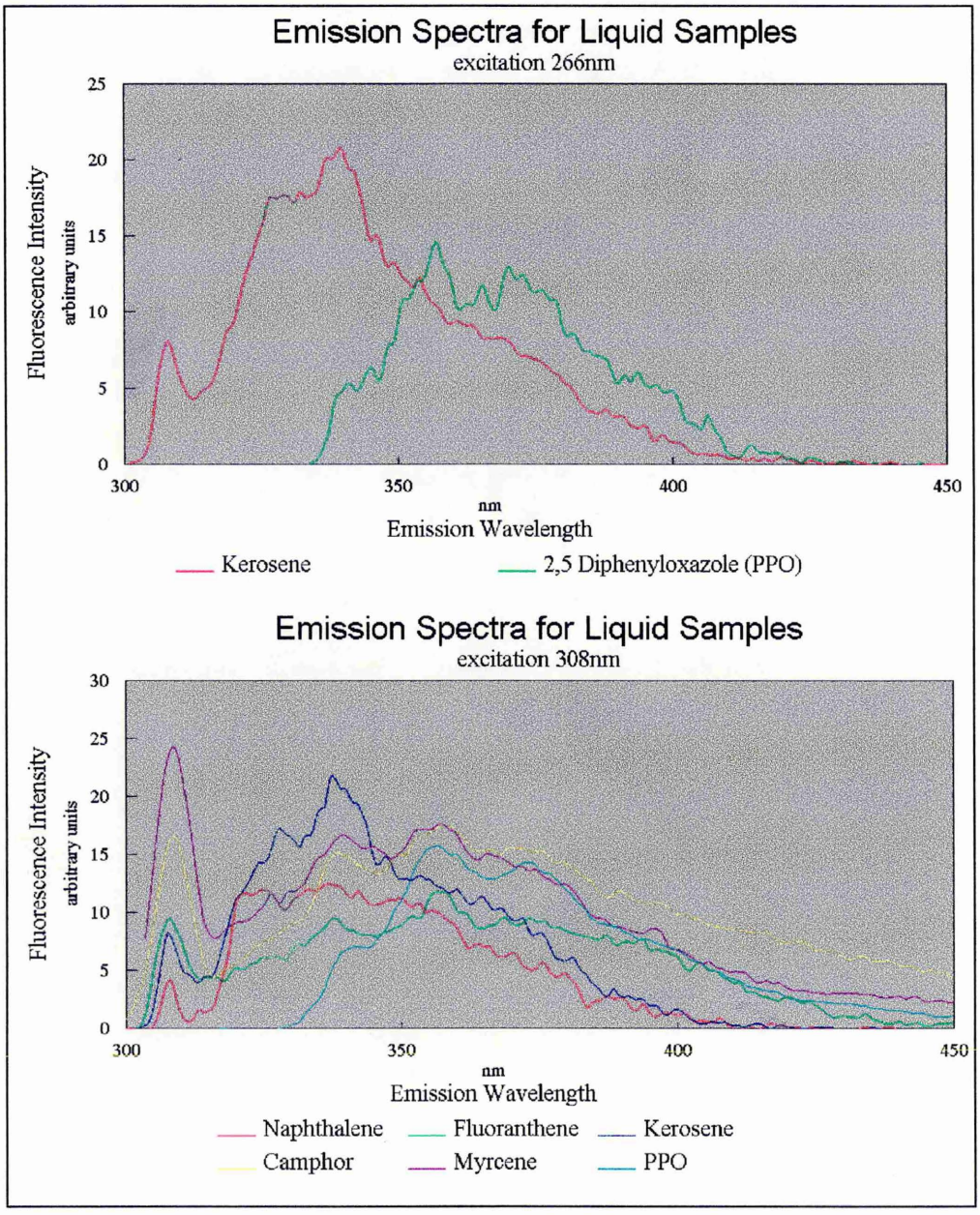

A2. Background Image (non-combusting) and Fluorescence Image (combusting)

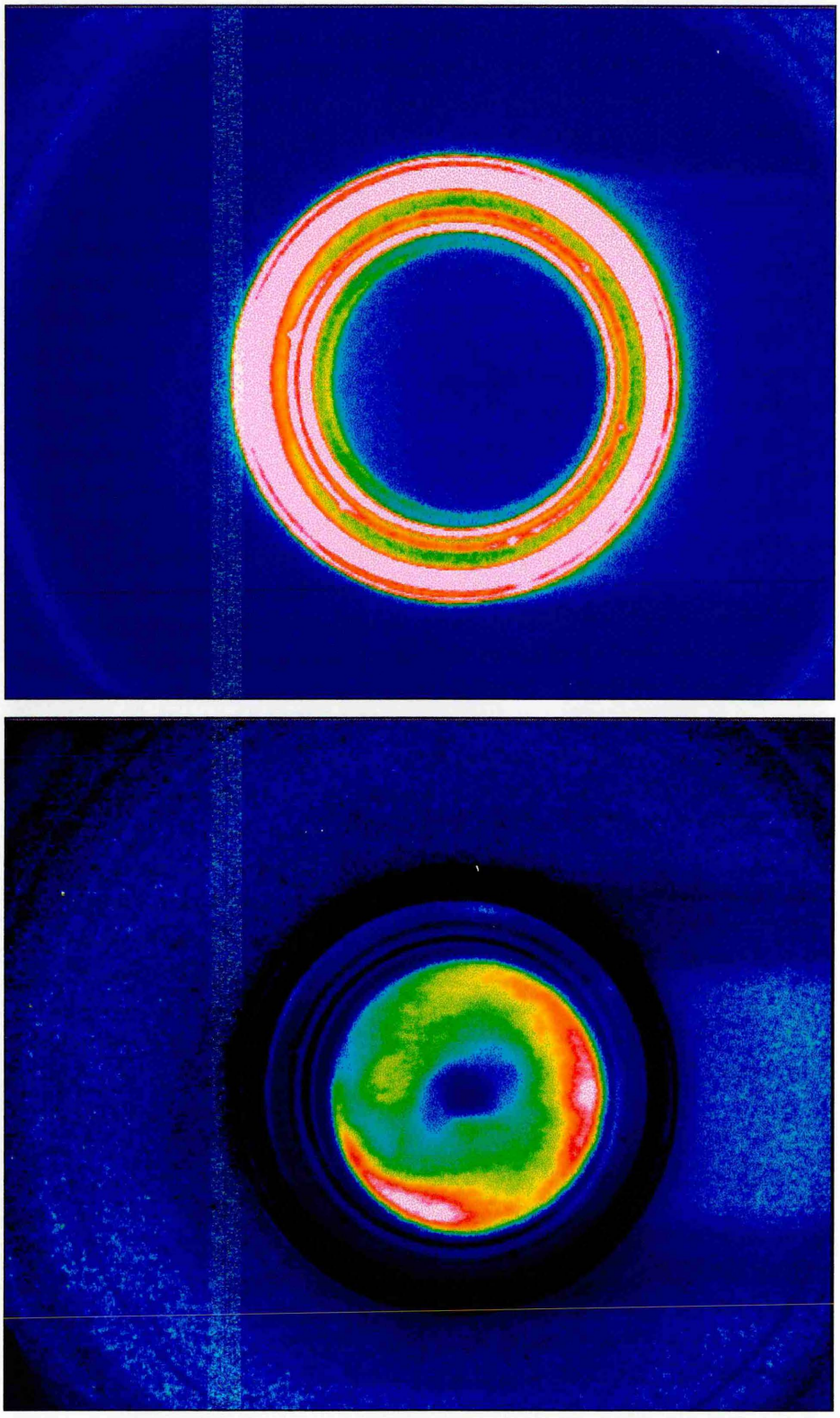

A3. Axial Image of Fluoranthene Flatfielded

This is the flatfielded image of fluoranthene fluorescence which contains laser structure. The structure could either be due to saturation of the fluoranthene excitation or more likely excessive structure in the flatfielding image.

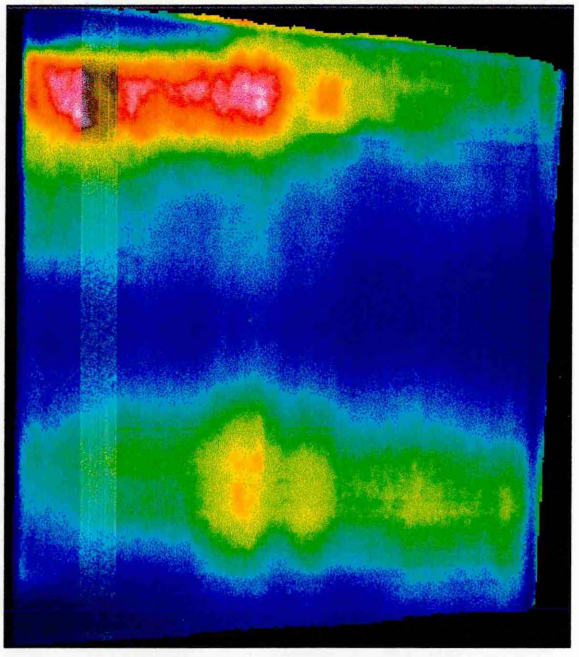

References

Adrian R.J. *Particle imaging techniques for experimental fluid mechanics* Annual review of Fluid Mechanics. 23, p261-304 1991.

Ahmad N.T., Andrews G.E., Kowkabi M.,Shrif S.F. *Centrifugal mixing in gas and liquid fuelled lean swirl stabilised primary zones.* ASME 85-GT-103 1985.

Aigner M., Mayer A., Schiessel P., Strittmatter W. *Second generation low emission combustor for ABB gas turbines: tests under full engine conditions.* ASME 90-GT-308. 1990.

Anand M.S., Gouldin F.C. *Combustion efficiency of a premixed continuous flow combustor.* Journal of Engineering for Gas Turbines and Power. Vol.107, p695, Jul 1985.

Anderson D.N. *Effect of hydrogen injection on the stability and emissions of an experimental premixed, prevaporized propane burner.* NASA TM X-3301 Oct 1975.

Baines W.D., Peterson E.G. *An investigation of flow through screens.* Transactions of A.S.M.E. July 1951.

Bilger R.W. *The structure of turbulent non-premixed flames.* Twenty Second Symposium (Int.) on Combustion. p475, 1988.

Bosque Fernandez M.A. *Effects of percentage of blockage and flameholder downstream counterbores on lean combustion limits of a premixed, prevaporized propane air mixture.* NASA TP-2227 1983.

Bowman C.T. *Control of combustion generated nitrogen oxide emissions: technology driven by regulation.* Twenty Fourth Symposium (Int.) on Combustion. p859, 1992.

Braynin V.I., Zhuk V.A., Maslov P.D., Mineev B.I., Secundov A.N. *Laser sheet application for investigation of unsteady formations in the boundary layer and in the premixed mode.* FED Vol 172, Experimental and numerical flow visualisation A.S.M.E. 1993.

Buchhave P. *Optics Toolkit* 1994.

Chevalier C., Pitz., W.J., Melenk H.Warnatz J., Westbrook C.K. *Hydrocarbon ignition: automatic generation of reaction mechanisms and applications to engine knock.* 24th symposium international on combustion. The Combustion Institute p93-101, 1992.

Corr R.A., Malte P.C., Marinov N.M. *Evaluation of NOx mechanisms for lean, premixed combustion.* ASME 91-GT-257, Jun 1991.

Correa S.M. *A review of NOx formation under gas turbine combustion conditions.* Combustion Science and Technology, Vol. 87, p329. 1992.

Correa S.M. *Carbon monoxide emissions in lean premixed combustion.* Journal of Propulsion and Power. Vol. 8, No. 6, Nov-Dec. 1992.

Cooper Larry. *Effect of degree of fuel vaporization on emissions for a premixed, partially vaporized system.* NASA TP-1582, 1986.

Cooper Larry,P. *Analysis of the effect of flameholder characteristics on lean, premixed, partially vaporized fuel air mixture quality and nitric oxide emissions.* NASA TP-1842, 1981.

Cowell L.H., Lefebvre A.H. *Influence of pressure on autoignition characteristics of gaseous hydrocarbon-air mixtures.* Society of Automotive Engineers. SAE Technical Paper., 1986.

Cox R.A., Cole J.A. *Chemical aspects of the autoignition of hydrocarbon-air mixtures.* Combustion and Flame 60, p109-123 1985.

Danis A.M., Namer I., Cernansky. N.P. *Fuel prevaporization effects on the minimum ignition energy of N-Heptane spray/vapour mixtures.* ASME 86-WA/HT-19, Dec 1986.

Darling D.D., Radhakrishnan K., Oyediran A., Cowan E. *Combustion - acoustic stability analysis for premixed gas turbine combustors* AIAA 95-2470.

Ducourneau F. *Inflammation spontane de milanges riches air kerosene.* Entropie Vol. 10, No. 59, p11-18, 1974.

Duerr R.A., Lyons V.J. *Effect of flameholder pressure drop on emissions and performance of premixed, prevaporized combustors.* NASA TP-2131, 1983.

Dunston W., Human M. *Aircraft Emission Requirements for the High Speed Civil Transport* AIAA report AIAA 95-3914. Sept. 1995.

Egofopoulos F.N. *Geometric and radiation effects on steady and unsteady strained laminar flames.* 25th Symposium (International) on Combustion p1375-1381, 1994

Eykam J.F. Chapter: 'Pure Liquids' (1895) p492 in *The Scattering of Light and other Electromagnetic Radiation.* ISBN. 0/12404550/2. (1895).

Farrugia N. Vector-Scaling Imaging in Combustion using PIV and LIF. PhD thesis, Cranfield University. 1995.

Fenimore C.P. *Formation of nitric oxide in premixed hydrocarbon flames.* Thirteenth (Int.) Symposium on Combustion. p373, 1971.

Freiholtz D., Krispinsson J., Sjunnesson A., Bernsteen P., Henriksen P. *LDA measurements and gas analysis in an experimental lean premixed low emission combustor.* AIAA 95-2997 1995.

Fric T.F. *Effects of fuel air unmixedness on NOx emissions.* Journal of Propulsion and Power. Vol. 9, No. 5, Sept.-Oct 1993.

Gibson C., Gray P., Griffiths F., Hasko S.M. *Spontaneous ignition of hydrocarbon and related fuels: a fundamental study of thermokinetic interactions.* Twentieth Symposium (Int.) on Combustion. p101, 1984.

Goodjer E.M., Eissa A.F.M. *Spontaneous ignition of falling droplets in the Cranfield pressure rig.* Journal of the Institute of Energy. [199] Dec 1987.

Graziadio M., Novelli G. *Confronto tra le misure di granulometria ottenute con phase-Doppler aerometrics interponendo tre finestre di tipo diverso tra lo spray e il ricervitore del P.D.P.A.* E.N.E.L.-C.R.T. internal report TO-03/91, October 1991.

Gupta A.K., Lilley D.G. *Combustion and environmental challenges for gas turbines in the 1990's.* AIAA, 1991.

Harding S.C. *The design, construction and gas flow characterisation of a versatile counterflow burner.* MSc. Thesis 1992, Cranfield University. 1992.

Hayashi S.Y., Yamada H., Shimodaira K., Saitoh T., Horiuchi S. *Spontaneous ignition of atomised kerosene air mixtures in a high pressure flowing system.* Nippon Kikai Gakkai Ronbunshu B. Hen. Vol 54, No. 501, p1145-1149, May 1988.

Hayhurst.A.N., Lawrence A.D. *Emissions of nitrous oxide from combustion sources.* Progress in Energy and Combustion Science. Vol. 18, p529-552, 1992.

Herzberg *Molecular spectra and molecular structure* Vol. 1, Spectra of Diatomic Molecules Van Nosrand Reinhold also Vols. I and II for polyatomic and infra red spectra. 1951.

Hicks Y.R., Locke R.J., Wey C.C., Bianco J. *A unique, optically accessible flame tube facility for lean combustor studies.* AIAA 95-2685

Honig R., Kappler G., Andresen P., Brehm N. *Multi-species detection in a liquid fuelled model combustor using tuneable excimer lasers.* Combustion Science and Technology. Vol.102, p 255-272. 1995

Hottell H.C., Egbert R.B.Trans A.S.M.E. Inst. of Chem. Engineers Vol. 38, p531-565, 1942.

Johnston H.S., Prather M.J., Watson R.T. *The atmospheric effects of statospheric aircraft: a topical review.* NASA reference publication 1250. 1991.

Hurn R.W., Hughes K.J. *Combustion characteristics of Diesel fuels as measured in a constant volume bomb.* SAE Transactions Vol. 6 p24-35, 1952.

Hurn R.W., Chase J.O., Ellis C.F., Hughes K.J. *Fuel heat gain and release in bomb ignition.* SAE Transactions Vol. 64, p703-711, 1956.

I.C.A.O. *Environmental Protection* International Civil Aviation Organisation. Annex 16. 1981 First Edition.

Karim G.A., Kibrya G., Wierzba I. *Flashback and flame propagation limits through streams of premixed fuel and air.* 1985 Spring meeting Central/Western States Sections Combustion Institute. April 1985.

Keller J.O. Bramlette T.T. Barr P.K., Alvarez J.R. *NOx and CO emissions from a pulse combustor operating in the lean, premixed mode.* Combustion and Flame 99, 460-466, 1994.

Kerker M. *The scattering of light and other electromagnetic radiation.* New York Academic Press. p666. 1969.

Kojima S. *Detailed modelling of n-butane autoignition chemistry.* Combustion and Flame 99, p87-136 1994.

Laster W.R., Sojka P.E. *Autoignition of H_2/Air/NOx mixtures: the effect of temperature P and pressure.* J.Propulsion Vol. 5., No.4, July 1989.

Laster W.R., Sojka P.E. *Autoignition of H2/Air: the effect of NOx addition.* Journal of Propulsion Vol.5, No.4, p385, Jul 1989.

Law C.K., Zhu D.L., Yu G. *Propagation and extinction of stretched premixed flames* 21st Symposium (International) on Combustion p1419-1426, 1986.

Lee C-M, Chun K.S. *Fuel-Air mixing effect on NOx emissions for a lean, premixed, prevaporized combustion system.* AIAA-95-0729. 1995.

Lee S.T., T'ien J.S. *A numerical of flame flashback in a premixed, laminar system.* Combustion and Flame 48, p273-285.

Lefebvre *Gas Turbine Combustion* McGraw Hill 1983.

Lewis A.J., Greenhalgh D.A. *Hydroperoxy N_2O: N_2O and NO formation in ultra-lean hydrocarbon air mixtures.* Joint Meeting of British and German Sections of the Combustion Institute. p172-175, March 1993.

Lewis B., von Elbe G. Combustion Flames and Explosions of Gases. p220-224., New York Academic Press.

Lockett R.D., Boulanger B., Harding S.C., Greenhalgh D.A. *Laser diagnostics in the counterflowing triple flame.* Proceedings of the Joint Meeting of the Portuguese, British, Spanish and Swedish Sections of the Combustion Institute, Madeira.part 8.4, 1996.

Lockett R.D., Greenhalgh D.A. *The extinction limits of premixed and diffusion flames in counterflow geometry* (working title) to be published in Combustion and Flame 1996.

Malte P.C. and Pratt D.T. *Measurement of atomic oxygen and nitrogen oxides in jet stirred combustion.* Fifteenth Symposium (Int.) on Combustion. 1973.

Marek C.J., Papathakos L.C., Verbulez P.W. *Preliminary studies of autoignition and flashback in a premixing prevaporised flame tube using Jet-A fuel at lean equivalence ratios.* NASA TM-X-3526 May 1987.

Martin R.J., Brown N.J. *Analysis and modelling of nitrous oxide chemistry in lean, premixed combustion.* Combustion and Flame. 82: p312-333, 1990.

Martin R.J., Brown N.J. *Nitrous formation and destruction in lean, premixed combustion.* Combustion and Flame 80: p238, 1990.

Melling A. *Seeding Gas Flows for Laser Anemometry.* AGARD CP. 399, 1986.

Micklow G.J., Dogra A.S. *Effect of vane twist on the performance of dome swirlers for gas turbine airblast atomisers.* AIAA 90-1955, July 1990.

Minetti R., Ribaucour M., Carlier M., Fittschen C., Sochet L.R. *Experimental and modelling studies of oxidation and autoignition of butane at high pressure.* Combustion and Flame 96. p201-211 1994.

Monmont F. Thesis to be published 1999, Cranfield University.

Morley C. *A fundamentally based correlation between alkane structure and octane number.* Combustion science and Technology Vol.55, p 115-123. 1987.

Mullins B.P. *Spontaneous ignition of fuels injected into a hot air stream.* Parts I-VIII Fuel No.3, 1951.

Najm H.N., Ghoneim A.F. *Coupling between vorticity and pressure oscillations in combustion instability.* Journal of Propulsion and Power. Vol. 10, No. 6, Nov-Dec 1994.

Nguyen Q.V., Edgar B.L., Dibble R.W., Gulati A. *Experimental and numerical comparisons of extractive and in situ laser measurements of non-equilibrium carbon monoxide in lean, premixed, natural combustion.* Combustion and Flame 100, p395-406, 1995.

Nicol D., Malte P.C., Lai J. Marinov N.N., Pratt D.T. *NOx sensitivities for gas turbine engines operating lean- premixed combustion and conventional flames.* A.S.M.E. 92-GT-115, 1992.

Odgers, Kretschmer *Gas turbine fuels and their influence on combustion.* Abacus Press. 1968.

Proctor M.P., T'ien J.S. *Combustor flame flashback: final report.* NASA CR-174961 Jun 1985.

Proctor M.P., T'ien J.S. *Flame flashback in a premixed dump combustor.* AIAA-85-0145. Jan 1985.

Puri I.K., Seshadri K. *Extinction of diffusion flames burning diluted methane and diluted propane in diluted air* Combustion and Flame 65, p137-150 1986.

Radhakrishnan K., Heywood J.B., Tabazynski J.B. *Premixing quality and flame stability: a theoretical and experimental study.* NASA CR-3216, 1979.

Rayleigh J.W.S. *The theory of sound: Vol II.*, Dover,New York 1945.

Roffe G. *Experimental study of the effects of secondary air on the emissions and stability of a lean premixed combustor.* NASA CR 165422, Aug 1981.

Roffe G., Ferri A. *Effect of premixing quality on quality on oxides of nitrogen in gas turbine combustors.* NASA CR-2657, Feb 1976.

Roffe G., Venkatramani K.S. *Experimental study of the effect of flameholder geometry on emissions and performance of lean premixed prevaporised combustors.* NASA CR-135424, Jun 1978.

Sattelmayer T., Felchin M.P., Haumann J., Hellat J., Styner D. *Second generation low emission combustors for ABB gas turbines: burner development and tests at atmospheric pressure.* Transactions of ASME Vol.114, p118, Jan 1992.

Schiestel R. *Modelisation et simulation des ecoulements turbulent.* p102. HERMES press 1991.

Seitzman J.M., Hanson R.K. *Planar fluorescence imaging in gases* from Instrumentation for Flows with Combustion (see Taylor).1993.

Sick V., Arnold A., Diebel E., Dreier T., Ketterle W., Lange B., Wolfrum J. *Two-dimensional laser diagnostic and modelling of counterflow diffusion flames* 23rd Symposium (International) on Combustion p495-501, 1990.

Singh R. *Combustors* unpublished lecture notes. 1992.

Smith A. Report from Harwell.

Smith K.O., Kurzynski F.R., Angello L.C. *Experimental evaluation of fuel injection configurations for a lean premixed low NOx gas turbine combustor.* ASME 87-gt-141, 9p, Jun 1987.

Smith K.O., Cowell L.H. *Experimental evaluation of a liquid fuelled, lean, premixed gas turbine combustor.* ASME GT264 8p, 1987.

Spadaccini L.J., Tevelde J.A. *Autoignition characteristics of aircraft type fuels.* NASA CR-159886, Jun 1980.

Spadaccini L.J. *Fuel Characterisation* presentation 15-9-93.

Spooner M. *Water Flow Analogy in a Premixing Duct - Video* unpublished, Rolls Royce.

Starner S.H., Bilger R.W., Dibble R.W., Barlow R.S. Long M.B. *Joint planar CH and OH LIF imaging in piloted turbulent jet diffusion flames near extinction.* 24th symposium (int) on combustion. The Combustion Institute p341-349. 1992.

Steele R.C., Malte P.C., Nicol D.G., Kramlich J.C. *NOx and N_2O in Lean, Premixed Jet Stirred Flames* 25th Symposium (International) on Combustion 1994.

Stringer F.W., Clarke A.E., Clarke J.S. *The spontaneous ignition of hydrocarbon fuels in a flowing system.* Proceedings of the Institute of Mechanical Engineering Vol. 184, part 3J, p212-215, 1969-70.

TeVelde J.A. Spadaccini L.J. *Autoignition characteristics of number 2 Diesel fuel.* R81-915281-1, United Technologies Research, NASA CR-16315.

Tait N.P., Greenhalgh D.A. *PLIF imaging of fuel fraction in practical devices and LII imaging of soot* presented at meeting "Laser Diagnostics for Industrial Processes" Heidelberg. June 1993

Tiat N.P., Harding S.C. *Fuel air mixing measurements in a phase 7 premixing duct using laser induced fluorescence.* Rolls Royce Internal Report. 1992.

Wierzba I., Oladipo A.B., Karim G.A. *The limits for flame flashback within streams of lean homogenous fuel-diluent-air mixtures involving hydrogen.* International Journal Hydrogen Energy. Vol 18. No. 3, p223, 1993.

Bibliography

Afrosimova V.N., Burtsev G.N., Kondrat'ev D.V., Shelukho S.I. *Study of autoignition conditions in a device for combustion chamber fuel-air mixture preparation.* Izvestiya VUZ., Aviatsionnaaya Tekhnika. Vol 32, No.4, p85, 1989.

Ahmad N.T., Andrews G.E. *Enclosed swirl flames: interaction between swirlers in lean primary zones.* ASME 86-GT-278 Jun 1986.

Ajinkya M.B. *Gas Premixing Techniques* Hydrodynamics of Gas Solids Fluidization. p571-572, 1984.

Alkabie H.S., Andrews G.E. *Ultra low NOx emissions for gas and liquid fuels using radial swirlers.* ASME 89-GT-322, Jun 1989

Ali Al-Shaikly A.F., Andrews G.E., Aniagolu C.O. *Jet shear layer turbulent diffusion flames for ultra low NOx emissions.* Journal of Engineering for Gas Turbines and Power Vol 114, p55, Jan 1992.

Anderson D.N. *Effect of premixing on Nitric Oxide formation.* NASA TM-X-68220 Jun 1973.

Anderson D. *Effect of equivalence ratio and dwell time on exhaust emissions from an experimental premixed prevaporised burner.* NASA Tech. Memorandum. TM-X-71592 1974.

Anderson D.L. *Analytical modelling of operating characteristics of premixed, prevaporised fuel air mixing passages.*NASA/CR-167990 Feb 1982.

Anderson D.L. *Modelling of premixed prevaporised fuel air passages.*NASA CP 2078.

Beam S.F. *The NASA high speed research programme.* PN93-16761, 1992.

Beretta F., Cincotti V., *Ultra violet and visible fluorescence in the fuel pyrolysis regions of gaseous and diffusion flames.* Combustion and Flame 61, p211-218, 1985.

Bergeron, Hallett. *Autoignition of single droplets of two-component fuels.* CTN-92-60454, 1991.

Bjoerge T., Lilleheie N.I., Horrigmo W. *Comparison of measurements and calculations from a premixed lean, propane combustor.* ISBN 82-595-6411-4, Nov. 1991.

Brena de la Rosa A., Wang G. Bachalo W.D. *The effect on swirl on the velocity and turbulence fields of liquid spray.* Transactions of ASME for Gas Turbines and Power Vol 114, p73, Jan 1992.

Buchner H. *The influence of pressure fluctuations on fuel air mixture formation in premixed combustion systems.* GASWARME Int. Vol 41, Heft 1, Jan 1992.

Butze H.F. *High altitude performance of an experimental tubular prevaporizing combustor.* NACA RM-E54I10 1954.

Cadiou Anne, Grienche G. *Experimental study of reverse flow combustor: influence of primary holes on combustor efficiency.* ASME GT249 7p, Jun 1989.

Cattolica R.J., Barr P.K., Mansour N.M. *Propagation of a premixed flame in a divided-chamber combustor.* 1984 Fall Meeting of the Western States Combustion Institute. 1984.

Corbett N.C., Lines N.P. *Control requirements for the RB-211 Low emission combustion system.* Journal of Engineering for Gas Turbines and Power. Vol 166, p527, July 1994.

Correa S.M. *Lean, premixed combustion for gas turbine review and required research.* ASME Fossil fuel combustion PD-Vol. 33, 1991.

Darder C.M., Powell C.A., Hayes W.D., Pierce A.D. George A.R. *Status of Sonic Boom Methodology and Understanding* NASA Conf. publ. 3027, 1989.

Dasgupta A., Li Z., Shih T. I-P. Kundu K., Deur J.M. *Computations of spray fuel-air mixing and combustion in a lean premixed prevaporised combustor.* AIAA-93-2069, Jun 1993.

Dickman R.A., Dodds, Ekstedt *Lean premixed prevaporised (LPP) combustor conceptual design study.* NASA CR-159629, May 1979.

DiPiazza J.T., Gerstein M., Weast R.C. *Flammability limits of hydrocarbon air mixtures.* Ind. and Eng. Chem. Vol 43, No.2, p2721-2725, Dec 1951.

Dodds W.J., Ekstedt E.E. *Evaluation of fuel preparation systems for lean premixing, prevaporizing combustors.* Transactions of ASME Journal of Engineering for Gas Turbines and Power Vol.108, No.2, Apr 1986.

Deur J.M., Kundu K.P., D.D., Cline C.C., Darling, Micklow G.J., Simons T.A., Harper M.R. *Analysis of lean, premixed, prevaporised combustion with KIVA II.* AIAA 94-3895-CP., 1994.

Duerr R.A. *The effect of flameholder blockage on emissions and performance of a premixed prevaporised combustor.* NASA CP-2078, 1979.

Farouk B., Alber W.B., Mellor A.M. *Spray evaporation in a prevaporising premixing fuel air passage.* Proceedings of the 1987 ASME-JSME Thermal Engineering Joint Conference. Vol 1, p159-164, Mar 1987.

Ferri A. *Better marks on pollution for the SST.* Aeronautics and Astronautics, July 1972.
Fiorentino A.J. *Lean, premixed, prevaporized fuel combustor conceptual design study.* NASA/CR-159647, May 1979.

Forch B.E., Miziolek A.W., Merrow C.M., Morris J.B., Locke R. *Ultra violet excimer based ignition of H_2/Air and H_2/O_2 premixed flows.* Army Ballistic Research Lab., Aberdeen. 1989.

Gleason C.C.deceased. Ekstedt E.E. *Externally vaporising system for gas turbine combustor - patent.* PATENT -4 838 029, 1989.

Gould R.D., Stevenson W.H., Thompson H.D. *Simultaneous velocity and temperature measurements in a premixed dump combustor.* Journal of Propulsion and Power. Vol. 10, No. 5, Sept-Oct 1994.

Gouldin F.C. *Effect of swirl on premixed combustion.* NASA CP 2078.

Greehhalgh D.A. *Emissions and Abatement.* unpublished lecture notes. 1992.

Greenhalgh D.A. *Inelastic scattering laser diagnostics; CARS, Planar LIF, Planer LII.* Optical Diagnostics for Flow Processes. 1994.

Gutmark E. *On the lean blowout limit of premixed flames.* AIAA-89/0154, Jan 1989.

Harrison A.J., Furzeland R.S., Summers R., Cairnie L.R. *An experimental and theoretical study of autoignition on a horizontal hot pipe.* Combustion and Flame 72: p119, 1988.

Hasegawa T., Arai A., Kadowaki S., Yamaguchi S. *Autoignition of a turbulent premixed gas.* Combustion Science and Technology. Vol. 84., p1-13, 1992.

Hasmamoto Y., Izumi M., Tomita E. *Effects of swirl and air-fuel ratio on premixed combustion in a closed vessel.* JSME Int. Journal series II, Vol. 33., No. 2., 1990.

Henein N.A., Akasaka Y. *Effect of physical properties and composition on fuels on autoignition and cetane rating.* Soc. of Automotive Engineers 871617. 1988.

Hibbard R.R., Metzler.A.J., Scull W.E. *Low pressure performance of experimental prevaporizing tubular combustor using approximately stoichiometric admission of fuel air mixture into the primary zone.* NACA RM E54f25a, 1954.

Honig R., Kappler G., Andreson P., Brehm N. *Multi species detection in a liquid fuelled model combustor using tuneable excimer lasers.* Combustion Science and Technology, Vol. 102, p 255-272, 1994.

Huck K.L., Marek C.J. *Lean combustion limits of a confined, premixed, prevaporized propane jet.* NASA TM-78868, Apr 1978.

Jarosinski J. *A survey of recent studies on flame extinction.* Progress in Energy Combustion and Science. Vol12. p81-116, 1986.

Johansen P., Sjurnesson. A, Olavsson S. *Development of an Experimental LPP Gas Turbine Combustor.* Trans ASME 94-GT-284, 1994.

Join-Lambert A.J. *Aerodynamic investigation of a tubular combustor.* Thesis Msc. 1992. Thesis, Cranfield University 1992.

Kinnison D.E., Wuebbbles D.J. *Preventing Depletion of Stratospheric Ozone - Implications on Future Aircraft Emissions.* UCRL-99926-Rev.1 De 89 0.13779, 1989.

Leonard G., Stegmaier J. *Development of an aero derivative gas turbine dry low emissions combustion system.* A.S.M.E. 93-GT-288. 1993.

Lin T.H., Law C.R., Chung S.H. *Theory of laminar flame propagation in off-stoichiometric dilute sprays.* International Journal of Heat and Mass Transfer. Vol.31 No.5 p1023-1034, May 1988.

Marek C.J., Baker C.E. *High pressure flame visualisation of autoignition and flashback phenomena with a liquid fuel spray.* NASA TM-83501, Oct. 1983.

Marek C.J., Papathakos L.C. *Exhaust emissions from a premixing, prevaporising flame tube using liquid Jet A fuel.* NASA TM X-3383, 1978.

McVey J.B., Kennedy J.B. *Lean stability augmentation study.* UTRC-R79-914104-18 United Technical Research Centre NASA3-20808, NASA CR-159536, April 1979.

Miziolek A.W., Sausa R.C. *Photochemical ignition studies: laser ignition of flowing premixed gases.* Army Ballistic Research Lab., Aberdeen., Feb 1985.

Nahigyan K.K. *Investigations of cone shaped prevaporizing-type burners in jet propulsion power plant.* NACA ARR No. E6F19, 1942.

NASA *High Speed Civil Transport.* NASA CR-192041.

NASA *Lean, Premixed, Prevaporized Combustion.* NASA CP-2016, 1977.

Nicholls J.A. *Effect of fuel sprays on emissions.* NASA CP 2078.

Nicol D.G., Steele R.C., Marinov N.M. Malte P.C. *The importance of the nitrous oxide pathway to NOx in lean- premixed combustion.* Trans A.S.M.E. Vol 177, p100, Jan 1995.

Onuma Y., Shibata K. *The spontaneous ignition of fuel spray in steady hot air flow.* Nippon Kikai Gakkai Ronbunshu Vol 52, No. 482, Oct 1986.

Polymeropaulos C.E., Das S. *Effect of droplet size on the burning velocity of kerosene air sprays.* Combustion and Flame Vol 25, No.2, p247, Oct 1975.

Proctor C.L., Mellor A.M. *Experimental examination of a prevaporised premixed combustor.* AIAA journal, Vol 25, No.4, p573-577, April 1987.

Putnam A.A., Jenson R.A. *Application of dimensionless numbers to flashback and other combustion phenomena.* 3rd Symposium International on Combustion, p40-44, 1949.

Ramos J.I., Somer H.T *Swirling flow in a research combustor.* AIAA Journal Vol. 23, No.2, p241.

Reeves D. *Radiation from flames in gas turbine combustors* SAE Trans. 68, 554, 1960.

Rizk N.K., Mongia H.C. *Low NOx rich-lean combustion concept application.* AIAA 1991.

Roberts P.B., Kubasco K.J., Sekas N.T. *Development of a low NOx lean, premixed annular combustor.* ASME paper no. 81-GT-40, May 1981.

Roberts R., Peduzzi A. *Experimental clean combustor program - Phase 1* Final Report. NASA CR-134736, October 1995.

Roberts P.B., Shekleton J.R., White D.J., Butze H.F. *Advanced low NOx combustors for supersonic high altitude aircraft gas turbines.* NASA Lewis Research Centre. 1975.

Roffe G. *Effect of inlet temperature and pressure on the emissions from a premixing gas turbine primary zone combustor.* NASA/CR-2740, Sept 1976.

Roffe G. *Emissions measurements for a lean premixed propane air systems at pressures up to 30 atm.* NASA CP 2078.

Roffe G., Ferri A. *Premixing and prevaporizing to obtain low NOx in gas turbine combustors* NASA CR-2495, Mar 1975.

Rolls Royce plc Internal Reports - Issue 1990.

Rolls Royce plc Internal Reports - Issue 1991.

Rutovski V.B., Kulyapin A.N., Zhdanov A.D. *Experimental investigation of the autoignition process during fuel injection into a heated flow.* Combustion, Explosion and Shock Waves Vol.25 , No.1, Jan 1989.

Sacks W. *The rate of evaporation of a kerosene spray.* Report No. MF. 2816,

Santavica, Steinberger, Gibbons, Citano, Mitto. *The effect of incomplete fuel air mixing on the lean limit and emission characterisation of an LPP combustor.* AGARD Fuels and Combustion Technology, N94-29240 08-25, Sept 1993.

Sasaki M., Kumakura H., Suzuki D. *Low NOx combustor for automotive gas turbine-conceptual. design.* ASME 91-GT-369. 1991.

Sasaki M., Itoh T. *A study on NOx emissions from gas turbine combustor.* ASME 86-GT-168 Jun 1986.

Sawyer R.F. *Stabilisation of premixed combustors.* NASA CP 2078.

Smallwood G.J. *A technique for two colour particle image velocimetry.* Thesis from Department of Mechanical Engineering, University of Ottawa. 1992.

Smith K.O. *Ultra low NOx gas turbine combustor. Final Report.* SR90-R-5357-45, GRI-90/0158 Oct 1985 - Jun 1990.

Smith K.O., Angello L.C., Kurzysnki F.R. *Design and testing of an ultra low NOx gas turbine combustor.* ASME paper 36-GT-263, 1986.

Smith K.O., Angello L.C., Kurzysnki F.R. *Preliminary development of an ultra low NOx gas turbine combustor.* Gas Waerme International Vol 37. No.1 Jan-Feb 1988 p31-37. 1988.

Smith K.O., Wade G.W., Samii M.H., Mak H.K. *Performance testing of a low emissions, natural gas fired small gas turbine combustor.* ASME 89-GT-266, Jun 1989.

Smyth K.C., Bryner N.P. *Short duration autoignition temperature measurements for hydrocarbon fuels.* Airforce Engineering and Services Centre, Tyndall. Jan 1991.

Snyder T.S., Rosfyord T.A., McVey J.B., Hu A.S., Schlein B.C. *Emission and performance of a lean, premixed gas fueled injector system for aero derivative gas turbine engines.* A.S.M.E. 94-GT-234. 1984.

Sokolov K.Y., Gutnik M.N., Mechanikov A.I. Tumanovsky A.G., Reshitko V.P., Grinshtein M.I. *Experimental investigation of GTE-115 combustor with premixed burner unit.* Journal of Engineering for Gas Turbines and Power July 1994, Vol. 116, p547, 1994.

Spadacinni L.J., Szetela E.J. *Approaches to the premixed prevaporized combustor concept of gas turbine burners.* ASME paper 75-GT-85, Mar 1975.

Spadaccini L.J. *Autoignition of fuels.* NASA CP 2078.

Sturgess G.J., Sloan D.J., Lesmireses A.L., Heneghan S.P., Ballal D.R. *Design and development of a research combustor for lean blow-out studies.* Journal of Engineering for Gas Turbines and Power Vol 144, p13, Jan 1992.

Suzuki T., Ohtaguchi K., Koide K. *Correlation and prediction of autoignition temperatures of hydrocarbons using molecular properties.* Journal of Chemical Engineering of Japan. Vol. 25, No.5, p606., Mar 1992.

Tacina R.R. *Autoignition in a premixed prevaporised fuel duct using three different fuel injection systems at inlet air temperatures of up to 1250 K.* NASA TM-82938 May 1983.

Tacina R.R. *Ignition of lean air mixtures in a premixed prevaporised duct at temperature up to 1000 K.* DOE/NASA/5104-9 1980, NASA TM-81645, Dec 1990,

Tacina R.R. *Experimental evaluation of premixed prevaporised fuel injection concepts for a gas turbine catalytic combustor.* NASA TM-73755, 1977.

Tacina R.R. *Low NOx potential of gas turbine engines.* NASA TM-102452, 1990.

Tacina R.R. *Performance of multiple Venturi fuel air preparation systems.* NASA CP 2078.

Tait N.P., Greenhalgh D.A. *PLIF imaging of fuel fraction in practical devices and LII imaging of soot.* Ber. Bunsenges. Phy.Chem. 97, 1619-1625 No. 12, 1993.

Talpallikar M.V., Smith C.E., lai M. *Rapid mix concepts for low emissions combustors in gas turbine engines: Final Report.* NASA CR-185292, Oct 1990.

Tam R.Y., Ludford G.S. *Lean flammability limit: a four step model.* Combustion and Flame Vol 72, No.1, p35-43, Apr 1988.

Terao K., Liao C. *The most inflammable state of a lean hydrocarbon-air mixture.* Japan Journal of Applied Physics Vol 31, p2308, July 1992.

Turns S.R., Myhr F.H. Bandaru R.V. Maund E.R. *Oxides of nitrogen emissions from turbulent jet flames: part II- fuel dilution and partial premixing.* Combustion and Flame 93:255-269, 1993.

Wear J.D., Cook W.P. *Effect of fuel properties on carbon deposition in atomising and prevaporising turbojet combustors.* NACA RME52C24, 1950's.

Wedlock M.I., Tilston J.R. *Low emissions combustor technology. Low NOx II., Task 2.2: LPP pilot zone development.*DRA., Farnborough. unpublished report, 1993.

Wigley G. *Phase Doppler Anemometry and its Applications to Liquid Fuel Spray Combustion* in Optical Diagnostics for Flow Processes. 1994.

Wilk R.D., Koert D.N., Cernansky N.P. *Low temperature carbon monoxide formation as a means of assessing the autoignition tendency of hydrocarbon and hydrocarbon blends.* Energy and Fuels 1989. 3 , p292, 1989.

Williams F.A. *Flame Stability of Premixed Turbulent Gases.* "Applied Mechanics Survey", 1966.

Winowich N.S. *Numerical prediction of turbulent flame stability in premixed, prevaporised (HSCT) combustors* (final report). NASA CR-188991, 1990.